Title	Electronic Structures of Mn Based Alloys and Transition Metal Intercalated IT-TiS2
Author(s)	木村, 昭夫
Citation	大阪大学, 1995, 博士論文
Version Type	VoR
URL	https://doi.org/10.11501/3081501
rights	
Note	

Electronic Structures of Mn-Based Alloys and Transition Metal Intercalated 1T-TiS$_2$

Doctoral Thesis

Akio Kimura

Department of Material Physics,
Faculty of Engineering Science,
Osaka University

Chapter 1

Electronic Structures of Mn Based Alloys

1.1 Introduction

1.1.1 Physical properties of several Mn alloys

Several Mn based alloys show much interesting properties in terms of complicated magnetic phase transition, strong magneto-optical effects and strong magnetic anisotropy, etc.. We will show first the much interesting physical properties of several Mn-based alloys. The alloys which we have investigated by means of several electron and optical spectroscopies are NiAs-type MnSb, famous Heusler alloys such as PtMnSb, NiMnSb and Ni_2MnSb which are very well known to show the attractive magneto-optical effects, for example, the remarkable Kerr rotation angle in the case of PtMnSb, and Cu_2Sb type Mn_2Sb and MnAlGe which shows the rather complicated magnetic phase transition with changing temperature and applied pressure and upon substitusion of the other atoms in the case of Mn_2Sb.

A: ***crystal and magnetic structures***

PtMnSb and NiMnSb crystallize in MgAgAs ($C1_b$) type crystal structure [1.1]. Crystal structure of MgAgAs ($C1_b$) type is shown in Fig.1.1.(a), where Pt (Ni) and Mn atoms form NaCl type lattice and the interpenetrated Sb lattice is fcc. Thus the Pt (Ni) and Mn atoms are surrounded by the four nearest Sb atoms. In the case of Ni_2MnSb, the structure is Cu_2MnAl ($L2_1$) type as depicted in Fig.1.1.(b), where Mn and Sb atoms form NaCl-type lattice [1.2], which interpenetrates the simple cubic Ni lattice. PtMnSb and NiMnSb show ferromagnetism with T_C of 575K and 730K, respectively [1.1]. In both alloys, the observed magnetic moments of Mn atom are about $4\mu_B$. MnSb shows a hexagonal NiAs type crystal structure and a ferromagnetism with T_C of 585K [1.3]. Mn_2Sb and MnAlGe have Cu_2Sb type crystal structure [1.4]. Mn_2Sb has two different magnetic sites I and II, where Mn(I) atoms are situated at the tetrahedral sites in regard to the surrounding Sb atoms and Mn(II) atoms are situated at the octahedral sites as shown in Fig.1.1.(d). Mn_2Sb shows ferrimagnetic structure with T_C of 550K. Neutron diffraction studies show the presence of a triple layer of Mn(II)-Mn(I)-Mn(II) with antiparallel magnetic moments on the Mn(I) and Mn(II) sites in ferrimagnetic structure. As shown in Table.1.1., the magnitude of magnetic moment of Mn(II) is about twice as large as that of Mn(I). On the other hand, MnAlGe is a simple ferromagnet with T_C of 518K since non-magnetic Al atoms preferentially occupy the II site, whereas Mn atoms occupy only the I site [1.4].

B: *magnet-optical effects*

The magneto-optical Kerr effect (MOKE) has been studied extensively over the past several years. Much of interest has centered on the use of this technique to investigate the electronic structure of magnetic systems. Also, part of the interest stems from the possibility of using the MOKE for erasable optical recording. For PtMnSb, it is reported that the polar Kerr effect -the rotation of the polarization of linearly polarized light by normal reflection at the surface of a ferromagnetic metal- is unusually high. For incident light with a wavelength of 720nm (~1.7eV), a rotation of -1.27° is found [1.5]. This is the highest rotation ever found for a metallic material at room temperature. Until this discovery, MnBi, which has the NiAs crystal structure, had the highest known Kerr rotation at room temperature, -0.70° at 633nm (~1.96eV) [1.6]. NiMnSb which has the same crystal structure as PtMnSb shows the smaller magnitude of the Kerr rotation angle compared with that of PtMnSb [1.7]. The maximum Kerr rotation of MnSb is a factor of 2 lower [1.8].

C: *magnetic anisotropy*

MnSb and MnBi are well known to show the strong uniaxial magnetic anisotropy [1.9]. At high temperatures, the c-axis is the easy direction of magnetization in both alloys. In MnSb the magnetic moment flops into the a-b plane at 510K. The magnetic moment of MnBi gradually deviates from the c-axis below 142K, and flops into the a-b plane at 90K. Such a spin reorientation phenomenon is also observed in Mn_2Sb. According to the neutron diffraction studies, there is a spin flop transition at T_{sf}=240K, where the atomic spins are aligned parallel and perpendicular to the c-axis above and below this temperature.

1.1.2 One-electron band pictures

A:*Exchange splitting*

One electron band calculations have been intensively carried out for several Mn alloys by many authors in order to understand the attractive physical properties. The electron number of Mn 3d states (n_d), the value of exchange splitting (ΔE), the magnetic moment (μ_d) and the ratio $I=\Delta E/\mu_d$ calculated by means of ASW method [1.10] for intermetallic compounds containing Mn and Sb are listed in Table.1.2.. It is noted that the calculated magnetic moments of Mn atoms vary strongly, whereas the ratio $I=\Delta E/\mu_d$ is nearly the same for all alloys and does not depend on the type of magnetic order in MnSb and Mn_2Sb.

The intra-atomic exchange interaction between Mn 3d electrons can be expressed in terms of the average interaction between parallel spins

$$J=\frac{1}{14}(F^{(2)}+F^{(4)})$$

where $F^{(2)}$ and $F^{(4)}$ are Slater integrals [1.11]. With the values $F^{(2)}=8.72eV$ and$F^{(4)}=5.20eV$ [1.12], one obtains J=0.99eV. The semiempirical relation

$$J=0.59+0.075(Z-21)$$

gives for Mn (Z=25) a value J=0.89eV [1.11]. If intra-atomic exchange interaction are the origin of the exchange splitting between spin-up and spin-down bands, one expects $I=\Delta E/\mu_d$ to be equal to J. The fact that the values of I obtained from the band structure calculations are very close to the atomic parameter J proves that *the exchange splitting between Mn 3d electrons is mainly caused by an intra-atomic effect.*

B: *Magneto-optical effects*

R.A.de Groot et al. performed a self-consistent and scalar relativistic band calculation on PtMnSb and NiMnSb and discussed the difference of MOKE between these alloys by the spin-polarized band structures [1.13,14]. Surprizingly, the calculated band structures of these alloys show unusual features, that is, the majority spin band crosses E_F, whereas the minority-spin band shows the semiconducting character. Generally speaking, the origin of the MOKE is derived by the imcomplete cancellation of optical transitions for left and right circularly polarized light. The calculated band structures of PtMnSb and NiMnSb for majority and minority spin electrons are shown in Figs.1.2.(a) and (b). The large MOKE of PtMnSb has been attributed to the peculiar electronic structure of this alloy. The top of the valence band Γ_4 for the minority spin direction is located just below the Fermi energy. The states at the top of the valence band are of primarily Sb 5p character. Under the influence of spin-orbit interaction this triply degenerate Γ_4 state splits into three equidistant singlets, with orbital quantum numbers m=-1, 0, and +1 (orbital quantization with respect to the direction of magnetization) as shown in Fig.1.3.. The highest singlet state m=+1 is located above the Fermi level, and therefore cannot serve as initial state for optical excitations. Thus the excitations from Γ_4 to the empty Γ_1 level (mainly Pt 6s character) are magneto-optically uncompensated. The oscillator strength of these transitions is large; the excitation energy coincides with the onset of the observed peak in the off diagonal part of the dielectric tensor leads to an enhancement of the MOKE at the plasma energy, which falls in this energy range. The combination of the two effects explains quite well the observed peak with a large MOKE at about 1.7eV in PtMnSb.

In comparing the band structures of PtMnSb and NiMnSb, a striking difference is the position of the first unoccupied Γ_1 state for minority spin electrons. This state is located at about 1eV above the top of the valence band in PtMnSb, but in NiMnSb it is about 4.2eV above the top of the valence band. The observed intensity of the excitation in NiMnSb is much lower, due to joint density of states or oscillator strength effect. In NiMnSb, a (weaker) peak in the off-diagonal part of the dielectric tensor is observed near 4eV. Thus the key question is why the final states in PtMnSb are so favorable and in NiMnSb are so unfavorable for the MOKE.

The main difference between PtMnSb and NiMnSb is the higher nuclear charge of Pt with respect to Ni. The character of the wave function of the final Γ_1 state is rather delocalized, with Pt 6s (or Ni 4s) character as dominant contributors. Relativistic effects can be separated into spin-orbit contributions and scalar relativistic effects, the so-called mass-velocity and Darwin terms. The latter two terms do not lead to splitting of energy levels, but produce energy shifts which are largest for s levels because of the finite value of the s wave function at the nucleus.

The band structures shown in Figs.1.2.(a) and (b). were calculated with the ASW method, including mass-velocity and Darwin terms. In order to explicitly find the influence of these relativistic terms they also performed a completely non-relativistic calculation of PtMnSb and NiMnSb. The main difference with the relativistic calculations is a shift of the Γ_1 level for minority spin electrons by 1.8eV in PtMnSb; the corresponding shift in NiMnSb is much smaller as shown in Figs.1.2 (c) and (d). Moreover, the strong interaction of this Γ_1 level with the empty Γ_4 level in NiMnSb (of primarily Mn 3d character) leads to a strong dispersion away from Γ_1, and a corresponding decrease of the strength of the magneto-optical transitions, due to a smaller joint density of states.

C:*Localized spin moments of itinerant electrons*

Although it is well known to show the localized spin character in the several Heusler alloys, the electronic structures have been well understood in terms of the one-electron band pictures. J.Kübler et al. [1.15] suggested in their systematic band calculations of $L2_1$-type Heusler alloys (X_2MnY) as follows: the Mn 3d majority spin states are almost completely occupied and the bandwidths indicate that they are just as delocalized as the d electrons of Co, Ni, Cu, or Pd as schematically described in Fig.1.4.. The Mn 3d minority spin states, however, are nearly empty. In other words, the spin-up d electrons of the Mn atoms join those of the X atoms in forming a common d band, whereas the spin-down d electrons are almost completely excluded from the Mn sites.

D:*Hybridization between Mn 3d and Sb 5p states*

Fig.1.5. shows the calculated DOS of MnSb by using the ASW method [1.16]. The band structure shows an exchange splitting of the Mn 3d band of about 3.5eV. For majority-spin direction there is a 2eV wide peak in the DOS around -2.5eV, which originates from states with Mn 3d character. Due to hybridization with the states in the underlying broad Sb 5p band, there is a tail in the Mn 3d partial DOS which extends to the region above E_F. A similar situation is found for the minority-spin direction. In this case we find a Mn 3d peak in the DOS at about 1eV above E_F. Because of the hybridization the calculated magnetic moment per Mn atoms is not $5\mu_B$, but only $3.24\mu_B$. The calculated partial DOS of Sb is described as follows:

1) The Sb 5s band, 10eV below E_F, with a width of about 3eV.

2) The Sb 5p band, from -5.7 to +3.0eV for majority-spin electrons and from -5.3 to +4.0eV for minority-spin electrons. Due to the hybridization with Mn 3d states, a small net magnetic moment of $-0.06\mu_B$ per Sb atom induced.

3) The Sb 5d band, strongly mixed with Mn 4s and 4p states, at energies above 4.0eV.

The pronounced structure in the Sb 5p partial DOS shows that the p-d hybridization cannot be described simply as an interaction of Mn 3d states with a structureless continuum of free-electron like Sb derived states. Furthermore, the exchange splitting of the Sb 5p band cannot be simply described by a single value because the p-d interaction depends on the symmetry properties of the bands.

The authors discussed the hybridization mechanism by analyzing in some detail the band structure of Γ point in the Brillouin zone. The Sb 5p band contains six p states per unit cell, which can be classified as

Γ_3^+ : z_1+z_2
Γ_6^- : $x_1+x_2\pm i(y_1+y_2)$
Γ_5^+ : $x_1-x_2\pm i(y_1-y_2)$
Γ_2^- : z_1-z_2

where x, y and x represents the p_x, p_y and p_z orbitals, respectively. Subscripts 1 and 2 refer to the two antimony sites. In neglecting the hybridization with Sb 5p states, the shape of the Mn 3d band is determined by the interaction between the neighboring Mn atoms along the c-axis. This is because the nearest-neighbor Mn-Mn distance along the c-axis (2.87Å) is much smaller than the distance of Mn atoms in the x-y plane (4.12Å). There are ten d states per unit cell per spin direction, which can be classified as

Γ_1^+ a^T_{1+} : $z^2{}_1+z^2{}_2$,
Γ_5^+ e_+ : $yz_1-yz_2\pm i(xz_1-xz_2)$,
Γ_5^+ e^T_+ : $xy_1+xy_2\pm i[(x^2-y^2)_1+(x^2-y^2)_2]$,
Γ_6^+ e^T_- : $xy_1-xy_2\pm i[(x^2-y^2)_1-(x^2-y^2)_2]$,
Γ_6^+ e_- : $yz_1+yz_2\pm i(xz_1+xz_2)$,
Γ_3^+ a^T_{1-} : $z^2{}_1-z^2{}_2$

where z^2, xy, yz, xz and (x^2-y^2) represent the $d_{3z^2-r^2}$, d_{xy}, d_{yz} and d_{xz} and $d_{x^2-y^2}$ orbitals. Subscript 1 and 2 refer to the two Mn sites. The notations $a^T{}_1$, e, and e^T, with + and - signs for binding and antibonding states, respectively.

The hybridization between Mn 3d and Sb 5p states is argued with a simple model. The hybridization between the Sb 5p and Mn 3d orbitals is described by σ bonding interactions of Mn 3d e_g-type orbitals with Sb 5p; π-bonding interactions of Mn 3d e^t_g and Mn a^t_{1g} orbitals with Sb 5p are neglected. It is assumed that the splitting into bonding and antibonding levels is symmetric; this is the case if the overlap integrals between the orbitals are zero. The calculated energy levels are shown in Fig.1.6. for the majority-spin and minority-spin directions, respectively. The left part of these diagrams gives the position of Mn 3d and Sb 5p states in the absence of the p-d hybridization, the right part gives the calculated energy levels.

1) Mn 3d states have positive parity, which implies that Γ_2^- and Γ_6^- states play no role in the p-d interaction. The same is true for Γ_6^+ manganese states, because there is no antimony Γ_6^+ state. Therefore the Γ_2^- and Γ_6^- states will have the same energy for the two spin directions.

2) Both Mn Γ_5^+ states can hybridize with the Sb Γ_5^+ state. The manganese states can combine to the states with e^t_g and e_g symmetry, of which only e_g states interact appreciably with the antimony states. Only this e_g state forms a σ-bonding and antibonding combination with the Sb Γ_5^+ state. The interaction is strongest for the minority spin electrons, because of the smaller energy distance between the interacting states.

3) From the energy distance between e^T_- and e_- states and the energy of the $\Gamma_5^+(e^t_g)$ state, the position of the e_+ and e^T_+ states has been derived.

4) From the energy distance between the Γ_1^+ (a^{T}_{1+}) state, which does not hybridize with Sb 5p states, and the $\Gamma_5^+(e_+)$ state, the position of the Γ_3^+ (a^{T}_{1-}) state can be derived.

5) The position of Sb 5p Γ_5^+ and Γ_3^+ states, without p-d hybridization, can be derived by assuming the mean energy of states that form bonding and anti-bonding combinations does not change. This is indeed the case if the overlap integral of the two orbitals is zero.

1.2 Magnetic circular dichroism observed in the soft X-ray absorption regions of Mn-based ferromagnetic alloys

1.2.1 Introduction

In order to clarify the spin dependent electronic structures of these alloys, we have observed the MCD spectra in the Mn 2p and 3p core excitation regions. In addition, the electronic states of the Ni 3d orbital will be discussed through the MCD spectra in the Ni 2p core excitation region of NiMnSb and Ni_2MnSb. The hybridization effect between Mn 3d and Sb 5p states will be also argued through the MCD spectra in the Sb 3d→5p excitation region.

The expected MCD spectrum will be shown with a simple model in the case of the transition metal 2p→3d excitation. In the upper part of Fig.1.7.. the transition metal 3d states are simply described for (a) non-magnetic system, (b) magnetic system with only a spin moment and (c) magnetic system with spin and orbital moments, where the shaded area represents the occupied electrons in the 3d states. According to the selection rules for a helically polarized light, only the transition with $\Delta m=+1(\Delta m=-1)$ is allowed. By taking the Gaunt's coefficients associated with the p→d transition into account [1.17], the corresponding transition probabilities strongly depend on the spin and angular momentums of the 3d states as shown in the lower panel of Fig.1.7.. The overall transition features are described as follows: In the case of the $2p_{3/2}$ core excitation, the transition probability to the up-spin 3d states with the larger angular momentum is dominant for $\Delta m=+1$, whereas the transition to the down-spin states with the lower m becomes dominant for $\Delta m=-1$. On the other hand, in the case of the $2p_{1/2}$ core excitation, the transition probability to the down-spin states with the larger m is dominant for $\Delta m=+1$, whereas the transition to the up-spin states with the lower m is dominant for Δm=-1. When the MCD spectrum is defined as I(m=+1)-I(m=-1), the MCD spectrum is expected to show negative and positive signs at $2p_{3/2}$ and $2p_{1/2}$ core excitations, respectively.

1.2.2 Experimental

The Mn 3p absorption and MCD spectra were measured by using synchrotron radiation at BL-28A of Photon Factory of the National Laboratory for High Energy Physics (KEK). The Mn 2p, Ni 2p and Sb 3d absorption and MCD spectra were measured at the NE1B of the TRISTAN Accumlation Ring (AR) in KEK. At both beamlines, circularly polarized light was supplied with a helical undulator, with which almost 100% circulary polarization would be obtained at the peak of the first harmonic radiation. In fact about 95% polarization with photon energy of 97eV was measured at BL-28A even after the grating monochromator. Although the polarization have not been measured at NE1B, the higher polarization as obtained in BL-28A is expected because the optics at NE1B includes only very grazing angles of incidence which would minimize possible reduction of circular polarization.

The spectra were measured by means of the total photoelectron yield method by directly measuring the sample current with changing the photon energy. It is widely known that the total photoelectron yield well represents the absorption in the core excitation region. The magnetic field of about 1.1Tesla was applied with using the permanent magnet made of the Nd-Fe-B alloy. The MCD spectra were taken for a particular helicity of light by reversing the applied magnetic field at every photon energy. In the present paper, the MCD spectrum is defined as $I_{\uparrow\uparrow}$ - $I_{\uparrow\downarrow}$ where $I_{\uparrow\uparrow}$ and $I_{\uparrow\downarrow}$ are the absorption intensity with the directions between the majority spin and the photon spin (helicity) parallel and antiparallel, respectively.

Clean surfaces were obtained by *in situ* scraping of the sample under the ultra high vacumm condition (1×10^{-9}Torr). The cleanliness of the sample surface was checked by the disappearance of the pre-edge structure which is characteristic of the Mn-oxides. The 3d electrons of the present Mn alloys are rather itinerant and their spectra are somewhat broader compared with the insulating Mn-oxides. We could also check the degree of contamination from the magnitude of the MCD signal because the amplitude grew and finally saturated if the sample surface become ultimately clean. We thought that the unscraped or contaminated surface was covered with the antiferromagnetic or paramagnetic compounds such as Mn-oxides, which hardly contribute to the MCD spectrum.

1.2.3 Results

A: *Absorption and MCD spectra in the Mn 2p core excitation region*

The total photoelectron yield (XAS) and MCD spectra in the Mn 2p core excitation of several Mn alloys are shown in Figs.1.8. (a)-(f). The clear multiplet structures are found in the Mn 2p XAS spectra of NiMnSb, Ni_2MnSb and PtMnSb. In these spectra, a sharp peak structure and a doublet are observed at Mn $2p_{3/2}$ and $2p_{1/2}$ core excitation thresholds, respectively. In addition, the shoulder structure is found on the larger energy side of $2p_{3/2}$ component in the XAS spectra of NiMnSb and PtMnSb. Such a shoulder is somewhat weaker in the cases of Ni_2MnSb. As for the MCD spectra of these materials, the negative and small positive signal is found within the $2p_{3/2}$ core excitation region with increasing hν and the small positive signal which has the double peak structure is recognized at the $2p_{1/2}$ region.

As shown in Fig.1-8(c), the 2p XAS spectrum of MnSb shows broader line shape with no clear multiplet structures both in the $2p_{3/2}$ and $2p_{1/2}$ components compared with those of NiMnSb, PtMnSb and Ni_2MnSb. In addition, the appreciable tail is recognizable toward the higher hν. The MCD spectrum shows the negative and positive sign within the $2p_{3/2}$ region with increasing photon energy (hν) and the only positive sign at $2p_{1/2}$ region. A doublet feature in the $2p_{1/2}$ region as observed in the spectra of Heusler alloys seems to be much broadened in the spectrum of MnSb. In addition, it is found that the spectral width of the negative MCD signal located on the lower energy side of the Mn $2p_{3/2}$ absorption region is considerably broader than those of Heusler alloys.

Mn 2p XAS spectrum of Mn_2Sb also shows no clear multiplet structures in a wide energy range of Mn 2p core excitation region and reveals the higher energy tail as observed in the spectrum of MnSb. The spectral width of the negative MCD signal located at the lower energy of $2p_{3/2}$ component is narrower than that of MnSb and is comparable to those of PtMnSb, NiMnSb and Ni_2MnSb (Heusler alloys). The double peak structure is not so much sharp compared with the spectra of NiMnSb, Ni_2MnSb and PtMnSb.

Among several Mn alloys mentioned above, the line shape of both of the XAS and MCD spectra of MnAlGe is quite different, that is, the XAS spectrum show the much broad and asymmetric line shapes at both of the $2p_{3/2}$ and $2p_{1/2}$ core excitation regions. Overall trend of the MCD spectrum of MnAlGe is similar to those of the other Mn alloys, i.e., the negative and positive signals are observed over the $2p_{3/2}$ region and the clear doublet positive structure exists in the $2p_{1/2}$ region. It is, however, there are some different points from those of the other materials as follows:

1) the spectral width of the negative MCD in the lower energy portion of the $2p_{3/2}$ component is quite broader.

2) the rather flat structure is found in the intermediate region between the $2p_{3/2}$ and $2p_{1/2}$ components.

B: *Absorption and MCD spectra in the other core excitation region*

We have also observed the absorption and MCD spectra in the Ni 2p core excitation region of NiMnSb and Ni_2MnSb. As shown in Fig.1.9.(a) and (b), the several multiplet structures are found along with the sharp main peak both in the $2p_{3/2}$ and $2p_{1/2}$ components of the XAS spectra of these two alloys. As for the MCD spectra of these alloys, it is found that the negative and positive MCD signals are observed at $2p_{3/2}$ and $2p_{1/2}$ components, respectively. It is, however, noticed that the small but quite sharp structure with the opposite sign to that of the main MCD signals appear prior to the $2p_{3/2}$ and $2p_{1/2}$ absorption peaks in the case of NiMnSb. On the other hand, such a feature is not observed in the MCD spectrum of Ni_2MnSb.

The weak but clear MCD features are observed even in the Sb 3d→5p excitation region for Mn_2Sb and NiMnSb (Figs.1.10.) The Sb 3d XAS spectrum of these alloys show the spin-orbit split components, i.e., $3d_{5/2}$ and $3d_{3/2}$ with the energy separation of about 10eV. The negative and positive MCD signals are observed at $3d_{5/2}$ and $3d_{3/2}$ components, respectively in both spectra of Mn_2Sb and NiMnSb. Such clear MCD spectra strongly indicate the induced magnetic moments on the Sb sites in Mn_2Sb and NiMnSb.

C: *Absorption and MCD spectra in the Mn 3p core excitation region*

The total photoelectron yield and MCD spectra taken over the Mn 3p core excitation region are given in Fig.1.11. (a)-(e) In the upper part of the figure, the polarization averaged absorption spectrum , $(I_{\uparrow\uparrow} + I_{\uparrow\downarrow})/2$, is shown and the MCD spectrum defined as $I_{\uparrow\uparrow} - I_{\uparrow\downarrow}$ is given in the lower part.

All the total photoelectron yield spectra show asymmetric line shapes with remarkable tail toward higher hν with no clear multiplet structures. It is recognized that the absorption spectrum of MnAlGe shows a quite broad line shape with a dip structure around hν=48eV, whereas the absorption spectra of the other materials have the peak structure around hν=52eV with no noticeable dip structure in the smaller hν region.

The MCD spectrum of MnAlGe has clear multiplet structures with the almost negative sign over the whole energy region as demonstrated in the lower portion of Fig.1.11.(d). The predominantly negative MCD is in a strong contrast to the result of the Mn 2p core excitation. On the other hand, the MCD of Mn_2Sb shows the rather complicated spectrum where a small positive peak appears around hν=49eV in addition to the strong negative (positive) signal around 51(53eV) [Fig.1.11.(e)]. Such a complicated MCD spectrum should be understood by considering the nonequivalent contributions of the Mn(I) and Mn(II) sites to the spectrum as will be discussed below.

In Figs.1.11.(a)-(c), the absorption and MCD spectra of MnSb, NiMnSb and Ni_2MnSb are shown. Although the normal MCD signals with the negative-positive peaks are observed for all the spectra, the differences among these spectra are found in the spectral width and shape. It is noticed that the onset of the MCD is located at the lowest hν in MnSb compared with those of NiMnSb and Ni_2MnSb and the width of the negative MCD signals of NiMnSb and Ni_2MnSb is narrower than that of MnSb.

1.2.4 Discussion

A: *Absorption and MCD spectra in the Mn 2p core excitation region*

First of all, the degree of the electron itinerancy and the electron number will be discussed below through the observed different line shapes between the Mn 2p XAS and MCD spectra of MnSb and the Heusler alloys (NiMnSb, Ni_2MnSb and PtMnSb). It has been shown that the overall similar features are observed in the Mn 2p XAS spectra of PtMnSb, NiMnSb and Ni_2MnSb, where the sharp peak structure with a shoulder at the larger energy part of the $2p_{3/2}$ and the clear doublet structure at the $2p_{1/2}$ are revealed. Such a feature is also observed in the Mn 2p XAS spectra of gas-phase Mn and impurity Mn diluted in noble metal hosts [1.18]. The multiplet calculation [1.19] for Mn 2p XAS spectrum assuming $3d^5$ configuration in the ground state well reproduces the above-mentioned experimental spectra except for the trivial differences. The broader spectral shapes with no clear multiplets as found in the Mn 2p XAS spectra of MnSb. Such a broadening is usually found in the metallc systems containing Mn atom. Fig.1.12. systematically shows the Mn 2p XAS spectra of gas-phase Mn, *Ag*Mn, *Cu*Mn and metallic Mn [1.18]. It is widely known that the itinerancy of Mn 3d electrons becomes stronger from atomic Mn to metallic Mn. Thus it can be clearly recognized that the spectrum becomes broader with increasing the itinerancy of Mn 3d electrons, which strongly indicates the correlation between the electron itinerancy and the spectral broadening. Fig.1.13. shows the calculated Mn 2p XAS spectra using the atomic multiplets assuming various possible ground state terms [1.20], where only the lowest energy initial-state terms are included. It is noticed that the spectral line shape is much sensitive to the groun-state electronic configurations and various states split only by spin-orbit interactions as in the $d^5(^4G_J)$, $d^4(^5D_J)$ and $d^6(^5D_J)$ manifolds. Since the spin-orbit splitting of these states is only in the meV range for 3d transition metals, this demonstrates that even though the resolution of spectroscopies involving core lines is in the eV range one can distinguish possible initial states separated in energy by only a few meV. As suggested by B.T.Thole et al. [1.20], if the bandwidth of the Mn 3d states becomes greater than the splitting between the ground-state terms, the XAS final state spectrum is expected to involve more than one multiplet terms or electronic configurations. Therefore *the broader line shape observed in the spectrum of MnSb is mainly considered to be due to the broader bandwidth* compared with those of the Heusler alloys.

The MCD spectrum with negative-positive signs at $2p_{3/2}$ component and positive sign at $2p_{1/2}$ component as observed in the spectra of NiMnSb, Ni_2MnSb and PtMnSb is also well reproduced by the multiplet calculation assuming the Mn $3d^5$ confuguration in the ground state with respect to the line shapes and energy separations between the intense multiplet lines [1.19].(Fig.1.14.) In contrast to these alloys, the negative MCD spectrum of MnSb is rather broader and shows no clear multiplet structures. Now, if the selection rule is taken into account, the negative MCD signal mainly reflect the minority spin band structure in the unoccupied electronic state as discussed in the previous section. According to the band calculation results, the DOS of NiMnSb, Ni_2MnSb and PtMnSb show the appreciable intraatomic exchange splitting of the Mn 3d states resulting in the almost occupied (unoccupied) majority (minority) spin state. Since the Ni 3d or Pt 5d states are considered to be almost occupied for both spin directions, the hybridization between the minority spin Mn 3d and the Ni 3d or Pt 5d states is considered to be not so much strong. Furthermore the hybridization between the neighboring

Mn atoms is also considered to be weak due to the much larger atomic distance of about 4Å [1.20, 21]. Therefore it is considered that the band width of the minority unoccupied states is resultingly narrower in NiMnSb, Ni_2MnSb and PtMnSb. In contrast to this, the band calculation shows that the hybridization between the neighboring Mn in MnSb is important compared with those of the Heusler alloys because the atomic distance between them is shorter (~2.87Å)[1.22].

Next, we will discuss about the 3d electron number of the present several Mn alloys , the almost $3d^5$ configuration is suggested by the band calculations of NiMnSb, Ni_2MnSb and PtMnSb as listed in Table.1.2 [1.10]. As discussed above, the present results of XAS and MCD spectrum is in good agreement with the band calculated results. On the other hand, the band calculation predicts that the 3d electron number belongs to the intermediate region between $3d^5$ and $3d^6$ configurations which may derive the different line shape of the Mn 2p XAS spectrum of MnSb, which is consistent with the broader spectral line shapes of the Mn 2p XAS and MCD spectrum.

Although the Mn 3d electrons of MnAlGe is considered to be rather itinerant, its quite different line shapes observed in the Mn 2p XAS and MCD spectra of MnAlGe can be qualitatively understood in terms of the atomic multiplet picture because the excited 3d electron is considered to be localized on the Mn site due to the strong Coulomb attraction between the 2p core hole and 3d electron. Fig.1.15. shows the calculated Fe 2p XAS and MCD spectra using the atomic multiplets assuming d^6 configuration in the ground state [1.19]. It is recognized that the broader spectral line shape and the asymmetry toward the higher energy is revealed in the absorption spectrum denoted by I. In addition, only a single peak structure is found in the $2p_{1/2}$ component in the absorption spectrum, where the clear double peak structure is observed in the corresponding spectrum for the d^5 system (Fig.1.14.). As for the calculated MCD spectrum which is represented as L-R, the negative and broader spectral line shape is definitely revealed in the lower energy region of $2p_{3/2}$ component. Besides, the flatness of the positive MCD at the higher energy region of $2p_{3/2}$ and the double peak structure at $2p_{1/2}$ region are found in this calculated spectrum. Such characteristic features found in the XAS and MCD spectra for d^6 system are possibly considered to explain the experimental spectra of MnAlGe. This indicates that the electron occupation number of the Mn 3d states is possibly close to 6.

In interpretating the Mn 2p XAS and MCD spectra of Mn_2Sb, the inequivalent contributions of the two Mn sites should be considered. It is known that there are two crystallographically inequivalent Mn sites, [Mn(I), Mn(II)] in Mn_2Sb [1.4]. According to the neutron diffraction study, the magnetic moment of Mn(II) is approximately twice as large as that of Mn(I) and the magnetic moments of these sites are mutually antiparallel, resulting in the formation of the ferrimagnetic structure. On the other hand, in the case of the same Cu_2Sb-type MnAlGe, the Mn atom occupy only the Mn(I) site and the nonmagnetic Al occupy the II site [1.4].

If the quantization axis is defined along the direction of the total magnetic moment, the axis of Mn_2Sb is the direction of the magnetic moment derived from the Mn(II) 3d majority spin. Then the Mn(I) 3d majority spin derived moment is antiparallel to the quantization axis. Since the total magnetic moment of MnAlGe is aligned along the Mn(I) 3d majority spin derived moment, the signs of the MCD signals from the Mn(I) should be opposite sign between Mn_2Sb and MnAlGe. Assuming that the Mn(I) 3d state is not much different between Mn_2Sb and MnAlGe, it can be considered that the MCD spectrum of Mn_2Sb should be composed of the two MCD spectra originated from the different Mn sites with mutually opposite signs.

Actually, the observed MCD spectrum of Mn_2Sb shows somewhat similar structure to those of the Heusler alloys except for the broader spectral shape of the double peak observed in the $2p_{1/2}$ region. This indicates that the MCD spectrum derived from the Mn(II) site dominantly contributes to the total MCD spectrum, i.e, the component of the MCD derived from the Mn(I) site is considered to be much weaker.

B: *Absorption and MCD spectra in the Mn 3p core excitation region*

It is noted that the broad and asymmetric line shape of the Mn 3p absorption spectra toward higher hν does not necessarily suggest the itinerant character of the Mn 3d electrons of these alloys because such an asymmetry is mainly caused by the interference between the discrete excitations

$$3p^63d^n \rightarrow 3p^53d^{n+1}$$

and the continuum transitions

$$3p^63d^n \rightarrow 3p^63d^{n-1}\varepsilon l$$

which are strongly coupled by the super Coster-Krönig decay channel given by

$$3p^53d^{n+1} \rightarrow 3p^63d^{n-1}\varepsilon l$$

Thus the asymmetry is expected to be found even in the spectrum of gas phase Mn [1.23], in which clear multiplet structures exist around the pre-threshold region but they are almost unaffected by the interference effect. In the case of pure metallic Mn, the gross feature of the spectral line shape is observed to be similar to that of the atomic Mn [1.23], but no multiplet structure is recognizable particularly around the pre-threshold region prior to the main absorption band. The delocalized character of Mn 3d electrons are also confirmed in the present Mn-alloys judging from the almost similar features recognized in the spectrum of highly delocalized Mn metal.

First, the different MCD features among the spectra of MnSb, NiMnSb and Ni_2MnSb which have rather similar core absorption spectra will be discussed below within one-electron band picture. The spin-polarized band calculation of NiMnSb has revealed the metallic character for the majority spin state and semiconducting character for the minority spin state [1.14]. Such "half-metallic" character is well known to be closely related with the magneto-optical effects. Ni_2MnSb is shown to be metallic for both spin directions by the calculation [1.24]. For these materials, it is suggested that Mn 3d electrons are rather itinerant because of the appreciable covalency between the majority Mn 3d state and the nearly filled Ni 3d state, whereas the magnetic moment is localized on the atomic site because the minority Mn 3d state is located almost completely in the unoccupied state due to the strong intra-atomic exchange interaction of the Mn 3d states. In the two Heusler alloys, the direct Mn-Mn hybridization seems to be unimportant because the atomic distance between the neighboring Mn is fairly large (4.2Å)[1.20, 21]. On the other hand, the direct hybridization between the neighboring Mn is considered to be relatively strong for MnSb because the nearest-neghbor distance is much shorter (-2.87Å)[1.22] than those of the NiMnSb and

Ni_2MnSb. Such a shorter atomic distance will cause the broader band width of Mn 3d states for both of the majority and minority Mn 3d states. As mentioned above, the negative MCD component related to the $3p_{3/2}$ absorption mostly reflects the transition to the Mn 3d minority unoccupied states. Therefore, the broader negative MCD spectrum of MnSb may indicate the broader band width of the minority Mn 3d unoccupied states, which is consistent with the shorter atomic distance between the neighboring Mn atoms as described above. On the other hand, the narrower negative MCD spectrum and its delayed MCD onset is consistent with the semiconducting character of the minority Mn 3d state in NiMnSb and the smaller hybridization between the neghboring Mn atoms in NiMnSb and Ni_2MnSb compared with the case of MnSb due to the large atomic distance.

The difference of the line shapes between the absorption and MCD spectra of MnAlGe and Mn_2Sb as pointed above is possibly thought to be mainly caused by the different unoccupied electronic states. As previously discussed in our paper on photoemission (PES) and inverse photoemission (IPES) experiments [1.25, 26] and in the band calculations [1.27, 28], the Mn(I) 3d electrons are more itinerant compared with the Mn(II) 3d electrons. Thus the fairly broad band width of the unoccupied state is expected for MnAlGe, whereas the sharper unoccupied density of states is expected for Mn_2Sb because the Mn(II) 3d states are superimposed on the broad Mn(I) 3d component, as confirmed in the IPES experiment. This fact will provide fairly structureless and broad absorption feature for MnAlGe and a prominent peak structure of the absoprption spectrum for Mn_2Sb.

The predominantly negative MCD spectrum of MnAlGe in a wide energy region is in a strong contrast to the case of the Mn 2p core excitation as discussed above. In the case the Mn 2p core excitation, the negative and positive MCD signals corresponding to the lower($2p_{3/2}$) and the higher($2p_{1/2}$) hν components are clearly found and its integrated value over the whole Mn 2p→3d core absorption region led to the almost negligible amount of the Mn 3d orbital moment. This discrepancy can be relaxed by considering the much smaller spin-orbit splitting of the Mn 3p core level than that of the Mn 2p core, i.e., the negative and positive MCD signal of the lower and higher hν components are thought to be appreciably cancelled out being due to the much smaller spin-orbit splitting.

As recognized in Fig.1.11.(e), the MCD spectrum of Mn_2Sb shows the small positive peak structure around hν=49eV in addition to the broader negative-positive signals with increasing hν. As mentioned above, there are two inequivalent Mn sites, [Mn(I), Mn(II)] in Mn_2Sb. According to the neutron diffraction experiment of Mn_2Sb, the magnetic moment of Mn(II) is approximately twice as large as that of Mn(I) and the magnetic moments of these sites are mutually antiparallel, resulting in the formation of the ferrimagnetic structure. Therefore the two different contributions should be taken into account in interpretating the MCD spectrum of Mn_2Sb. On the other hand, the Mn atom occupy only the Mn(I) site and the nonmagnetic Al occupy the II site in MnAlGe.

As mentioned above, if the quantization axis is defined along the direction of the total magnetic moment, the axis of Mn_2Sb is the direction of the magnetic moment derived from the Mn(II) 3d majority spin. Then the Mn(I) 3d majority spin derived moment is antiparallel to the quantization axis. Since the total magnetic moment of MnAlGe is aligned along the Mn(I) 3d majority spin derived moment, the sign of the MCD signal derived from the Mn(I) should have opposite sign between Mn_2Sb and MnAlGe. Assuming that the Mn(I) 3d state is not much different between Mn_2Sb and MnAlGe including the effect from the Auger decay, it is considered that the MCD signal from the Mn(I) is almost positive over the whole energy range in the spectrum of Mn_2Sb. It is possible to interpret the observed large positive MCD signal located on the higher energy side as derived from the superposition of the Mn(I) on the spectrum of Mn(II) in the higher hν region.

1.2.5 Conclusion

In summary, the core absorption and MCD spectra of some Heusler alloys (PtMnSb, NiMnSb and Ni_2MnSb), NiAs-type MnSb and Cu_2Sb-type MnAlGe and Mn_2Sb have been measured. The XAS and MCD spectra in the Mn 2p and 3p core excitation regions of these alloys show the remarkable different spectral features in terms of the spectral widths and line shapes reflecting the different electronic structures of these materials. The broader spectral shape observed in the Mn 2p and 3p XAS spectrum indicates the highly delocalized character of the Mn 3d electrons as observed in MnSb compared with those of the Heusler alloys, which is consistent with the different atomic distance between the neighboring Mn mainly resulting in the different band width of the Mn 3d states. In addition, it is revealed that the electron number of the Mn 3d orbital (n_d) is close to 5 in the Heusler alloys, whereas the corresponding value is approximately 6 in MnAlGe judging from the spectral line shape of the Mn 2p XAS and MCD spectra, which is qualitatively in good agreement with the thoretical values derived from the band calculations.

The MCD spectrum in the Mn 3p core excitation region of MnAlGe revealed quite different feature from that in the Mn 2p core excitation, which is partly due to the cancellation of the negative and positive MCD signals observed in the MCD spectrum in the Mn 2p core excitation region. It should be ,however, taken into account, the different final states or the interference effect characteristic of the absorption from the shallower core state.

The absorption spectrum of Sb 3d XAS spectra of some Mn pnictides clearly revealed the asymmetry with the different light polarizations, which strongly indicates the importance of the hybridization between the Mn 3d and Sb 5p orbitals.

References

[1.1] K.Adachi and S.Ogawa, *Landolt-Börnstein New Series* III/27a, ed. H.P.J.Wijn (Springer, Berlin, 1988) p.385.

[1.2] K.Adachi and S.Ogawa, *Landolt-Börnstein New Series* III/27a, ed. H.P.J.Wijn (Springer, Berlin, 1988) p.400.

[1.3] K.Adachi and S.Ogawa, *Landolt-Börnstein New Series* III/27a, ed.H.P.J.Wijn (Springer, Berlin, 1988) p.148.

[1.4] K.Adachi and S.Ogawa, *Landolt-Börnstein New Series* III/27a, ed.H.P.J.Wijn (Springer, Berlin, 1988) p.265.

[1.5] P.G.van Engen, K.H.J.Buschow, R.Jongebreuer and M.Erman, Appl. Phys. Lett. **42** (1983) 202.

[1.6] K.Egashira and T.Yamada, J.Appl. Phys. 45 (1973) 3643.

[1.7] K.Takahashi, J.Watanabe, G.Kido and H.Fujimori, Jpn. J. Appl. Phys. **29L** (1990) 306.

[1.8] P.G.van Engen, unpublished.

[1.9] T.Okita and Y.Makino, J. Phys. Soc. Jpn. **25** (1968) 120.

[1.10] C.Haas and R.A.de Groot, *Recent Advances in Magnetism of Transition Metal Compounds*, eds. A.Kotani and N.Suzuki (World Scientific, Singapore, 1993) p.78.

[1.11] D.van der Marel and G.A.Sawatzky, Phys. Rev. B **37** (1988) 10674.

[1.12] J.S.Griffith, *The Theory of Transition Metal Ions* (Cambridge University Press, Cambridge, 1961).

[1.13] R.A.de Groot, F.M.Mueller, P.G. van Engen and K.H.J.Buschow, J.Appl.Phys. **55** (1984) 2151.

[1.14] J.H.Wijingaard, C.Haas and R.A.de Groot, Phys. Rev. B **40**(1989) 9318.

[1.15] J.Kübler, A.R.Williams and C.B.Sommers, Phys. Rev. B. **28** (1983) 1745.

[1.16] R.Coehoorn, C.Haas and R.A.de Groot, Phys. Rev. B **31** (1985)

[1.17] E.U.Condon and G.H.Shortley, *Theory of Atomic Spectra* (Cambridge University, London, 1959)

[1.18] U.Arp, F.Federmann, E.Källne, B.Sonntag and S.L.Sorensen, J. Phys. B: At. Mol. Opt. Phys. **25** (1992) 3747.

[1.19] G.van der Laan and B.T.Thole, Phys. Rev. B **43** (1991) 13401.

[1.20] B.T.Thole, R.D.Cowan, G.A.Sawatzky, J.Fink and J.C.Fuggle, Phys. Rev. B **31** (1985) 6856.

[1.21] P.J.Webster, R.M.Mankikar, J. Magn. Magn. Mater. **42** (1986) 300.

[1.22] I.Teramoto, A.M.J.G.van Run, J. Phys. Chem. Solids **29** (1968) 347.

[1.23] R.Bruhn, B.Sonntag and H.W.Wolff, Phys. Lett. **69A** (1978) 9.

[1.24] E.Kulatov and I.I.Mazin, J. Phys.:Condens. Matter **2** (1990) 343.

[1.25] A.Kimura, S.Suga, H.Matsubara, T.Matsushita, Y.Saitoh, H.Daimon, T.Kaneko and T.Kanomata, Solid State Commun. **81** (1992) 707.

[1.26] A.Kimura, S.Suga, T.Matsushita, T.Kaneko and T.Kanomata, Solid State Commun. **85** (1993) 901.

[1.27] K.Motizuki, T.Korenari and M.Shirai, J. Magn. & Magn. Mater. **104-107** (1992) 1923.

[1.28] M.Suzuki, M.Shirai and K.Motizuki, J. Phys.:Condens. Matter **4** (1992) L33.

Figure captions

Fig. 1.1.

Crystal structures of (a)PtMnSb (NiMnSb) [MgAgAs ($C1_b$)], (b) Ni_2MnSb [Cu_2MnAl ($L2_1$)], (c) MnSb [NiAs] and (d)Mn_2Sb (MnAlGe) [Cu_2Sb].

Fig. 1.2

Band structures of (a)PtMnSb and (b)NiMnSb for majority (upper part) and minority spin electrons (lower part), calculated with the ASW method including the scalar relativistic effects. For comparison the corresponding band structures of (c)PtMnSb and (d)NiMnSb calculated without the scalar relativistic effects.

Fig. 1.3.

Energy levels around the Fermi energy for the minority-spin direction. The arrows indicate the various allowed transitions. The excitations which are eliminated by the crossing of the m=+1 level and the Fermi level have been drawn with broken lines.

Fig. 1.4.

Localized magnetic moment from delocalized electrons. Schematic energy diagram of up-spin and down-spin d electrons in Heusler alloys

Fig. 1.5.

(a) Calculated total DOS of ferromagnetic MnSb, (b) partial Mn DOS, (c) partial Sb DOS. Units; stateseV^{-1}(unit cell)$^{-1}$.

Fig. 1.6.

Analysis of the hybridization mechanism for ferromagnetic MnSb at the Γ point in the cases of majority-spin (left part) and minority-spin (right part) electrons. (a)Energy levels in the absence of p-d hybridization. (b)Calculated energy levels. Heavy lines indicate degenerate states.

Fig. 1.7.

Upper partt; Schematic description of transition metal 3d orbitals. Shaded area indicates the occupied states.:*Lower part* :p-d photo-excitation probability with different photon polarizations.

Fig. 1.8.

Total photoelectron yield spectra (full and open rhombs) and the MCD spectra (full circles) in the Mn 2p core excitation region of (a)NiMnSb, (b)PtMnSb, (c)MnSb, (d)Ni_2MnSb, (e)MnAlGe and (f)Mn_2Sb. The open (full) rhombs denote the absorption intensity $I_{\uparrow\uparrow}$ ($I_{\uparrow\downarrow}$) with the directions between the majority-spin and photon spin parallel (antiparallel). MCD spectrum is plotted by full circles at lower part of the figure, which is defined as $I_{\uparrow\uparrow}-I_{\uparrow\downarrow}$.

Fig. 1.9.

Total photoelectron yield spectra (full and open rhombs) and the MCD spectra (full circles) in the Ni 2p core excitation region of (a)NiMnSb and (b)Ni_2MnSb. The open (full) rhombs denote the absorption intensity $I_{\uparrow\uparrow}$ ($I_{\uparrow\downarrow}$) with the directions between the majority-spin and photon spin parallel (antiparallel). MCD spectrum is plotted by full circles at lower part of the figure, which is defined as $I_{\uparrow\uparrow}-I_{\uparrow\downarrow}$.

Fig. 1.10

Total photoelectron yield spectra (full and open rhombs) and the MCD spectra (full circles) in the Sb 3d core excitation region of (a)Mn_2Sb and (b)NiMnSb. The open (full) rhombs denote the absorption intensity $I_{\uparrow\uparrow}$ ($I_{\uparrow\downarrow}$) with the directions between the majority-spin and photon spin parallel (antiparallel). MCD spectrum is plotted by full circles at lower part of the figure, which is defined as $I_{\uparrow\uparrow}$-$I_{\uparrow\downarrow}$.

Fig. 1.11.

Total photoelectron yield spectra (solid line) and the MCD spectra (dots) in the Mn 3p core excitation region of (a)NiMnSb, (b)Ni_2MnSb, (c)MnSb, (d)MnAlGe and (e)Mn_2Sb. The MCD spectrum is defined as $I_{\uparrow\uparrow}$-$I_{\uparrow\downarrow}$.

Fig. 1.12.

Comparison of the experimental soft x-ray absorption and electron energy loss spectra in the Mn 2p core excitation region. (a)atomic Mn, (b)5% Mn as an impurity in Ag, (c)3.5% Mn as an impurity in Cu, (d) Mn metal. The spectra are normalized to the same hight of the main peak.

Fig. 1.13.

Calculated EELS or XAS spectra for various possible ground state terms. Only the lowest-energy configurations and terms for Mn are included.

Fig. 1.14.

Calculated Mn 2p XAS and MCD spectra using the atomc multiplets asuming $3d^5$ configuration in the ground state. In the upper (lower) panel, the scaling factor z of the 3d spin-orbit interaction is equal to 1(0).

In this calculation, the Slater integrals and spin-orbit parameters are 80% and 100% of the atomic values.

Fig. 1.15.

Calculated Fe 2p XAS and MCD spectra using the atomc multiplets asuming $3d^6$ configuration in the ground state. In the upper (lower) panel, the scaling factor z of the 3d spin-orbit interaction is equal to 1(0). In this calculation, the Slater integrals and spin-orbit parameters are 80% and 100% of the atomic values.

Chapter 2

Electronic structures of transition metal intercalated 1T-TiS_2

2.1 Introduction

2.1.1 Physical properties of M_xTiS_2

Transition metal dichalcogenides with layered structures have the weakly coupled van der Waals gap, into which various guest atoms can be intercalated. Among them, the transition metal(M) intercalated 1T-TiS_2 (M_xTiS_2) show various unusual physical properties which dramatically change with the intercalated guest atom species and its concentration.

A: ***Structural properties***

The interatomic distances between the guest atom (M) and the nearest host S atom R(M-S) are extracted by systematic EXAFS measurements of M_xTiS_2 [2.1]. It is found that the interatomic distances R(M-S) strongly depends on the guest atom M and the concentration x. The interatomic distances R(M-S) obtained at room temperature are plotted as a function of the concentration x as shown in Fig.2.1., where the dotted line indicates the estimated distances between the octahedral vacant site and the S atom of about 2.43Å in the host TiS_2. It is noted that the interatomic distance is exceptionally larger than that of the host TiS_2 in the case of Mn intercalated compound, whereas those of Fe, Co and Ni intercalated materials are reduced by 0.03~0.06Å. It is also found that the variations of R(M-S) with x for these intercalation compounds are much small. Fig.2.1. shows the variation of the interatomic distances as a function of the guest atom M. In addition, the interlayer spacing c evaluated from X-ray diffraction [2.2] is also shown for comparison. The relative change in R(M-S) with changing the intercalant M is fairly in good agreement with that in lattice spacing c, which indicates the strong correlation between the local atomic distance R(M-S) and the averaged lattice spacing c.

B: *Magnetic structures*

The magnetic properties of M_xTiS_2 have been extensively investigated by the low-field ac magnetic susceptibility and magnetization measurements [2.3]. Mn_xTiS_2 is a paramagnetic material over the whole composition of x. Co_xTiS_2 shows weak-ferromagnetism in the restricted range of $0.075 \leq x \leq 1/3$. Similarly a ferromagnetic state is found in Ni_xTiS_2 for $1/2 \leq x \leq 3/4$. Among the other M_xTiS_2, Fe_xTiS_2 show particular magnetic properties, where the various types of the magnetic structures appear depending on the concentration x. In the region $x \leq 0.2$, spin-glass (SG) phase appears and cluster-glass (CG) phase is found in the concentration of $0.2 \leq x \leq 0.4$. In the concentration range above $x=0.4$, Fe_xTiS_2 shows ferromagnetism with the easy axis parallel to the c-axis.

C: *Specific heats*

The specific heats were measured for M_xTiS_2 over the temperature range 1.6-300K using an ac calorimetry technique [2.4]. The values of γ obtained for various M_xTiS_2 are plotted in Figs.2.2. as functions of the guest concentration x and the atomic number of the 3d metals, respectively. It is noted that γ increases from 2 to several tens $mJ/mole.K^2$ with increasing x, followed by a slight decrease at higher concentrations in the cases of V, Cr and Ni intercalated 1T-TiS_2. The enhancement of γ upon intercalation is particularly noticeable for Mn and

Cr metals. Moreover, it is found that the observed values of γ for M_xTiS_2 are of the order of 2-100mJ/mole.K^2, which are larger than those of normal metals (~100mJ/mole.K^2), pure 3d transition metals (5-10mJ/mole.K^2), and of various pyrite-type compounds such as FeS_2, CoS_2 and NiS_2 (5-30mJ/mole.K^2).

2.1.2 Several electron and optical spectroscopies on M_xTiS_2

A: *Angle resolved photoemission and inverse photoemission*

Angle resolved ultra-violet photoemission (ARUPS) and inverse photoemission spectroscopies (IPES) of the host TiS_2 have been intensively performed [2.5, 6]. It is well known that the occupied (unoccupied) experimental band dispersions can be extracted from the ARUPS (IPES) spectra measured with changing polar angle normal to the sample surface of the emitted (incident) electrons.

The obtained bands for TiS_2 are in good agreement with the band calculated results. The characteristic features of the experimental band structures for this material are as follows:

1) The remarkable dispersion is observed for the S 3p derived band. It spreads over a wide energy region and shows the good agreement with the several band calculations.

2) The observed band gap is estimated to be about 0.3eV which is consistent with the other experiments. In fact, the experimental spectrum shows the small intensity peak just below E_F, nevertheless TiS_2 is considered to have semiconducting character. This is most

likely due to the extra electron filling of the Ti 3d band derived from the excess Ti atom included in the pure material.

As for the transition metal intercalated system (M_xTiS_2), the systematic measurements of ARUPS has been carried out by our group. For instance, the dispersion of $Ni_{1/3}TiS_2$ probed at hν=28eV for the Γ(A)-M(L) direction is shown in Fig.2.3.. The strength of the observed structures is schematically represented by the large full circle, large empty circle and small empty circle with decreasing intensity. It is noticed that the dispersions of the structures with the binding energy (E_B) larger than 3eV are qualitatively similar between $Ni_{1/3}TiS_2$ and TiS_2. The appearance of structures around E_B=1eV and 0.2eV (just below the Fermi level (E_F) in the whole Brillouin zone is the new feature of the Ni intercalated TiS_2, which has been ascribed to the Ni 3d and Ti 3d t_{2g} derived states respectively according to the previous transition metal 3p core resonance photoemission study.

Although no significant difference is observed with respect to the dispersions with E_B larger than 3eV for the other M_xTiS_2, remarkable variation of the electronic structures is recognized in the region of E_B=0-2eV. In $Co_{1/3}TiS_2$, for example, two dispersionless structures are found at E_B~0.2 (just below E_F) and 0.5eV, whereas only single structure is observed just below E_F (E_B~0.2eV) in $Fe_{1/3}TiS_2$ and $Mn_{1/4}TiS_2$.

B: *VUV-reflectance spectra*

The optical properties of TiS_2 in the visible and ultraviolet region were intensively investigated by reflectance, transmission and electron energy loss experiments [2.7-10]. On the other hand, such a optical spectroscopy using the visible and VUV light of M_xTiS_2 have not yet been carried out except for by our group.

Fig.2.4. shows the reflectance specvtrum of $Fe_{1/3}TiS_2$ compared with that of TiS_2. The reflectance spectrum in the 2-30eV region can be separated into the following 4 regions with distinct dip structures

(I) the region extending up to 3eV
(II) the region up to 8eV
(III) the region up to about 12eV
(IV) the region extending from 12eV beyond 20eV

According to the band calculation, the transitions between S 3p valence band and the lower Ti 3d conduction bands which have t_{2g} symmetry are dominant in the region I. The region II consists of states with e_g symmetry. The transition between the bonding and antibonding orbitals occur in the region III. In the spectrum of $Fe_{1/3}TiS_2$, the new sharp peak around 3.5eV appears in the region II. This structure may be related to the Fe 3d state.

C: *Core-level and valence band XPS spectra*

The Ti 2p core-level XPS spectra exibit much more pronounced broadening and binding energy shift on going from TiS_2 to the intercalated compounds [2.10], which suggest an overlap of different component in the Ti 2p XPS spectra. The author interpreted such a broadening as a final state effect induced by the core hole potential. Namely the core-hole potential pulls down a localized screening level of Ti 3d character below E_F, which is either occupied by an electron transferred from the conduction band or unoccupied in the final state, giving rise to two components in the core-level XPS spectrum. Thus the Ti 2p XPS spectra of M_xTiS_2 were fitted to a superposition of two spin-orbit doublets corresponding to a well-screened peak and a poorly screened peak appearing at lower and higher binding energies, respectively. It is noted that the lifetime width of the poorly screened peak increases with guest-atom concentration. This can be understood if we consider the decay process of the poorly screened core-hole state into the well-screened state by filling the screening level via an Auger-type transition leaving two holes in the Ti 3d conduction band. The probability of this transition will increase with the number of Ti 3d conduction electrons supplied by the guest atoms.

For the Ti 2p XPS spectrum of TiS_2, although the screening level may be formed on the core-hole site, well screened peaks are expected to be weak, because the Ti 3d conduction band is almost empty in TiS_2 and electron transfer from the conduction band to the screening level cannot occur effectively when the core hole is created suddenly. Indeed, the Ti 2p XPS peak energies for TiS_2 are found to be close to those of the poorly screened peaks for M_xTiS_2.

They also measured the guest atom M 2p XPS spectra, where the satellite structures accompanying the spin-orbit split main peaks are revealed. Such a satellite feature is well understood in terms of the configuration interaction (CI) picture including the on site Coulomb interaction and hybridization, which is often applied to the strongly correlated systems including rare earth and 3d transition metal compounds. These results suggest that the intra-atomic Coulomb and exchange energies for the M 3d electrons and the M3d-S3p hybridization dominate the M 3d band width. In addition these features indicate that M 3d states have the divalent high spin state except for Co in $Co_{1/4}TiS_2$, which is considered to be in the low-spin divalent state by comparing the line shape with that of CoS_2.

The valence band XPS spectra of M_xTiS_2 are also shown in Fig.2.5. [2.10]. Additionally difference spectra between M_xTiS_2 and TiS_2 are shown by solid curves, which represent principally contribution from the M 3d states. While the band calculations have shown that the intercalated M 3d states are strongly hybridized in the whole S 3p band region [2.12], the calculations cannot explain the broad structure distributing in the binding energy region between S 3p and 3s (centered at -13eV) states. The above difference spectra of the intercalated compounds resemble the valence band photoemission spectra of MnS, FeS and NiS, which suggests that the CI picture well explains the characteristic features of the difference spectra.

D: *Transition metal 3p core resonance photoemission spectra*

A measure of the Ti 3d partial density of states can be derived by subtracting the valence band spectrum measured at off-resonance (hν=35eV) from that at just on-resonance (hν=48eV) [2.13]. Curves 1 and 2 in Fig.2.6. are the photoemission spectra of TiS_2 at hν=48eV and 35eV, respectively, and curve 3 is their difference after the normalization of the intensities to the monochromator output. The difference spectrum 3 peaking at E_B=3.5eV with two shoulders at 2.2 and 5.0eV reflects the energy distribution of the Ti 3d partial density of states (DOS) in TiS_2 which spreads over several eV in energy. Similar difference spectra for M_xTiS_2 (M=Mn, Fe, Co and Ni) obtained from the photoemission spectra at on-resonance (hν=48eV) and at off-resonance (hν=35eV) are shown by the curves from (b) to (f) for $Mn_{1/4}TiS_2$, $Fe_{1/3}TiS_2$, $Co_{1/4}TiS_2$, $Co_{1/3}TiS_2$ and $Ni_{1/3}TiS_2$, respectively. These spectra for intercalated materials also reflect the Ti 3d partial DOS in the M_xTiS_2. It is surprising that the energy of the shallowest peak is almost constant through $Mn_{1/4}TiS_2$ to $Ni_{1/3}TiS_2$, in contrast to the remarkable shift in the raw data of $Co_{1/4}TiS_2$ at 62eV. These difference spectra spread over the range E_B=0-6eV, and the two shoulders are smeared out by intercalation. According to their

CIS spectra covering the Ti and guest atom 3p core excitation regions, the enhancements are observed in the wide binding energy region at both of the Ti and M 3p core absorption thresholds, which suggests the strong hybridization character of Ti and M 3d states.

2.1.3 Theoretical aspects

A: *Band calculations*

The band structures were systematically investigated on M_xTiS_2 by N.Suzuki et al. using APW method [2.12]. They revealed the inapplicabilty of the rigid band model for the band structure of the intercalated TiS_2. Their calculated total densities of states (DOS) as well as the Ti 3d, M 3d and S 3p partial DOS of $M_{1/3}TiS_2$ (M=Mn, Fe, Co, Ni) are depicted in Fig.2.7.. It is found that their DOS are mainly separated into four regions as marked by the indeces (i), (ii), (iii) and (iv) independent of the intercalated species. They also extracted the bonding natures between the guest atom and the host by calculating the bond-orders for $Fe_{1/3}TiS_2$ and $Ni_{1/3}TiS_2$. According to the calculation, for example, the bonding nature of $Fe_{1/3}TiS_2$ is described as follows:

1) Part (i) corresponds to the bonding states of Fe 3dγ -S 3p and of Ti 3dγ-S 3p.

2) Part (ii) mainly consists of the strong hybridization states between Fe 3dε and Ti 3dε states.

3) Part (iii) consists of the Ti3dε and Fe 3dε mixing band and the anti-bonding state between Fe 3 dγ and S 3p orbitals.

4) Part (iv) consists of the anti-bonding states of Ti 3dγ-S 3p and F 3dγ and S 3p.

As for $Ni_{1/3}TiS_2$ the gross features of the bond orders are almost the same except for the following differences:

a) the magnitude of the bond order between the Ni 3dγ and S 3p orbitals in parts (iii) and (iv) are smaller than those of the bond order between the Fe 3dγ and S 3p orbitals.

b) anti-bonding character between the Ni 3dγ and S 3p orbitals is seen even in part (ii) in $Ni_{1/3}TiS_2$. These spectra can be ascribed to the difference of the atomic energy level of the M 3d states, i.e., the atomic 3d level of Ni is closer to the atomic S 3p level compared with the atomic 3d level of Fe.

It is noted that the DOS at the Fermi level (E_F) decrease with increasing the atomic number of the guest atom M. Such a trend is consistent with the observed electronic specific heat coefficient (γ) except for the quite smaller magnitude of the calculated γ compared with the observed ones.

B: *Configuration interaction (CI) picture*

The single particle descriptions are often inappricable in order to understand the electronic structures of the strongly correlated materials, such as transition metal oxides, rare earth compounds and other insulating compounds. For such strong correlated systems, the high energy spectroscopies such as photoemission and photoabsorption are powerful tool to understand these electronic states. In the final state of core-level

XPS, in general, a created core-hole strongly interacts with valence electrons. In order to screen the core-hole charge, electron rearrangement can take place interatomically. For example, it is well established that the satellite peaks in the 2p XPS of late transition metal compounds are due primarily to charge transfer (CT) from the valence orbitals of the anions to the transition metal 3d state.

Configuration interaction approach has been successfully used to extract several important physical parameters such as charge transfer energy (Δ) and on-site Coulomb interaction energy (U_{dd}) by analyzing the above-mentioned spectra. Now we consider the simple system octahedrally surrounded by anions with $3d^0$ configuration in the ground state, which correspond to the cases of some Ti compounds. The ground state wave function assuming only two configurations is described as follows:

$$\Phi_g = a\,|\,d^0\rangle + b\,|\,d^1\underline{L}\rangle$$

where $\underline{L}$ denotes ligand hole state. If the charge transfer energy (Δ) is defined as $E[3d^1\underline{L}]-E[3d^0]$, the energy difference between the two final states, $\underline{c}3d^1\underline{L}$ and $\underline{c}3d^0$ is described as $E[\underline{c}3d^1\underline{L}]-E[\underline{c}3d^0]=\Delta-U_{dc}$. The effective hybridization strength (off diagonal matrix element) between the $3d^0$ and $3d^1\underline{L}$ states V_{eff} is given by $[6V(t_{2g})^2+4V(e_g)^2]^{1/2}$ (6 and 4 are the orbital and spin degeneracies of t_{2g} and e_g states, respectively). The energy difference between the obtained two eigenvalues for the final states is given by $[(\Delta-U_{dc})^2+4V_{eff}^2]^{1/2}$.

In the case of the early transition metal compounds, such as Sc trihalaides and Ti tetrahalides and oxides, TM 2p core-level XPS spectrum show the satellite structure at the higher energy of the main peak, which is interpreted to be the CT satellite as described above.

Thus the energy separation between the main peak and satellite is given by $[(\Delta\text{-}U_{dc})^2+4V_{eff}^2]^{1/2}$. In the limit of $|\Delta\text{-}U_{dc}|«2V_{eff}$, it can be approximated as $2V_{eff}$, and the energy separation is not expected to depend on U_{dc}. On the other hand, the energy separation approximately becomes $|\Delta\text{-}U_{dc}|$ in the limit of $|\Delta\text{-}U_{dc}|«2V_{eff}$. For example, $|\Delta\text{-}U_{dc}|$=2eV and $2V_{eff}$=14eV are applied to the spectrum of TiO_2, which corresponds to the former case.

K.Okada et al.[2.14] suggest that the lowest main Ti 2p XPS peak is assigned to be a split-off state formed as a result of the strong hybridization between $\underline{2p}d^0$ and $\underline{2p}d^1\underline{L}$ configurations. They calculated the Ti 2p XPS spectrum of TiO_2 using the impurity Anderson model including the full multiplet in terms of the CI picture. As shown in Fig.2.8., the main structure of the Ti 2p-XPS consists of a pair separated by the spin-orbit splitting of Ti 2p levels (≈6eV), each of which is accompanied by a satellite about 13eV above the main peak. It is found that the main peak of $2p_{1/2}$-XPS is considerably broader than that of $2p_{3/2}$-XPS. The calculated spectrum well reproduce the experimental spectrum. In their calculation, U_{df}=4.5eV, $V(e_g)$=3eV, Δ=3eV and 10Dq=1.7eV are applied. The same parameters are also applied to Ti 3p and 3s XPS spectra, where the agreement is quite well.

The total energy scheme is illustrated in the upper part of Fig.2.9.. The lowest main peak consists of only single line, which remind us of the $\underline{c}3d^0$ final states. In fact the character of the final states corresponding to the main peak is rather $\underline{c}3d^1\underline{L}$ than $\underline{c}3d^0$ because $\Delta\text{-}U_{dc}$ is negative in this case. As shown in both of the experimental and theoretical spectra, the rather broad structure spread in the region between the bonding (main) and antibonding (satellite) states. In the Ti 2p XPS spectrum, the broad structure is superimposed on the Ti $2p_{1/2}$ main structure. Such a broad structure is assigned to the non-bonding states which is *not in phase* between $\underline{c}3d^1\underline{L}$ and $\underline{c}3d^0$ configurations. These structure are weak because the dipole transition of the direct photoemission from the *in-phase* ground state to the final states which is *not in phase* is forbidden.

K.Okada et al. pointed out the close relationship between the valence band PES for trivalent Ti compounds (d^0 systems) and the core-level XPS in the tetra valenct Ti compounds (d^1 systems)[2.14]. On the basis of the CI theory, the ground state of the trivalent Ti compounds can be described by a linear combination of the electron configurations starting from $3d^1$. Accordingly the final states of the valence band photoemission are described by the electron configurations starting from $3d^0$, which is the same as those for the final states of the core-level XPS, as far as the valence electrons are concerned. Since the CT energy (Δ) in the trivalent Ti system is defined by the energy difference between the $3d^1$ and $3d^2\underline{L}$ states, the energy difference is given by Δ-U_{dd} between the $3d^0$ and $3d^1\underline{L}$ final state configurations as illustlated in the lower part of Fig.2.9.. By comparing the upper and lower part of Fig.2.9., the main peak and the satellite in the core-level XPS correspond to the two split-off states in the valence band photoemission spectrum. In the calculated valence band photoemission spectrum of Ti_2O_3, only the lower energy split-off state has a spectral intensity. The binding energy (E_B) of the lower energy split-off state relative to the valence band is about 5eV, which is due primarily to the strong hybridization between the Ti 3d and O 2p orbitals.

The CI approach is also applied for the core-level and valence band photoemission spectra of M_xTiS_2. As mentioned above, the guest atom M 2p core XPS spectra show the satellite feature which is accompanied by the main peak. A.E.Boucquet et al. calculated the M 2p XPS spectra using the CI cluster model systematically on M_xTiS_2[2.15]. According to the calculated results, the main and satellite structures of Mn 2p XPS spectrum are assigned to the $d^6\underline{L}$- and d^5 dominated states for $Mn_{1/4}TiS_2$, respectively. In the case of $Fe_{1/3}TiS_2$, the main and satellite peaks of Fe 2p XPS spectrum are ascribed to the $d^7\underline{L}$- and d^6-like states. As for $Ni_{1/3}TiS_2$, the main and satellite structures of $Ni_{1/3}TiS_2$ are mainly derived from the $d^9\underline{L}$ and $d^{10}\underline{L}^2$ configurations. It is shown that since Δ is smaller than U_{dd} for all the materials, the local electronic structures of M 3d state belong to the CT regime [2.15]. It is found that the charge transfer energy Δ decreases and U_{dd} increases with increasing the atomic number of M atom. By comparing the fitted parameters of M_xTiS_2 with those of the other oxides and sulfides, U_{dd} is seen to decrease along the series $MO \rightarrow M_xTiS_2$ probably due to the increased polarizability of the ligand species. For a series $MO \rightarrow M_xTiS_2 \rightarrow MS_2$, a general decrease in the overlap integral $(pd\sigma)$ as the ligand changes. This reflects the fact that the metal-sulfur distances are larger in the intercalation compounds than in the metal-oxygen distances in the oxides, and even larger interatomic metal-sulfur distances found in the pyrite-type compounds.

As for the valence band photoemission spectra of M_xTiS_2, the CI cluster calculation as used in the analysis of the core-level XPS spectra is also applied [2.10]. As mentioned above, the difference spectrum between M_xTiS_2 and host TiS_2 shows the broad structure in the region of S 3s-3p band gap, which is not explained in terms of the one-electron band picture. In the case of $Ni_{1/3}TiS_2$, the cluster model assumes the ground state of the form,

$$\Phi_g = a|d^8\rangle + b|d^9\underline{L}\rangle$$

The final states are given as

$$\Phi_f = a_f|d^7\rangle + b_f|d^8\underline{L}\rangle + c_f|d^9\underline{L}^2\rangle$$

The calculated spectrum with Δ=2.0eV, (pdπ)=-1/2(pdσ)=0.75eV and U_{dd}=5.5eV well reproduces the broad satellite feature located in the S 3s-3p band gap region. The above parameter values are similar to those for NiS as would be expected from the similar S coordination of the Ni atom in both systems. The distribution of the d^7, $d^8\underline{L}$ and $d^9\underline{L}^2$ configurations in the final state is found to be such that the main band and the satellite are predominantly $d^8\underline{L}$-and d^7-like, respectively. The $Mn_{1/4}TiS_2$-TiS_2 difference spectrum is also compared with a CI calculation on the MnS^{6-} cluster model. The CI spectrum calculated with Δ=E[$d^6\underline{L}$]-E[d^5]=3.5eV, (pdπ)=-1/2(pdσ)=0.42eV and U_{dd}=7.5eV gives the best fit to the experiment. The main Mn 3d state at E_B=0-6eV is much broader than that of $Ni_{1/3}TiS_2$ due to the different multiplet structures. As in the case of $Ni_{1/3}TiS_2$, the main band and the satellite are predominantly $d^5\underline{L}$- and d^4-like, respectively.

C: *Calculated results of resonance photoemission spectra on 3d transition metal compounds*

Recently, the resonant photoemission spectroscopy with soft X-rays has been developed in 3d transition metals and their compounds and 4f rare earth systems in order to investigate their electronic structures. In 3d transition metal compounds, for example, the 2p core electron is photoexcited into an unoccupied 3d state in the intermediate state of the resonance photoemission. Then due to the Coster-Krönig decay, a 3d, 3p or 3s electron is emitted as a photoelectron and a 3d electron returns to the 2p core state. The useful points of the resonant photoemission with soft X-rays are as follows:

1) Resonances in shallower core photoemission are possible in addition to the valence band photoemission.

2) Differences in various selection rules between on- and off-resonances are clearly reflected in spectra due to stronger resonances compared with those in vacuum ultraviolet region.

In Fig.2.10., Ti 3d and 3p photoemission spectra of TiO_2 at various 2p core excitations including the off resonance spectrum are shown. The final state of the 3d photoemission is mainly composed of $3d^0\underline{L}$, $3d^1(t_{2g})\underline{L}^2$ and $3d^1(e_g)\underline{L}^2$ configurations. In the off resonance spectrum, the main and satellite (marked by A) structures are found with the energy separation of about 10eV, which correspnd to the bonding and anti-bonding states, respectively. The final state wave function $3d^1\underline{L}^2$ is described as a linear combination of the $3d^1(t_{2g})\underline{L}^2$ and $3d^1(e_g)\underline{L}^2$ configurations. In the above-mentioned bonding and antibonding states, the wave function of $3d^1\underline{L}^2$ is *in phase* in regard to the configurations $3d^1(t_{2g})\underline{L}^2$ and $3d^1(e_g)\underline{L}^2$. At on resonances, the additional structure which is marked by B appears between the main and satellite peaks. This structure corresponds to the mixture of $3d^0\underline{L}$ and $3d^1\underline{L}^2$ with the $3d^1(t_{2g})\underline{L}^2$ and $3d^1(e_g)\underline{L}^2$ configurations are *not in phase*, which is therefore orthogonal to the states corresponding to the main and satellite peaks. A reduction of the peak B at off-resonance is due to the selection rule, i.e., the direct dipole transition starting from the *in phase* ground state to the *not in phase* final state is "forbidden".

At on resonances, the final state is reached by Coster-Krönig decay from the internediate state of the 2nd order optical process. The transition into the state corresponding to the peak B is therefore not "forbidden" in this case. It is found that the center of gravity of the structure B shifts toward the larger E_B with the excitation energy moves from t_{2g} to e_g. This is because that the $t_{2g}(e_g)$ state is preferentially contained in the state with the lower (higher) E_B and a selection of the photon energy with different symmetry leads to a shift of the relative satellite intensity from B to A with increasing photon energy.

In discussing the resonance features observed in the Ti 3p XPS spectra, the similar considerations as taken in the valence band photoemission spectrum can be applied. The final state of the Ti 3p photoemission is mainly composed of $\underline{3p}^5 3d^0$, $\underline{3p}^5 3d^1 \underline{L}$. As shown in the off resonance spectrum, the main and satellite (marked by A) structures are found. Additionally, a weak intensity satellite (marked by B) is also found between the main and satellite B. The main peak and the satellite A correspond to the bonding and antibonding states between the $\underline{3p}^5 3d^0$ and $\underline{3p}^5 3d^1 \underline{L}$ configurations, where the $\underline{3p}^5 3d^1 \underline{L}$ multiplets are *in phase*. Since $3d^1 \underline{L}$ states composed of $3d^1(t_{2g})$ and $3d^1(e_g)$ are *in phase* in the ground state, the dipole transition suppresses the transition into the final state which is *not in phase*. At on-resonances, the satellite B recovers its intensity due to the same reason as that discussed in the case of 3d photoemission. These features are consistent with the experimental results.

2.2 Electronic structures of M_xTiS_2 probed by 2p core resonance photoemission as well as 2p core absorption and photoemission spectroscopies.

2.2.1 Introduction

A large number of resonance photoemission studies have been carried out on the 3d transition metals and their compounds for the photon energies near the transition metal 3p excitation threshold [2.16]. Recently, the 2p core resonance photoemission measurement has become possible owing to high performance of the soft X-ray beam lines and monochromators [2.17, 18] Although the photoionization cross section of the 3d state in the region of the 2p to 3d excitation threshold is smaller than that in the 3p to 3d threshold region, the intensity ratio between the resonance maximum and minimum is much larger in the case of the 2p resonance photoemission. Therefore the assignment of the electronic character is easier in the 2p resonance photoemission. Another advantage is that the high photon energy (hν) enables one less surface sensitive measurement of the valence band with kinetic energies considerably higher than those corresponding to the minimum mean free path. If we combine the photoelectron spectra taken at the 3p and 2p core excitation threshold, the surface effect can be argued.

We have studied the transition metal 2p resonance photoemission spectroscopies of the host TiS_2 and its intercalated compounds $Mn_{1/4}TiS_2$, $Fe_{1/3}TiS_2$, $Co_{1/3}TiS_2$ and $Ni_{1/3}TiS_2$. The transition metal 3p core excited resonance photoemission study of M_xTiS_2 (M=Mn, Fe, Co, Ni) has already been performed [2.13]. There remains, however, some ambiguity for the assignments of the electronic states of the guest atoms because of their small concentration and the weaker resonance behavior in the 3p core excitation region. Therefore the 2p resonance photoemission is considered to be much useful to probe the precise local electronic structure of the intercalated guest atom M as well as that of the host Ti atom.

2.2.2 Experimental

The 2p core absorption (XAS) and 2p core resonance photoemission measurements were performed at the BL-2B of Photon Factory of the Institute for High Energy Physics (KEK) with using the 10m grazing incidence monochromator (10m GIM) [2.16]. The 2p XAS spectra were recorded by the total photoelectron method. The resolution of hν was set to about 0.15 and 0.5eV at the Ti 2p and Ni 2p excitation threshold, respectively. A double stage cylindrical mirror analyzer (DCMA) was used to measure the kinetic enenrgies of the photoemitted electrons in the 2p resonance photoemission experiment. The pass energy of the analyzer was set to 50eV. The spectra were measured on the surfaces of the single crystal samples which were obtained by cleaving in the UHV chamber. The degree of the surface contamination was checked by the C or O 1s XPS signal and found to be negligible.

2.2.3 Results

A: *Ti 2p XPS spectra*

In the Ti 2p XPS spectrum of TiS_2, the main spin-orbit doublet with 6eV separation is clearly observed and three additional structures are found at -10, -16 and -22eV larger E_B of the Ti $2p_{3/2}$ main peak (E_B=456eV) as shown in Fig.2.11.(a). They are tentatively named S_1, S_2 and S_3. The S 2p XPS spectrum measured for comparison has shown an energy loss structure due to a plasmon at 21eV from main peak.

Therefore the satellite structure S_3 may be ascribed to the plasmon satellite.

The Ti 2p XPS spectra of M_xTiS_2 are shown in Fig.2.11.(b)-(e). It is recognized that the spectral width of Ti 2p XPS main peaks of the intercalated compounds is remarkably broader compared with that of TiS_2. Some additional structures are found at almost the same E_B as in the spectrum of TiS_2, namely, the structures located at -10, -16eV larger E_B of the main peak ($E_B \approx 456$eV). In addition, the fairly broad structure is observed in a wide E_B region centered at $E_B \approx 480$eV, which is in contrast to the case of the host material.

B: *Ti 2p XAS spectra*

The Ti 2p XAS spectra of M_xTiS_2 including the host material are summarized in Fig.2.12.(a)-(e). The spectrum of TiS_2 shows clear four peak structures. The splitting between the first(second) and the third(fourth) peak is about 6eV and thought to be resulting mainly from the spin-orbit splitting. As for the internal structure of each spin-orbit component of TiS_2, the origin of the doublet splitting of ~2.3eV may be most likely due to the crystal field splitting of the Ti 3d conduction band in a slightly distorted O_h field, where the low(high) hν component corresponds to the excitation to the t_{2g}(e_g)-like state. Besides these structures, shoulder structures or weak satellites are observed in the regions of A, B and C. The weak satellite B shows a clear doublet feature with the energy separation almost equal to the crystal field induced splitting found in the Ti 2p XAS main peak (~2.3eV). The doublet feature of B is also considered to be mainly derived from the crystal field effect on the 3d final state. In addition a very weak prethreshold structure is observed at -4eV.

The spectral line shapes of the Ti 2p XAS spectra of $Mn_{1/4}TiS_2$, $Fe_{1/3}TiS_2$, $Co_{1/3}TiS_2$ and $Ni_{1/3}TiS_2$ have a common feature as shown in Fig.2.12.(b)-(e). It is noted, however, that these spectral line shapes are noticeably different from the spectrum of the host material, that is, the intensity of the lower photon energy part of each spin-orbit component is much reduced and slightly broadened as shown in the figure. The higher energy components of each doublet are also considerably broadened in the intercalated materials. The structures of the main peaks are somewhat distinct in the spectrum of $Mn_{1/4}TiS_2$ compared with those of the other spectra of the intercalated compounds. The satellite structure can be observed at the same hν as the satellite B in the spectrum TiS_2. The doublet structure as found in the spectrum of TiS_2 is seems to be smeared out and become structureless upon intercalation.

C: *Valence band photoemission spectra in the Ti 2p core excitation threshold.*

Valence band photoemission spectra, taken in the Ti 2p core excitation region of TiS_2 are shown in Fig.2.13.(a) Whole spectra are normalized by the peak height of the S 2p core state and the E_B scale is caliblated by that of the S 2p core state. The raw data are plotted by dots. The numbers on the left hand side indicate the excitation photon energies. The difference from the off resonance spectrum 1 is shown by the broken lines, demonstrating the enhancement of the Ti 3d component for the Ti 2p core resonance excitation.

As shown in this figure, the resonance enhancement is observed in a wide region with E_B=0-8eV. It is recognized in the spectra 2 and 3 of Fig.2.13.(a). that a small structure crosses E_F. This XPS structure recognizable as a result of the enhancement at the Ti 2p core excitation threshold is also found in the ARUPS spectra near the M(L) point, which is derived from the electron filling into the empty Ti 3d t_{2g} band by the excess Ti atom self-intercalated in the stoichiometric TiS_2. A remarkable enhancement is observed for the structure located at E_B=3.5eV. In addition, the broader structure in the region of E_B>4eV also shows the enhancement at the Ti 2p core excitation threshold. It is noticed that the center of gravity of this structure shifts with increasing photon energy. Such a behavior is seems to be a characteristic phenomenon of the Auger electron emission if the E_B of the structure linearly increases with increasing photon energy. It is, however, that the center of gravity of this structure does not linearly shift and the line shape seems to change with changing photon energy. It is rather complicated, but it can be roughly said that the enhancements are mainly found around E_B=6 and 8eV at the photon energies corresponding to the Ti $2p_{3/2}\rightarrow 3dt_{2g}$ and $2p_{3/2}\rightarrow 3de_g$ excitations, respectively. We also show the resonance photoemission spectra in the Ti $2p_{1/2}$ region. It is recognized especially in the CIS spectra as shown in Fig.2.14. that the resonance enhancement in the $2p_{1/2}$ excitation region is much weaker than the case of the $2p_{3/2}$ excitation for several E_B of the valence band although the Ti 2p XAS intensity is almost comparable that of the $2p_{3/2}$ excitation region.

The resonance photoemission spectra of $Mn_{1/4}TiS_2$, $Fe_{1/3}TiS_2$, $Co_{1/3}TiS_2$ and $Ni_{1/3}TiS_2$ are likewise measured. The resonace features are almost similar to each other. The observed characteristic features for the spectra of the intercalated compounds are described as follows:

The intensity enhancement is most clearly observed for the structure with the peak at E_B=0.5eV as shown in Figs.2.13.(b)-(e) In addition, the resonance enhancement is also recognized for the structure at E_B=3.5eV. On the larger E_B side of the main peak structure, a broad structure appears above the Ti 2p core excitation threshold as shown by the dashed curve. This structure almost linearly shifts toward larger E_B with increasing the photon energy. This broad structure is considered to be mainly consists of the $L_{23}VV$ Auger states.

The intensity variation at some E_B is plotted as a function of the photon energy in Figs.2.14.(b)-(e). As recognized in these constant initial state (CIS) spectra, *the resonance enhancement for E_B=0.5eV is much stronger for the excitation to the Ti "e_g" state than to the "t_{2g}" state, where the dominant component is indicated with the quotation marks.* On the cleaved surface of M_xTiS_2, the M atoms are randomly distributed. So it is natural that the dispersion of the M 3d state along the surface is not appreciable. But the observed ARUPS structure at E_B=0.2eV with negligible dispersion can not be ascribed to the M 3d state because the Ti 3d character is confirmed for this structure.

D: *Ti 3p core level*

In the off resonance spectrum of TiS_2, the Ti 3p main peak is observed at E_B=35eV as shown in Fig.2.15.(a) The intensity of the Ti 3p main peak enhances above the Ti 2p core excitation threshold. Furthermore, more remarlkable enhancement is observed in the larger E_B region of the Ti 3p main peak. In addition, a small structure appear around E_B=48eV as obviously recognized in the spectrum 5. The intensity variations of the Ti 3p main peak ($E_B \approx$35eV) and other structures are plotted as a function of hν in Fig.2.16.(a) Thus obtained CIS spectrum of the Ti 3p main peak shows a clear doublet peak corresponding to the two peaks of the XAS spectrum, revealing the resonance process between the Ti 2p core absorption and the Ti 3p core photoemission. It is noticed that the intensity of the lower hν peak is remarkably enhanced compared with the higher hν peak in the CIS spectrum of the Ti 3p state in contrast to the XAS spectrum.

In the off resonance spectra of $Mn_{1/4}TiS_2$, $Fe_{1/3}TiS_2$, $Co_{1/3}TiS_2$ and $Ni_{1/3}TiS_2$, the Ti 3p main peak is observed at E_B=35.5eV as shown in Figs.2.15.(b)-(e). The FWHM of the main peak is about 3.6eV which is remarkably broader than that of the host material (about 2.4eV). The clear resonance enhancement is also recognized in the larger E_B region of the Ti 3p main peak. In the similar way of TiS_2, the CIS spectrum of Ti 3p main peak shows the clear doublet structure corresponding to the "t_{2g}" and "e_g" excitation peaks of the Ti 2p XAS spectrum. *In this spectrum the lower hν peak is remarkably enhanced compared with the higher hν peak as observed in the corresponding spectrum of* TiS_2.

E: *$L_{23}M_{23}M_{23}$ Auger final state*

Fig.2.17 shows the photoemission spectra of TiS_2 in Ti 3s core region. It is noticed that the intensity enhancement is remarkable in the larger E_B region of the Ti 3s state. The binding energy (E_B) of the two prominent structures is plotted in Fig.2.18 as a function of hν . As revealed in this figure, the binding energies of these peaks linearly increase with increasing the photon energy.

F: *Guset atom M 2p XAS spectra*

Mn 2p XAS spectrum of $Mn_{1/4}TiS_2$ is shown in Fig.2.19.(a) There are several multiplet structures in each spin orbit component, i.e., the shoulder structure is found at 3.7eV larger energy of the main $2p_{3/2}$ peak and the clear doublet structure exists in the $2p_{1/2}$ excitation region. The Mn 2p XAS spectrum of $Mn_{1/4}TiS_2$ fairly resembles that of MnS [2.19] where Mn atom is octahedrally coordinated by the six S atoms. Such a spectrum is well reproduced in the 2p XAS multiplet calculation including the crystal field (10Dq) with $3d^5$ configuration being assumed in the ground state [2.20]. By comparing the calculated spectra with our result, the 10 Dq value can be roughly estimated to be 0.6eV.

In Fig.2.19.(b), Fe 2p XAS spectrum of $Fe_{1/3}TiS_2$ is shown. The spectrum shows no clear multiplets. The two broad satellites are found on the 7.7eV larger energy side of the $2p_{3/2}$ and $2p_{1/2}$ main peaks.

In Co 2p XAS specrtum of $Co_{1/3}TiS_2$, the slight shoulder as well as the shrap main peak is recognized in the $2p_{3/2}$ excitation region, whereas such a shoulder is not found in the $2p_{1/2}$ excitation region. Additionally, the satellite structures are clearly observed at 7.7eV higher energy of the Co $2p_{3/2}$ and $2p_{1/2}$ main peaks, respectively.

Ni 2p XAS spectrum of $Ni_{1/3}TiS_2$ is also measured as shown in Fig.2.19.(d). In each spin-orbit component, a sharp main peak with a satellite structure at about 7.7eV higher energy is found. Such a satellite structure is often found in Ni compounds. In the configuration interaction cluster approach [2.21], the main(satellite) peak mainly consists of $2p^53d^9$($2p^53d^{10}$) configuration if the mixing character of $3d^8$ and $3d^9\underline{L}$ configurations are assumed in the ground state.

G: *Valence band photoemission spectra of M_xTiS_2 in the M 2p excitation region*

The valence band resonance photoemission spectra of $Mn_{1/4}TiS_2$ the Mn 2p core excitation threshold are shown in Fig.2.20.(a). The intensity enhancement is observed in a quite wide energy region of about 12eV from E_F, which indicates that the Mn 3d states spread over a wide energy range due to the hybridization or the multiplets. At the photon energy corresponding to the Mn $2p_{3/2}$ absorption maximum, a strong enhancement is found for the structure around E_B=4.5eV and a shoulder is observed in the difference spectra given by the solid curve in the smaller E_B region as shown in Fig.2.20.(a). It is noticed that the intensity around E_F is very small. In addition, the spread of the spectrum is very remarkable in the larger E_B region of the main peak.

As for $Fe_{1/3}TiS_2$ and $Co_{1/3}TiS_2$, the enhancements above the Fe or Co 2p core excitation are also recognized in a wide energy region which also indicates that the Fe or Co 3d states spread over a wide energy range due to the strong hybridization or multiplets.(Figs.2.20.(b) and (c)) In both cases, the enhanced structures are quite broad and structureless in contrast to the case of $Mn_{1/4}TiS_2$.

The valence band resonance photoemission results of $Ni_{1/3}TiS_2$ taken at the Ni 2p core excitation region are shown in Fig.2.20.(d). Whole structures between the Fermi energy (E_F) and E_B=8eV show enhancement above the Ni 2p core excitation threshold. It suggests the contribution of the Ni 3d component in a wide energy region due to the Ni 3d hybridization with S 3p and Ti 3d states. In particular, a remarkable enhancements are observed around the binding energies of 3 and 6.5eV.

H: *M 3p core level XPS spectra in the M 2p core excitation region*

In the case of $Mn_{1/4}TiS_2$, the main peak of the Mn 3p photoemission is observed at E_B=48eV. The intensity enhancement occurs over a wide energy region between Mn 3p and Ti 3s (E_B=60eV) states as indicated in Fig.2.21.(a). It is noticed that the magnitude of the enhancement is remarkable for the structure situated between the Mn 3p and Ti 3s main peaks compared with that of the Mn 3p main peak.

In Fig.2.21.(b), Fe 3p XPS spectra of $Fe_{1/3}TiS_2$ taken in Fe 2p core excitation region are shown. The off resonance spectrum (1) shows the two peak structures at E_B=54 and 60eV, which correspond to the Fe 3p and Ti 3s main peaks. At on resonances, it is shown that the intensity of the structures distributed above the Fe 3p main peak grows. As found in the spectra at the excitation energy above the Fe $2p_{3/2}$ excitation threshold, the doublet peak structures with the energy separation of about 6eV are dominantly distributed in this region and these structures shift toward the larger E_B with increasing hν.

Co 3p XPS spectra taken in the Co 2p core excitation region are shown in Fig.2.21.(c). As shown in the off resonance spectrum marked by 1, the Co 3p XPS main peak is located at E_B=60eV, which is considered to be superimposed on the Ti 3s main peak. The Co 3p main peak shows a enhancement above the Co 3p core excitation threshold. In addition, it is recognized that a strong enhancement occurs for the structure at E_B=69eV.

Fig.2.21.(d) shows the Ni 3p XPS spectra of $Ni_{1/3}TiS_2$. Ni 3p main peak is located at E_B=67eV as clearly shown in the off-resonance spectrum marked by 1. At on resonances, a remarkable enhancement is observed for the structures located on the higher E_B side of the Ni 3p main peak at the excitation energy corresponding to the Ni $2p_{3/2}$ XAS main peak. We can find these intense structures at E_B=72 and 78.5eV, for example, in the on resonance spectrum 8.

2.2.4 Discussions

A: *Ti 2p XPS spectra*

First, we discuss the spectral lineshape and the origin of the satellite structures in the Ti 2p XPS spectra of TiS_2 and M_xTiS_2. Similar satellites are reported at 13eV larger E_B of the Ti $2p_{3/2}$ and $2p_{1/2}$ main peaks in the core XPS spectra of nominally tetravalent Ti oxides [2.22]. K.Okada et al.[2.23] calculated the Ti 2p XPS and XAS spectra for nominally tetravalent Ti oxides in terms of the $[TiO_6]^{8-}$ cluster including multiplets. They interpreted those satellite structures as the anion-to-metal charge transfer (CT) satellites. According to their calculation, the bonding and antibonding split-off states derived from the strong hybridization between the $\underline{2p}3d^0$ and $\underline{2p}3d^1\underline{L}$ states form the main and satellite structures respectively when the $3d^0$, $3d^1\underline{L}$ and $3d^2\underline{L}^2$ configurations are assumed in the ground state, where $\underline{2p}$ and $\underline{L}$ denote the 2p core hole and ligand hole, respectively.

In the present 2p XPS spectrum of TiS_2, the energy separation between the S_1 and S_2 structures is nearly equal to that between the main peaks. Therefore, the S_1 and S_2 satellites can be considered to be located at 10eV larger E_B of the $2p_{3/2}$ and $2p_{1/2}$ main peaks, respectively. This value is about 3eV smaller than in the oxides. This result may be simply understood as the smaller final state hybridization strength V_{eff} compared with that of the oxides. Such a relatively smaller hybridization is consistent with the larger atomic distance between the Ti atom and the anion, e.g., 2.43Å in TiS_2 and 1.96Å in TiO_2 [2.24]. The energy difference between the $\underline{2p}d^0$- and $\underline{2p}d^1\underline{L}$- dominated final state configurations is represented as $\sqrt{(\Delta-U_{dc})^2+4V_{eff}^2}$, according to the simple configuration interaction analysis assuming the d^0 and $d^1\underline{L}$ configurations in the ground state, where Δ is defined as $E(d^1\underline{L})-E(d^0)$ and U_{dc} represents the Coulomb attraction energy between the Ti 2p core hole and the 3d electron. The adopted parameters Δ and U_{dc} are 3 and 6eV in order to reproduce the Ti 2p XPS spectrum of TiO_2 [2.23]. In TiS_2, U_{dc} is expected to have the same value of 6eV, while Δ is thought to be 2eV smaller than that of the oxide because of the smaller electron negativity as seen in the late transition metal 2p XPS spectra [2.15]. Thus the final state hybridization V_{eff} is estimated to be about 4.5eV with using U_{dc}=6eV, Δ=0.5-1eV and the above-mentioned value of 10eV.

In the above model, only the hybridization between the Ti 3d and S 3p states is considered. It is found in the M_xTiS_2 intercalation compound that the Ti 2p XPS main peak is broader than in the host TiS_2. The broadening of the Ti 2p XPS spectra of the intercalated materials is possibly due to the following reasons:

1) In this case, we should take into account the hybridization between the guest transition metal (M) 3d and the host Ti 3d states in addition to that between the Ti 3d and S 3p states. Therefore, the lineshape of the Ti 2p XPS spectra may be governed by the superposed effects of the two hybridizations such as Ti 3d-M 3d and Ti 3d-S 3p.

Fujimori et al. have interpreted in their paper on the Ti 2p XPS spectra of TiS_2 and M_xTiS_2 that the main peak in the host TiS_2 is attributed to the state with "poorly-screened" character and the broader spectral shape of the main peak of the Ti 2p XPS spectra in M_xTiS_2 is ascribed to the superposition of the "well-screened" state at around 1.5eV smaller E_B [2.10]. In M_xTiS_2, the screening level with the Ti 3d character is thought to be filled by means of the charge transfer from the guest atom (M) 3d state to the host Ti 3d state, whereas such screening state is not filled in TiS_2 because the Ti 3d conduction band is almost empty. Accordingly the additional component found in the broad Ti 2p XPS spectra of M_xTiS_2 can be ascribed to the hybridization states between the guest atom (M) 3d and Ti 3d states.

2) As revealed in the different line shape of the Ti 2p XAS spectra of M_xTiS_2 compared with that of TiS_2, the electron number of the Ti 3d states increases upon the intercalation, which will lead to the increase of the multiplet lines of the Ti 2p XPS final state. K.Okada et al. has pointed out that if the strong hybridization exists between the $\underline{2p}3d^n$ and $\underline{2p}3d^{n+1}$ configurations, the bonding (antibonding) split-off state which in generally forms the main peak (satellite) of the 2p XPS spectrum reflects

the $\underline{2p}3d^n$ multiplets due to a phase matching effect between these configurations [2.14]. In the case of the "$3d^0$" system, the wave function is mainly described by a linear combination of the $3d^0$ and $3d^1\underline{L}$ configurations in the ground state. Therefore the 2p XPS spectrum is considered to show only single line because the $\underline{2p}3d^0$ state has no multiplet. On the other hand, since the wave function of $3d^1$ system is mainly described by a linear combination of $3d^1$ and $3d^2\underline{L}$ configurations in the ground state, the 2p XPS final state reveals the several multiplets which is characteristic of $\underline{2p}3d^1$ configuration. It is considered that the Ti 2p XPS spectrum of TiS_2 belongs to the former case. The spectrum of the intercalated TiS_2 is thought to belong to the latter case which will lead to the broadening of the main peak.

From the above discussions, it is concluded that *the configuration interaction picture between $3d^0$ and $3d^1\underline{L}$ is available to discuss the character of the Ti 3d states of TiS_2. It can be also considered that the CI between $3d^1$ and $3d^2\underline{L}$ configurations can be applied to investigate the Ti 3d character of the intercalated system.*

B: ***Ti 2p XAS spectra***

Characteristic features as observed in the Ti 2p XAS spectrrum of TiS_2 are also found in the corresponding spectra of nominally tetravalent Ti oxides such as TiO_2 and $SrTiO_3$ [2.25]. Their spectra are well reproduced by the full-multiplet CT theory with using the TiO_6 cluster, in which the ground state consists of $3d^0$, $3d^1\underline{L}$ and $3d^2\underline{L}^2$ states, where $\underline{L}$ represents the ligand hole [2.23]. According to the calculation, the lowest energy peak consists of a single line, while other components consist of a large number of lines. Therefore the broader structures found in the Ti $2p_{1/2}$ region is mainly due to the multiplet effect. Of course, the L_2L_3V Coster-Krönig Auger decay effect is not negligible in addition to the multiplet effect. Besides the abovementioned main structures, the extra structures also appear at the excitation energy of 13eV measured from the main peaks which is ascribed to the t_{2g} excitation states of $2p_{3/2}$ and $2p_{1/2}$ components, respectively. These XAS satellite features as well as those of the main peaks are well reproduced by the calculation with the parameters of U_{dd}=4eV, U_{dc}=6eV, Δ=3eV and V_{eff}=7eV being applied.

In the case of TiS_2, the higher energy satellite structures are also observed but the intensity and energy separation of the satellites measured from the XAS main peak are different from the cases of Ti-oxides. In order to understand such satellite features, the strong hybridization between the $\underline{2p}3d^1$ and $\underline{2p}3d^2\underline{L}$ configurations as discussed in the Ti 2p XPS spectrum of Ti compounds. It is noticed that the main feature of the Ti 2p XAS spectrum in TiS_2 is apparently well reproduced only by the $\underline{2p}3d^1$ crystal field calculation including the multiplet [2.20]. However this never means that the Ti 2p XAS main structures consists of $\underline{2p}3d^1$ components because the strong hybridization between the $\underline{2p}3d^1$ and $\underline{2p}3d^2$ usually leads to the bonding state which shows the similar structure to that of the $\underline{2p}3d^1$ configuration due to the phase matching effect as mentioned in the previous section.

The energy separation beween the main peak and the satellite of the Ti 2p XAS spectrum is estimated to be about 8.5eV in TiS_2 by measuring the energy distance between the $2p_{1/2}$ main peak and the higher energy satellite B. From this result, the effective hybridization strength V_{eff}' between the $\underline{2p}d^1$ and $2pd^2\underline{L}$ configurations is estimated to be about 4.2eV according to the simple two configuration interaction analysis as applied for the Ti 2p XPS spectrum, where the same values of Δ' and U_{dc} as those used in the Ti 2p XPS spectrum are adopted and U_{dd} of 4eV is tentatively applied as in the case of TiO_2 [2.23]. In the present case, the energy difference between the $\underline{2p}3d^1$ and $\underline{2p}3d^2\underline{L}$ configurations is represented as

$\sqrt{(\Delta'-U_{dc})^2+4V'^2_{eff}}$. This value of $V_{eff}'\approx4.2eV$ seems to be slightly smaller than that obtained from Ti 2p XPS result ($V_{eff}'\approx4.5eV$). This may be due to the decreased degeneracy of the Ti 3d conduction band in the XAS final state.

Furthermore the on-site Coulomb interaction U_{dd} should be taken into account in order to understand the Ti 2p XAS spectral feature because the energy difference between the $\underline{2p}3d^1$ and $\underline{2p}3d^2\underline{L}$ states can be represented as $\Delta'-U_{cd}+U_{dd}$ when neglecting the hybridization. According to the calculation by K.Okada et al.[2.23], the intensity of the satellite structure is much sensitive to this value, i.e., the satellite intensity gradually grows up with decreasing U_{dd} although the energy separation between the main and satellite structures is almost constant even if the magnitude of U_{dd} changes. The present Ti 2p XAS spectrum of TiS_2 shows more pronounced satellite structure compared with that of TiO_2. This may suggest the smaller on-site Coulomb interaction between the Ti 3d electrons in TiS_2 than in TiO_2.

The Ti 2p XAS spectra of the intercalated materials resembles that of VO_2 [2.26], which has nominally d^1 configuration in the ground state. Therefore it is possible to interpret that the spectral change found in the Ti 2p XAS spectra of M_xTiS_2 is derived from the charge transfer from the guest atom to the Ti atom. Additionally, the satellite structure is observed at the almost same hν as that of the TiS_2. In the similar way to the argument of the spectrum of the host material, the main (satellite) structure of the Ti 2p XAS spectra in the M intercalated TiS_2 is thought to be mainly derived from the bonding (anti-bonding) state due to the strong hybridization between the $\underline{2p}3d^2$ and $\underline{2p}3d^3\underline{L}$ configurations. Therefore, the difference of the spectral line shapes observed in the the main and satellite structure between those of TiS_2 and M_xTiS_2 is considered to be due to the different multiplet structures between $\underline{2p}3d^1$ and $\underline{2p}3d^2$ configurations, respectively.

C: *Valence band photoemission spectra*

Satellite states far away from the main valence band are often observed in the photoemission spectra of the light transition metal oxides and fluorides [2.22]. In the case of TiO_2 [2.22], the valence band satellite is located around 14.5eV away from the valence band maximum, It is suggested that such a satellite feature found in the valence band photoemission spectrum is possibly derived from the configuration interaction (CI) between the $d^1\underline{L}^2$ and $d^0\underline{L}$ final states. The resonance enhancement mainly takes place between the following processes:

(direct photoemission)

$d^0 + h\nu \rightarrow d^0\underline{L}\varepsilon l$ - (a)
$d^1\underline{L} + h\nu \rightarrow d^0\underline{L}\varepsilon l$ - (b)
$\rightarrow d^1\underline{L}^2\varepsilon l$ - (c)

(2p core excitation and following Auger deexcitation)

$d^0 + h\nu \rightarrow \underline{2p}d^1 \rightarrow d^0\underline{L}\varepsilon l$ (interatomic) - (1)
$d^1\underline{L} + h\nu \rightarrow \underline{2p}d^2\underline{L} \rightarrow d^0\underline{L}\varepsilon l$ (intraatomic) - (2)
$\rightarrow d^1\underline{L}^2\varepsilon l$ (interatomic) - (3)

Therefore, the processes between the direct photoemission and the Auger deexcitation followed by the 2p core excitation have the common initial and final states and a resonance enhancement is expected. The final state $d^0\underline{L}\varepsilon l$ is expected to be created with the high probability because the the process (2) includes the intraatomic Auger decay as a result of the strong d-d Coulomb repulsion. On the other hand, the process (1) and (3) is considered to occur with low probability because the processes contain the weak Coulomb interaction between the interatomic d-p electrons. Resultingly the resonance enhancement of the final state $d^0\underline{L}\varepsilon l$ is expected to be strongest among several final states considered above.

In the case of TiS_2, it is difficult to verify the existence of the satellite structures because the $L_{23}VV$ Auger state is prominent and the S 3s state is overlapping in the corresponding binding energy region in the present data.

According to the ARUPS study, the intercalation-induced new structure in Mn, Fe, Co and Ni intercalated TiS_2 appears just below E_F and shows almost flat dispersion in a wide wave vector region. The band calculation and the ARUPS spectrum of TiS_2 show that the conduction band minimum derived from the Ti 3d state is located at the L point, around which the electron pocket is made. If the electron of the guest atom is partially transferred to the empty Ti 3d states of the host without modifying the band structure, the band near the L point should move downward relative to E_F a larger electron pocket will be observed around the L point near E_F.

Now we consider the charge transfer (CT) from the valence orbital (S 3p) to the Ti 3d e_g state in a system with the Ti $3d^1$ ground state. It seems to be sufficient to represent the ground state as a linear combination of $d^1(t_{2g})$ and $d^2(t_{2g},e_g)\underline{L}$ configurations. For this system, the p-d charge transfer energy Δ can be defined as $E(d^2\underline{L})-E(d^1)$, where $\underline{L}$ denotes the ligand hole. In the photoemission final state of the valence band of this system, the $d^1\underline{L}$ and d^0 final states (with the energy difference of $\Delta-U_{dd}$) strongly hybridize via the off diagonal matrix element V_{eff}, where U_{dd} represents the d-d Coulomb repulsion energy. This strong hybridization will realize a strong photoemission peak near E_F.

K.Okada et al. discussed on the character of the sharp photoemission structure often found in the Ti^{3+} or V^{2+} compounds just below E_F by considering the $d^2\underline{L}$ and d^1 configurations in the ground state [2.14]. They interpreted such a structure as the split-off state derived from the strong final state hybridization between the d^0 and $d^1\underline{L}$ configurations. In our case of M_xTiS_2, the originally tetravalent Ti in the host TiS_2 seems to become trivalent by the charge transfer from M. The negligible dispersion of these states along the k direction (parallel to the surface) may be due to the relatively long distance between the intercalated M atoms forming the $\sqrt{3}\times\sqrt{3}$ superlattice in the case of $M_{1/3}TiS_2$. If the charge transfer (CT) takes place along the c-axis, the Ti t_{2g} d_{z^2} state will be populated as the M-Ti bonding state. Other Ti t_{2g} states will stay as nonbonding states. We consider that the Ti t_{2g} d_{z^2} bonding state is responsible for the structure at E_B~1eV in $Ni_{1/3}TiS_2$ and that the Ti t_{2g} nonbonding state is responsible for the structure at E_B~0.2eV in all M_xTiS_2. The trend of the energy shift of the former structure with the M species and the stability of the latter structure are consistently interpretable in this model.

It is generally known that the Ti e_g component is strongly hybridized with the S 3p valence band in TiS_2 and its intercalated compounds. It is thought that the Auger decay resulting in two holes with different symmetry orbitals such as one hole in the e_g and the other hole in the t_{2g} states will be weaker than the Auger decay with two holes of the same symmetry according to the smaller overlap of the two d states with different symmetry.

For the ground state configuration mainly composed of $d^1(t_{2g})$ and $d^2(t_{2g}e_g)\underline{L}$ states, the Ti 2p XAS final state configuration corresponding to the excitation to the "t_{2g}" state can be $\underline{2p}3d(t^2_{2g})$ and $\underline{2p}3d^3(t^2_{2g}e_g)\underline{L}$ configurations as schematically described in Fig.2.23. The Coster-Krönig

Auger decay process most effectively takes place with leaving two holes in the t_{2g} state and realizing the final state with the configuration of $3d^0$ and $3d^1(e_g)\underline{L}$. Likewise the XAS final state for the excitation to the "e_g" state is $\underline{2p}3d^2(t_{2g}e_g)$ and $\underline{2p}3d^3(t_{2g}e^2{}_g)\underline{L}$. Then the Auger decay with leaving two holes in the e_g state most effectively takes place with yielding the final state with the configuration of $3d^1(t_{2g})\underline{L}$. This process strongly interferes with the direct photoemission from the $3d^2(t_{2g}e_g)\underline{L}$ state to the $3d^1(t_{2g})\underline{L}$ state. *Thus the $3d^1(t_{2g})\underline{L}$ state is considered to be predominant in the observed sharp photoemission structure just below E_F.*

D: *Ti 3p XPS spectra*

The resonance feature observed in the Ti 3p XPS spectrum in the Ti 2p core excitation region of TiS_2 will be discussed in this section. It has been shown that the resonance enhancement is stronger for the excitation to the Ti 3d t_{2g} excitation than to the e_g states clearly recognized in the CIS spectrum of TiS_2. A resonance processes of the Ti 3p photoemission are described as follows:

1) $3p^63d^n + h\nu \rightarrow 3p^53d^n\varepsilon l$ (Ti 3p direct photoemission)

2) $3p^63d^n + h\nu \rightarrow \underline{2p}3p^63d^{n+1} \rightarrow 3p^53d^n\varepsilon l$
(Coster Krönig Auger decay)

By considering the less itinerant (or more localized) character of the t_{2g} state than e_g state in the octahedral coordination, one may recognize that the $2p3p3d(t_{2g})$ Auger decay is stronger than the $2p3p3d(e_g)$ Auger decay. Now we take the ground state wave function as a linear combination of $3d^0$ and $3d^1(e_g)\underline{L}$ configurations. Then, the Ti 2p XAS final state configurations corresponding to the excitations to the

"t_{2g}" state can be $\underline{2p}3d^1(t_{2g})$ and $\underline{2p}3d^2(e_g,t_{2g})\underline{L}$ configurations as schematically described in Fig.2.24.. Finally the $\underline{3p}3d^0$ and $\underline{3p}3d^1(e_g)\underline{L}$ states are created after the predominant $2p3p3d(t_{2g})$ Auger decay from the intermediate $\underline{2p}3d^1(t_{2g})$ and $\underline{2p}3d^2(e_g,t_{2g})\underline{L}$ states, respectively. Likewise the XAS final states for the excitation to the "e_g" state are $\underline{2p}3d^1(e_g)$ and $\underline{2p}3d^2(e^2{}_g)\underline{L}$. In this case, the $2p3p3d(t_{2g})$ Auger decay process is impossible because the Ti 3d state does not include the t_{2g} electron. Thus the strong resonance enhancement of the Ti 3p main peak at the Ti 3d t_{2g} excitation peak is qualitatively explained.

In regard to the new structures which emerge on the the larger E_B side of the Ti 3p main peak of TiS_2, a doublet feature is observed above the absorption threshold. The splitting energy of about 2.7eV is much smaller than the spin-orbit splitting energy of the Ti 2p core state ($\approx$6eV) and slightly larger than the "e_g"-"t_{2g}" splitting (~2.3eV). As shown in Fig.2.15., these structures almost linearly shift toward the larger binding energy side with increasing $h\nu$. There is, however, a difficulty to conclude that these structures are simply derived from the normal Auger electron emission. The normal Auger final states created from the $3d^n$ ground state configuration appear through the following process:

$$3p^63d^n + h\nu \rightarrow \underline{2p}3p^63d^n\varepsilon'l \rightarrow 3p^53d^{n-1}\varepsilon'l\varepsilon l \text{ -(*)}$$

where $\varepsilon'l$ and εl denote the continuum states associated with the intermediate electron exitation and photoemitted electron state, respectively. One notices that the kinetic energy of $\varepsilon'l$ is very small whereas that of εl is very large. For a system with no 3d electron in the ground state at the Ti site and near E_F, such an Auger process will not be allowed. If the final state configuration has one 3p hole and more than one 3d electrons, 3p-3d Coulomb and exchange interactions will provide multiplet structures for the final states. Such final states can be easily derived from a $3d^2$ ground state. It is, however, not plausible that the $3d^2$ state dominantly exists in the ground state.

Under the resonance excitation, the following two processes can interfere with each other even in the system with the $3d^1$ ground state:

1) $3p^63d^1 + h\nu \rightarrow 3p^53d^1\varepsilon l$ (Ti 3p direct photoemission)

2) $3p^63d^1 + h\nu \rightarrow \underline{2p}3p^63d^2 \rightarrow 3p^53d^1\varepsilon l$ ----------(**)

(Coster Krönig Auger decay)

the exchange interaction between a 3p hole and a 3d electron gives the doublet with spin parallel and spin antiparallel configurations. Even if the excitation does not satisfy the condition (**), the exchange interaction between the 3p hole and the $\varepsilon' l$ electron will take place as far as the E_k of $\varepsilon' l$ is negligibly small. Thus we interpret the splittings as the exchange interaction between the 3p hole and the 3d (or $\varepsilon' l$) electron. Besides the intensity enhancement of the structure is caused by the interference between the above mentioned two processes.

In addition to these states, a broad hump structure is found at about 10eV larger E_B of the Ti 3p main peak. Since the satellite is found at the same energy measured from that of the Ti 3p main peak as observed in the Ti 2p XPS spectrum, it is also considered that the main and satellite structures consists of the bonding and antobonding states derived from the strong hybridization between $\underline{3p}3d^0$ and $\underline{3p}3d^1\underline{L}$ configurations.

We have shown that the resonance enhancement at the hv corresponding to the excitation to the "t_{2g}" state is stronger than that to the "e_g" state. Such behavior can be also understood by the consideration as taken in the Ti 3p XPS of TiS_2.

In this case, the linear combination of the Ti $3d^1(t_{2g})$ and $3d^2(t_{2g},e_g)\underline{L}$ configurations are taken into account for the ground state. Then the intermediate states of the resonance photoemission process (Ti 2p XAS final state) corresponding to the excitation to the "t_{2g}" state are $\underline{2p}3d^2(t_{2g}{}^2)$ and $\underline{2p}3d^3(t_{2g}{}^2,e_g)\underline{L}$ configurations as schematically shown in Fig.2.25.. After the predominant $2p3p3d(t_{2g})$ Coster Krönig decay takes place, the $\underline{3p}3d^1(t_{2g})$ and $\underline{3p}3d^2(t_{2g},e_g)\underline{L}$ states are created from the $\underline{2p}3d^2(t_{2g}{}^2)$ and $\underline{2p}3d^3(t_{2g}{}^2,e_g)\underline{L}$ configurations, respectively. It is noted that these processes described above can interfere with the Ti 3p direct photoemission processes yielding the $\underline{3p}3d^1(t_{2g})$ and $\underline{3p}3d^2(t_{2g},e_g)\underline{L}$ final states from the ground states such as $3d^1(t_{2g})$ and $3d^2(t_{2g},e_g)\underline{L}$. On the contrary, in the case of the "e_g" excitation, such a interference does not occur because the possible Ti 3p photoemission final states are the $\underline{3p}3d^1(e_g)$ and $\underline{3p}3d^2(e_g{}^2)\underline{L}$ which are produced as a result of the $2p3p3d(t_{2g})$ Auger decay. These photoemission final states can not be obtained from the ground states such as $3d^1(t_{2g})$ and $3d^2(t_{2g},e_g)\underline{L}$ configurations. Therefore, in the case of the excitation to the "t_{2g}" states, it can be considered that such an interference effect derives the strong resonance enhancement of the Ti 3p main peak, whereas the resonance enhancement at the Ti 3d "e_g" excitation peak is thought to be relatively weak due to the weak intereference compared with the case of the excitation to the "t_{2g}" state.

E: $L_{23}M_{23}M_{23}$ *Auger final state*

We have shown that the higher binding energy structure of Ti 3s main peak linearly shifts with increasing the photon energy. It has been revealed that there is no higher kinetic energy (lower E_B) structure in contrast to the observation in the 2p core resonance photoemission spectra of the ionic crystals and the rare gases with $3d^0$ configuration in the ground state[2.27-32]. As for the $3d^0$ compound, the higher kinetic energy (smaller binding energy) structure associated with the 2p3p3p Auger decay is deduced from the following process:

$$3p^63d^0 + h\nu \rightarrow \underline{2p}3p^63d^1 \rightarrow 3p^43d^1\varepsilon l \qquad \text{-(1)}$$

On the other hand, the normal Auger final state occurs through the following process:

$$3p^63d^0 + h\nu \rightarrow \underline{2p}3p^63d^0\varepsilon'l \rightarrow 3p^43d^0\varepsilon'l\varepsilon l \quad \text{-(2)}$$

where εl and $\varepsilon' l$ represent the continuum states with respect to the photoemission and the intermediate electron transition, respectively.

In the cases of the ionic crystals such as CaF_2 etc. with the ground state of $3d^0$ configuration, the higher kinetic energy structure appears as result of the process (1) [2.27, 28]. On the other hand, in the case of TiS_2, the normal Auger structure seems to dominate the spectrum on the larger E_B side of the Ti 3s peak which may be due to the delocalized character of the Ti 3d electron.

F: ***Valence band photoemission spectra in the guest atom M 2p core excitation region***

The larger E_B structure as observed in the resonance photoemission spectra in the Mn 2p core excitation region of $Mn_{1/4}TiS_2$ can not be simply explained by the one electron band picture. The result of the APW band calculation of $Mn_{1/3}TiS_2$ [2.12] only shows the density of states (DOS) spreading from E_F to about 5eV. On the other hand, the configuration interaction (CI) cluster calculation including the on site Coulomb interaction (U_{dd}) and the charge transfer from the anion p to

Mn 3d can reproduce the broad satellite structures. In the case of MnO [2.33, 34], for example, the fitting parameters such as U_{dd}=7.5eV and the charge transfer energy Δ=7.0eV were used in the CI cluster calculation. Therefore the on site Coulomb interaction of the Mn 3d electrons is also considered to be important in the case of $Mn_{1/4}TiS_2$.

As shown in the on-resonance photoemission spectra of $Fe_{1/3}TiS_2$ taken at the Fe $2p_{3/2}$ excitation threshold, the enhancement occurs for the structure centered at E_B=5eV and the enhanced structure spreads over a quite wide energy range of about 15eV. Such a wide energy distribution of the Fe 3d states cannot be simply explained by the one-electron band picture. In the valence band XPS spectra of $Fe_{1/3}TiS_2$ measured by A.Fujimori et al., the wide energy distribution of the Fe 3d states with a satellite at E_B=6-10eV is also revealed in the $Fe_{1/3}TiS_2$-TiS_2 difference spectrum [2.10]. A.Fujimori et al. also pointed out that the difference spectrum is similar to the spectrum of the high-spin FeS and suggested that the Fe 3d electrons in $Fe_{1/3}TiS_2$ are almost localized because FeS is the antiferromagnetic insulator and is known to have U_{dd} of about 5eV according to their CI cluster calculation. The above-mentioned behavior of the resonance photoemission at the Fe 2p core excitation threshold is consistent with the calculated result of the corresponding spectra of FeO performed by A.Tanaka et al [2.35], where the remarkable enhancement is revealed for the structure centered at E_B=5eV in a wide energy range extending from E_F to about15eV.

In Fig.2.20.(c), the resonance photoemission spectra of $Co_{1/3}TiS_2$ in the Co 2p core excitation threshold are shown. It is recognized that the resonance behavior is quite similar to the case of $Fe_{1/3}TiS_2$. This also indicates that the Co 3d state spreads over a wide energy region due to the strong hybridization or the multiplets. The calculated result of the Co 2p core excited resonance photoemission spectra of CoO also shows the remarkable enhancement at the Co 2p core excitation threshold and the enhancement spreads over a wide energy region of about 15eV, but the calculated spectra reveal the quite different line shapes depending on the excitation energies because the different intermediate states would lead to the different multiplet structures of the photoemission final states. Since the line shapes of the enhanced structures are rather broad and structureless in the present data because of the limitted resolution or the solid state effects, the detailed comparison is difficult for the moment. As discussed in the previous section, the line shape of Co 2p XAS spectrum is quite different from that of the high-spin CoO and is similar to that of the low-spin CoS_2, it can be possibly considered that the Co 3d states of $Co_{1/3}TiS_2$ have the low-spin state in the ground state. Therefore the different final states of the resonance photoemission are expected. We hope the detailed theoretical calculations on the rsonance photoemission spectra of the low-spin Co compounds.

As mentioned above, the 2p XAS main peak mainly consists of the $2p^5 3d^9$ configuration. Therefore the dominant decay channel at the excitation energy corresponding to the Ni 2p XAS main peak is as follows:

$$3d^8 + h\nu \rightarrow \underline{2p}3d^9 \rightarrow 3d^7\varepsilon l$$

In this way, the possible photoemission final state when the excitation energy corresponds to the Ni 2p XAS main peak is considered to have the Ni $3d^7$ configuration. Recently, A.Tanaka et al.[2.21] have calculated the resonance photoemission spectra at the Ni 2p threshold for $NiCl_2$ and NiO that have the different degree of hybridization to each other. According to their cluster calculation including the multiplet effect, the 2p XAS main (satellite) peak has the bonding (antibonding) character of $2p^5 3d^9$

transfer from the M atom to the t_{2g} state of the Ti atom and the strong hybridization between the Ti 3d e_g and S 3p states are responsible for this new valence band features just below E_F. The satellite features of the Ti 2p XPS and 2p XAS spectra have also revealed the importance of the hybridization between the Ti 3d and S 3p states.

References

[2.1] H.Negishi, S.Ohara, Y.Takata, T.Yokoyama, M.Taniguchi and M.Inoue, in *INTERCALATION COMPOUNDS ISIC-6*, eds. D.Tchoubar and J.Conard (Trans Tech Pub., Switzerland-Germany-UK-USA, 1992) p.603.

[2.2] M.Inoue and H.Negishi, J. Phys. Chem. **90** (1986) 235.

[2.3] M.Inoue and H.Negishi, *Recent Advances in Magnetism of Transition Metal Compounds*, eds. A.Kotani and N.Suzuki (World Scientific, Singapore, 1993) p.193.

[2.4] M.Inoue, M.Matsumoto, H.Negishi and H.Sakai, J. Magn. Magn. Mater. 53 (1985) 131.

[2.5] C.H.Chen, W.Fabian, F.C.Brown, K.C.Woo, B.Davies and B.DeLong, Phys. Rev. B **21**, 615 (1980).

[2.6] J.J.Barry, H.P.Hughes, P.C.Klipstein and R.H.Friend, J. Phys. C:Solid State Phys., **16**, 393 (1983).

[2.7] D.L.Greenaway and R.Nitsche, J. Phys. Chem. Solids **26**, 1445 (1965).

[2.8] A.R.Beal, J.C.Knights and W.Y.Liang, J.Phys. C **5**, 3531 (1972).

[2.9] M.R.Vilanove, C. R. Acad. Sci. Paris B **271**, 1101 (1970).

[2.10] A.Fujimori, S.Suga, H.Negishi and M.Inoue, Phys. Rev. B **38**, 3676 (1988), and references therein.

[2.11] A.Kotani and Y.Toyozawa, J. Phys. Soc. Jpn. **37**, 912 (1974).

[2.12] N.Suzuki, T.Yamasaki and K.Motizuki, J. Phys. Soc. Jpn., **58**, 3280 (1989).

[2.13] Y.Ueda, H.Negishi, M.Koyano, M.Inoue, K.Soda, H.Sakamoto and S.Suga, Solid. State. Commun. **57** (1986) 839.:
Y.Ueda, K.Fukushima, H.Negishi, M.Inoue, M.Taniguchi and S.Suga, J. Phys. Soc. Jpn. **56** (1987) 2471.

[2.14] K.Okada, T.Uozumi and A.Kotani, ISSP Tech. Rep. A2809 (1994) The University of Tokyo.

[2.15] A.E.Bocquet, T.Mizokawa, T.Saitoh, H.Namatame and A.Fujimori, Phys. Rev. B **46**, 3771 (1992). For example, the best fit values of the charge transfer energy are 4.5eV for NiO and 2.5eV for NiS.

[2.16] L.C.Davis, J. Appl. Phys. **59** (1986) R25.

[2.17] C.T.Chen and F.Sette, Rev. Sci. Instrum. **60** (1989) 1616.

[2.18] A.Yagishita, S.Masui, T.Toyoshima, H.Maezawa and E.Shigemasa, Rev. Sci. Instrum. **63** (1992) 1351.

[2.19] S.P.Cramer, F.M.F. de Groot, Y.Ma, C.T.Chen, F.Sette, C.A.Kipke, D.M.Eichhorn, M.K.Chan, W.H.Armstrong, E.Libby, G.Christou, S.Brooker, V.McKee, O.C.Mullins and J.C.Fuggle, J. Am. Chem. Soc. **113** (1991) 7937.

[2.20] F.M.F. de Groot, J.C.Fuggle, B.T.Thole and G.A.Sawatzky, Phys. Rev. B **42** (1990) 5459.

[2.21] A.Tanaka and T.Jo, J. Phys. Soc. Jpn. **61** (1992) 3837.

[2.22] S.Shin, Y.Tezuka, T.Ishii and Y.Ueda, Solid State Commun. **87** (1993) 1051.

[2.23] K.Okada and A.Kotani, J. Electron Spectrosc. Relat. Phenom. **62** (1993) 131.

[2.24] T.Uozumi, K.Okada and A.Kotani, J. Phys. Soc. Jpn. **62**, L2595 (1993).

[2.25] G. van der Laan, Phys. Rev. B **41** (1990) 12366.

[2.26] M.Abbate, F.M.F. de Groot, J.C.Fuggle, Y.J.Ma, C.T.Chen, F.Sette, A.Fujimori, Y.Ueda and K.Kosuge, Phys. Rev. B **43**, 7263 (1991).

[2.27] T.Tiedje, K.M.Colbow, D.Rogers and W.Eberhardt, Phys. Rev. Lett. 65 (1990) 1243.

[2.28] M.Elango, A.Ausmees, A.Kikas, E.Nommiste, R.Ruus, A.Saar, J.F.van Acker, J.N.Anderson, R.Nyholm and I.Martinson, Phys. Rev.B **47** (1993) 11736.

[2.29] M.Qvarford, J.N.Anderson, R.Nyholm, J.F. van Acker, E.Lundgren, I.Lindau, S.Soderholm, H.Bernhoff U.O.Karlsson and S.A.Flodstorm, Phys. rev. B **46** (1992) 14126.

[2.30] H.Aksela, S.Aksela, H.Pulkkinen, G.M.Bancroft and K.H.Tan, Phys.Rev. A **37** (1988) 1798.

[2.31] M.Meyer, E.V.Raven, B.Sonntag and J.E.Hansen, Phys. Rev. A **43** (1991) 177.

[2.32] W.Wurth, GRocker, P.Feulner, R.Scheuerer, LZhu and D.Menzei, Phys. Rev. B **47** (1993) 6697.

[2.33] A.Fujimori, N.Kimizuka, T.Akahane, T.Chiba, S.Kimura, F.Minami, K.Shiratori, M.Taniguchi, S.Ogawa and S.Suga, Phys. Rev. B **42** (1990) 7580.

[2.34] J.van Elp, R.H.Potze, H.Eskes, R.Berger and G.A.Sawatzky, Phys. Rev. B **44** (1991) 1530.

[2.35] A.Tanaka and T.Jo, J. Phys. Soc. Jpn **63** (1994) 2788.

[2.36] G. van der Laan, B.T.Thole, H.Ogasawara, Y.Seino and A.Kotani, Phys. Rev. B **46** (1992) 7221.

[2.37] G. van der Laan, M.Surman, M.A.Hoyland, C.F.J.Flipse, B.T.Thole, Y.Seino, H.Ogasawara and A.Kotani, Phys. Rev. B **46** (1992) 9336.

Figure captions

Fig. 2.1.

(Left) Interatomic distances between the guest 3d metals M and the nearest host S atom R(M-S) plotted against the guest concentration x for various M_xTiS_2. (Right) Comparison of interatomic distances R(M-S) and interlayer spacing c for M_xTiS_2

Fig. 2.2.

Electronic specific heat coefficient γ of M_xTiS_2 plotted against (a) 3d metal concentration and (b) the atomic number of the metals (x=1/10 and 1/4).

Fig. 2.3.

Experimental band dispersion along the Γ(A)-M(L) direction of $Ni_{1/3}TiS_2$ probed by ARUPS at hν=28eV.

Fig. 2.4.

Reflectance spectra in the 2-30eV region of TiS_2 (top) and $Fe_{1/3}TiS_2$ (bottom).

Fig. 2.5.

(a) Ti 2p core level XPS spectra of TiS_2 and M_xTiS_2. The vertical line marks the $2p_{3/2}$ peak position for TiS_2. (b) 2p corelevel XPS spectra of guest 3d-transition metal atoms in M_xTiS_2. The $2p_{3/2}$ peaks of different compounds have been aligned. $h\omega_p$ marks approximately the bulk plasmon energy position of the plasmon satellite accompanying the S 2p core-level XPS peak. (c) XPS spectra of TiS_2 and M_xTiS_2 in the valence band region. Difference spectra between M_xTiS_2 and TiS_2 are shown by solid curves below each of the M_xTiS_2 spectra. The TiS_2 spectrum is compared with a result of band calculation (solid line).

Fig. 2.6.

Curve 1, the photoemission spectrum at hν=48eV (on-resonance), curve 2 the spectrum at 35eV (off-resonance) and curve 3 the difference spectrum for TiS_2. The difference spectra for (b) $Mn_{1/4}TiS_2$, (c) $Fe_{1/3}TiS_2$, (d) $Co_{1/4}TiS_2$, (e) $Co_{1/3}TiS_2$ and (f) $Ni_{1/3}TiS_2$.

Fig. 2.7.

Total and partial density of states calculated by APW method for (a) $Mn_{1/3}TiS_2$, (b) $Fe_{1/3}TiS_2$, (c) $Co_{1/3}TiS_2$ and (d) $Ni_{1/3}TiS_2$.

Fig. 2.8

Experimental and theoretical Ti 2p XPS. The experimental data is shown in (a). (b) is calculated by means of the multiplet CT theory. (c) is the Ti 2p-XPS for a free Ti^{4+} ion obtained by the CF calculation.

Fig. 2.9.

The final state structure of the core-level XPS for the tetravalent Ti compounds and that of the valence band photoemission for the trivalent Ti compounds are illustrated.

Fig. 2.10.

The calculated 3d and 3p photoemission spectra of TiO_2 for the incident photon energy corresponding to various multiplets of 2p core absorption spectrum. For comparison, the off-resonance spectrum is also shown.

Fig. 2.11

Ti 2p XPS spectra of (a) TiS_2, (b) $Mn_{1/4}TiS_2$, (c) $Fe_{1/3}TiS_2$, (d) $Co_{1/3}TiS_2$ and (e) $Ni_{1/3}TiS_2$. The S 2p XPS spectrum of TiS_2 is also shown for comparison. S_1, S_2 and S_3 denote the satellite structures accompanying the Ti 2p XPS main peak of TiS_2.

Fig. 2.12.

Ti 2p XAS spectra of (a) TiS_2, (b) $Mn_{1/4}TiS_2$, (c) $Fe_{1/3}TiS_2$, (d) $Co_{1/3}TiS_2$ and (e) $Ni_{1/3}TiS_2$.

Fig. 2.13

Valence band photoemission spectra of (a)TiS_2, (b)$Mn_{1/4}TiS_2$, (c)$Fe_{1/3}TiS_2$, (d)$Co_{1/3}TiS_2$ and (e)$Ni_{1/3}TiS_2$ measured at the photon energies of the Ti 2p→3d core excitation region. The numerals indicate the excitation energies. The solid dots represent the raw data, whereas the broken lines or solid lines indicate the difference spectra from the off resonance spectrum marked by 1.

Fig. 2.14.

Constant initial state spectra (CIS) of (a)TiS_2, (b)$Mn_{1/4}TiS_2$, (c)$Fe_{1/3}TiS_2$, (d)$Co_{1/3}TiS_2$ and (e)$Ni_{1/3}TiS_2$ for several binding energies of valence band region taken at the photon energies in the Ti 2p→3d core excitation region. At the top of this figure, the Ti 2p XAS spectrum is shown with the solid line for reference.

Fig. 2.15.

Ti 3p photoemission spectra of (a)TiS_2, (b)$Mn_{1/4}TiS_2$, (c)$Fe_{1/3}TiS_2$, (d)$Co_{1/3}TiS_2$ and (e)$Ni_{1/3}TiS_2$ for the photon energies in the Ti 2p→3d core excitation region.

Fig. 2.16.

Constant initial state spectra (CIS) of (a)TiS_2, (b)$Mn_{1/4}TiS_2$, (c)$Fe_{1/3}TiS_2$, (d)$Co_{1/3}TiS_2$ and (e)$Ni_{1/3}TiS_2$for several binding energies of Ti 3p region taken at the photon energies in the Ti 2p→3d core excitation region. At the top of this figure, the Ti 2p XAS spectrum shown with the solid line for reference.

Fig. 2.17.

Ti 3s photoemission spectra of TiS_2 taken at the photon energies in the Ti 2p→3d core excitation region.

Fig. 2.18.

The binding energy shift of the structures appearing in the Ti 3s state region of TiS_2 plotted as a function of hv in the Ti 2p→3d excitation region.

Fig. 2.19.

The guest atom M 2p XAS spectrum of M_xTiS_2. (a)$Mn_{1/4}TiS_2$, (b)$Fe_{1/3}TiS_2$, (c)$Co_{1/3}TiS_2$ and (d)$Ni_{1/3}TiS_2$.

Fig. 2.20.

Valence band photoemission spectra of M_xTiS_2 taken at the photon energies in the M 2p→3d excitation region. (a)$Mn_{1/4}TiS_2$, (b)$Fe_{1/3}TiS_2$, (c)$Co_{1/3}TiS_2$ and (d)$Ni_{1/3}TiS_2$.

Fig. 2.21.

M 3p photoemission spectra of M_xTiS_2 taken at the photon energies in the M 2p→3d excitation region. (a)$Mn_{1/4}TiS_2$, (b)$Fe_{1/3}TiS_2$, (c)$Co_{1/3}TiS_2$ and (d)$Ni_{1/3}TiS_2$.

Fig. 2.22.

Schematic description of valence band photoemission from the ground state with $3d^0$ configuration in the octahedral coordination at the 2p core excitation threshold.

Fig. 2.23.

Schematic description of valence band photoemission from the ground state with $3d^1$ configuration in the octahedral coordination at the 2p core excitation threshold.

Fig. 2.24.

Schematic description of 3p core photoemission from the ground state with $3d^0$ configuration in the octahedral coordination at the 2p core excitation threshold.

Fig. 2.25

Schematic description of 3p core photoemission from the ground state with $3d^1$ configuration in the octahedral coordination at the 2p core excitation threshold.

Acknowledgments

I would like to thank my principal supervisor and mentor, Professor Shigemasa Suga, whose insight and great knowledge of the field of photoemission was a great inspiration to me.

I would also like to thank:

Professor Hiroshi Daimon and Dr. Shin Imada, staff of Suga Lab.;

Yuji Saitoh and Hiroyuki Nishimoto, my good colleague during my Master and Doctor course;

Miss Taneyo Ukawa for her encouragement for my work;

all the members of the Suga research group;

Professor Takeshi Kanomata for the supply of many high quality samples;

Professor Akio Kotani and Atsushi Fujimori for their useful discussions on a part of my works;

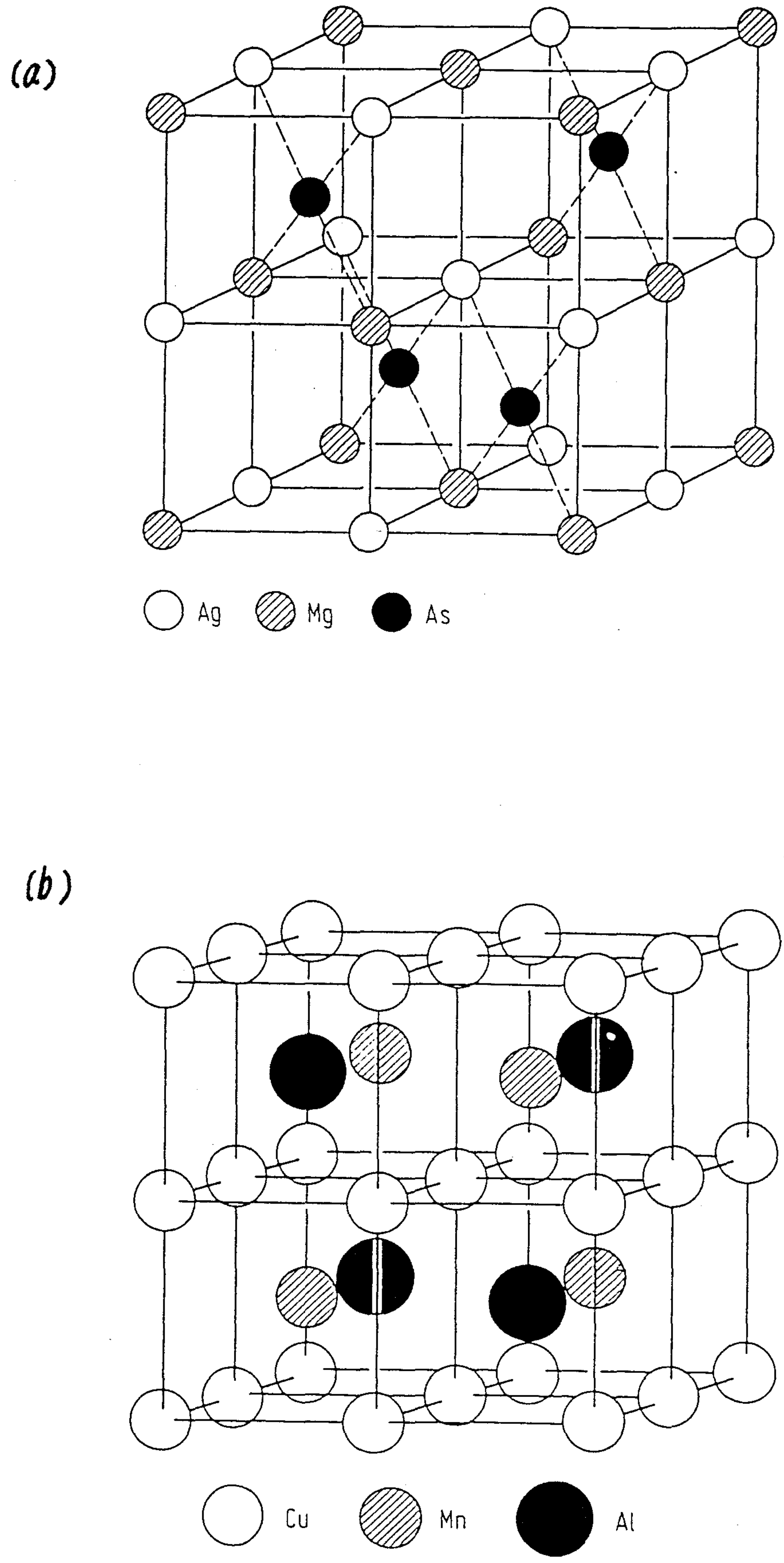

Fig. 1.1.

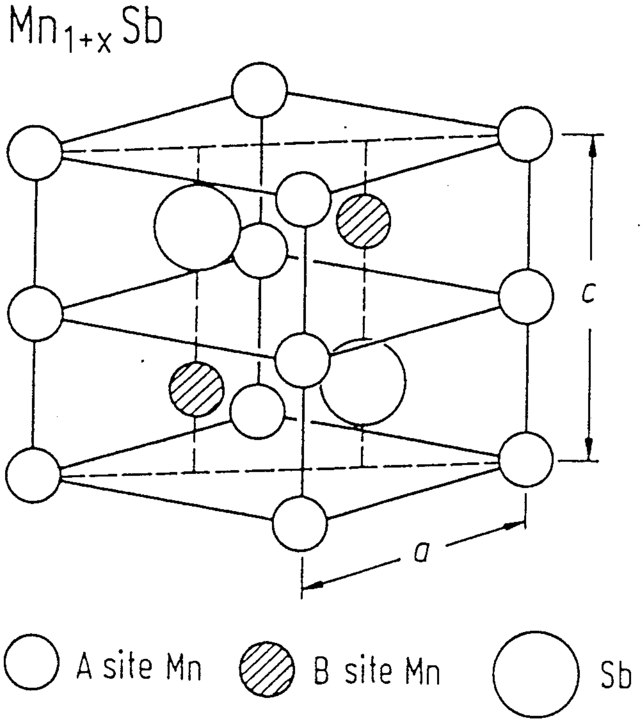
$Mn_{1+x}Sb$
c
a
A site Mn
B site Mn
Sb

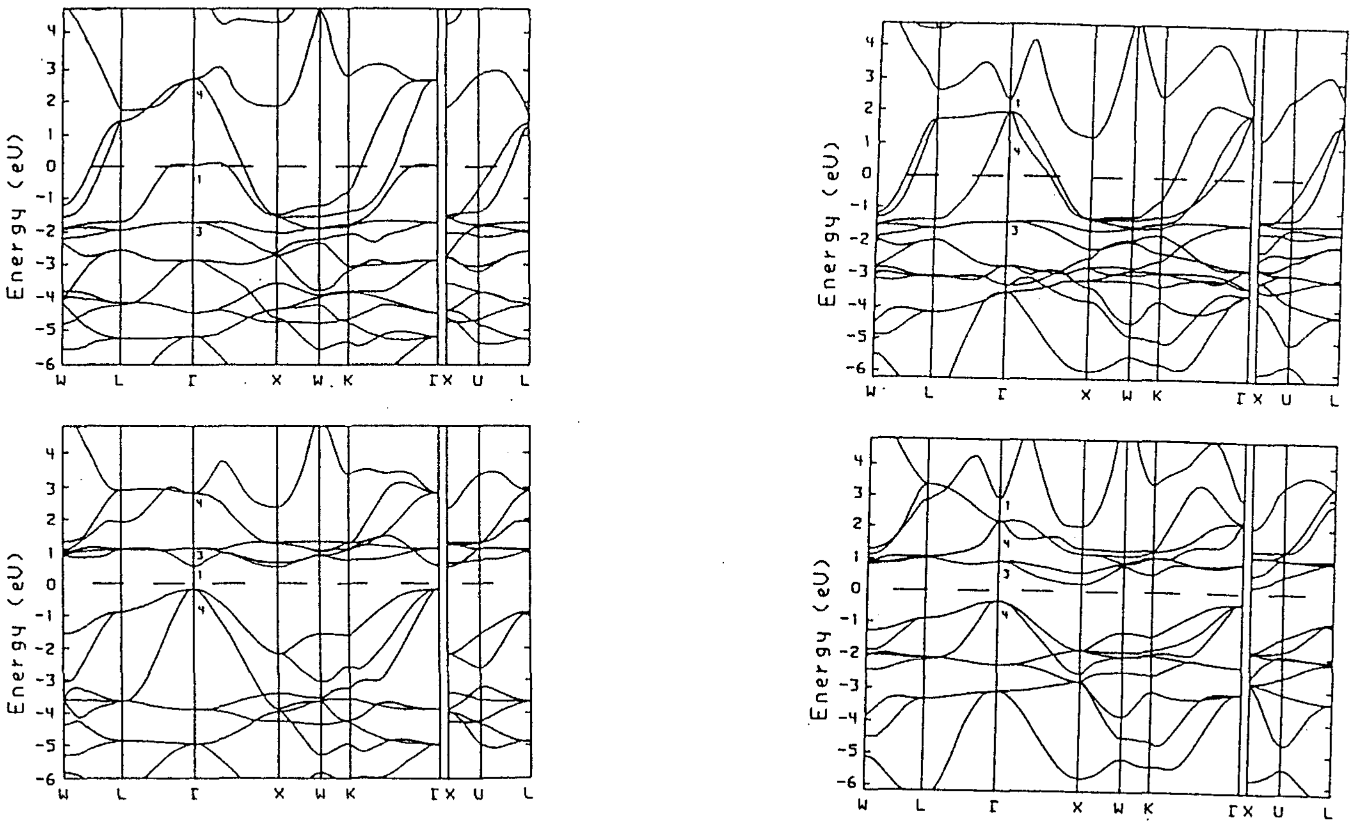

(a)

(b)

Fig. 1.2

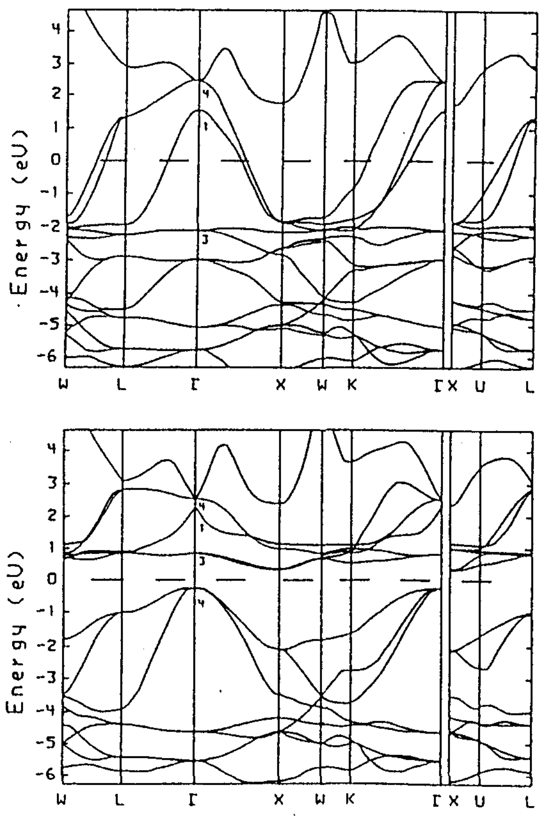
Energy (eV)
4
3
2
1
0
-1
-2
-3
-4
-5
-6
W
L
Γ
X
W
K
Γ
X
U
L
4
1
3

(c)

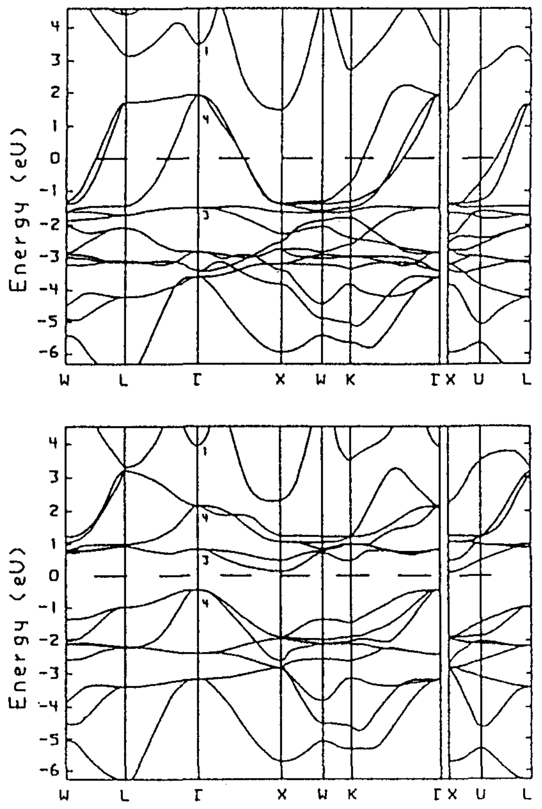
Energy (eV)
4
3
2
1
0
-1
-2
-3
-4
-5
-6
W
L
Γ
X
W
K
Γ
X
U
L
1
4
3

(d)

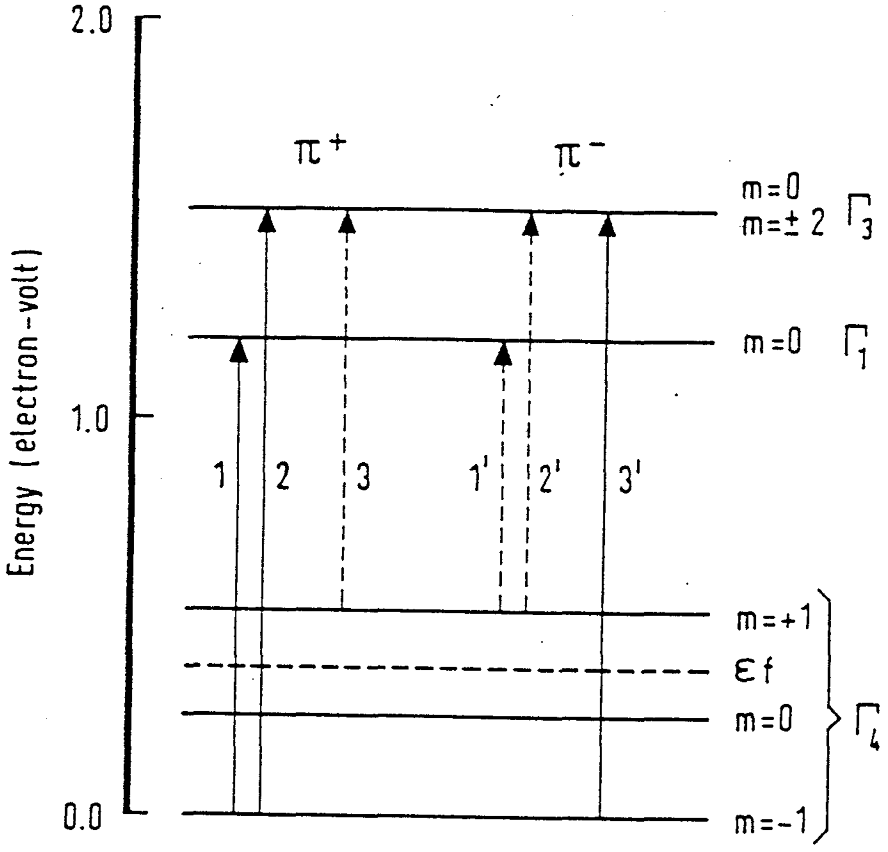
2.0
1.0
0.0
Energy (electron-volt)
π+
π−
m=0
m=± 2
Γ3
m=0
Γ1
1
2
3
1'
2'
3'
m=+1
εf
m=0
Γ4
m=-1

Fig. 1.3.

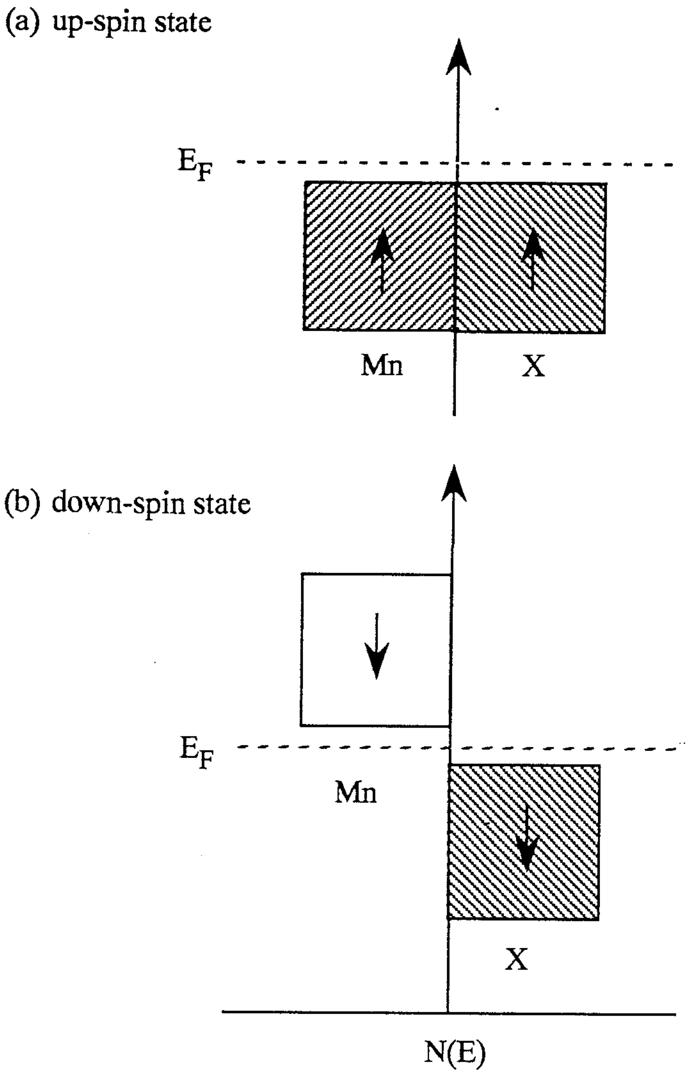

Fig. 1.4.

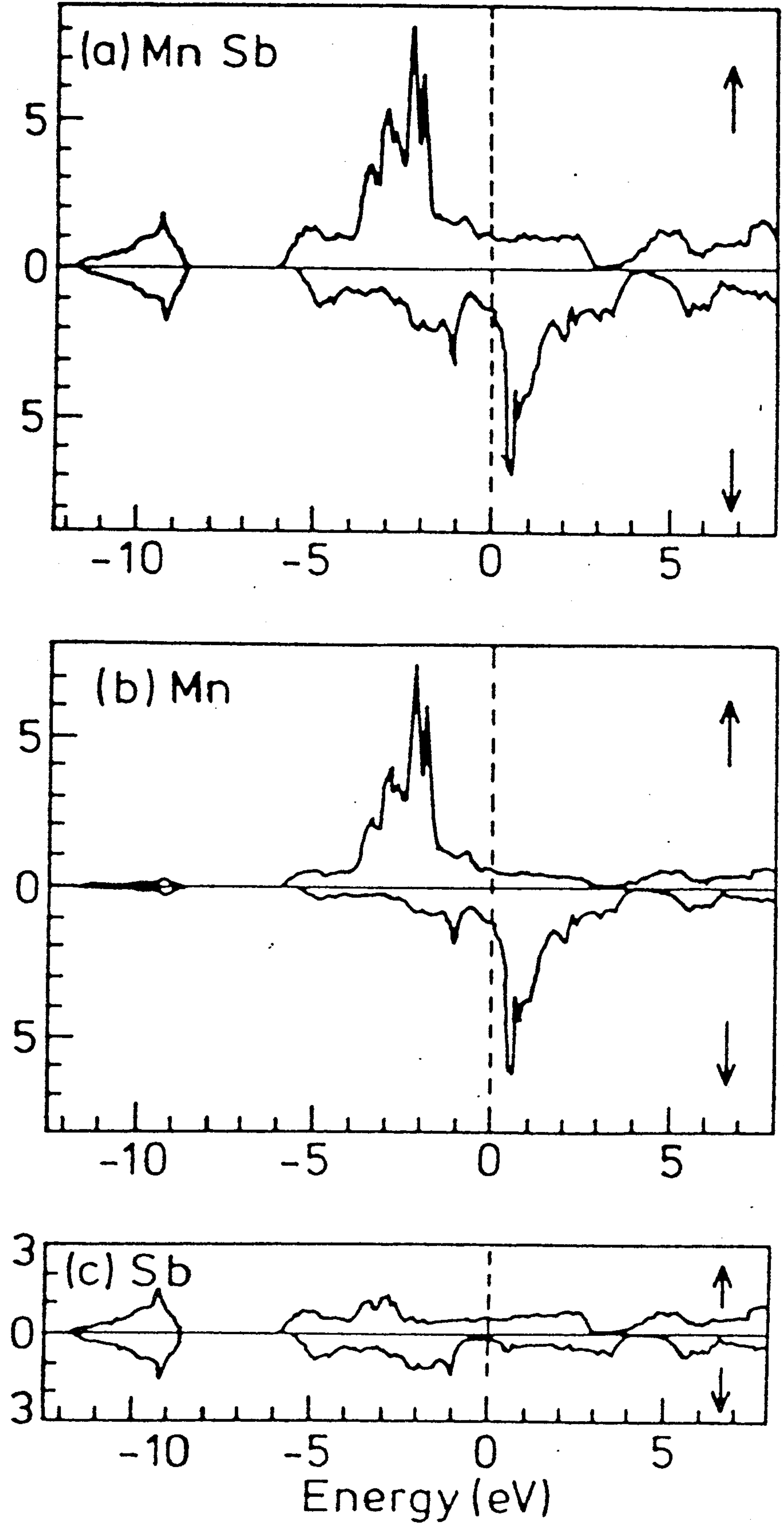

Fig. 1.5.

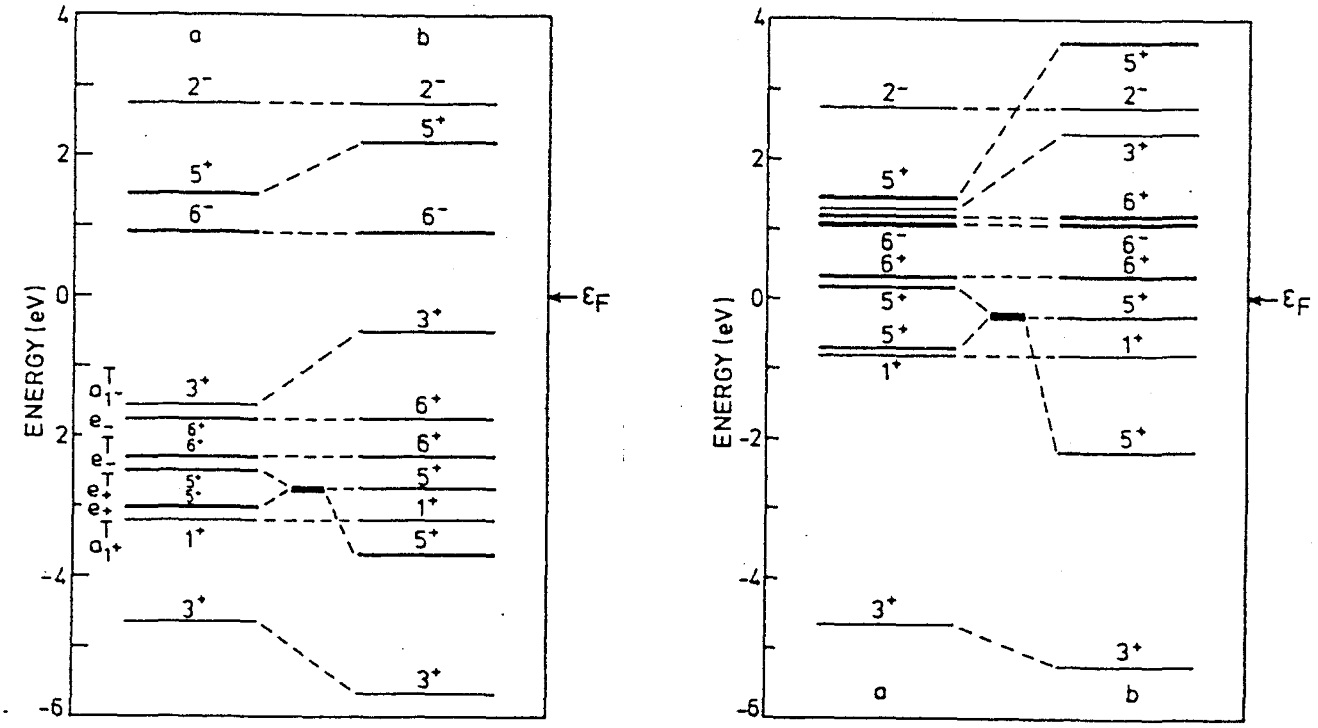

Fig. 1.6.

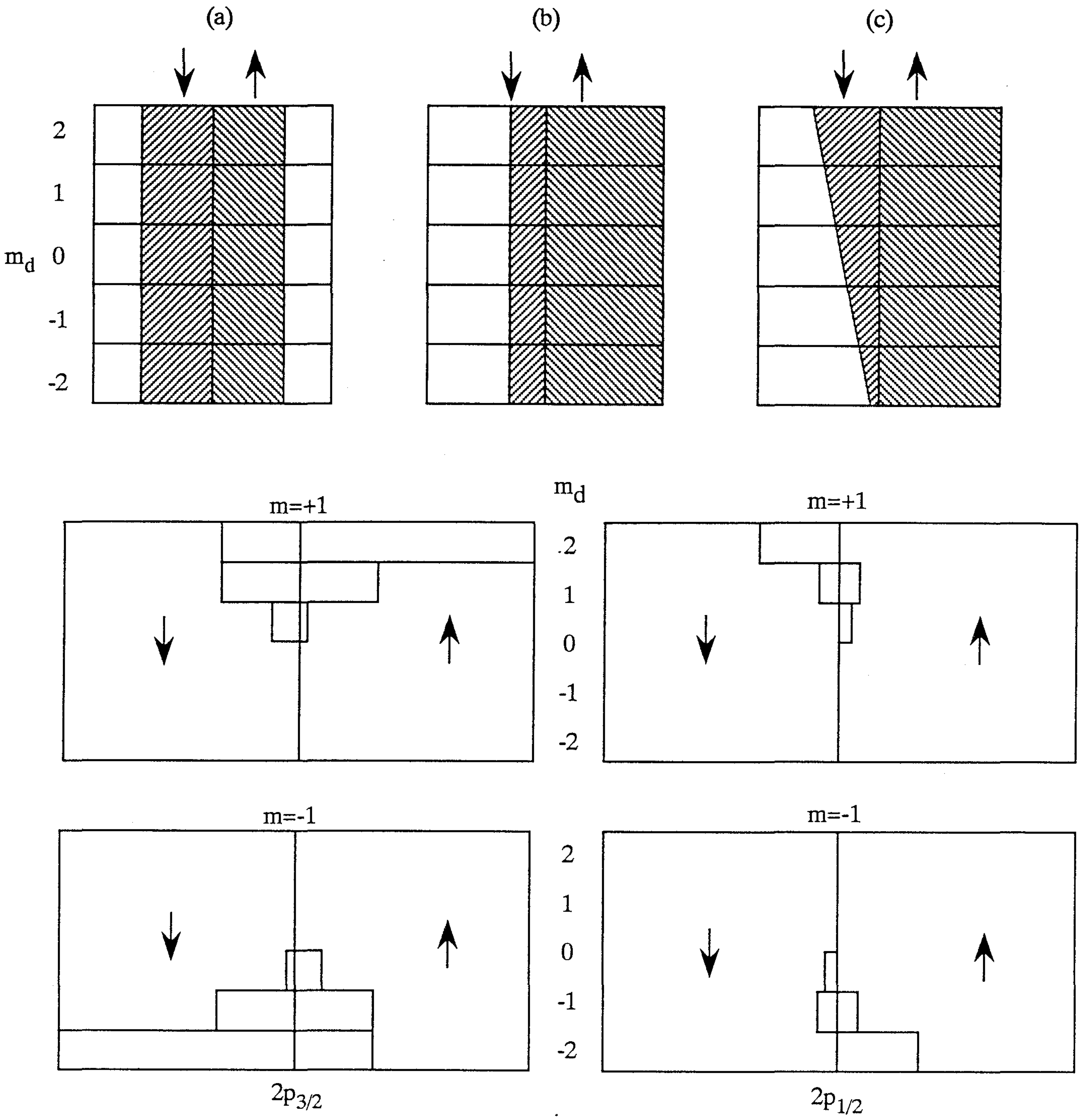

MCD spectrum: I(m=+1) - I(m=-1)

Fig. 1.7.

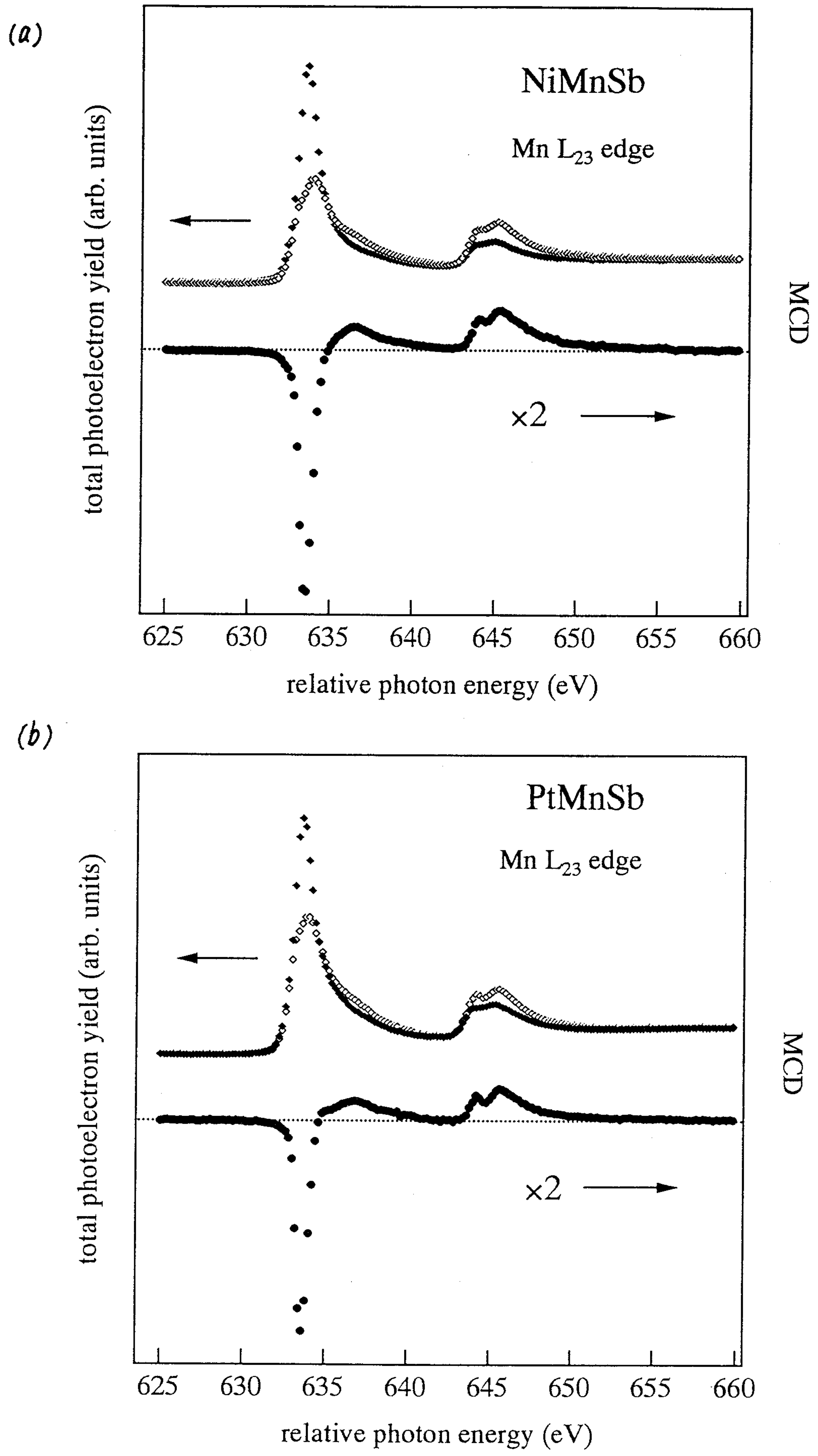
(a)
NiMnSb
Mn L23 edge
×2
total photoelectron yield (arb. units)
MCD
625
630
635
640
645
650
655
660
relative photon energy (eV)
(b)
PtMnSb
Mn L23 edge
×2
total photoelectron yield (arb. units)
MCD
625
630
635
640
645
650
655
660
relative photon energy (eV)

Fig. 1.8.

(c)

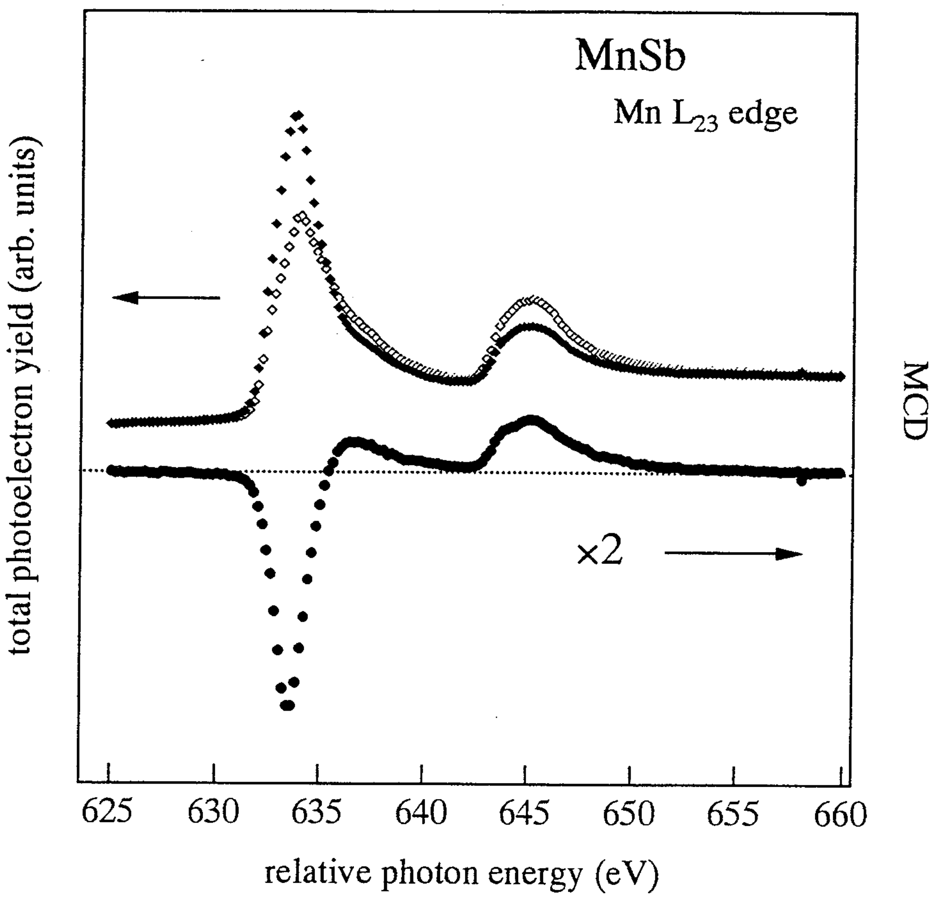
MnSb
Mn L_{23} edge
×2
MCD
total photoelectron yield (arb. units)
625
630
635
640
645
650
655
660
relative photon energy (eV)

(d)

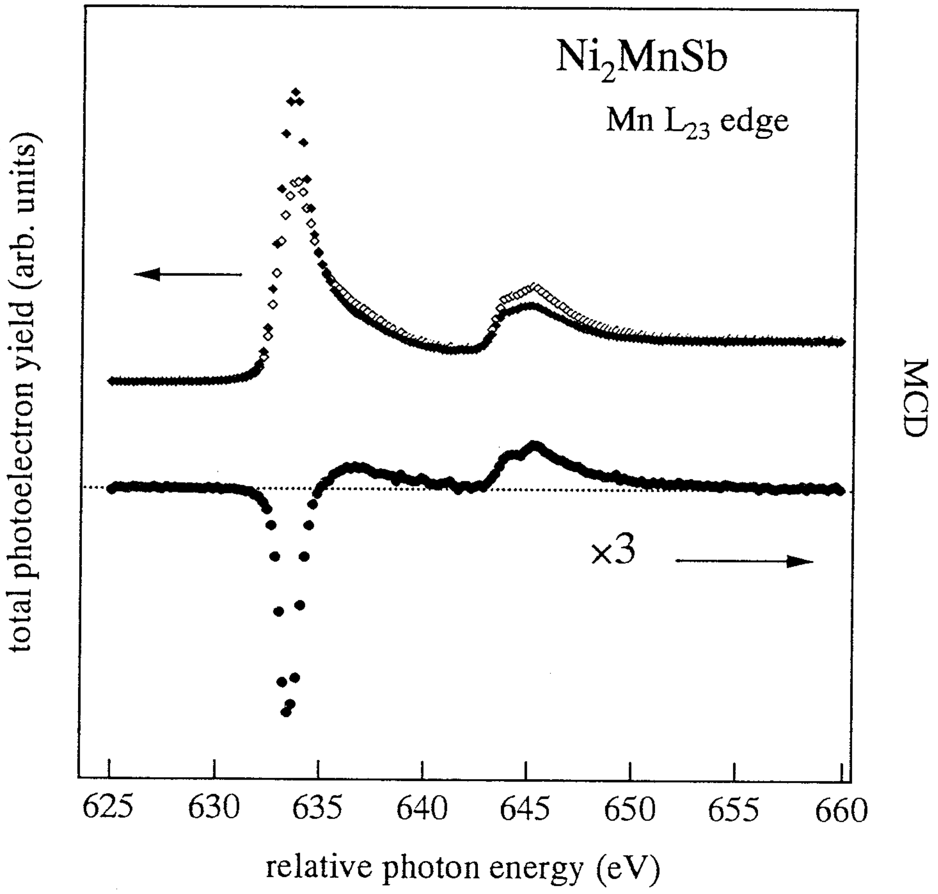
Ni_2MnSb
Mn L_{23} edge
×3
MCD
total photoelectron yield (arb. units)
625
630
635
640
645
650
655
660
relative photon energy (eV)

(e)

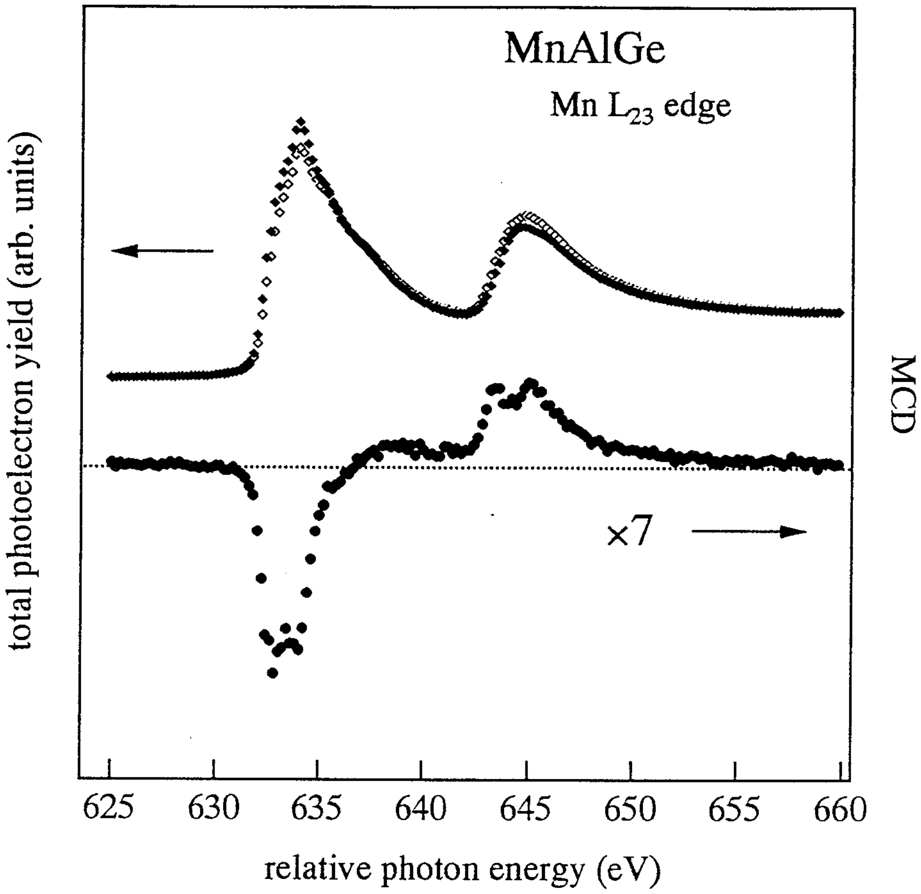
MnAlGe
Mn L23 edge
total photoelectron yield (arb. units)
MCD
×7
625
630
635
640
645
650
655
660
relative photon energy (eV)

(f)

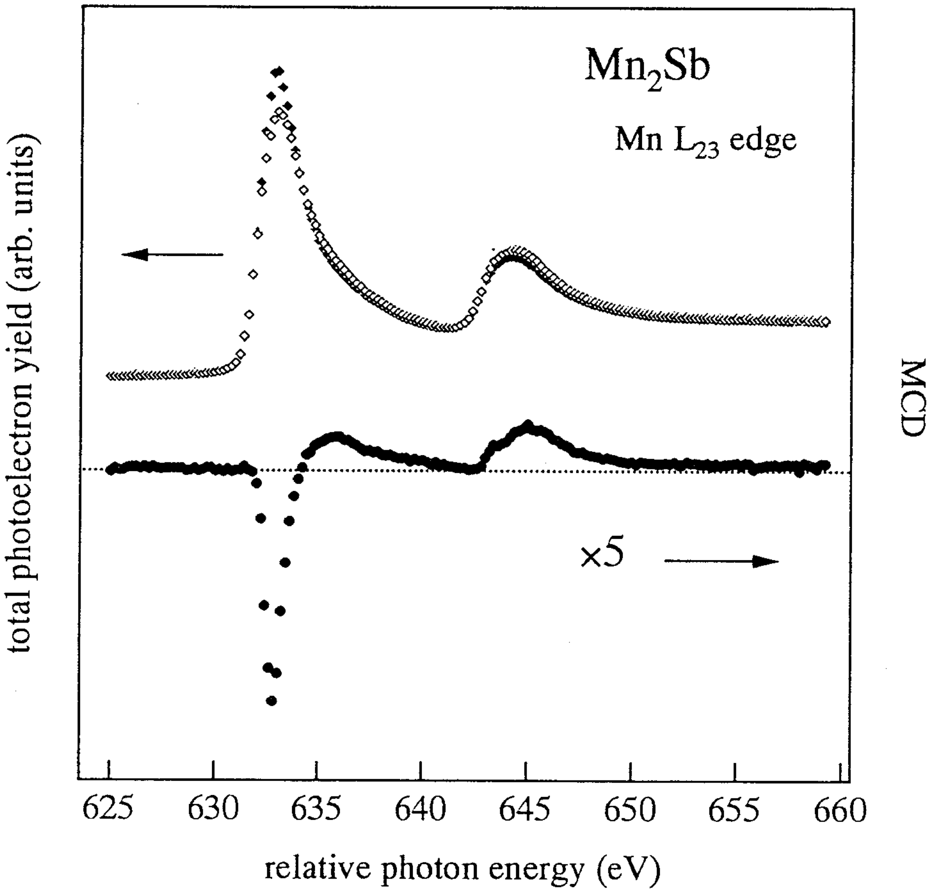
Mn2Sb
Mn L23 edge
total photoelectron yield (arb. units)
MCD
×5
625
630
635
640
645
650
655
660
relative photon energy (eV)

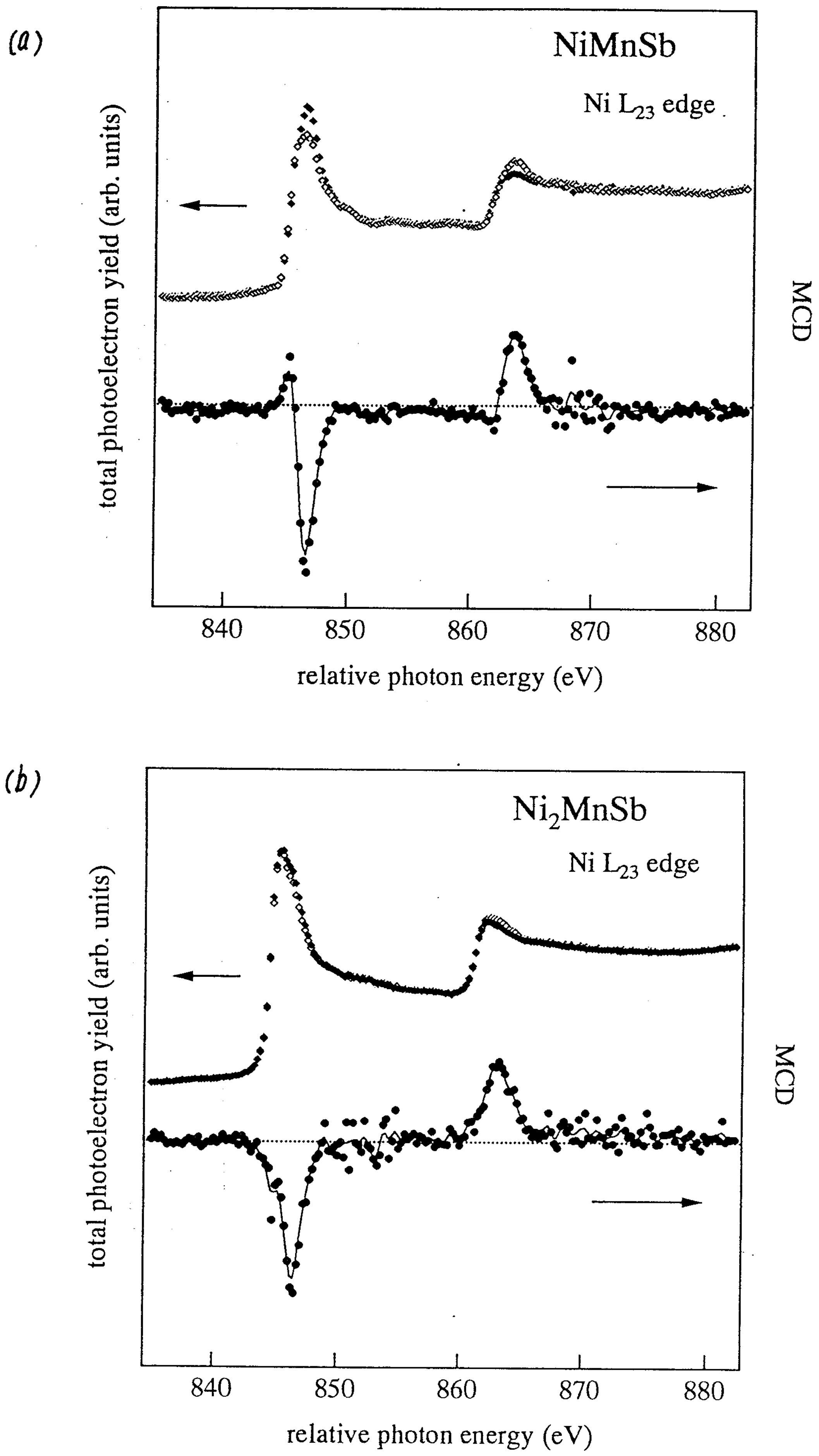
(a)
NiMnSb
Ni L_{23} edge
total photoelectron yield (arb. units)
MCD
840
850
860
870
880
relative photon energy (eV)
(b)
Ni_2MnSb
Ni L_{23} edge
total photoelectron yield (arb. units)
MCD
840
850
860
870
880
relative photon energy (eV)

Fig. 1.9.

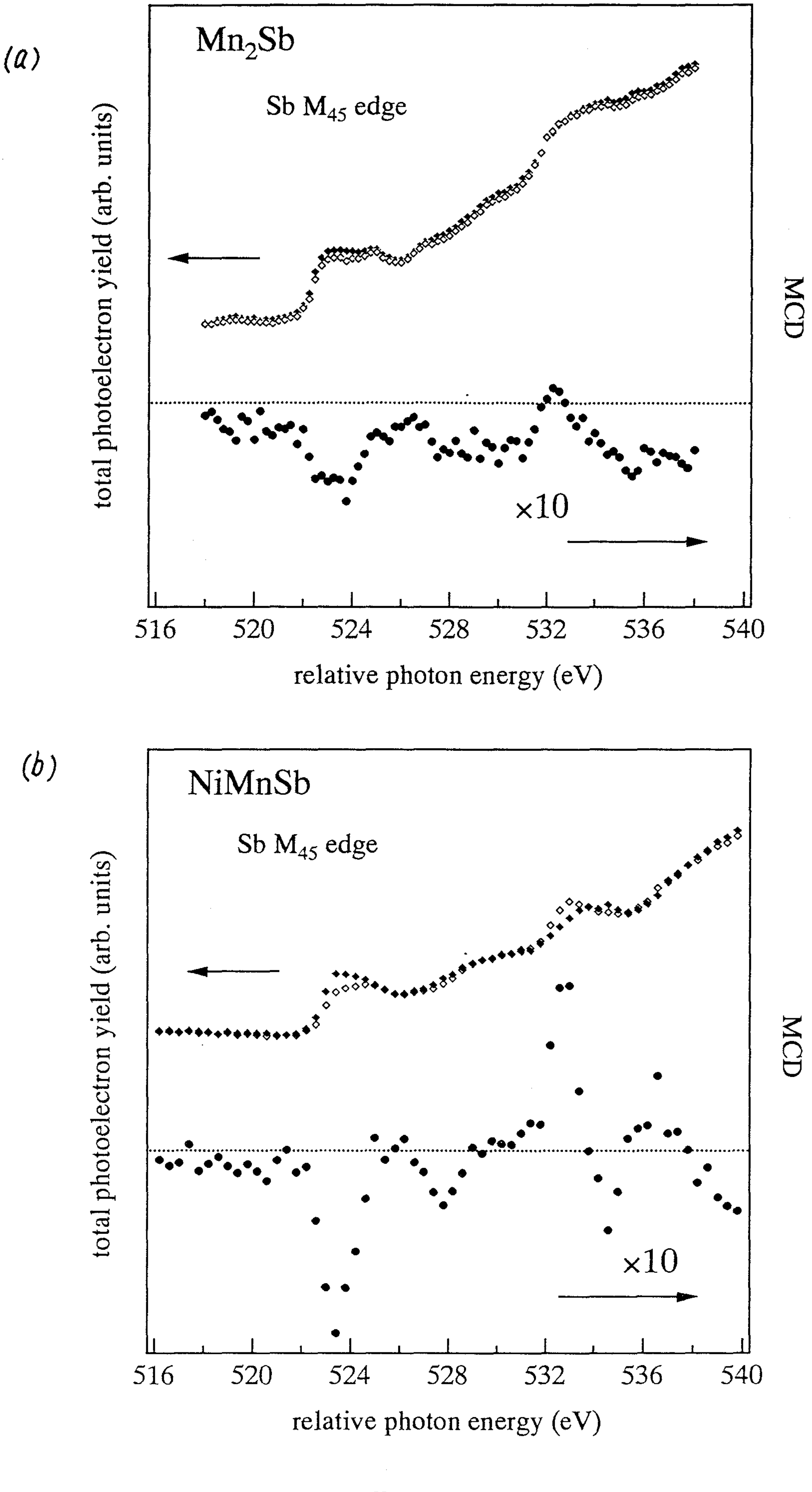
(a)
Mn2Sb
Sb M45 edge
total photoelectron yield (arb. units)
MCD
×10
516
520
524
528
532
536
540
relative photon energy (eV)
(b)
NiMnSb
Sb M45 edge
total photoelectron yield (arb. units)
MCD
×10
516
520
524
528
532
536
540
relative photon energy (eV)

Fig. 1.10

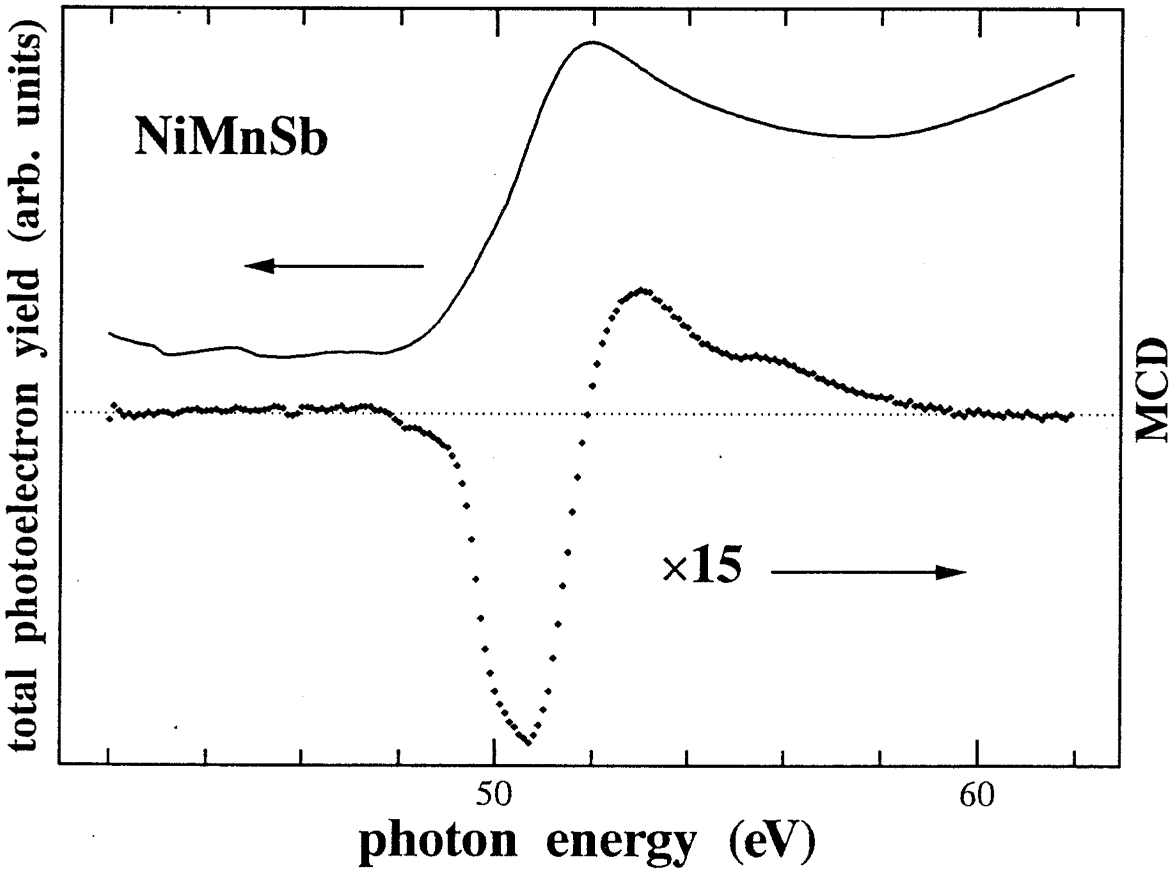
total photoelectron yield (arb. units)
NiMnSb
MCD
×15
50
60
photon energy (eV)

Fig. 1.11. (a)

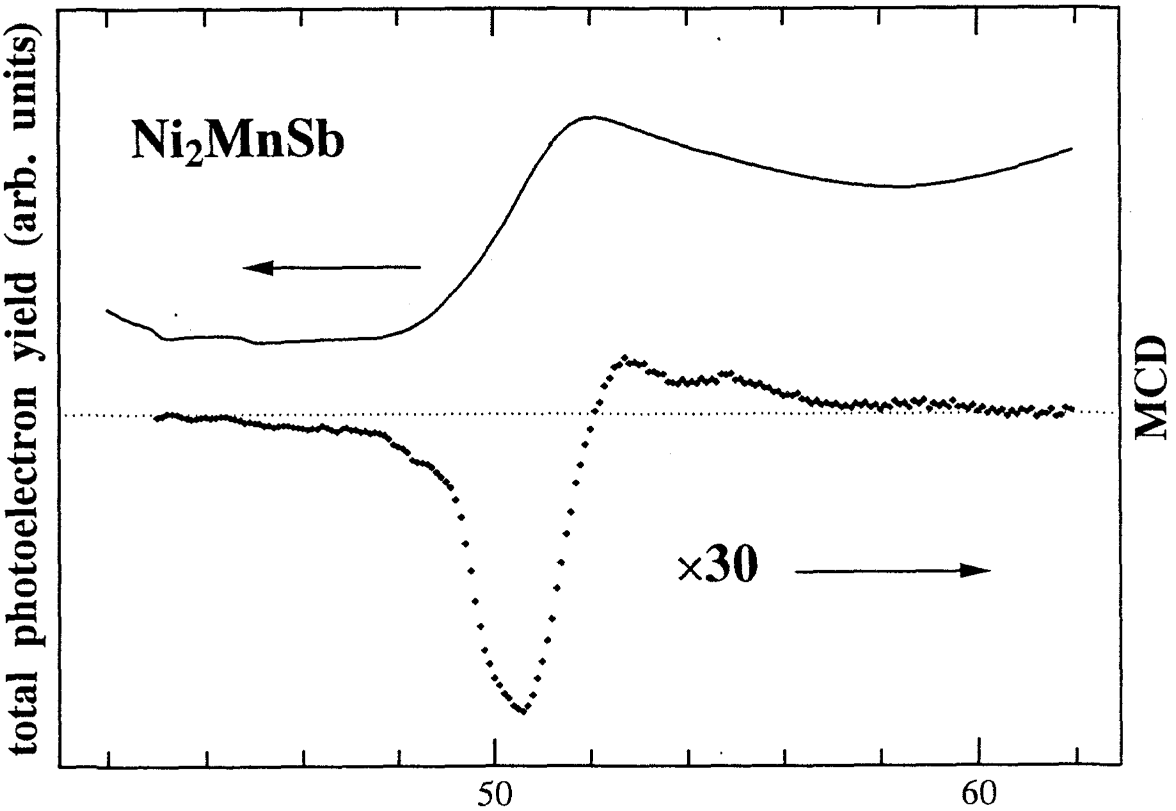
total photoelectron yield (arb. units)
Ni₂MnSb
×30
MCD
50
60
photon energy (eV)

(b)

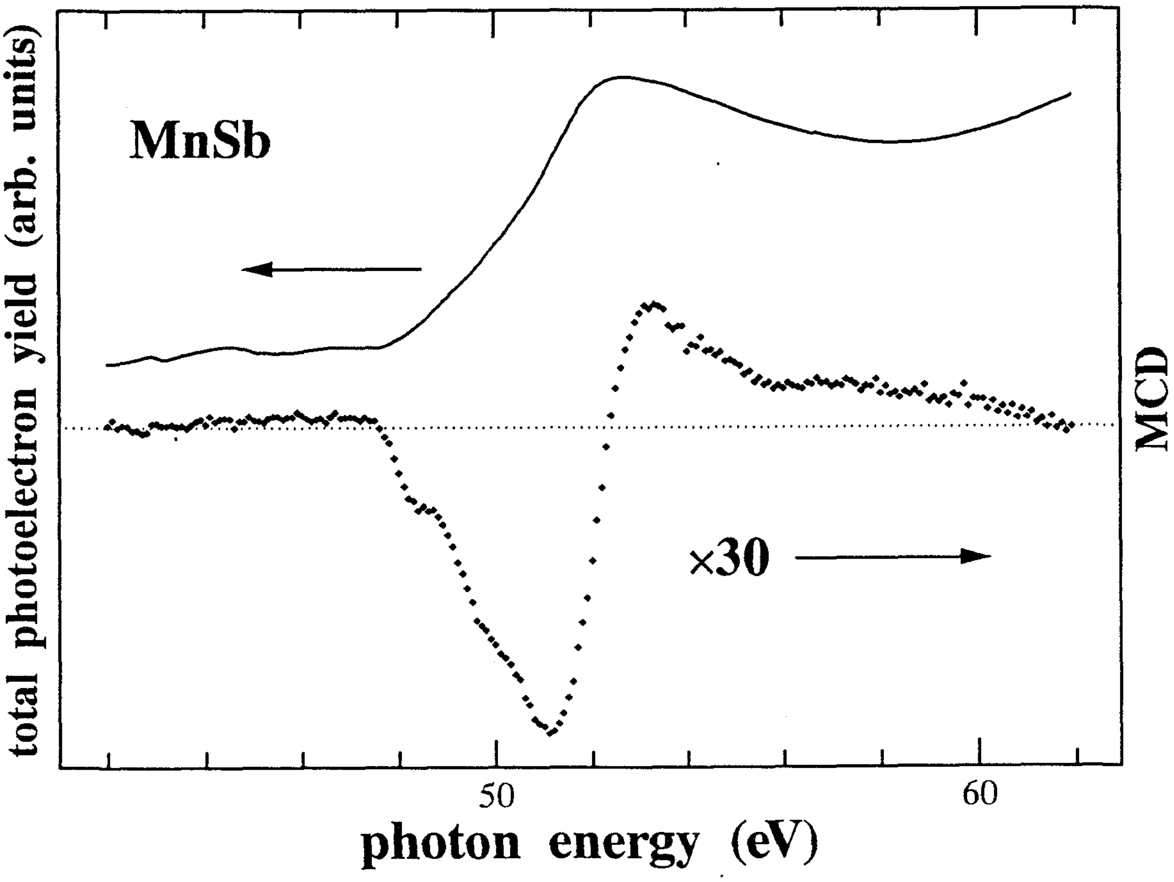
total photoelectron yield (arb. units)
MnSb
×30
MCD
50
60
photon energy (eV)

(c)

(d)

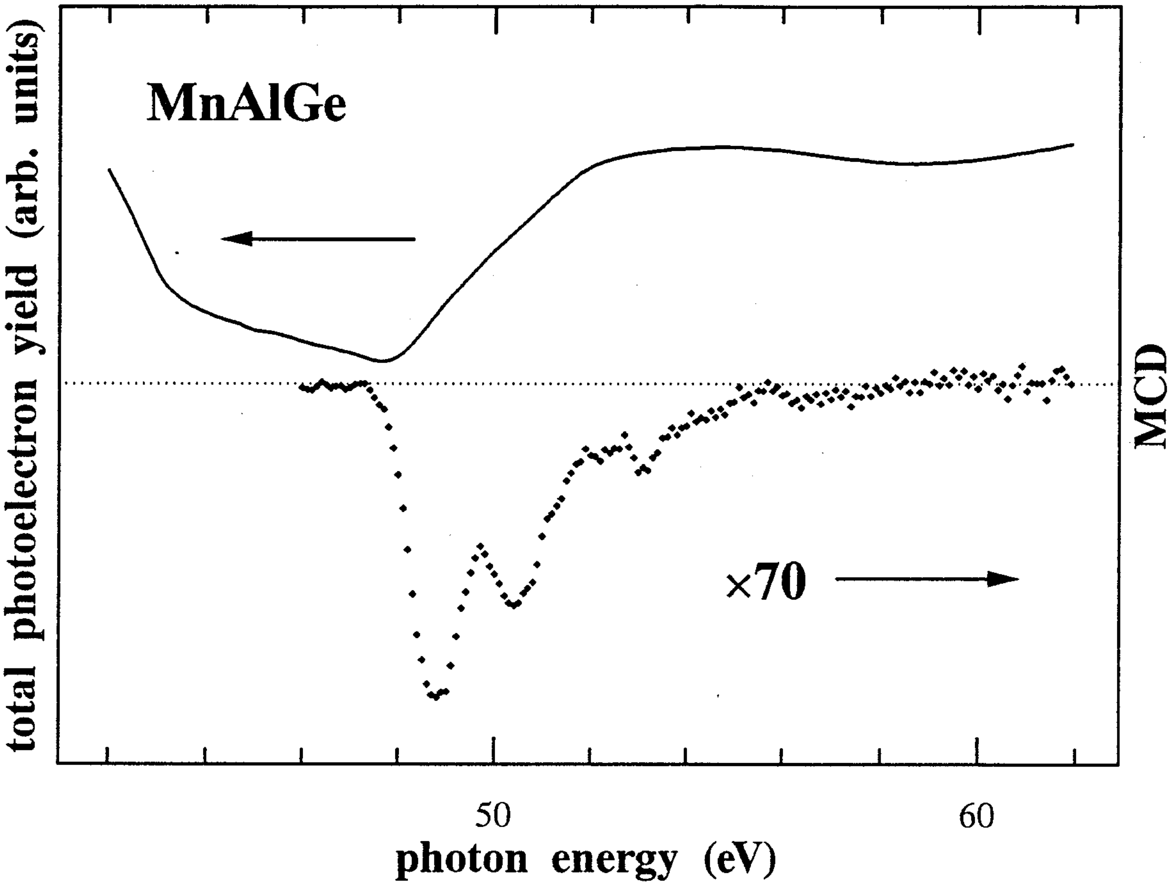
MnAlGe
total photoelectron yield (arb. units)
MCD
×70
50
60
photon energy (eV)

(e)

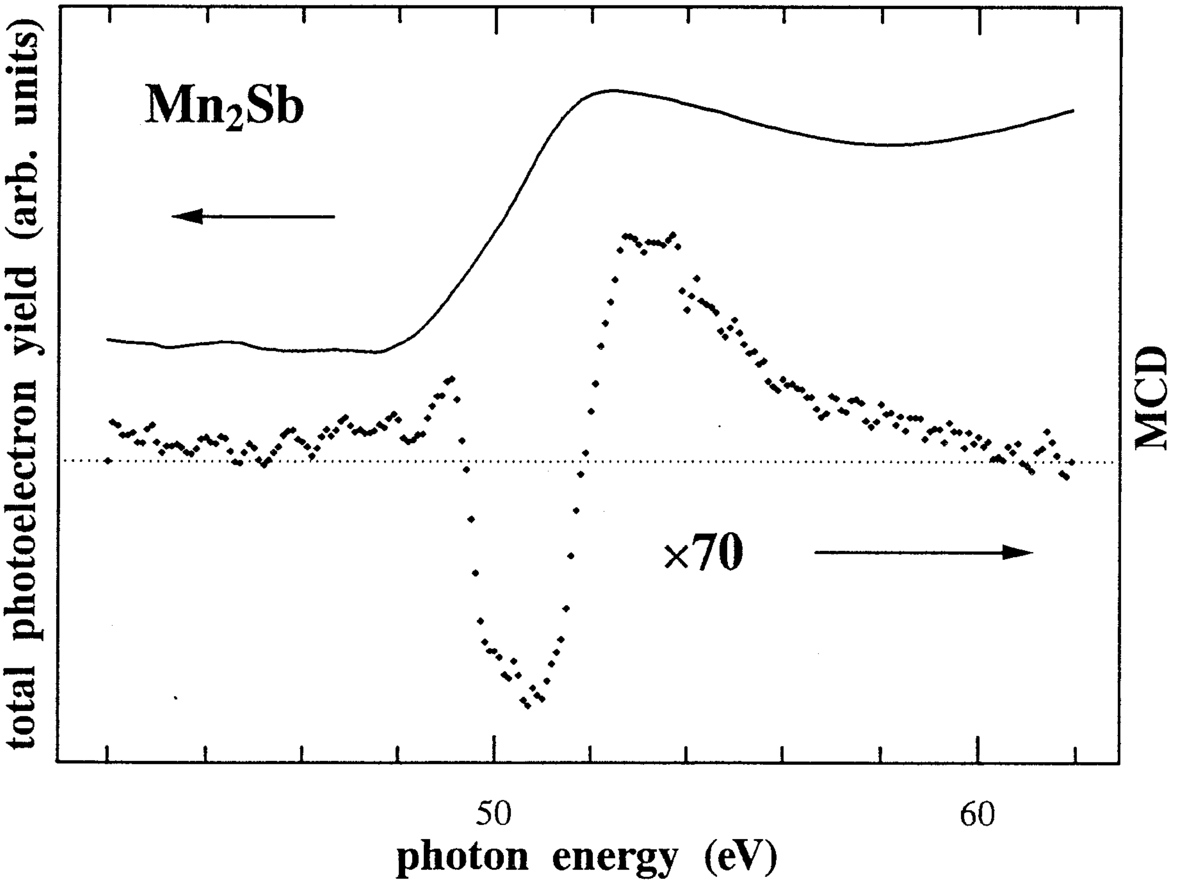
Mn2Sb
total photoelectron yield (arb. units)
MCD
×70
50
60
photon energy (eV)

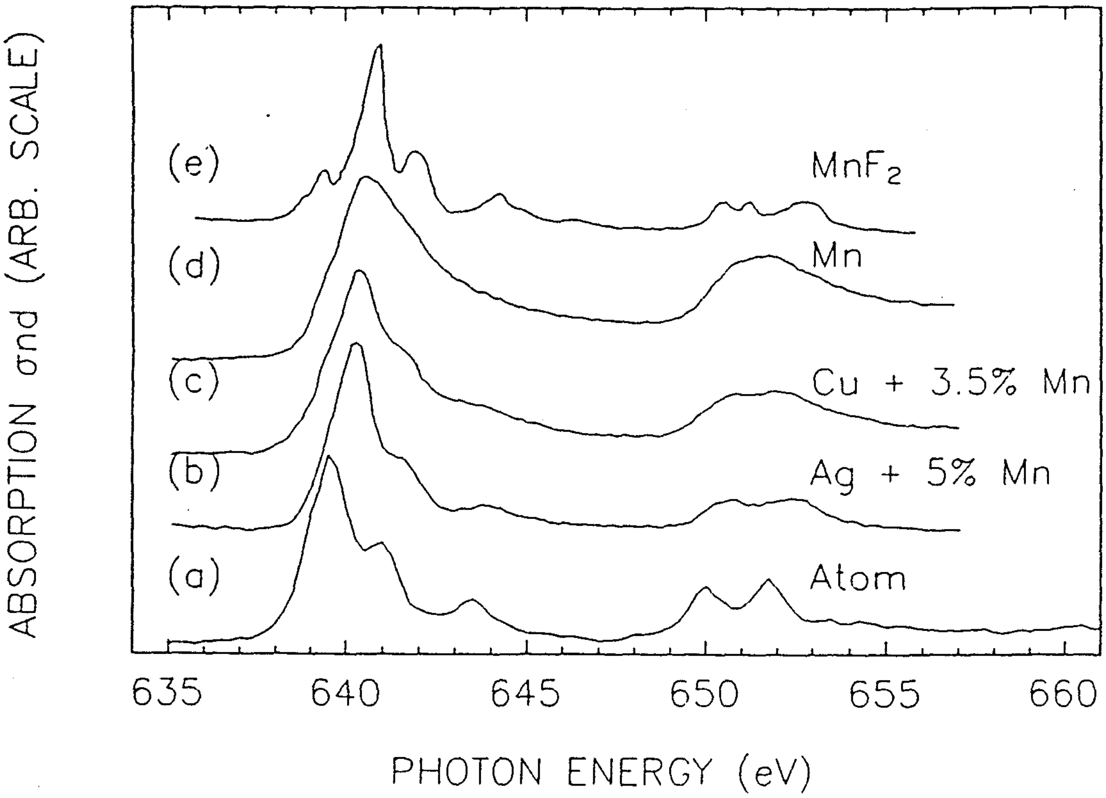

ABSORPTION σnd (ARB. SCALE)
(e)
MnF₂
(d)
Mn
(c)
Cu + 3.5% Mn
(b)
Ag + 5% Mn
(a)
Atom
635
640
645
650
655
660
PHOTON ENERGY (eV)

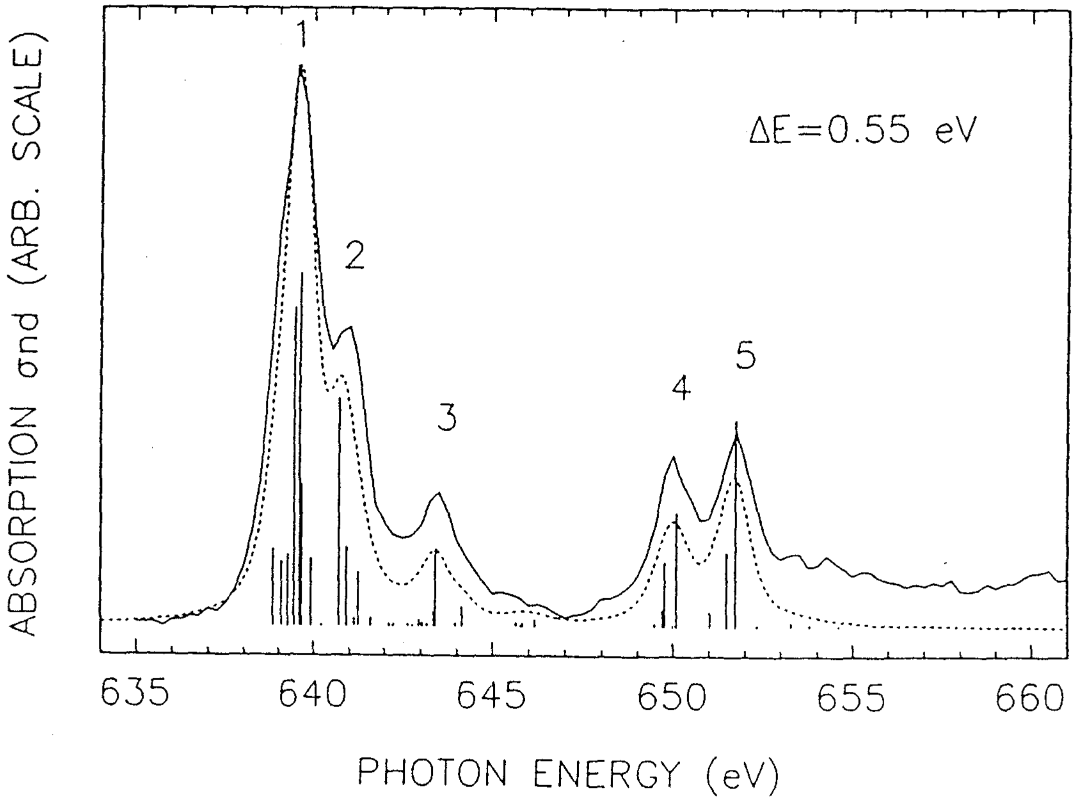

ABSORPTION σnd (ARB. SCALE)
1
2
3
4
5
ΔE=0.55 eV
635
640
645
650
655
660
PHOTON ENERGY (eV)

Fig. 1.12.

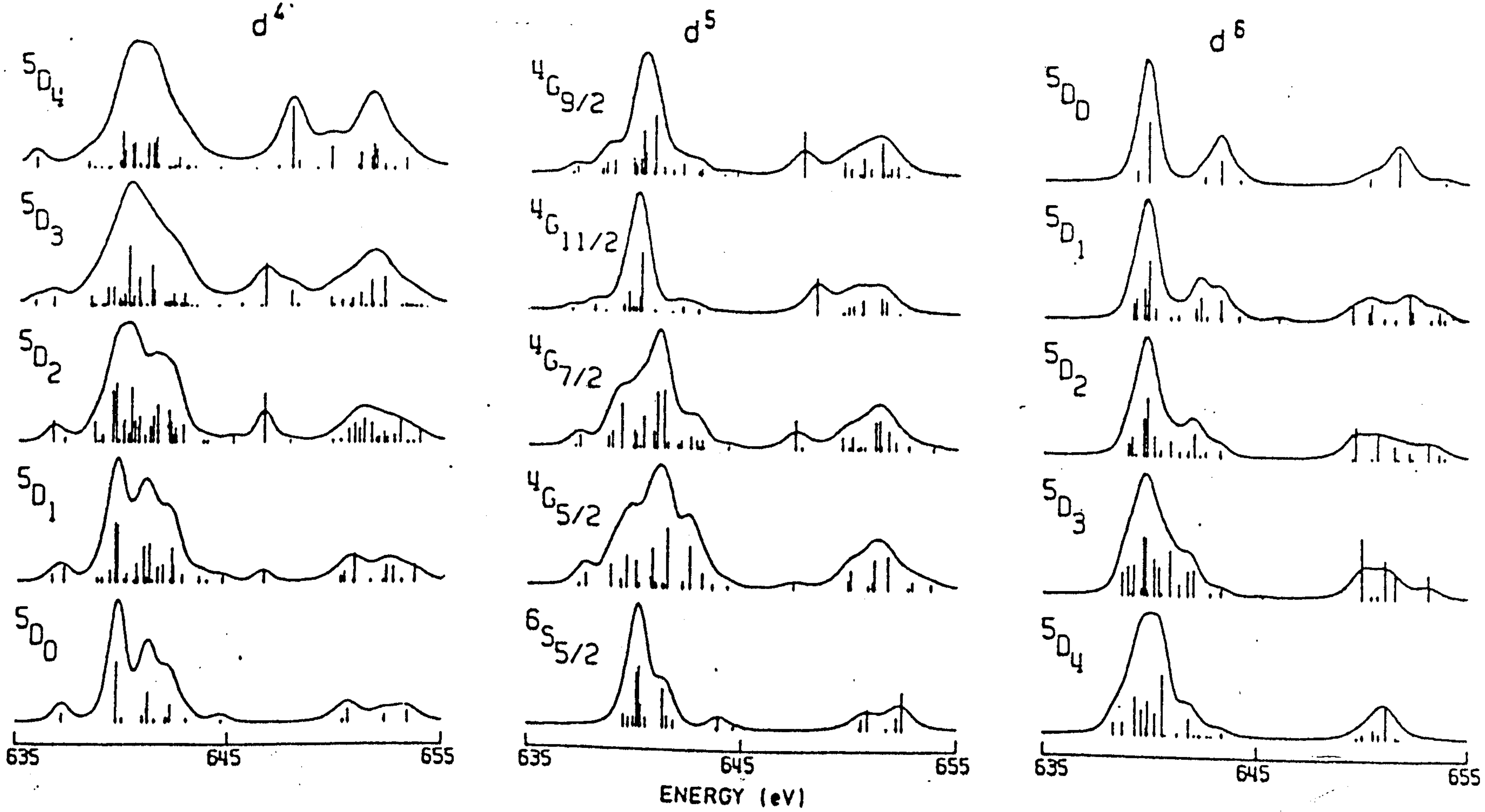
d4
d5
d6
5D4
5D3
5D2
5D1
5D0
4G9/2
4G11/2
4G7/2
4G5/2
6S5/2
5D0
5D1
5D2
5D3
5D4
635
645
655
635
645
655
635
645
655
ENERGY (eV)

Fig. 1.13.

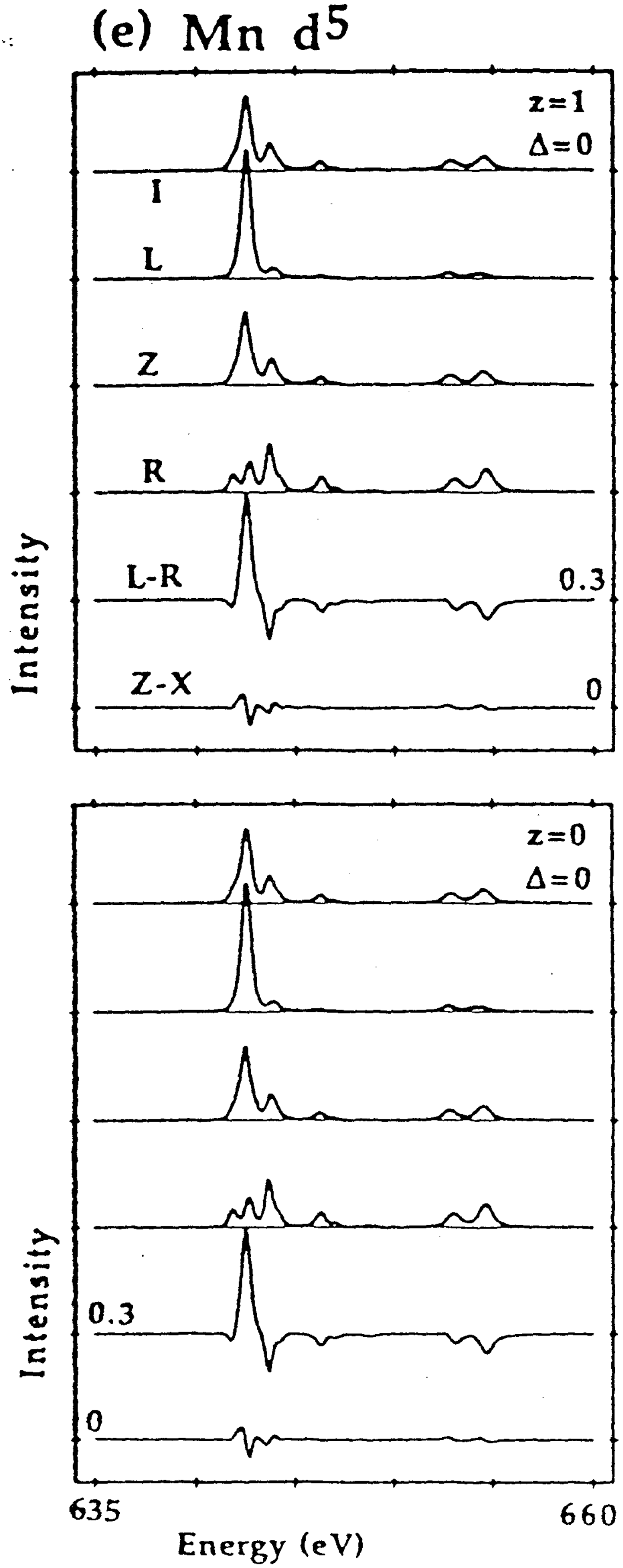
(e) Mn d^5
z=1
Δ=0
I
L
Z
R
L-R
0.3
Z-X
0
Intensity
z=0
Δ=0
0.3
0
Intensity
635
660
Energy (eV)

Fig. 1.14.

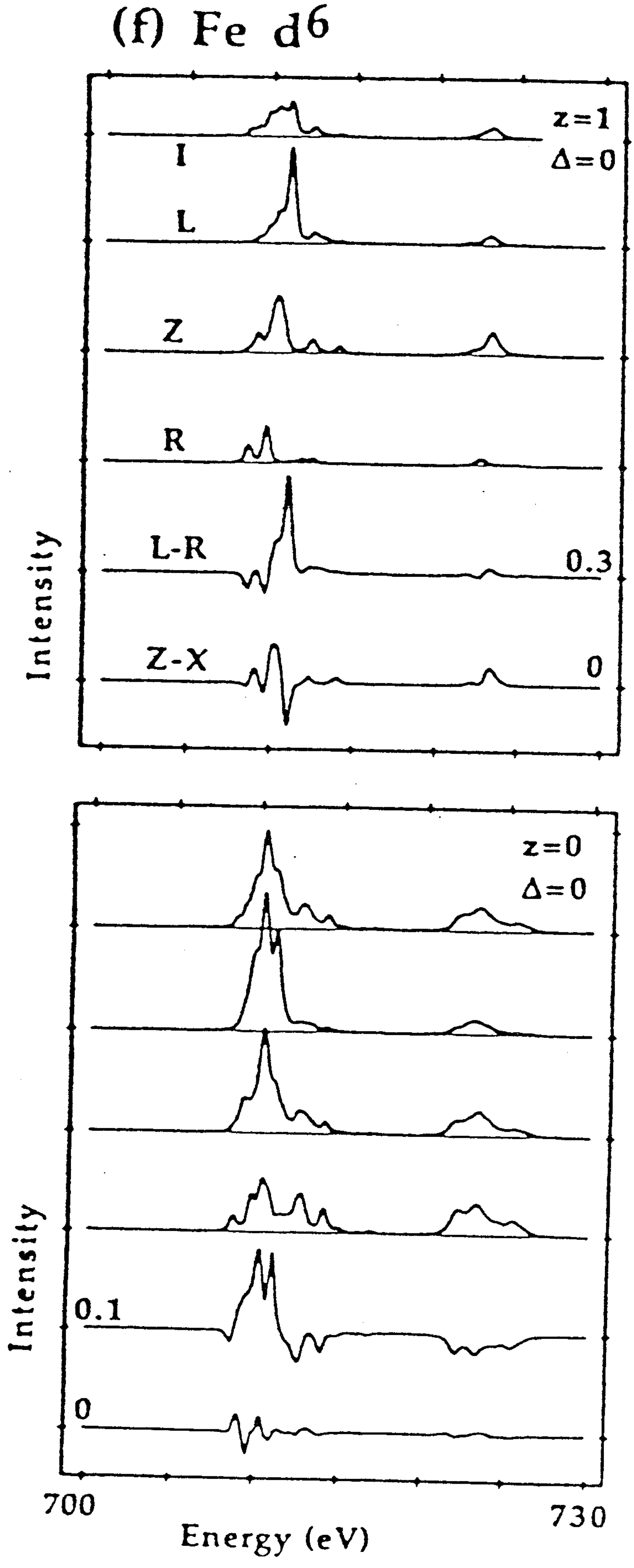
(f) Fe d^6
z=1
Δ=0
I
L
Z
R
L-R
0.3
Z-X
0
Intensity
z=0
Δ=0
0.1
0
Intensity
700
730
Energy (eV)

Fig. 1.15.

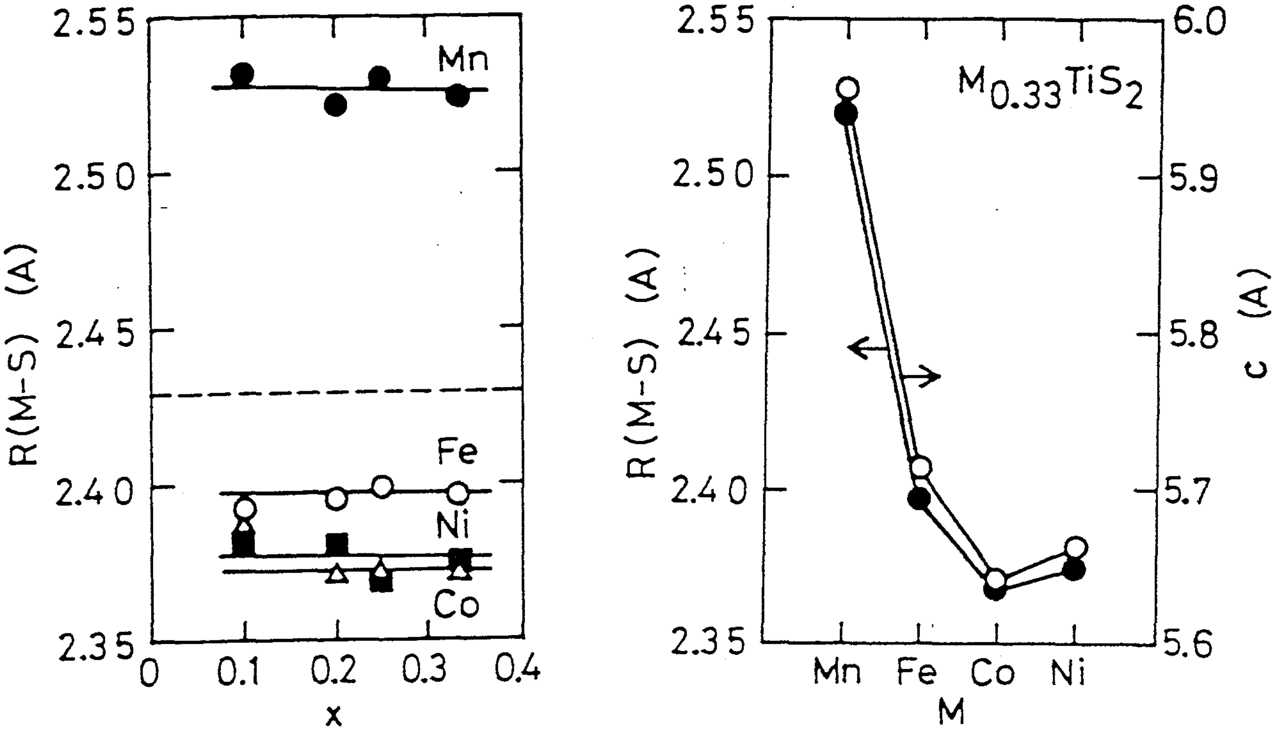
2.55
2.50
2.45
2.40
2.35
R(M-S) (A)
Mn
Fe
Ni
Co
0
0.1
0.2
0.3
0.4
x
$M_{0.33}TiS_2$
6.0
5.9
5.8
5.7
5.6
c (A)
Mn
Fe
Co
Ni
M

Fig. 2.1.

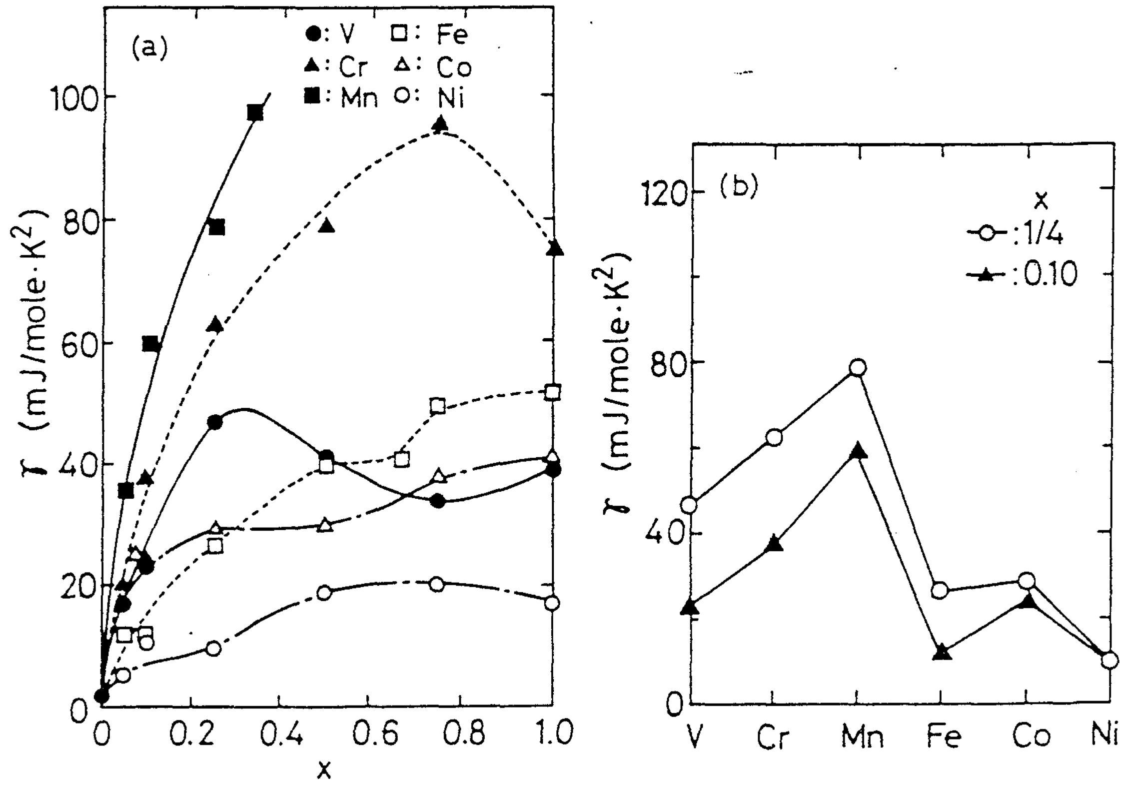
(a)
●: V
▲: Cr
■: Mn
□: Fe
△: Co
○: Ni
γ (mJ/mole·K^2)
0
20
40
60
80
100
0
0.2
0.4
0.6
0.8
1.0
x
(b)
x
○: 1/4
▲: 0.10
γ (mJ/mole·K^2)
0
40
80
120
V
Cr
Mn
Fe
Co
Ni

Fig. 2.2.

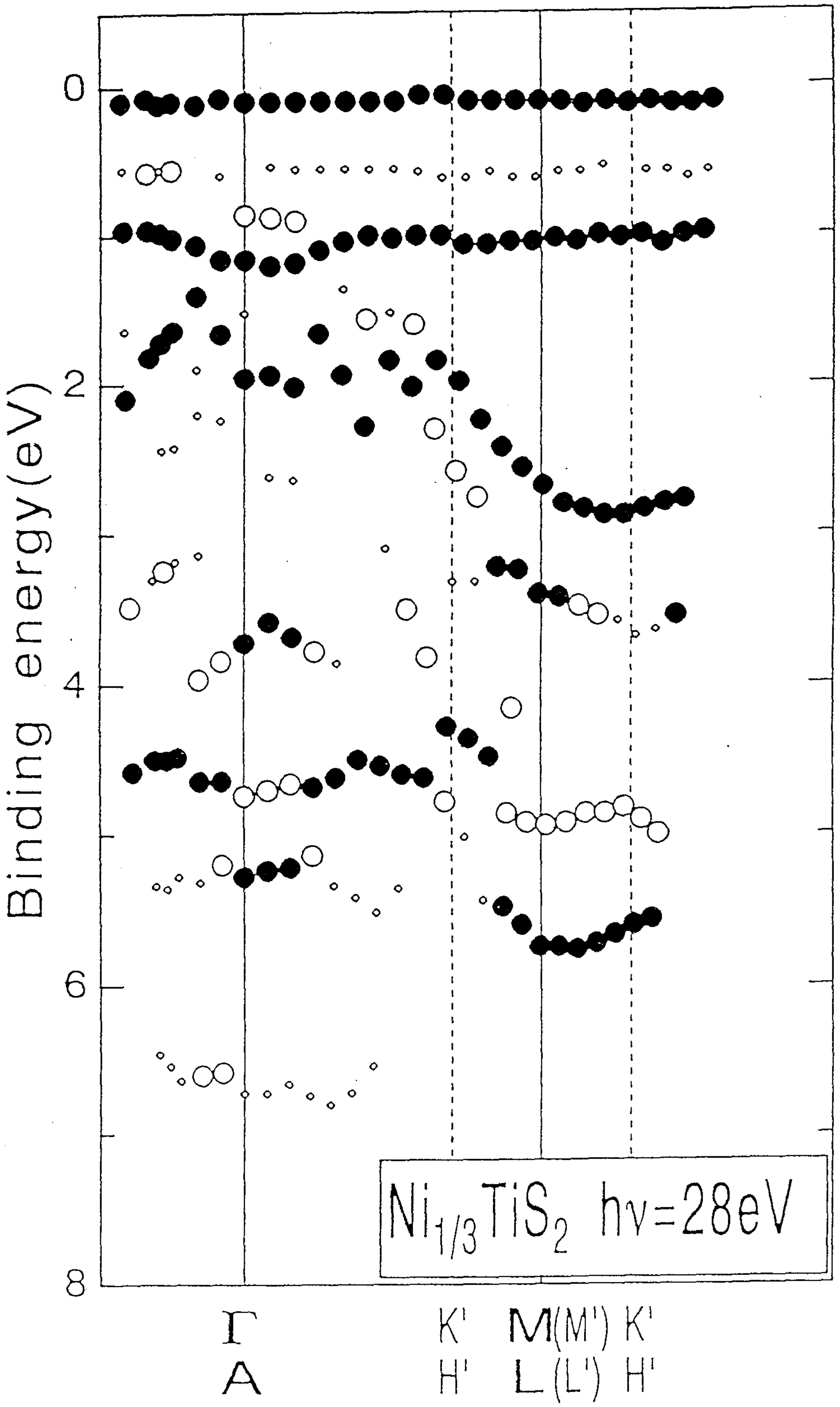

Fig. 2.3.

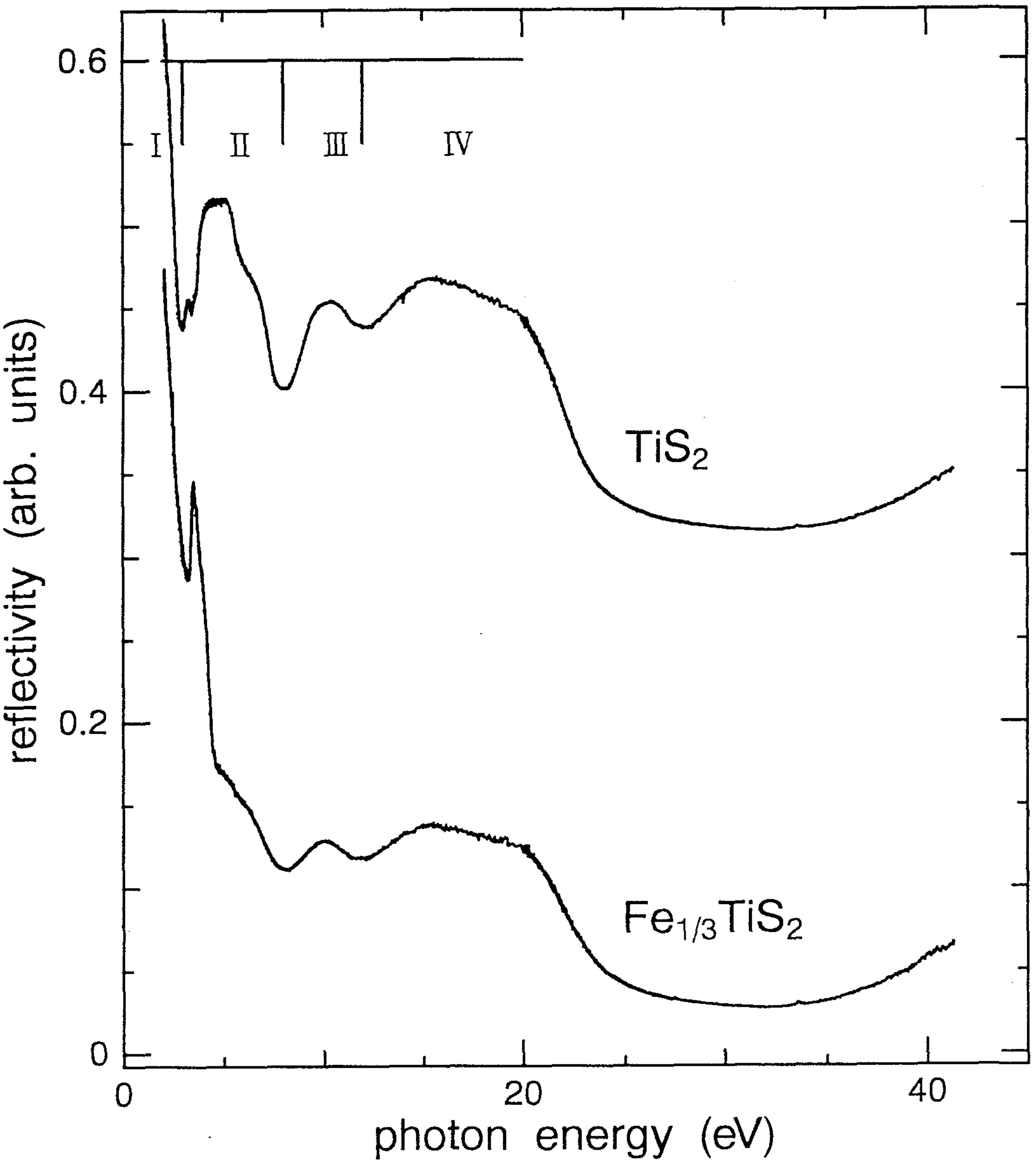
0.6
0.4
0.2
0
reflectivity (arb. units)
0
20
40
photon energy (eV)
I
II
III
IV
TiS_2
$Fe_{1/3}TiS_2$

Fig. 2.4.

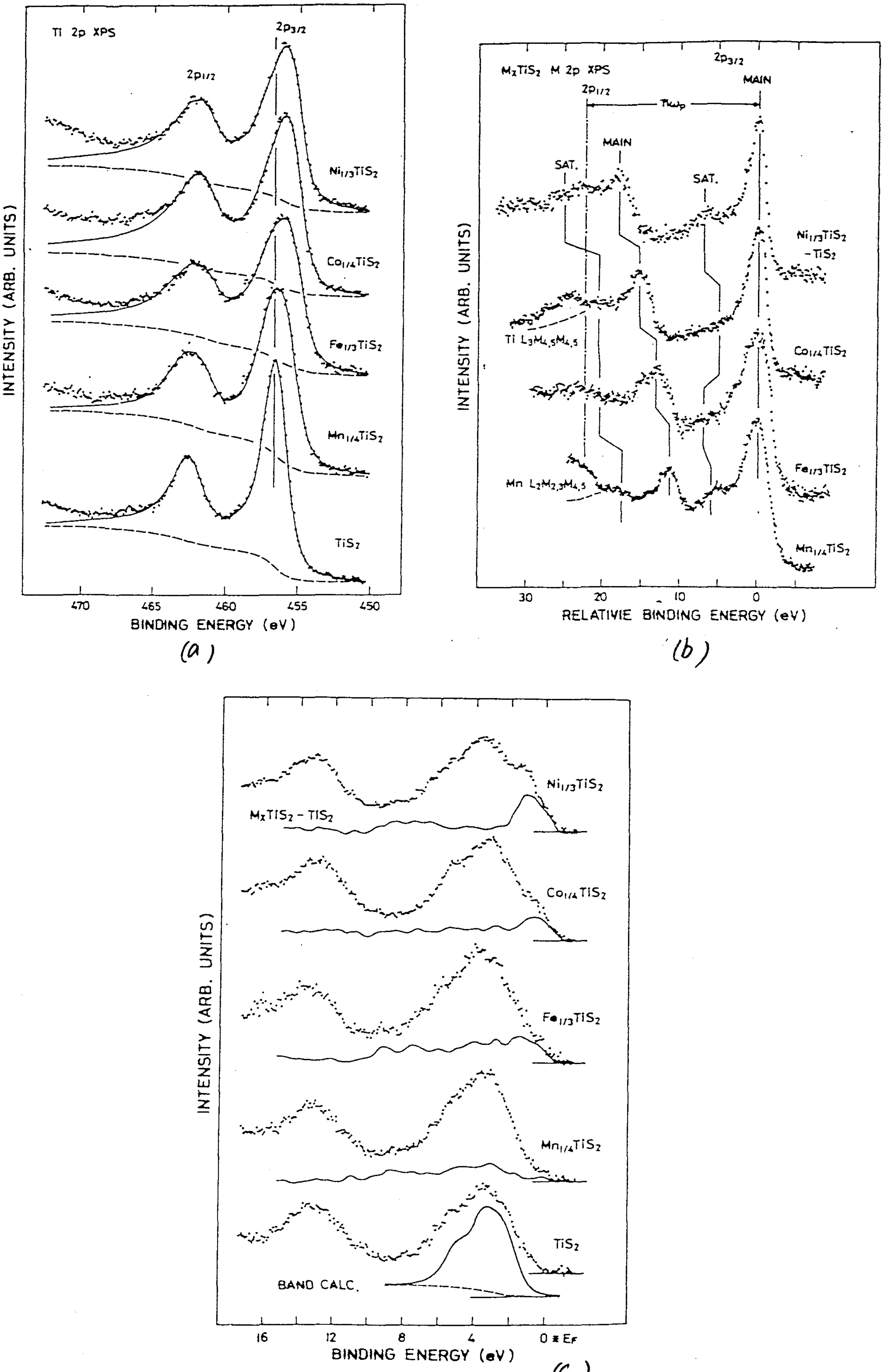

Ti 2p XPS
2p1/2
2p3/2
Ni1/3TiS2
Co1/4TiS2
Fe1/3TiS2
Mn1/4TiS2
TiS2
INTENSITY (ARB. UNITS)
470
465
460
455
450
BINDING ENERGY (eV)
MxTiS2 M 2p XPS
2p1/2
2p3/2
MAIN
ħωp
SAT.
MAIN
SAT.
Ni1/3TiS2 -TiS2
Ti L3M4,5M4,5
Co1/4TiS2
Fe1/3TiS2
Mn L2M2,3M4,5
Mn1/4TiS2
INTENSITY (ARB. UNITS)
30
20
10
0
RELATIVIE BINDING ENERGY (eV)
Ni1/3TiS2
MxTiS2 - TiS2
Co1/4TiS2
Fe1/3TiS2
Mn1/4TiS2
TiS2
BAND CALC.
INTENSITY (ARB. UNITS)
16
12
8
4
0 ≡ EF
BINDING ENERGY (eV)

(a)

(b)

(c)

Fig. 2.5.

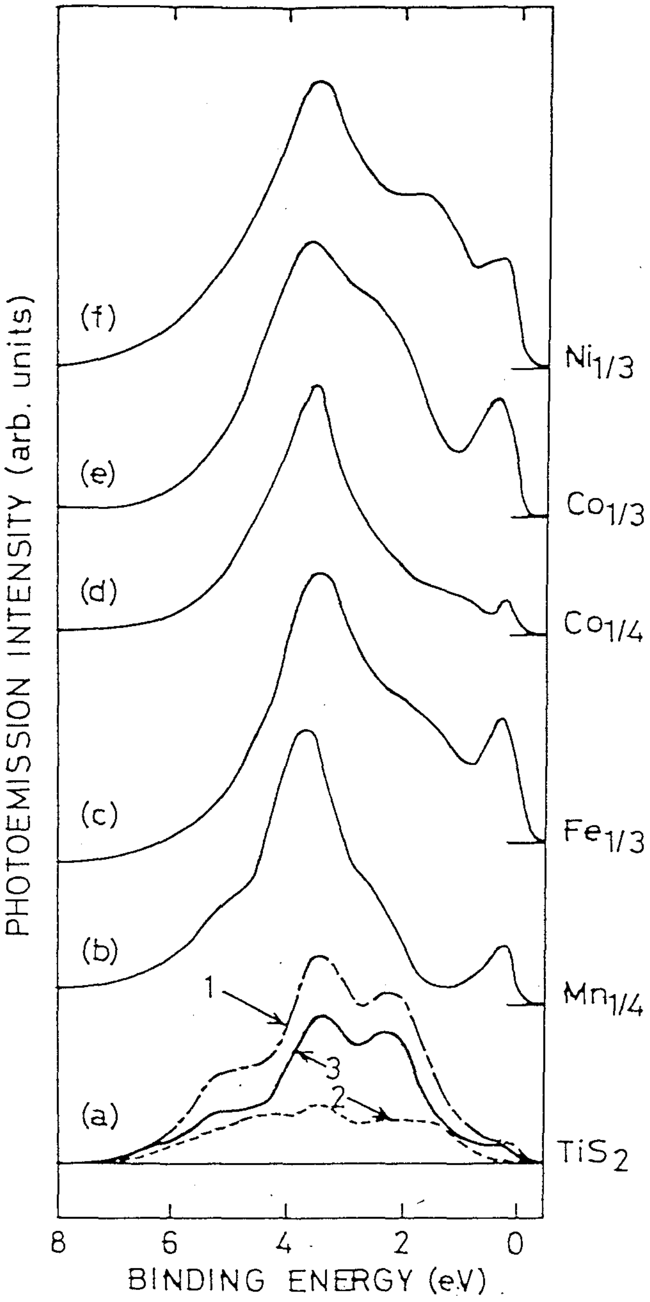
PHOTOEMISSION INTENSITY (arb. units)
(f)
Ni$_{1/3}$
(e)
Co$_{1/3}$
(d)
Co$_{1/4}$
(c)
Fe$_{1/3}$
(b)
Mn$_{1/4}$
1
3
2
(a)
TiS$_2$
8
6
4
2
0
BINDING ENERGY (eV)

Fig. 2.6.

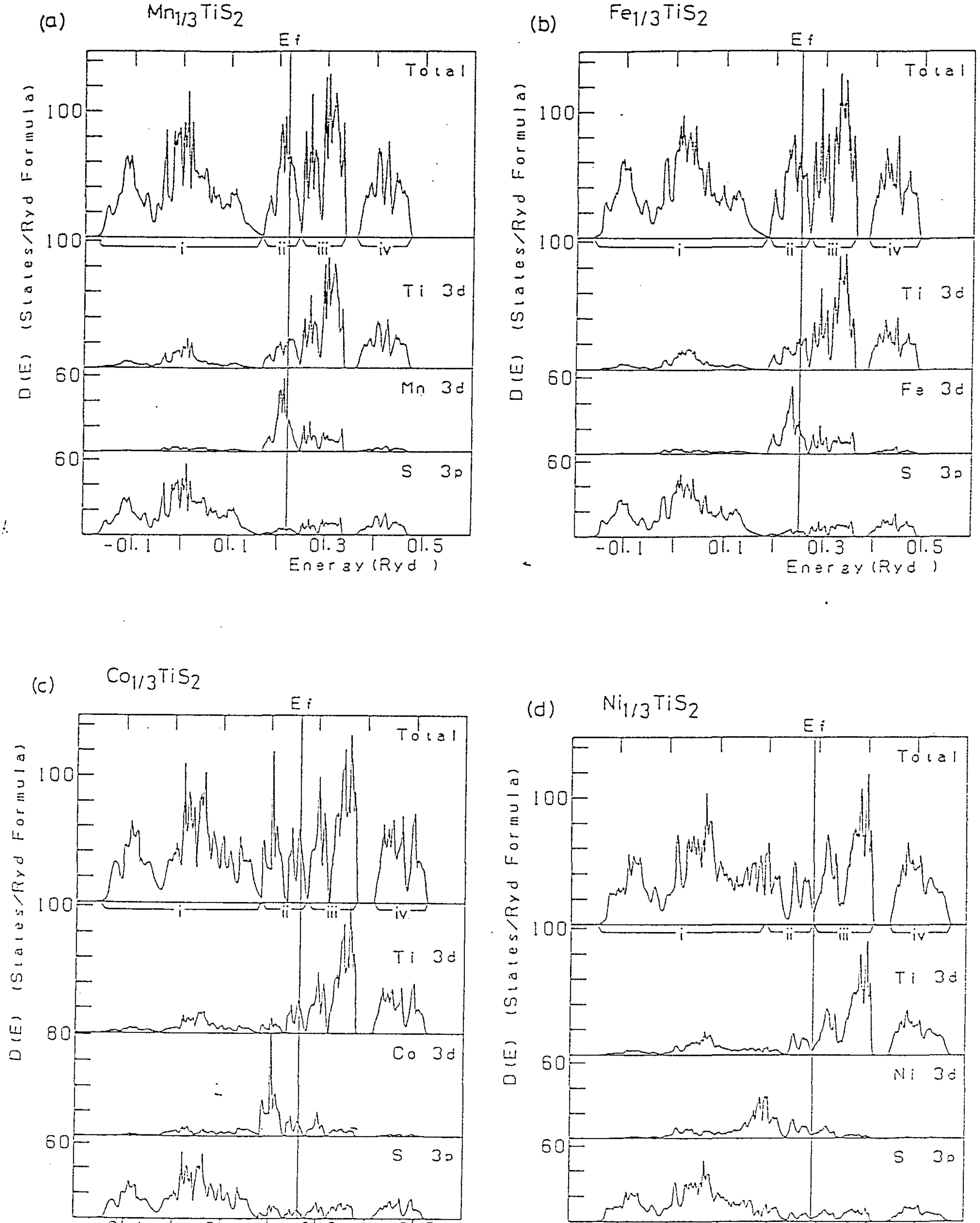
(a) Mn1/3TiS2
(b) Fe1/3TiS2
(c) Co1/3TiS2
(d) Ni1/3TiS2
Ef
Total
Ti 3d
Mn 3d
Fe 3d
Co 3d
Ni 3d
S 3p
i
ii
iii
iv
100
80
60
D(E) (States/Ryd Formula)
-01.1
01.1
01.3
01.5
Energy (Ryd)

Fig. 2.7.

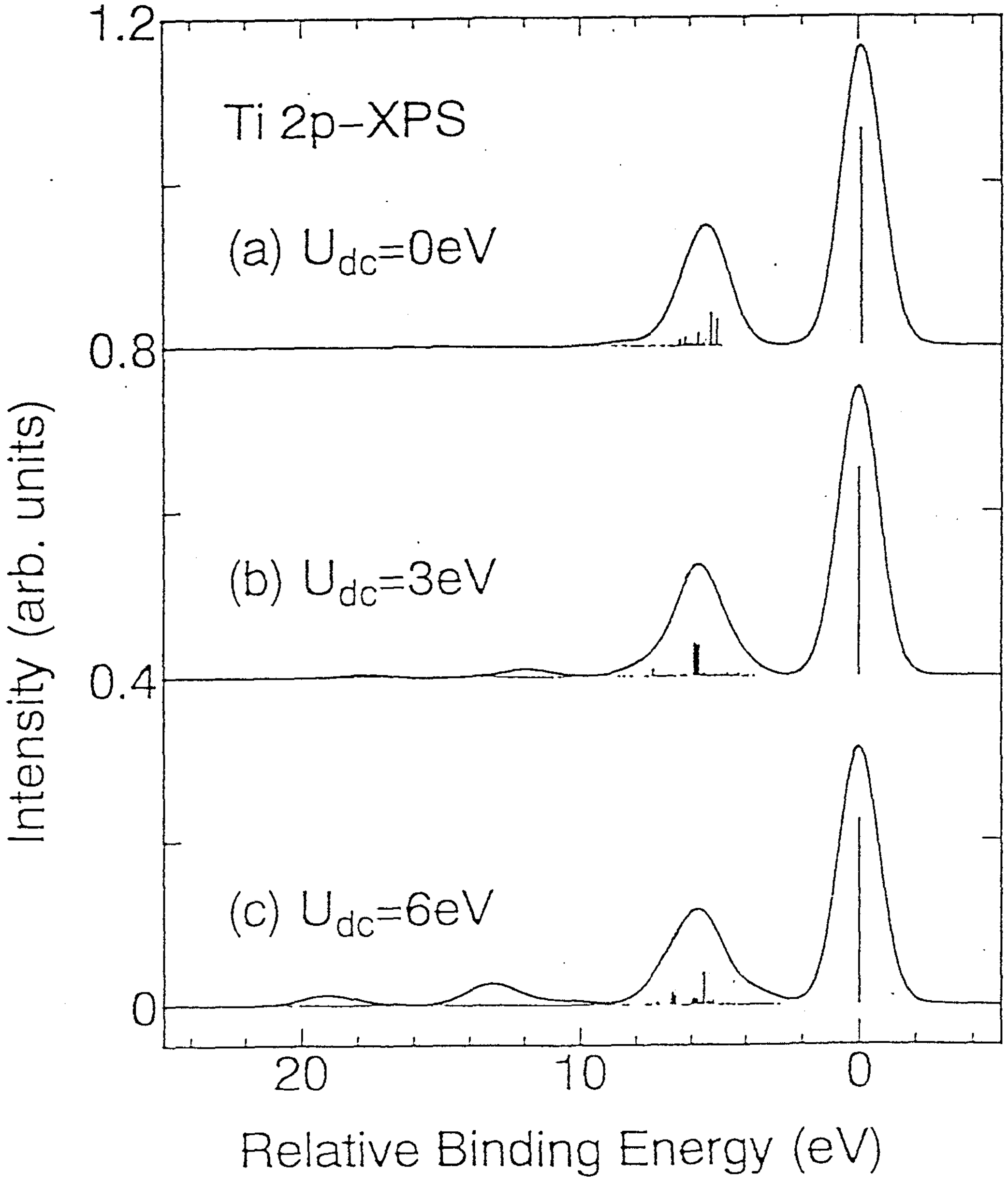
1.2
0.8
0.4
0
Ti 2p–XPS
(a) U_{dc}=0eV
(b) U_{dc}=3eV
(c) U_{dc}=6eV
Intensity (arb. units)
20
10
0
Relative Binding Energy (eV)

Fig. 2.8

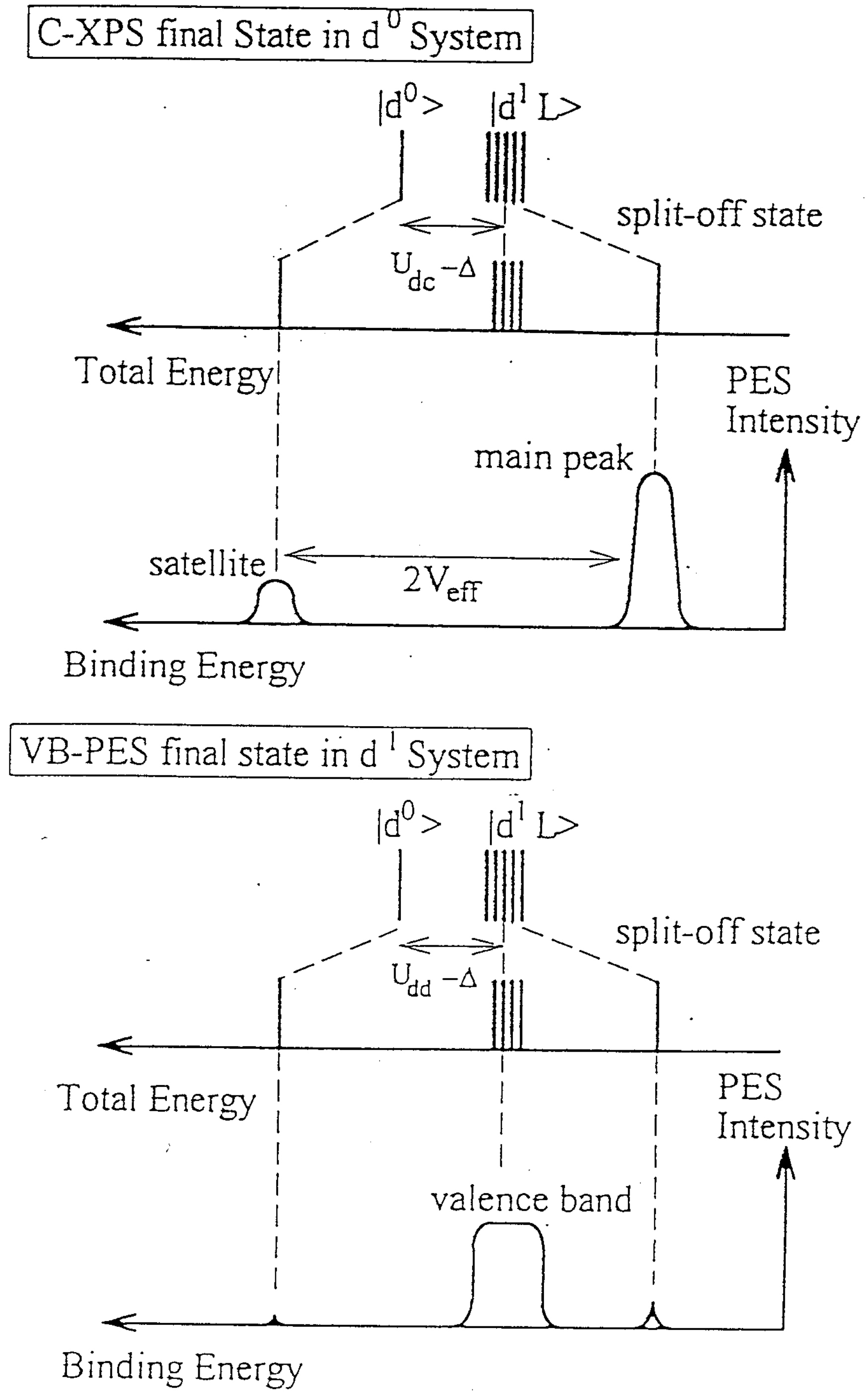
C-XPS final State in d^0 System
|d^0>
|d^1 L>
split-off state
$U_{dc} - \Delta$
Total Energy
PES Intensity
main peak
satellite
$2V_{eff}$
Binding Energy
VB-PES final state in d^1 System
|d^0>
|d^1 L>
split-off state
$U_{dd} - \Delta$
Total Energy
PES Intensity
valence band
Binding Energy

Fig. 2.9.

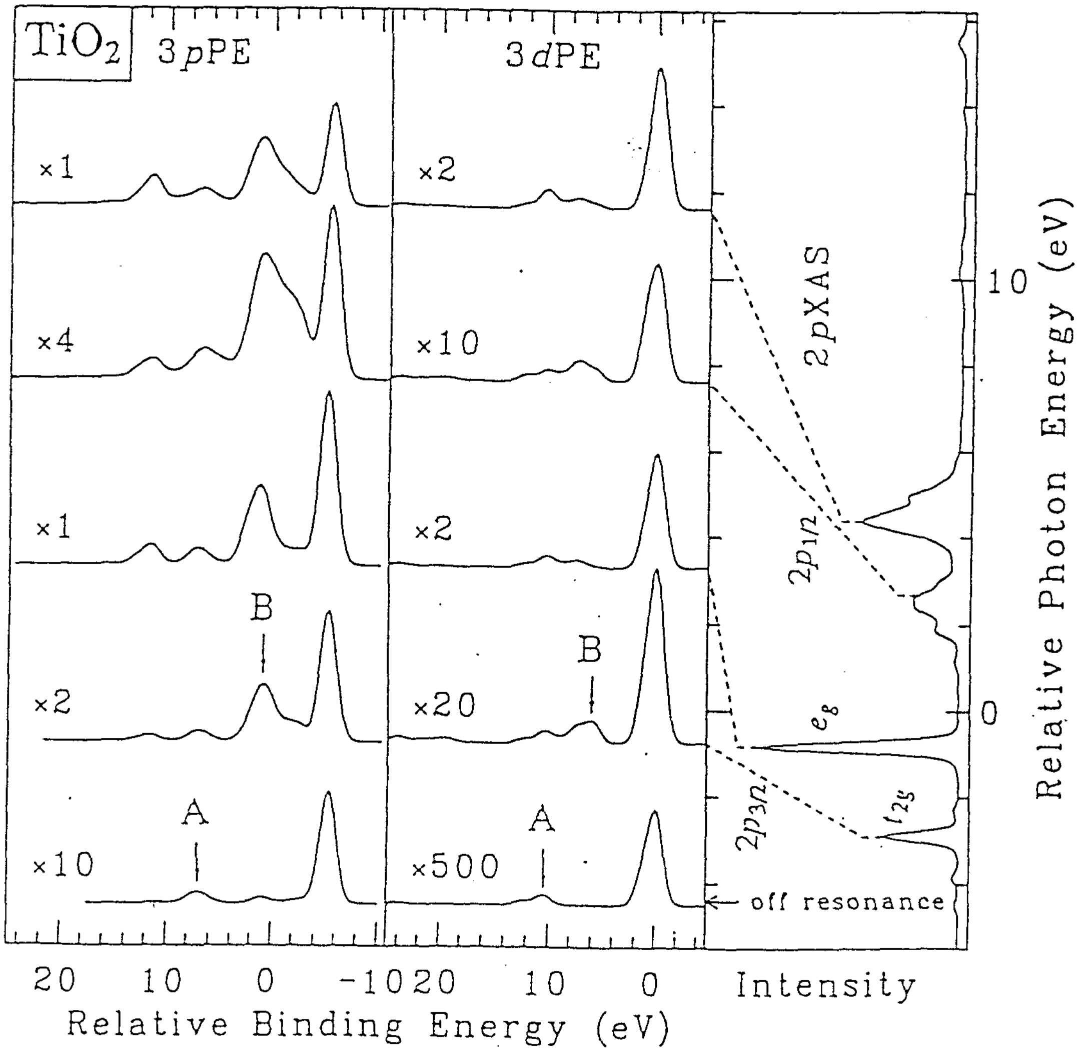
TiO$_2$
3pPE
3dPE
×1
×4
×1
×2
×10
×2
×10
×2
×20
×500
A
B
B
A
2pXAS
$2p_{1/2}$
e_g
$2p_{3/2}$
t_{2g}
off resonance
10
0
Relative Photon Energy (eV)
20
10
0
-10
20
10
0
Relative Binding Energy (eV)
Intensity

Fig. 2.10.

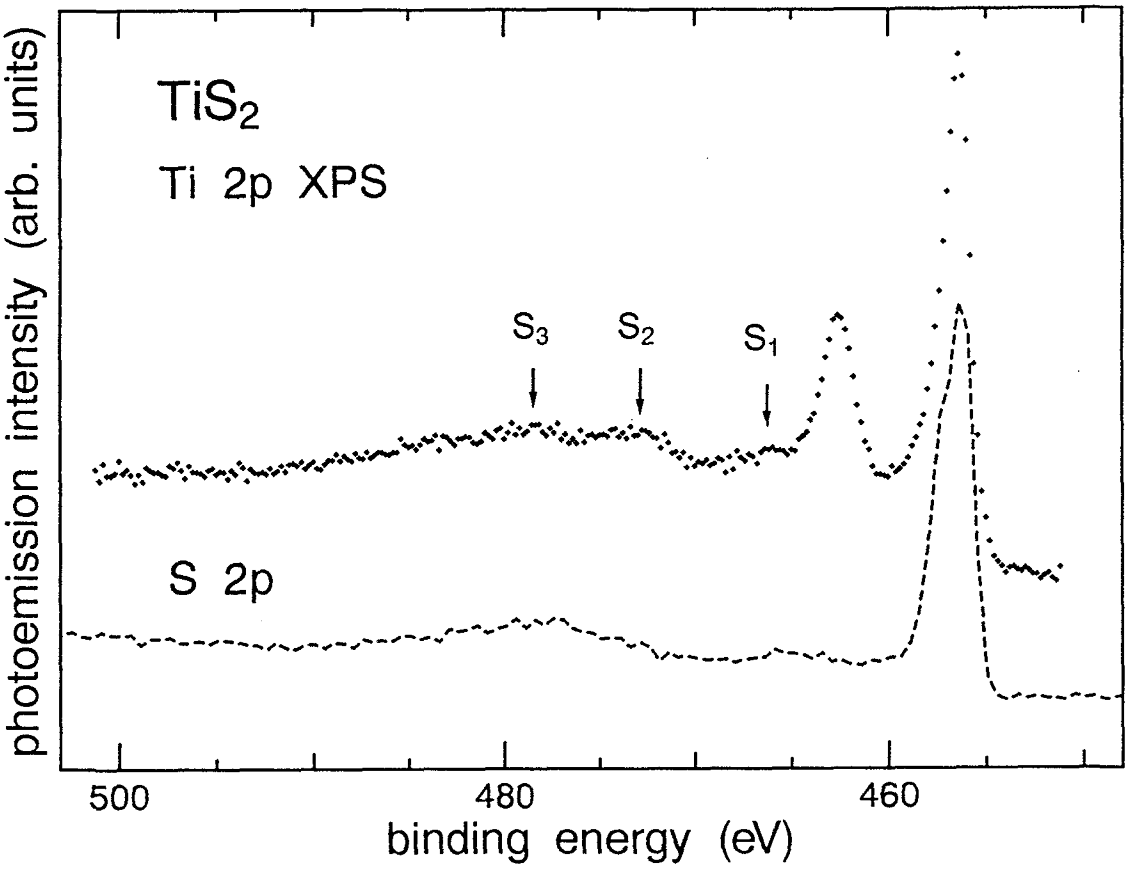
TiS$_2$
Ti 2p XPS
S 2p
S$_3$
S$_2$
S$_1$
photoemission intensity (arb. units)
500
480
460
binding energy (eV)

Fig. 2.11 (a)

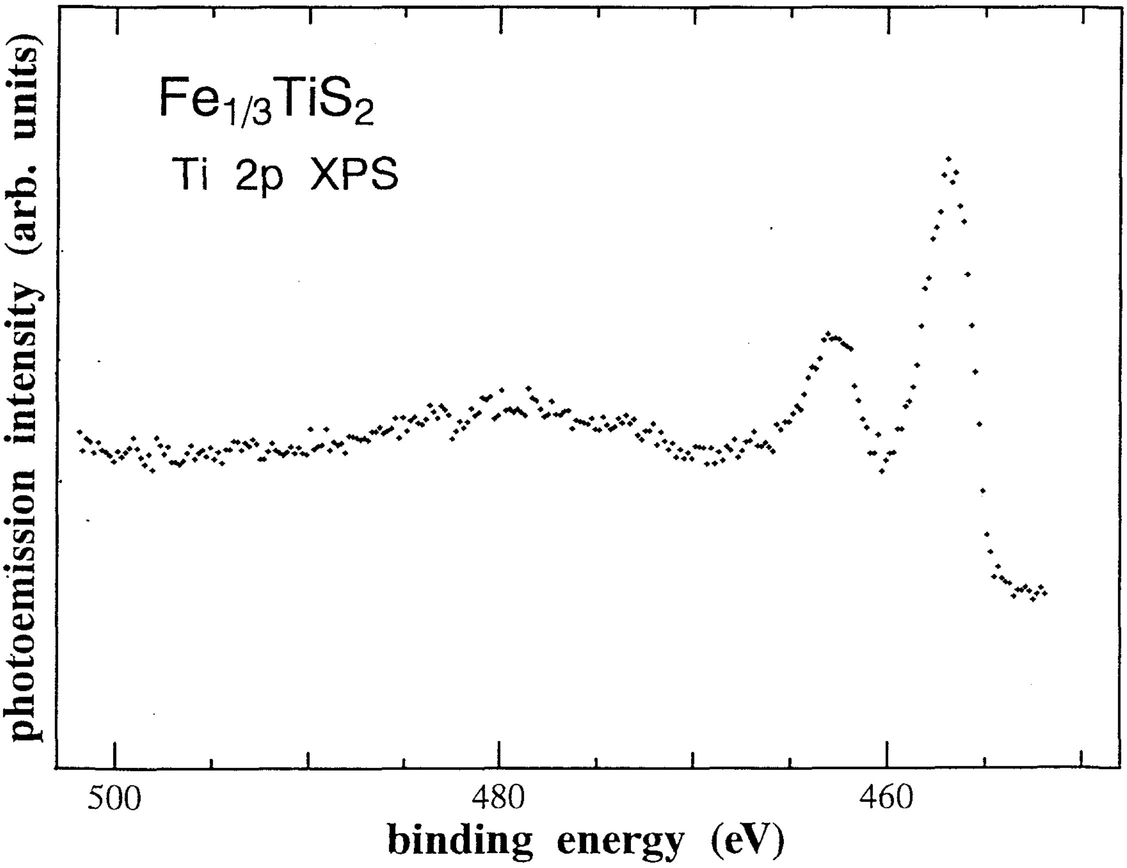

$Fe_{1/3}TiS_2$
Ti 2p XPS
photoemission intensity (arb. units)
500
480
460
binding energy (eV)

(c)

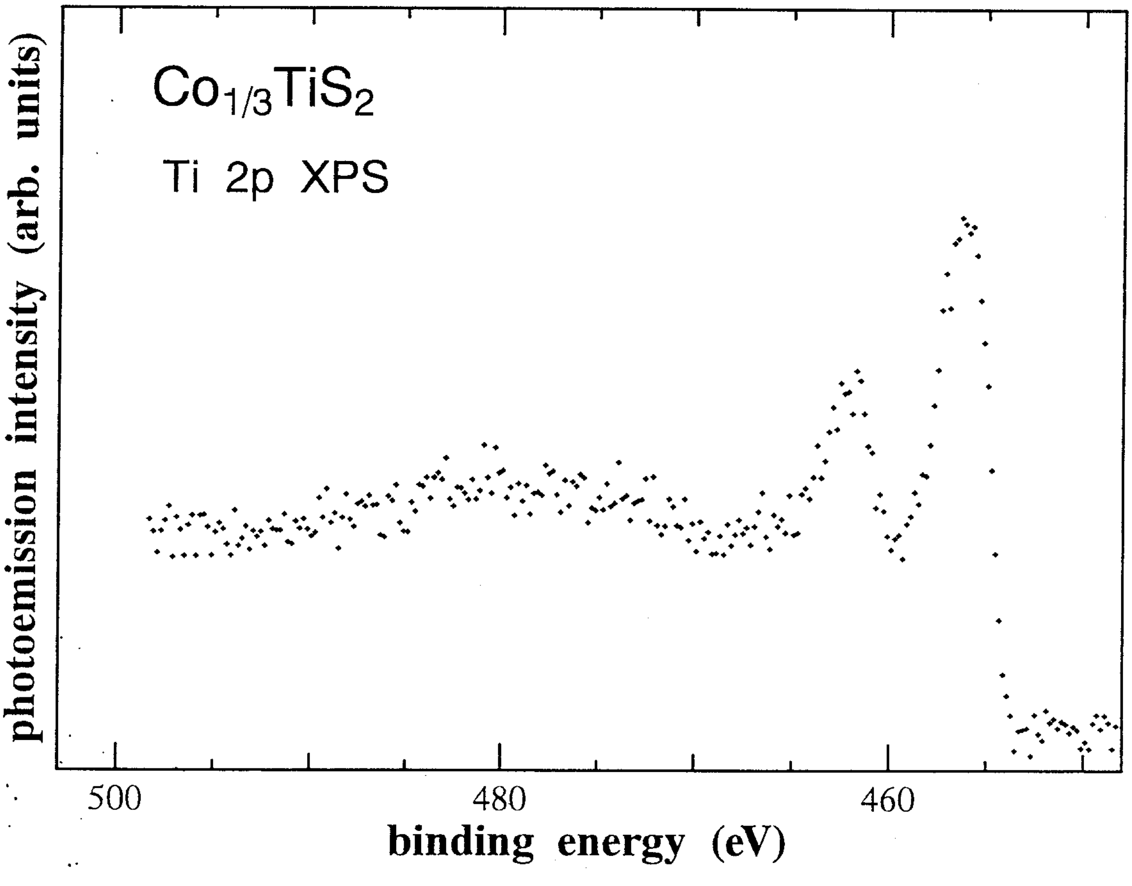
$Co_{1/3}TiS_2$
Ti 2p XPS
photoemission intensity (arb. units)
500
480
460
binding energy (eV)

(d)

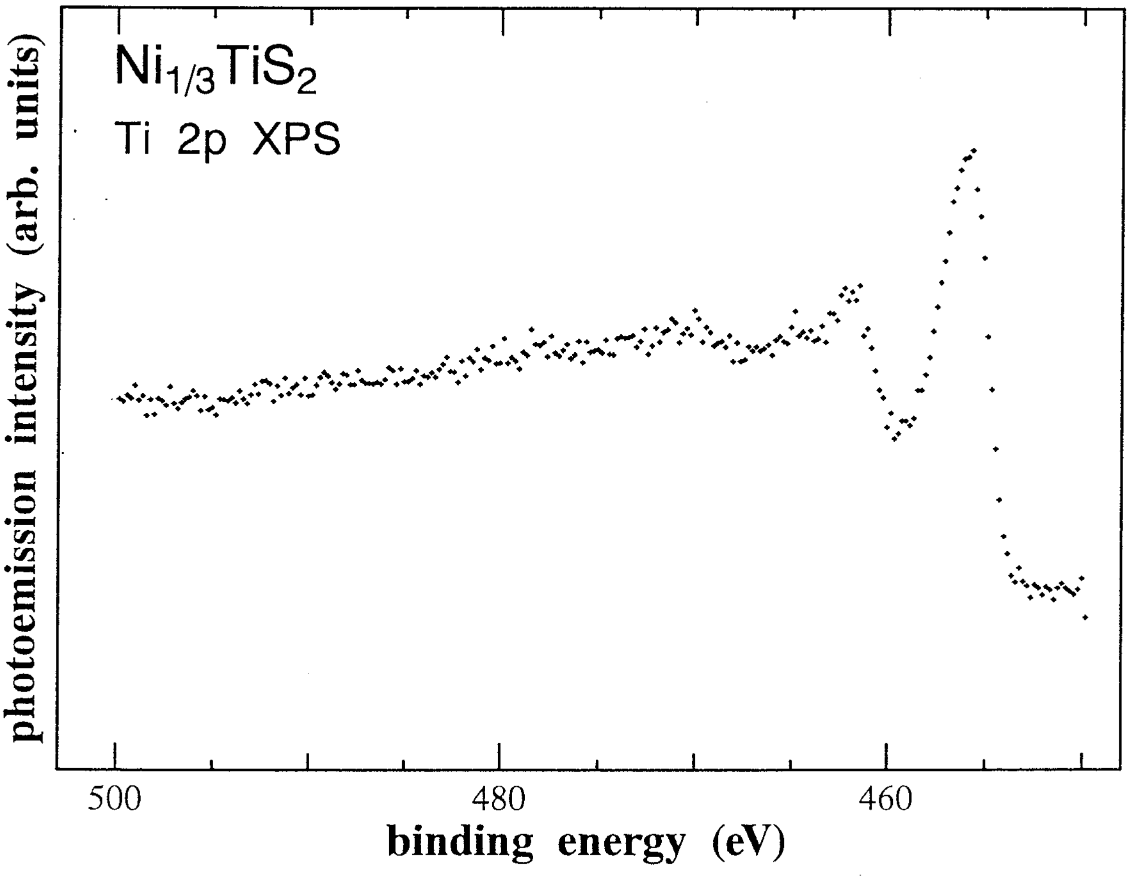
$Ni_{1/3}TiS_2$
Ti 2p XPS
photoemission intensity (arb. units)
500
480
460
binding energy (eV)

(e)

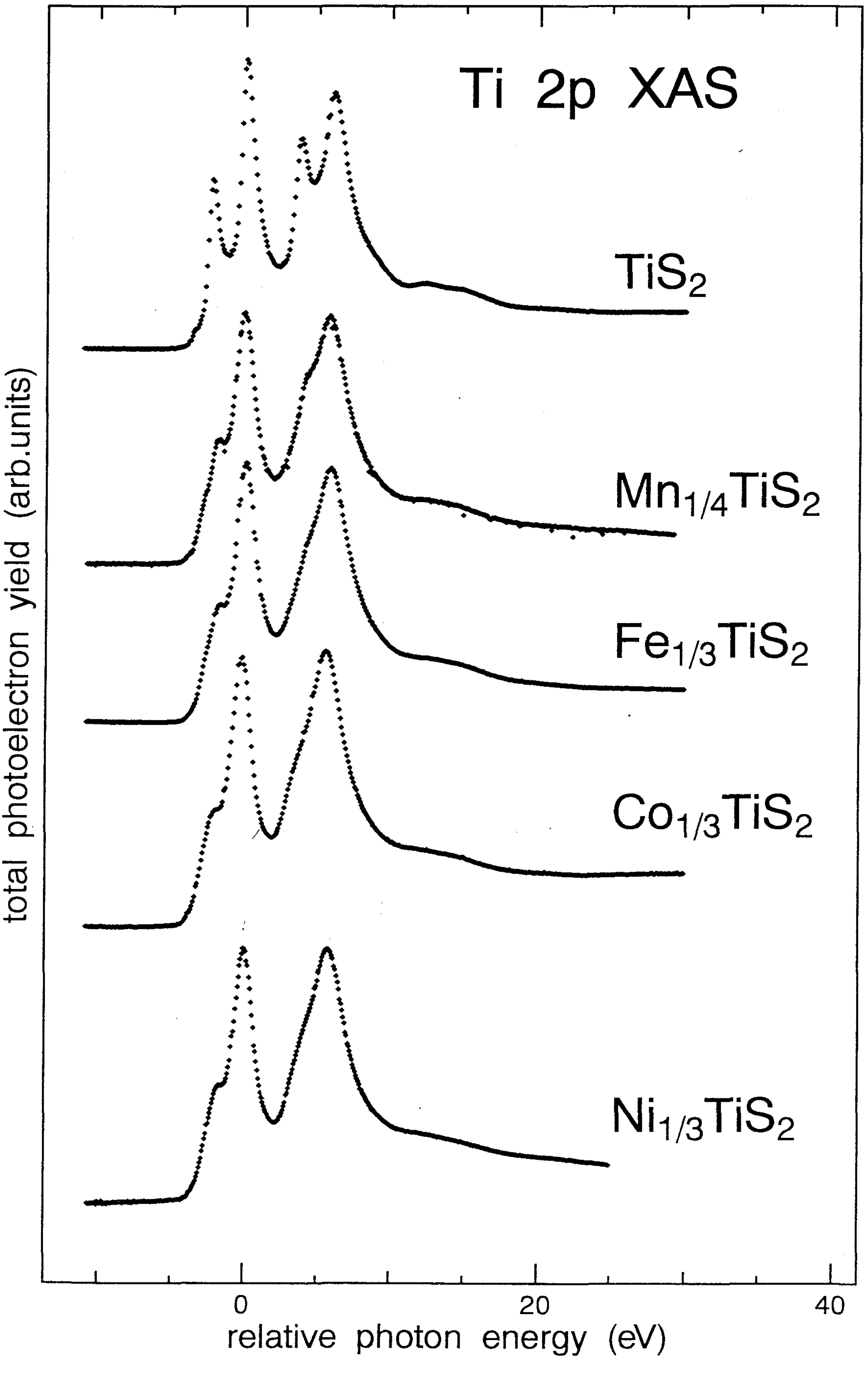
Ti 2p XAS
TiS_2
$Mn_{1/4}TiS_2$
$Fe_{1/3}TiS_2$
$Co_{1/3}TiS_2$
$Ni_{1/3}TiS_2$
total photoelectron yield (arb.units)
0
20
40
relative photon energy (eV)

Fig. 2.12.

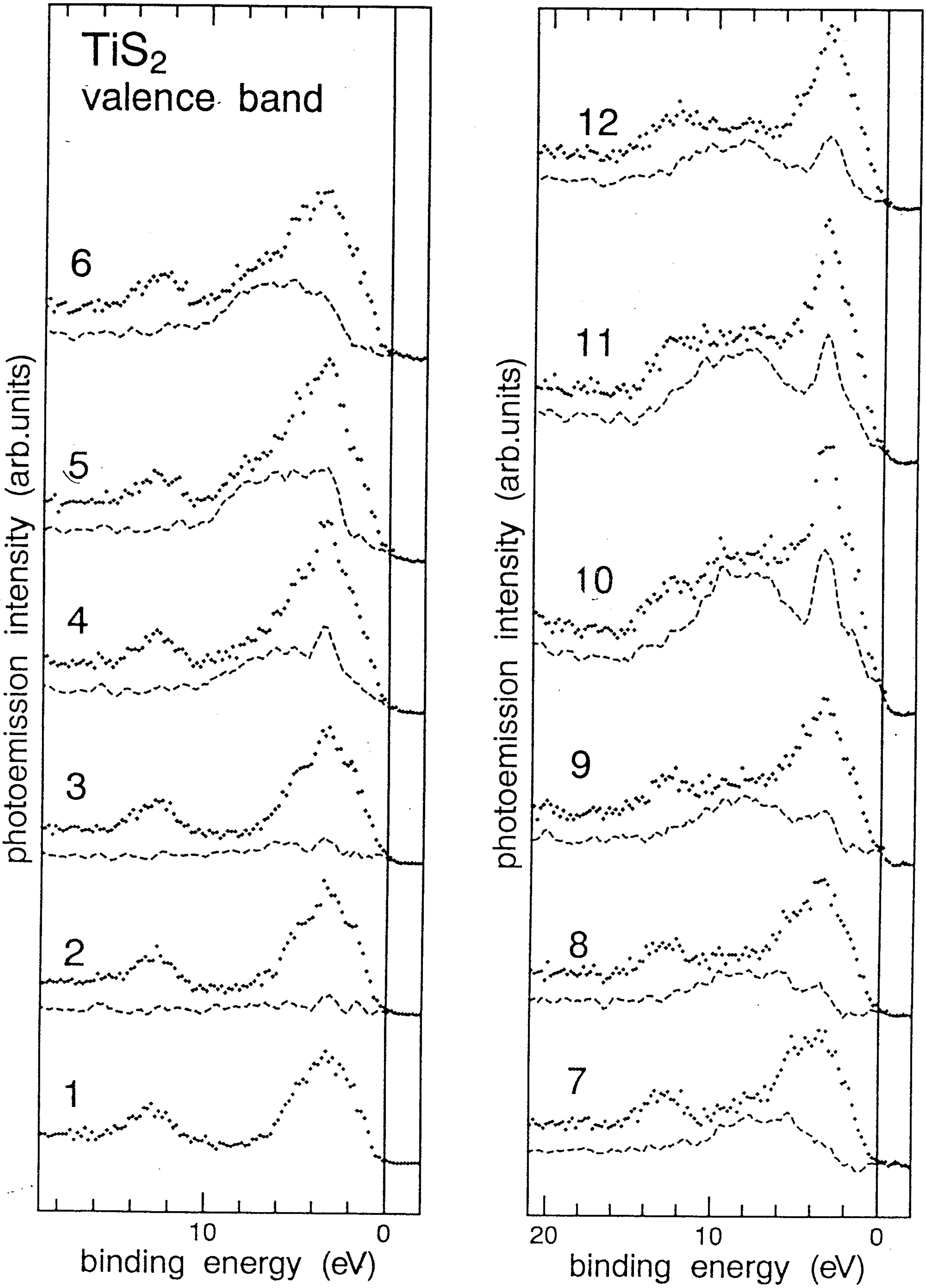
TiS$_2$
valence band
6
5
4
3
2
1
12
11
10
9
8
7
photoemission intensity (arb.units)
photoemission intensity (arb.units)
10
0
20
10
0
binding energy (eV)
binding energy (eV)

(a)

Fig. 2.13

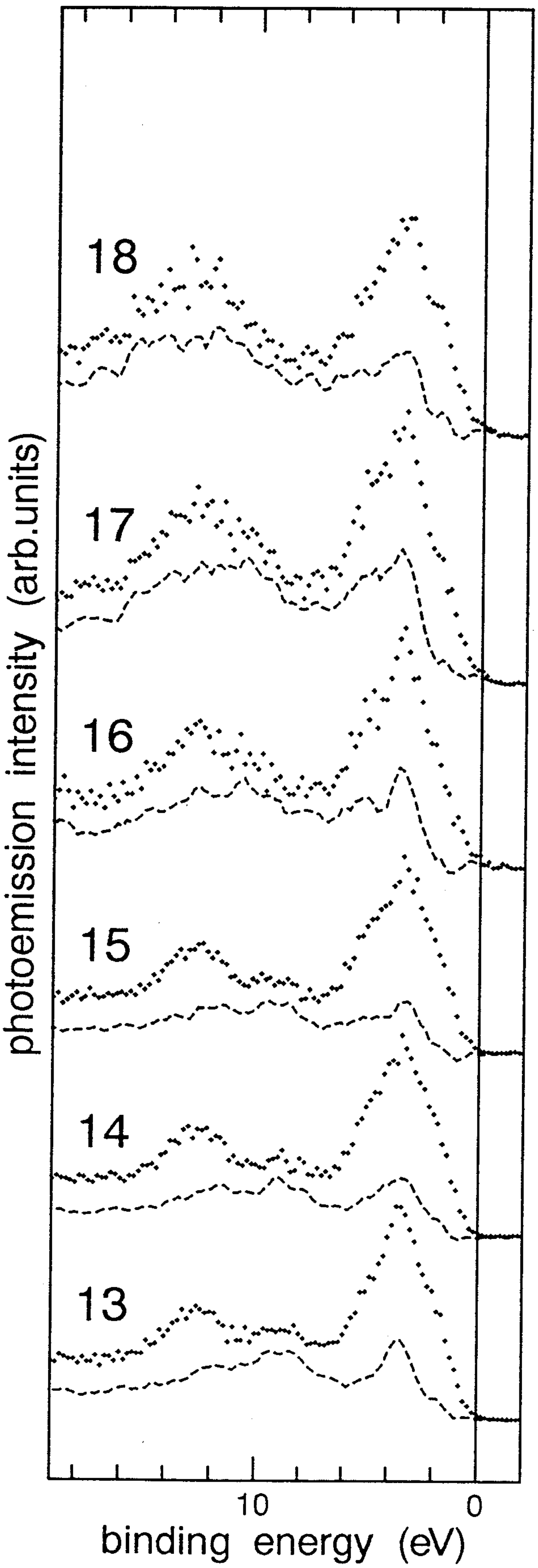
18
17
16
15
14
13
photoemission intensity (arb.units)
10
0
binding energy (eV)

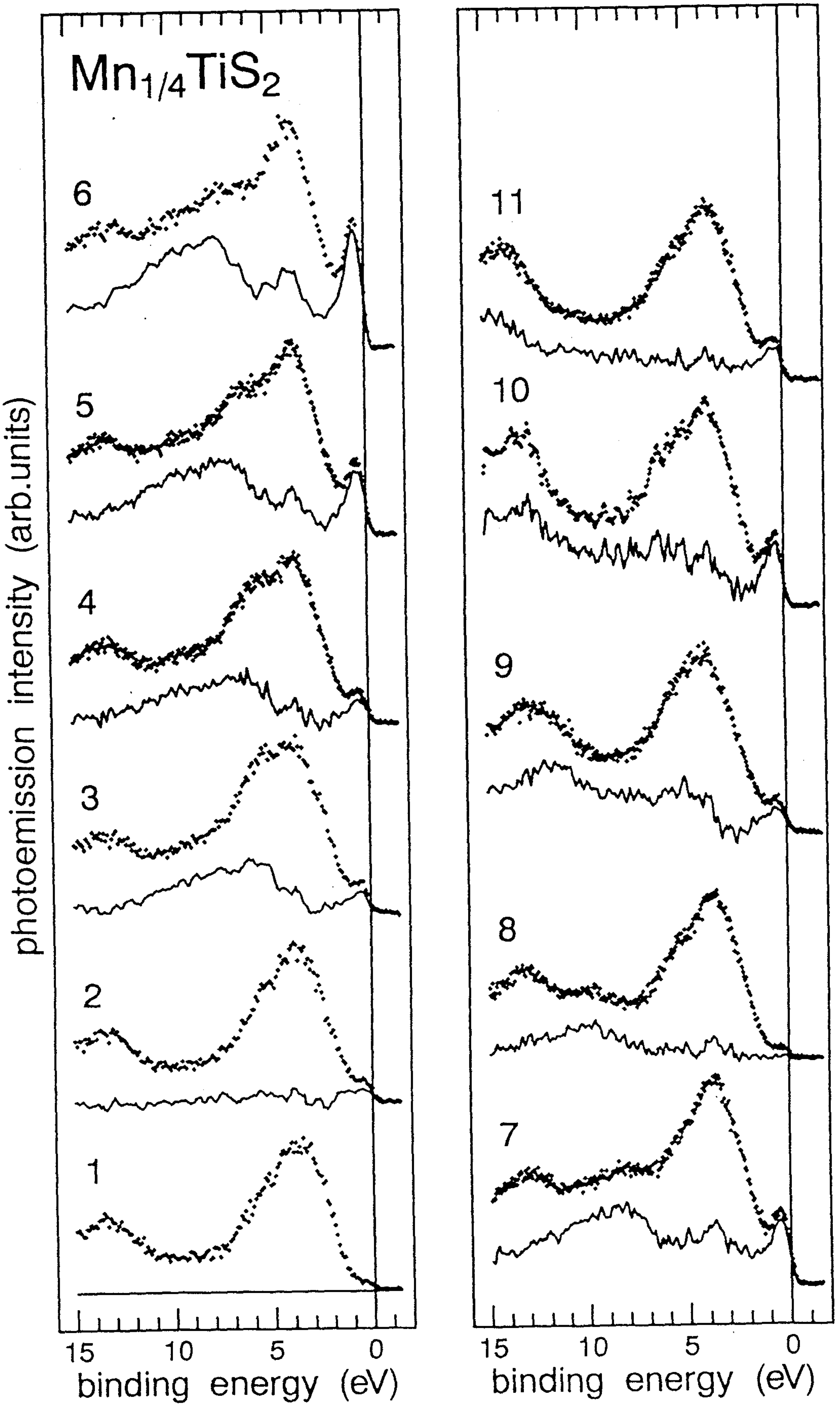

Mn$_{1/4}$TiS$_2$
photoemission intensity (arb.units)
6
5
4
3
2
1
11
10
9
8
7
15
10
5
0
binding energy (eV)
15
10
5
0
binding energy (eV)

(b)

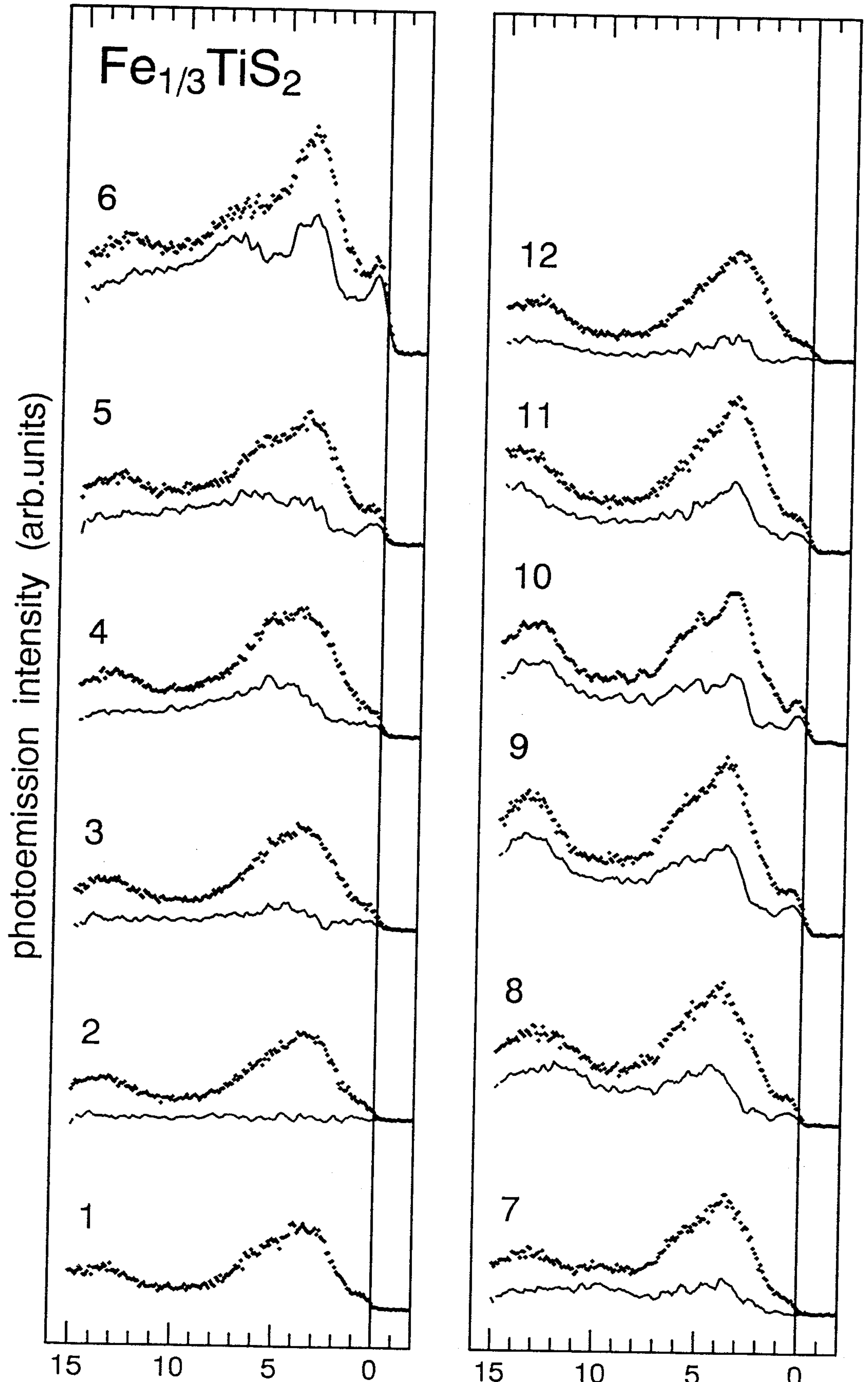
$Fe_{1/3}TiS_2$
6
5
4
3
2
1
12
11
10
9
8
7
photoemission intensity (arb.units)
15
10
5
0
binding energy (eV)
15
10
5
0
binding energy (eV)

(c)

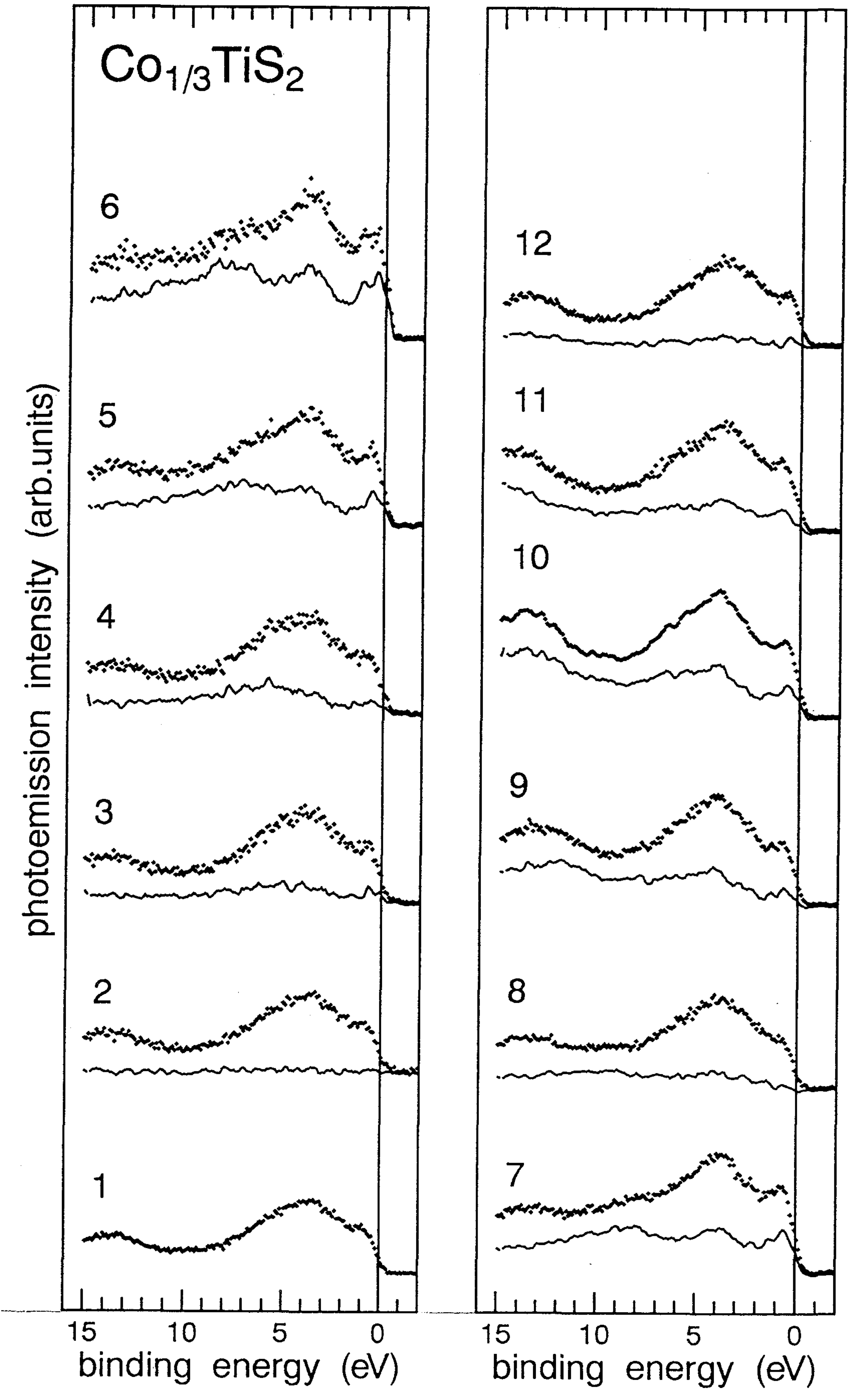
Co$_{1/3}$TiS$_2$
photoemission intensity (arb.units)
6
5
4
3
2
1
12
11
10
9
8
7
15
10
5
0
binding energy (eV)
15
10
5
0
binding energy (eV)

(d)

Ti 2p→3d excitation region

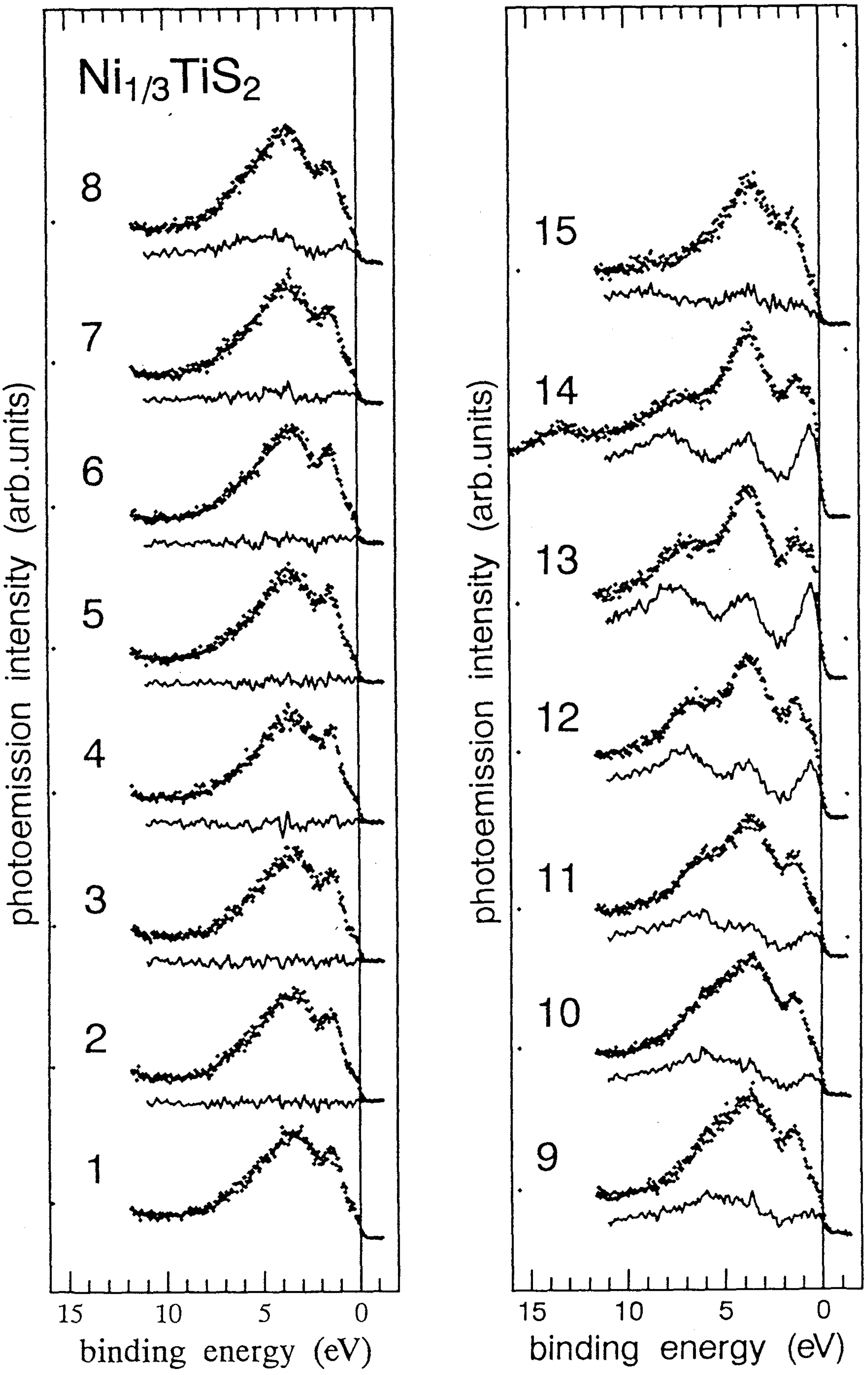

(e)

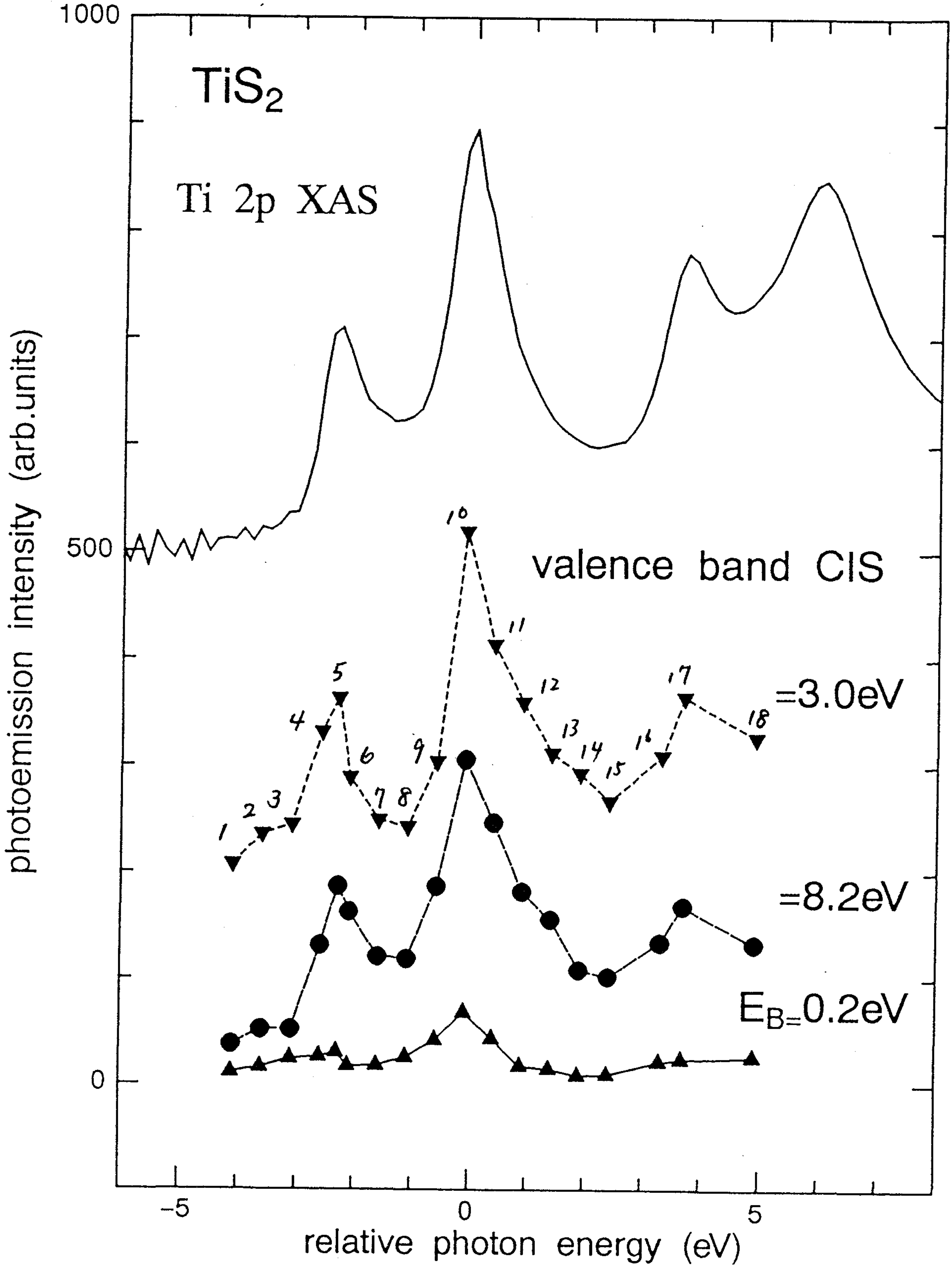

TiS$_2$
Ti 2p XAS
valence band CIS
=3.0eV
=8.2eV
E$_B$=0.2eV
1 2 3 4 5 6 7 8 9 10 11 12 13 14 15 16 17 18
1000
500
0
-5
0
5
photoemission intensity (arb.units)
relative photon energy (eV)

Fig. 2.14. (a)

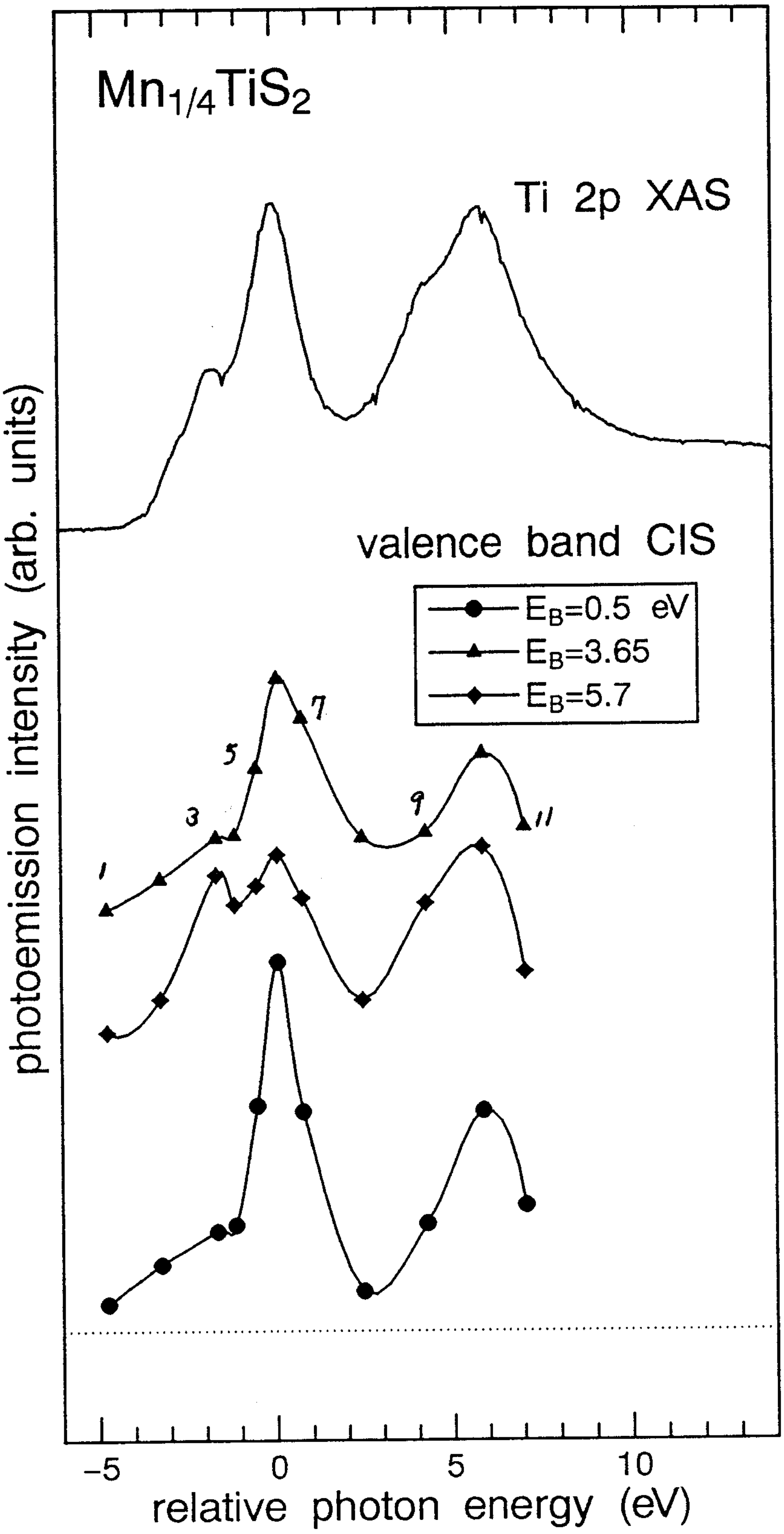
Mn$_{1/4}$TiS$_2$
Ti 2p XAS
valence band CIS
E$_B$=0.5 eV
E$_B$=3.65
E$_B$=5.7
1
3
5
7
9
11
photoemission intensity (arb. units)
−5
0
5
10
relative photon energy (eV)

(b)

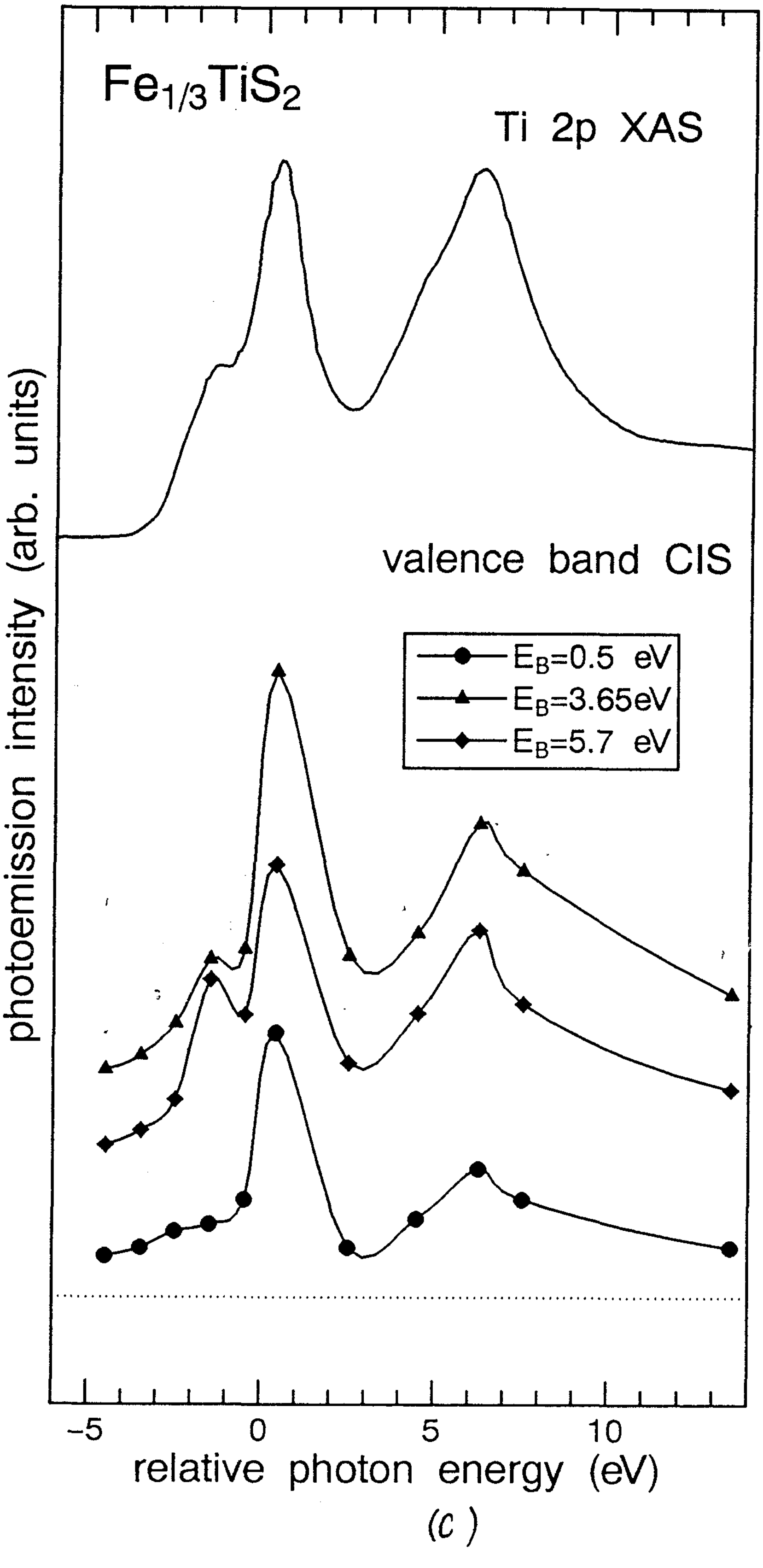
Fe$_{1/3}$TiS$_2$
Ti 2p XAS
valence band CIS
E$_B$=0.5 eV
E$_B$=3.65eV
E$_B$=5.7 eV
photoemission intensity (arb. units)
−5
0
5
10
relative photon energy (eV)

(c)

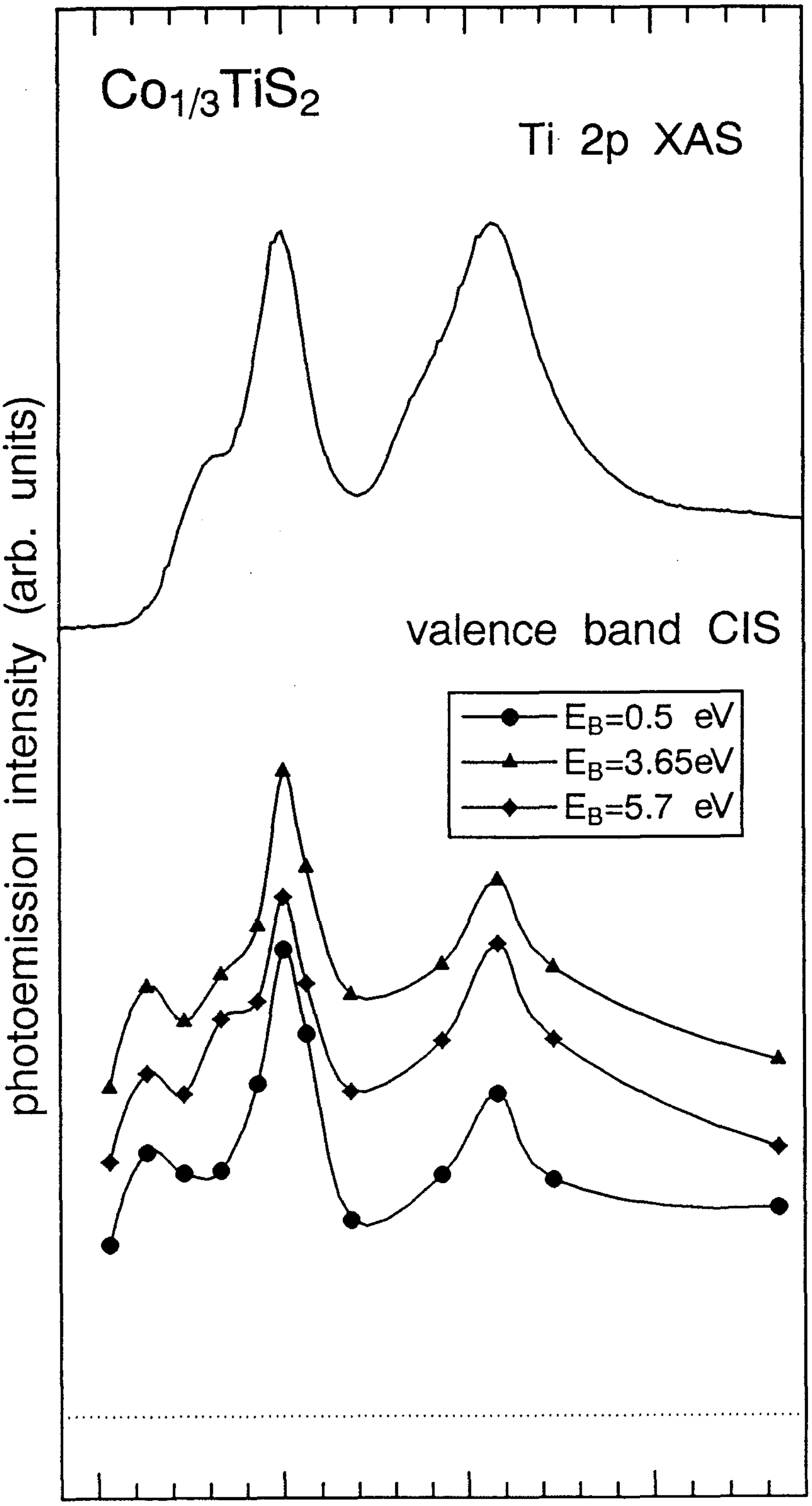
$Co_{1/3}TiS_2$
Ti 2p XAS
valence band CIS
E_B=0.5 eV
E_B=3.65eV
E_B=5.7 eV
photoemission intensity (arb. units)
−5
0
5
10
relative photon energy (eV)

(d)

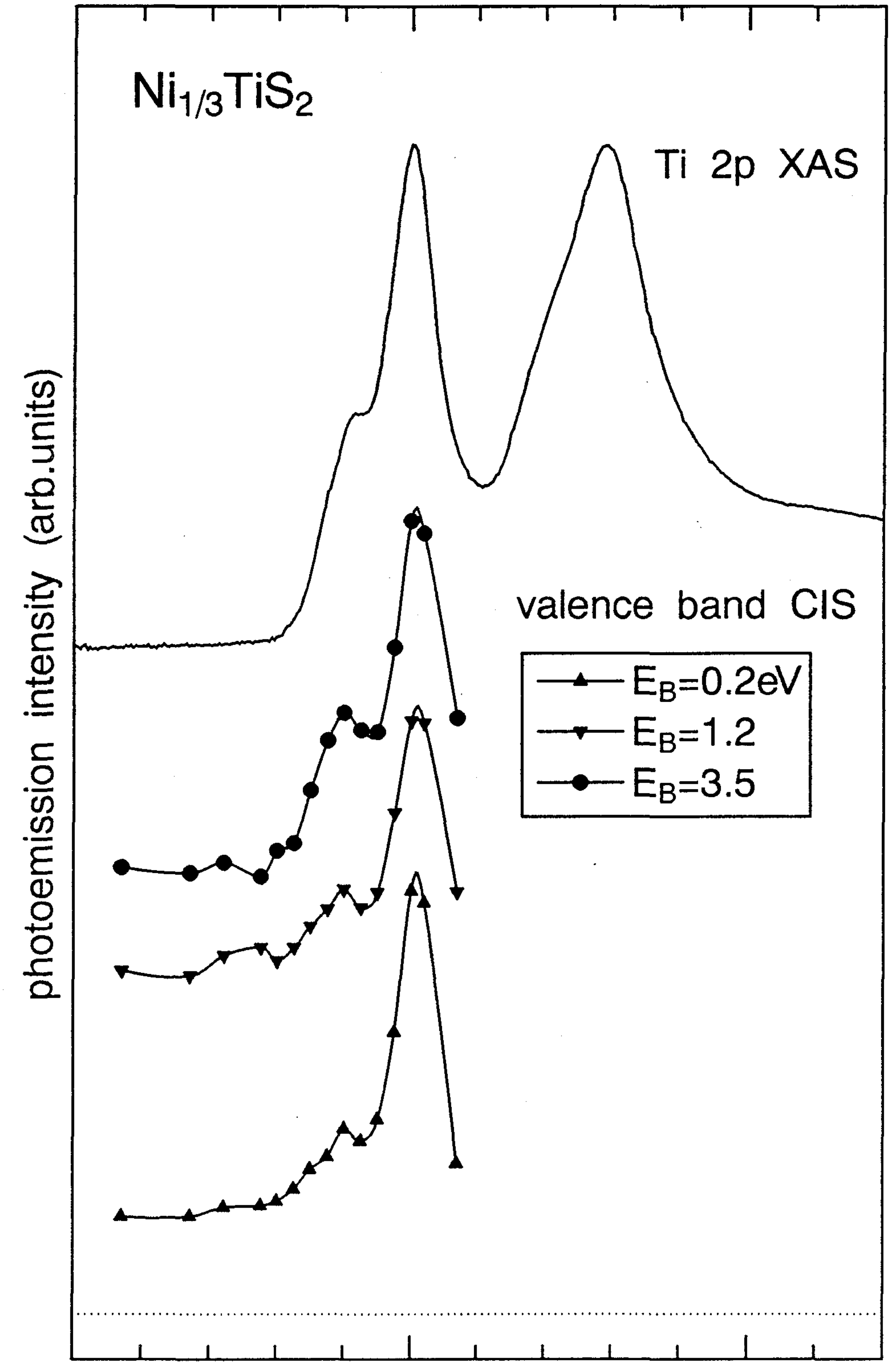
$Ni_{1/3}TiS_2$
Ti 2p XAS
valence band CIS
E_B=0.2eV
E_B=1.2
E_B=3.5
photoemission intensity (arb.units)
−10
0
10
relative photon energy (eV)

(e)

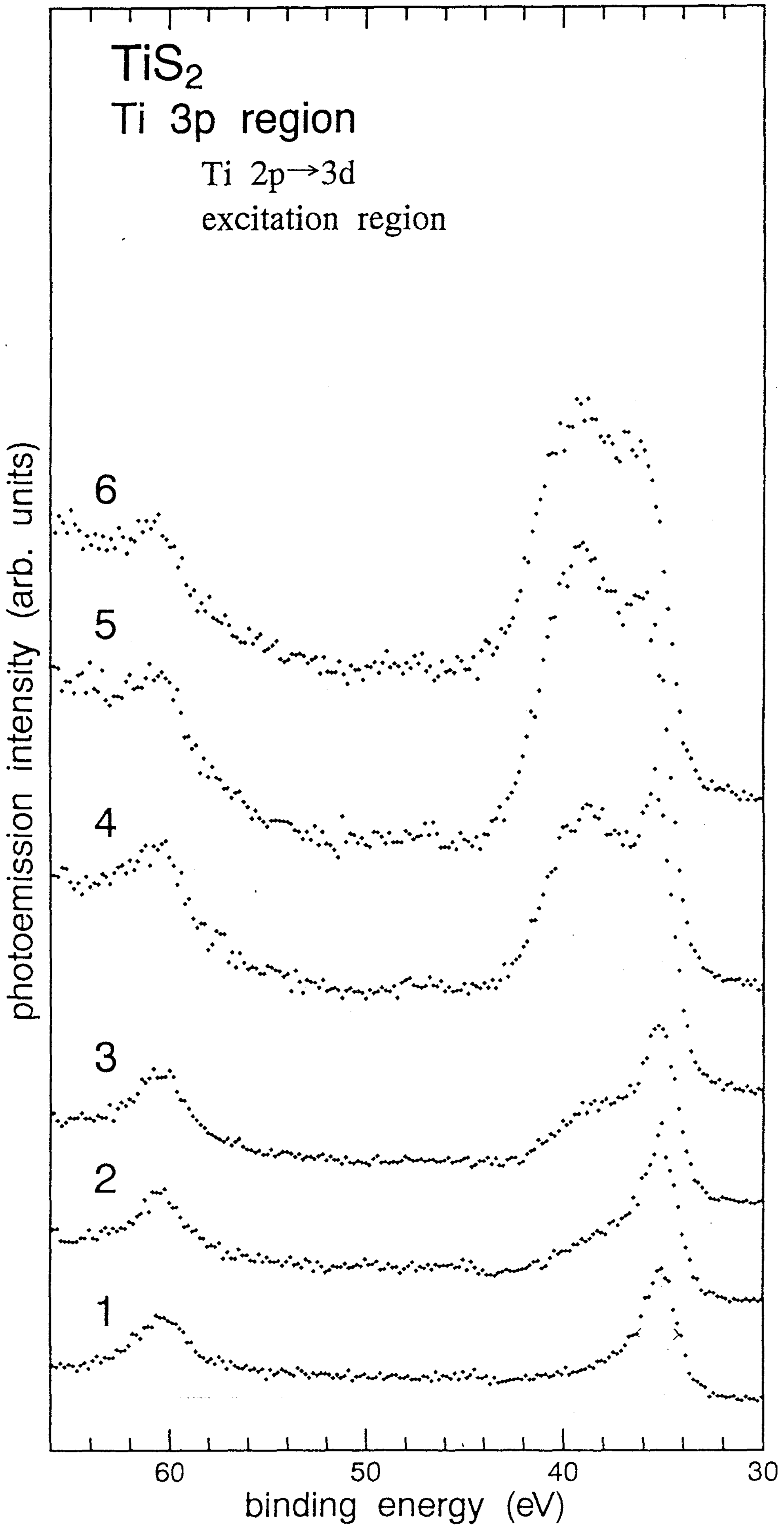
TiS$_2$
Ti 3p region
Ti 2p→3d
excitation region
6
5
4
3
2
1
photoemission intensity (arb. units)
60
50
40
30
binding energy (eV)

Fig. 2.15. (a)

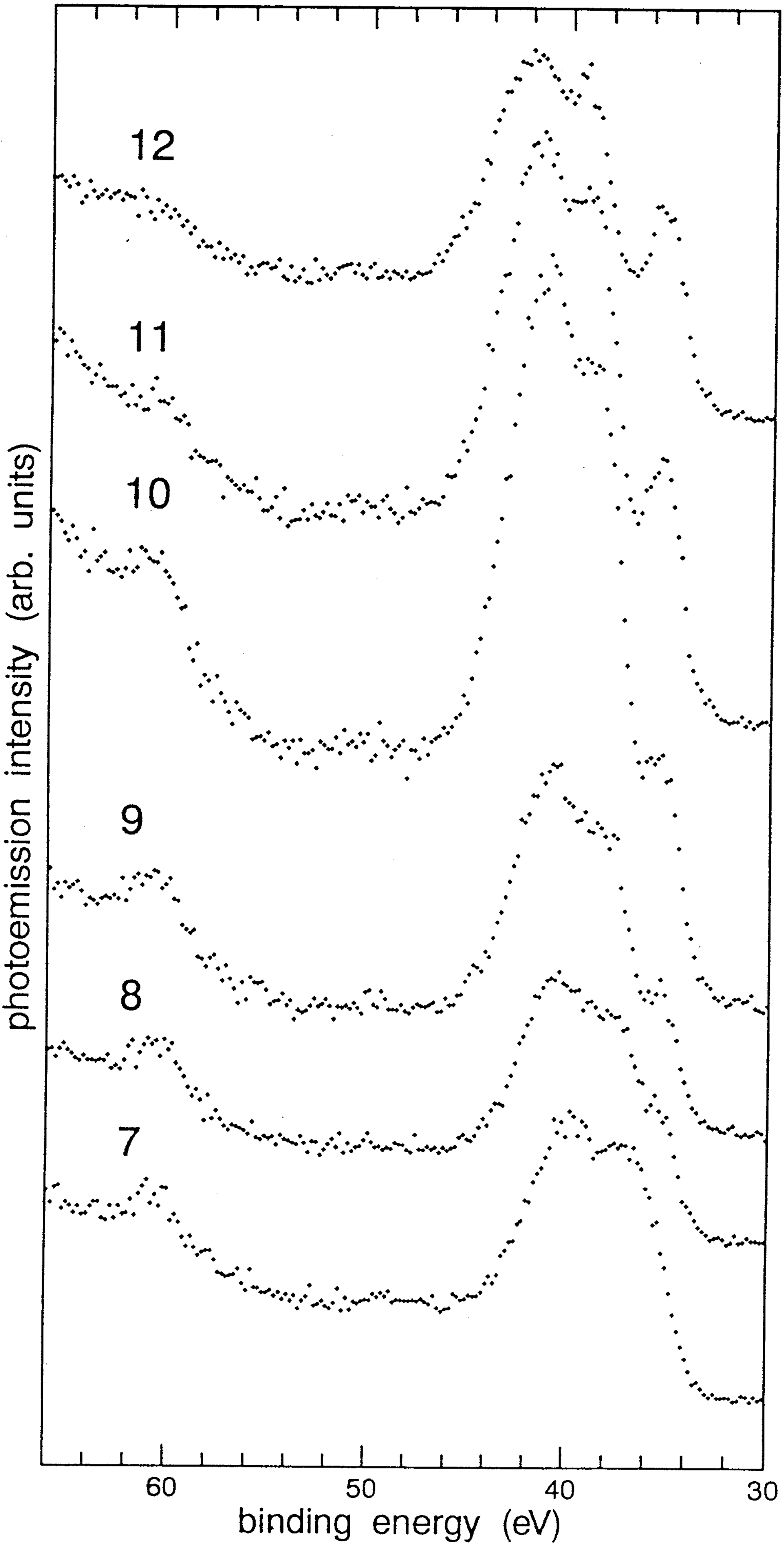
12
11
10
9
8
7
photoemission intensity (arb. units)
60
50
40
30
binding energy (eV)

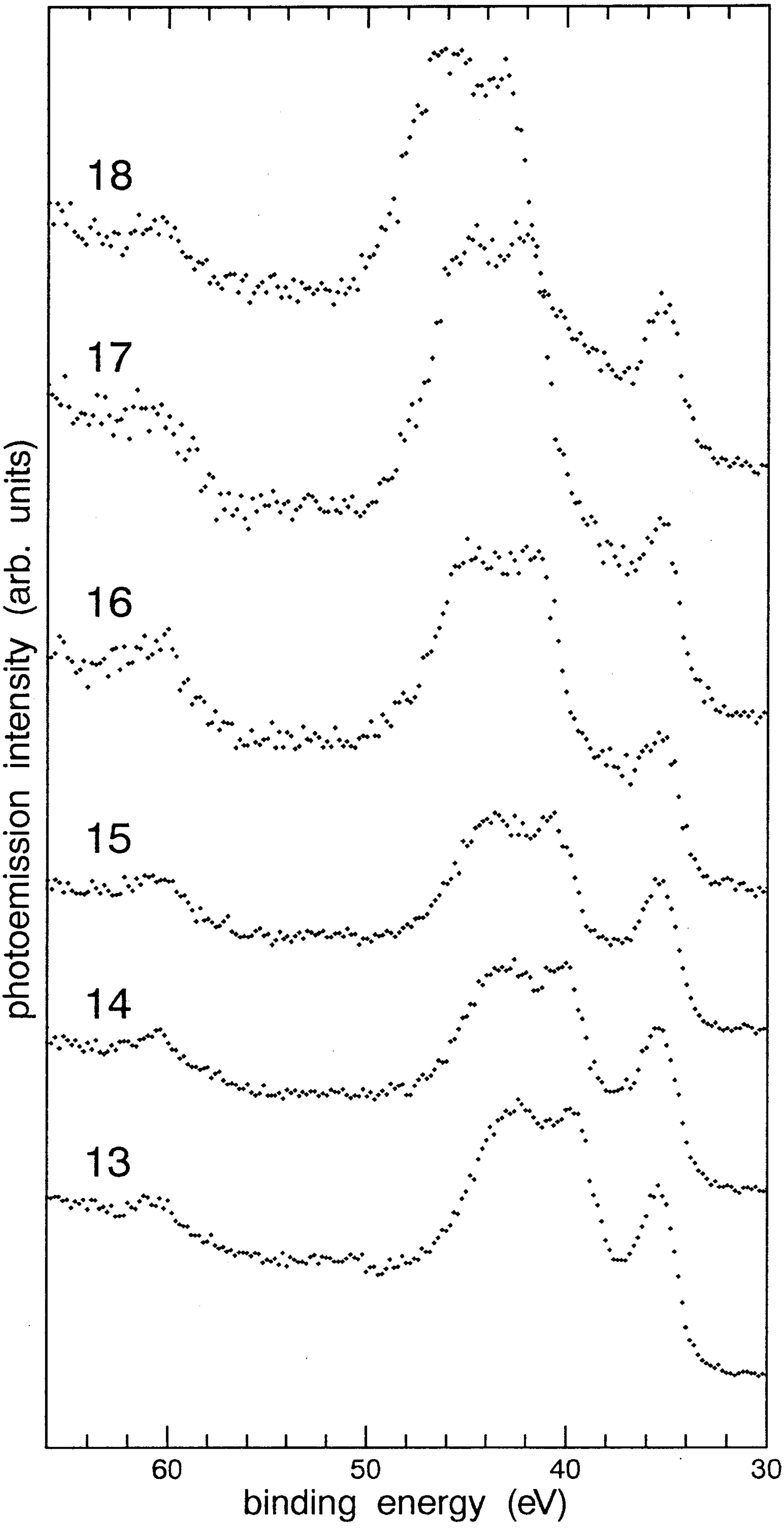
18
17
16
15
14
13
photoemission intensity (arb. units)
60
50
40
30
binding energy (eV)

$Mn_{1/4}TiS_2$

Ti 2p→3d excitation region

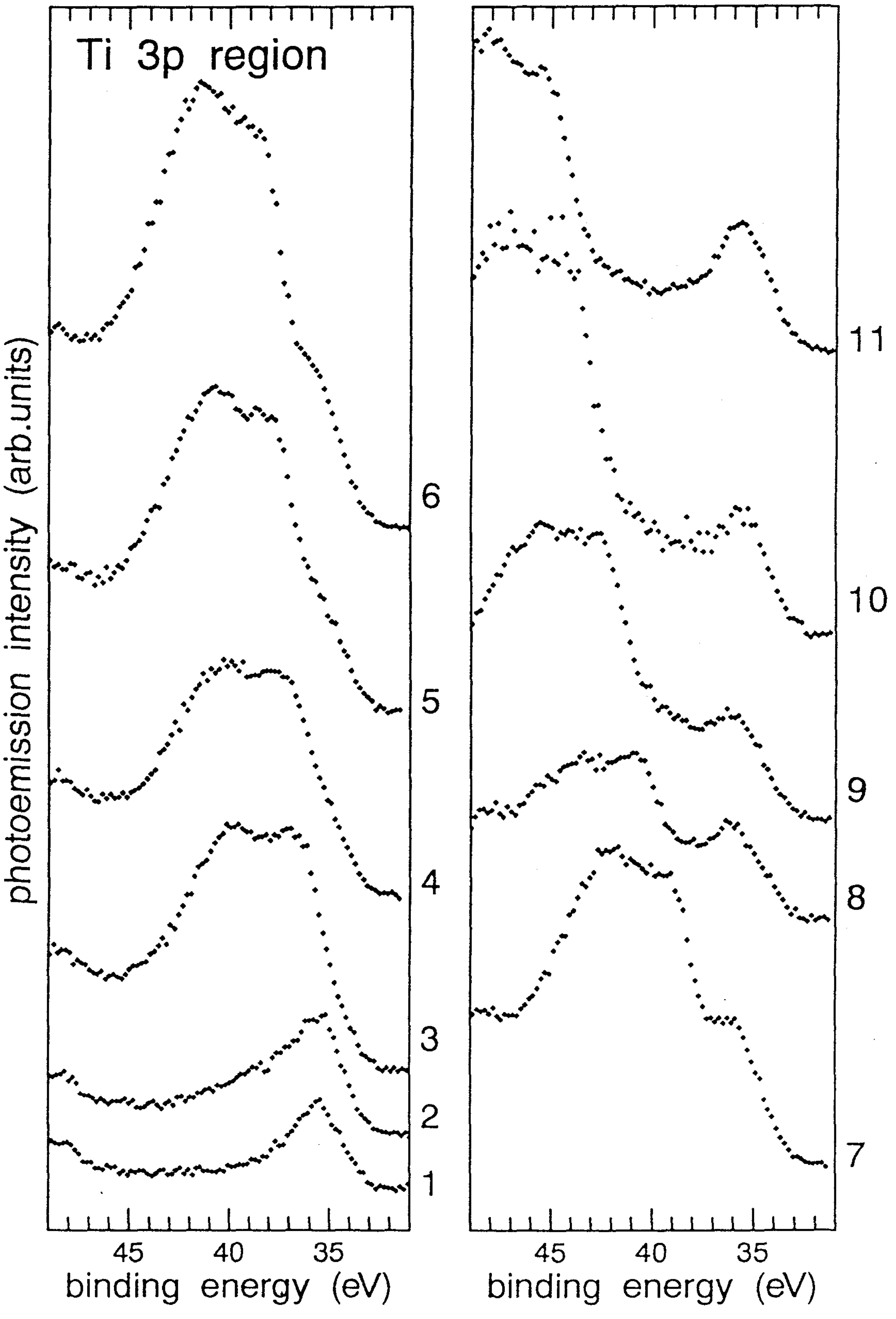

Fig. 2.15. (a)

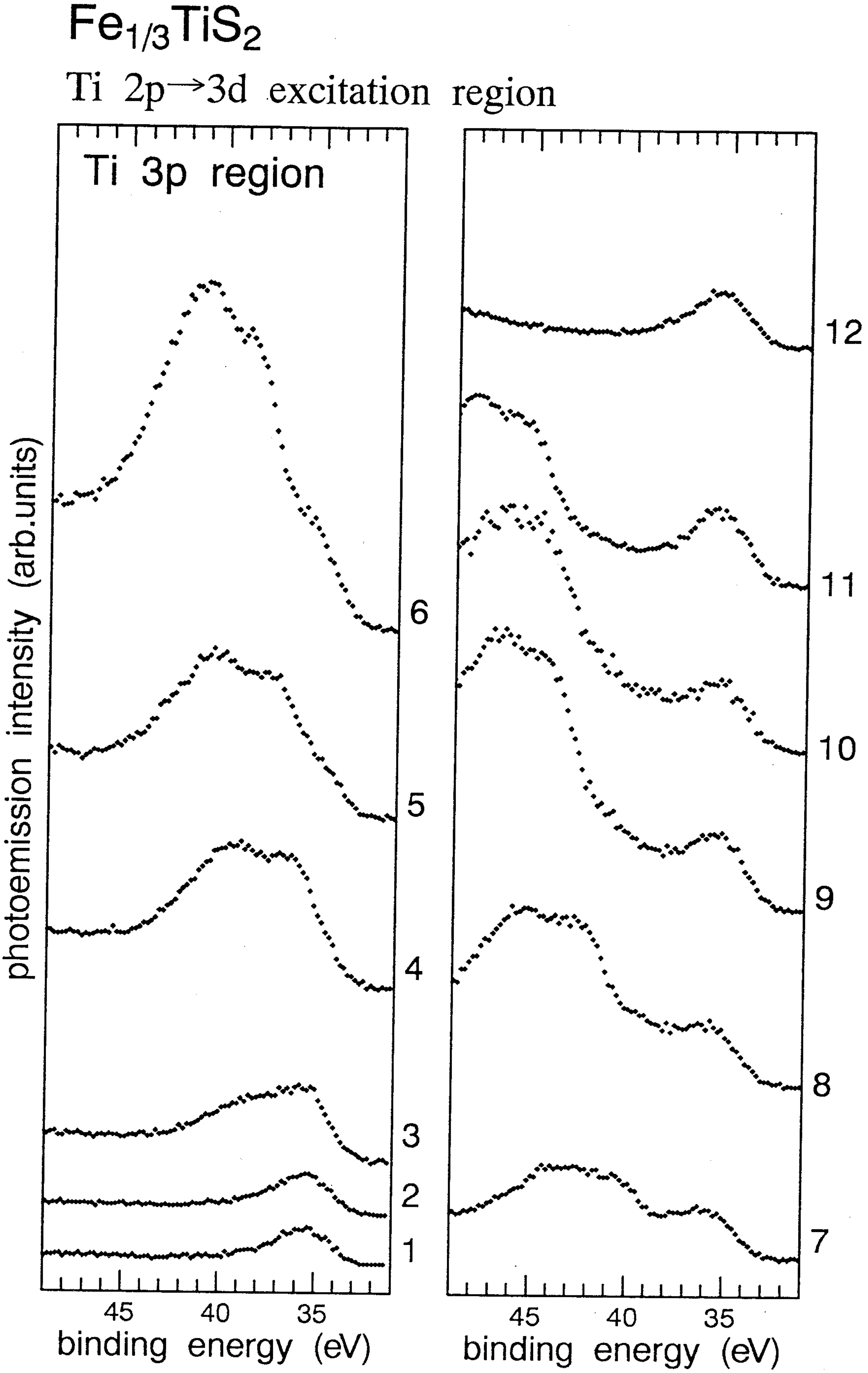
$Fe_{1/3}TiS_2$
Ti 2p→3d excitation region
Ti 3p region
photoemission intensity (arb.units)
1
2
3
4
5
6
7
8
9
10
11
12
45
40
35
binding energy (eV)
45
40
35
binding energy (eV)

(c)

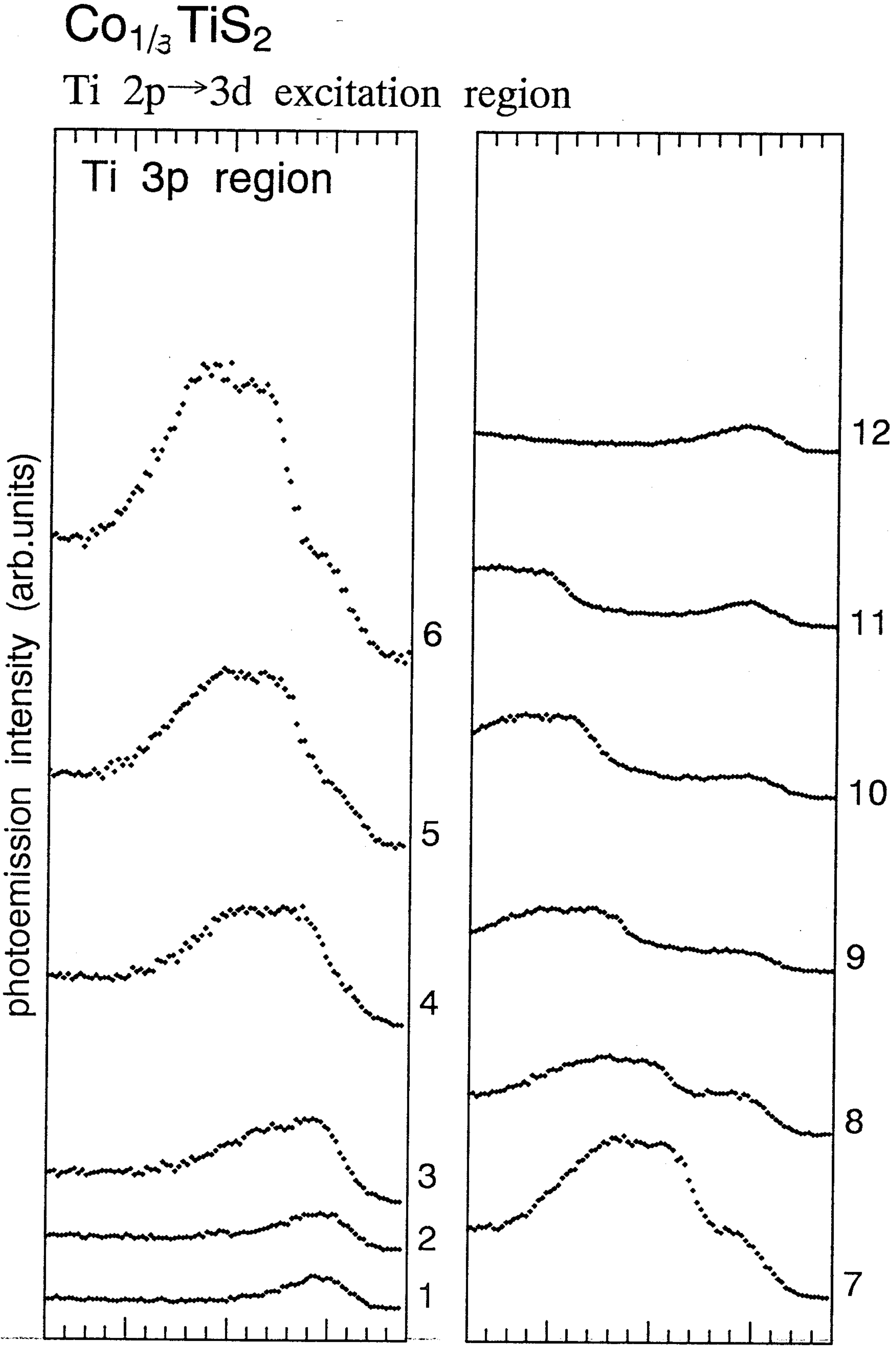
$Co_{1/3}TiS_2$
Ti 2p→3d excitation region
Ti 3p region
photoemission intensity (arb.units)
1
2
3
4
5
6
7
8
9
10
11
12
45
40
35
binding energy (eV)
45
40
35
binding energy (eV)

(d)

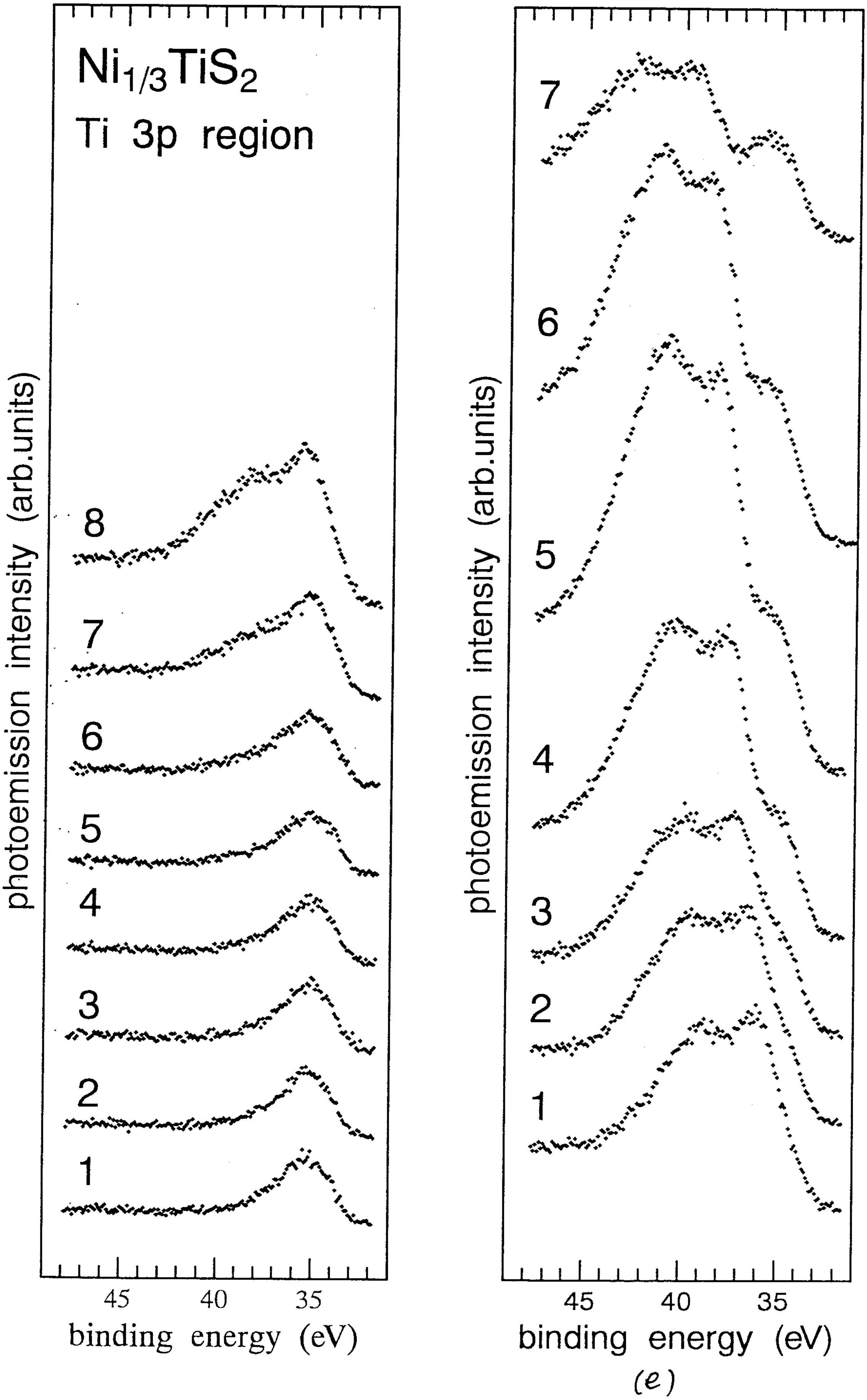
Ni$_{1/3}$TiS$_2$
Ti 3p region
8
7
6
5
4
3
2
1
photoemission intensity (arb.units)
45
40
35
binding energy (eV)
7
6
5
4
3
2
1
photoemission intensity (arb.units)
45
40
35
binding energy (eV)

(e)

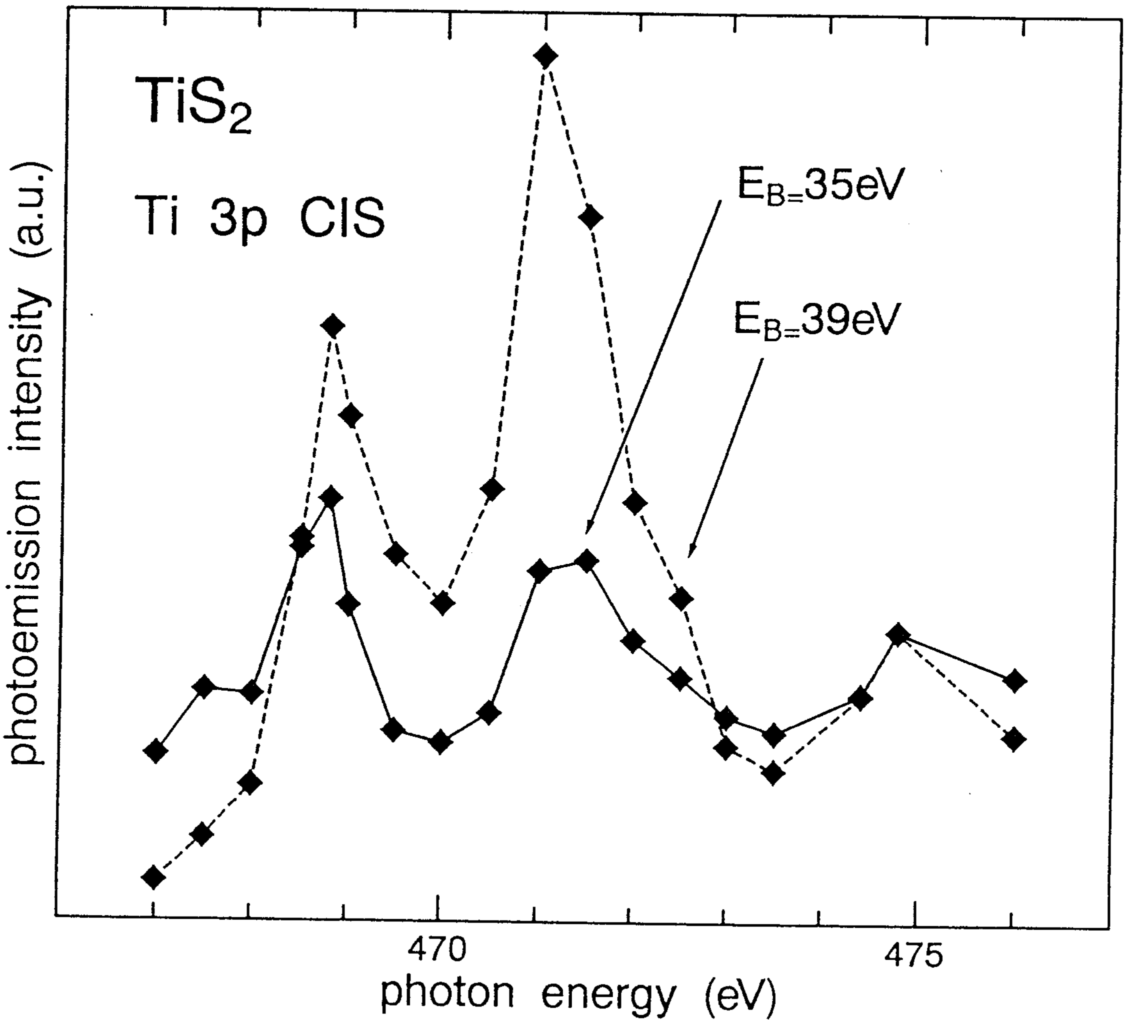
TiS$_2$
Ti 3p CIS
E$_B$=35eV
E$_B$=39eV
photoemission intensity (a.u.)
470
475
photon energy (eV)

Fig. 2.16. (a)

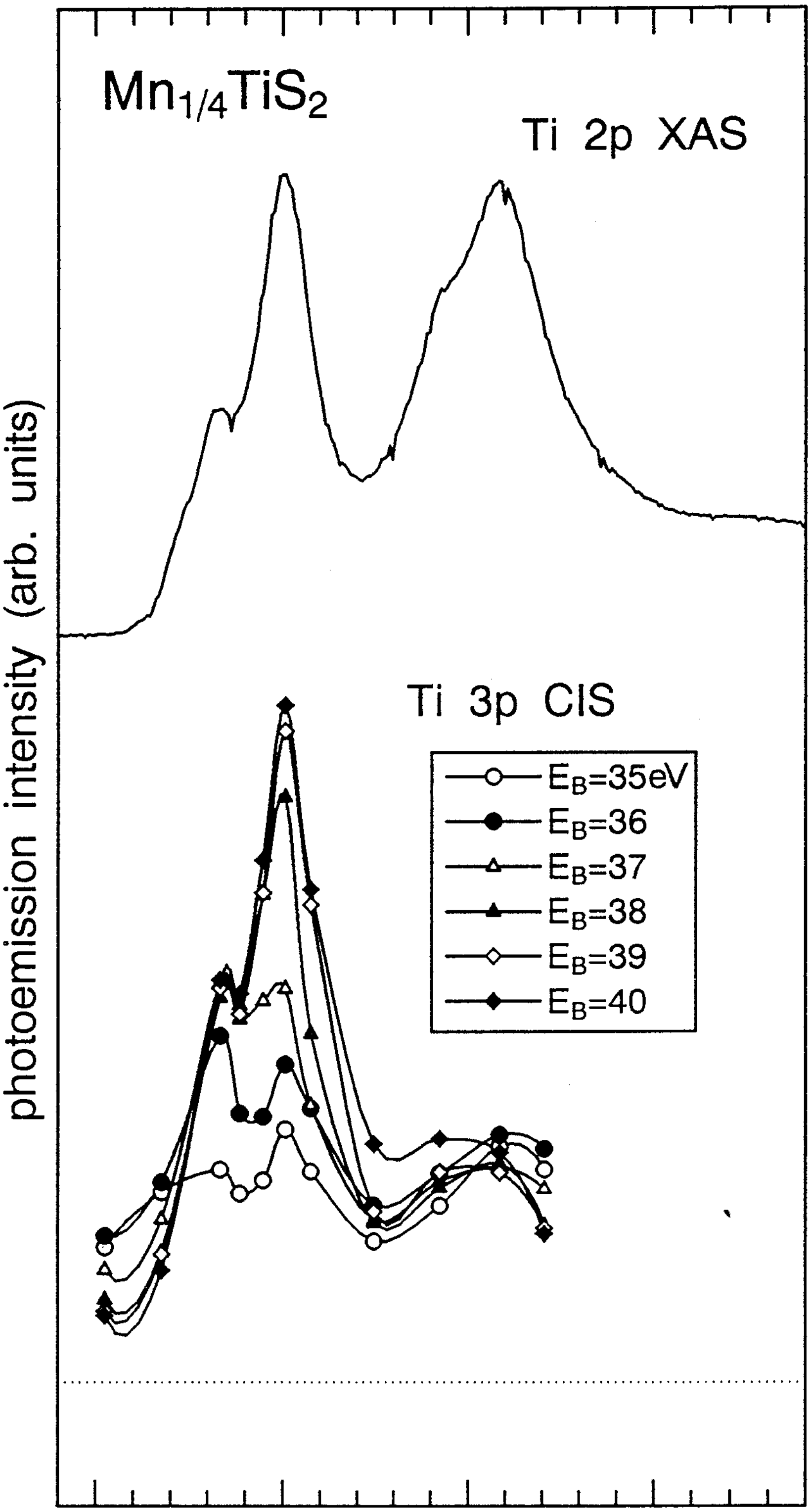

Mn$_{1/4}$TiS$_2$
Ti 2p XAS
Ti 3p CIS
E$_B$=35eV
E$_B$=36
E$_B$=37
E$_B$=38
E$_B$=39
E$_B$=40
photoemission intensity (arb. units)
-5
0
5
10
relative photon energy (eV)

(b)

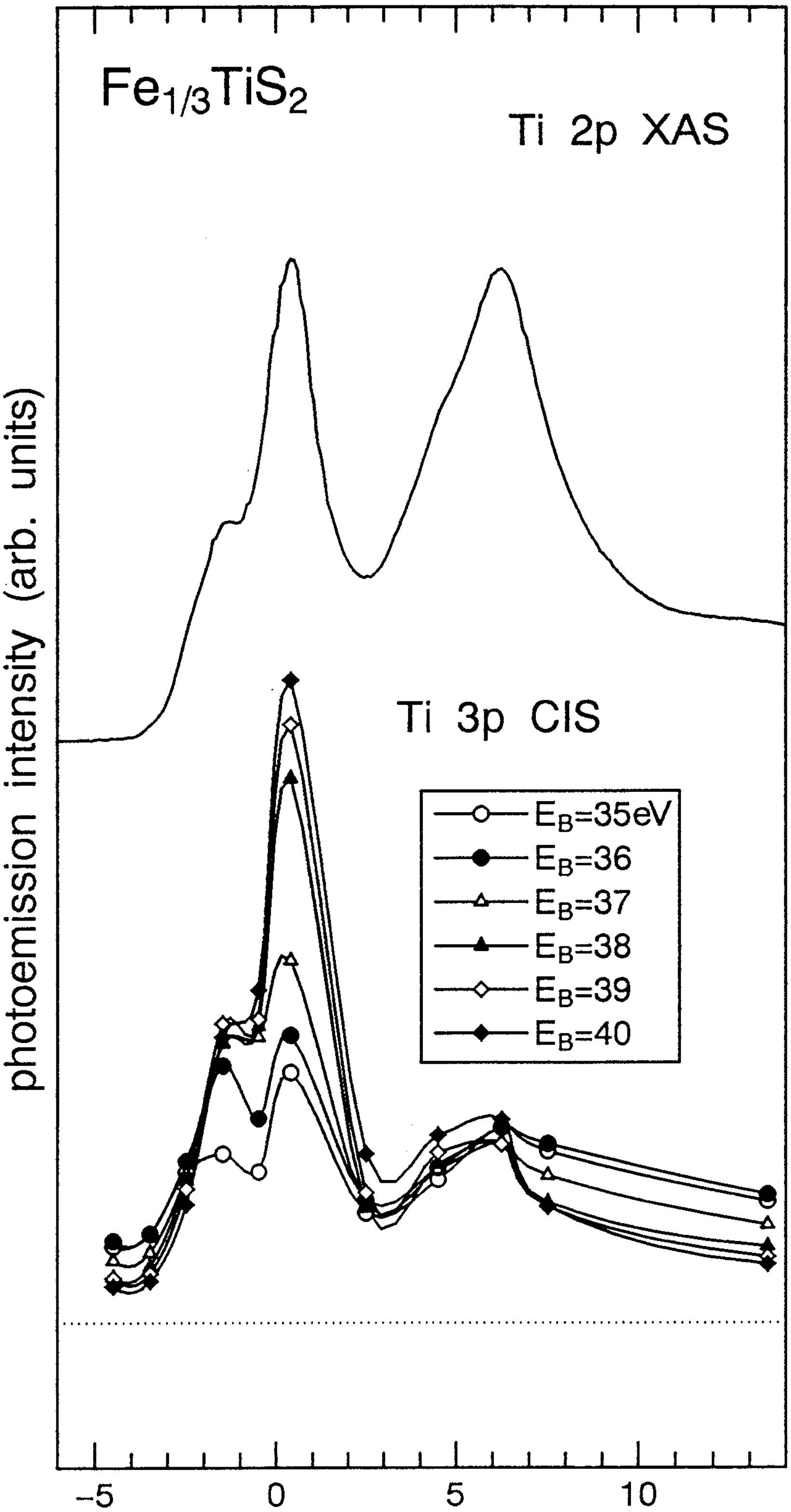
Fe$_{1/3}$TiS$_2$
Ti 2p XAS
Ti 3p CIS
E$_B$=35eV
E$_B$=36
E$_B$=37
E$_B$=38
E$_B$=39
E$_B$=40
photoemission intensity (arb. units)
−5
0
5
10
relative photon energy (eV)

(c)

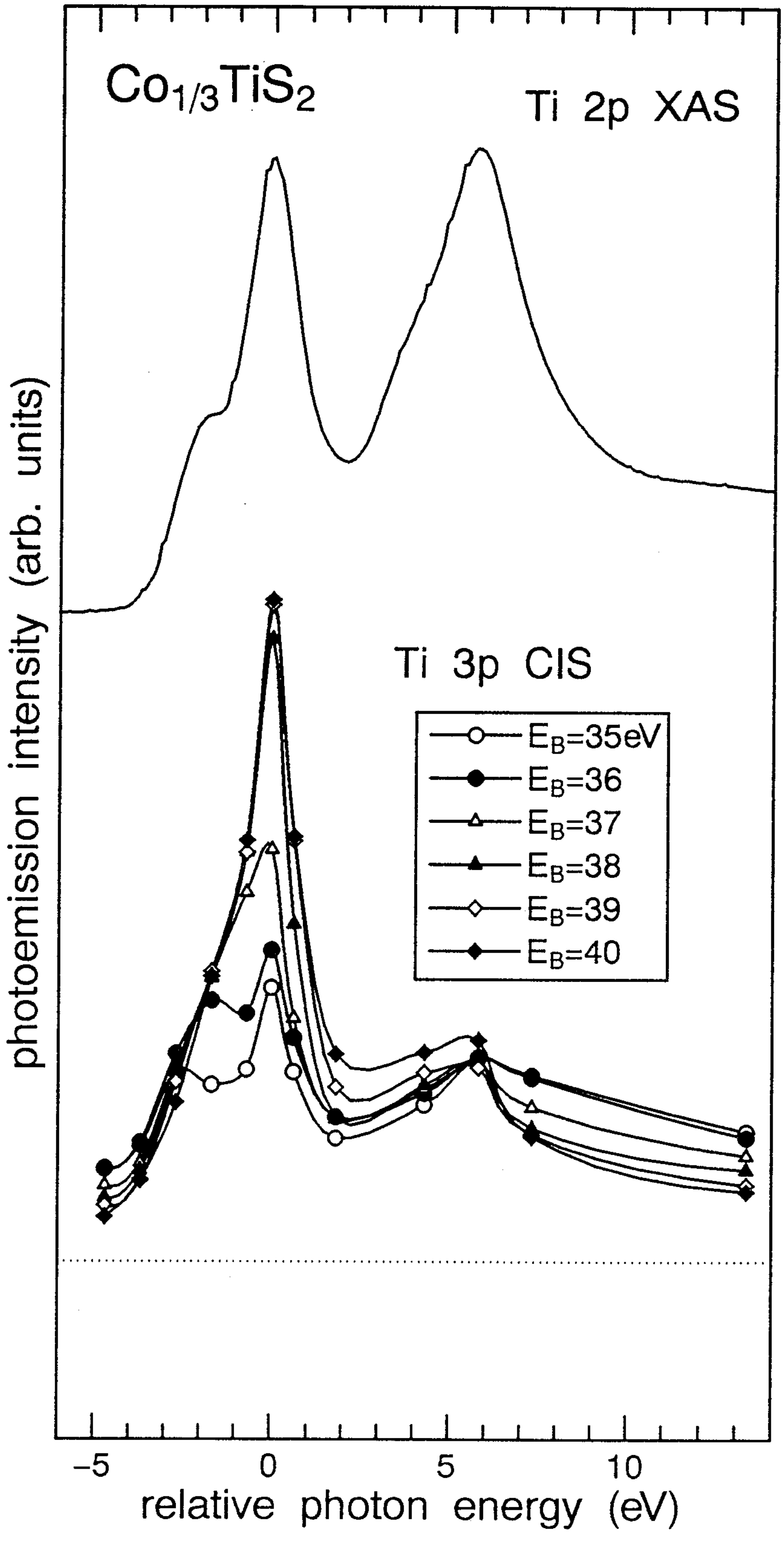

Co$_{1/3}$TiS$_2$
Ti 2p XAS
Ti 3p CIS
○ E$_B$=35eV
● E$_B$=36
△ E$_B$=37
▲ E$_B$=38
◇ E$_B$=39
◆ E$_B$=40
photoemission intensity (arb. units)
−5
0
5
10
relative photon energy (eV)

(d)

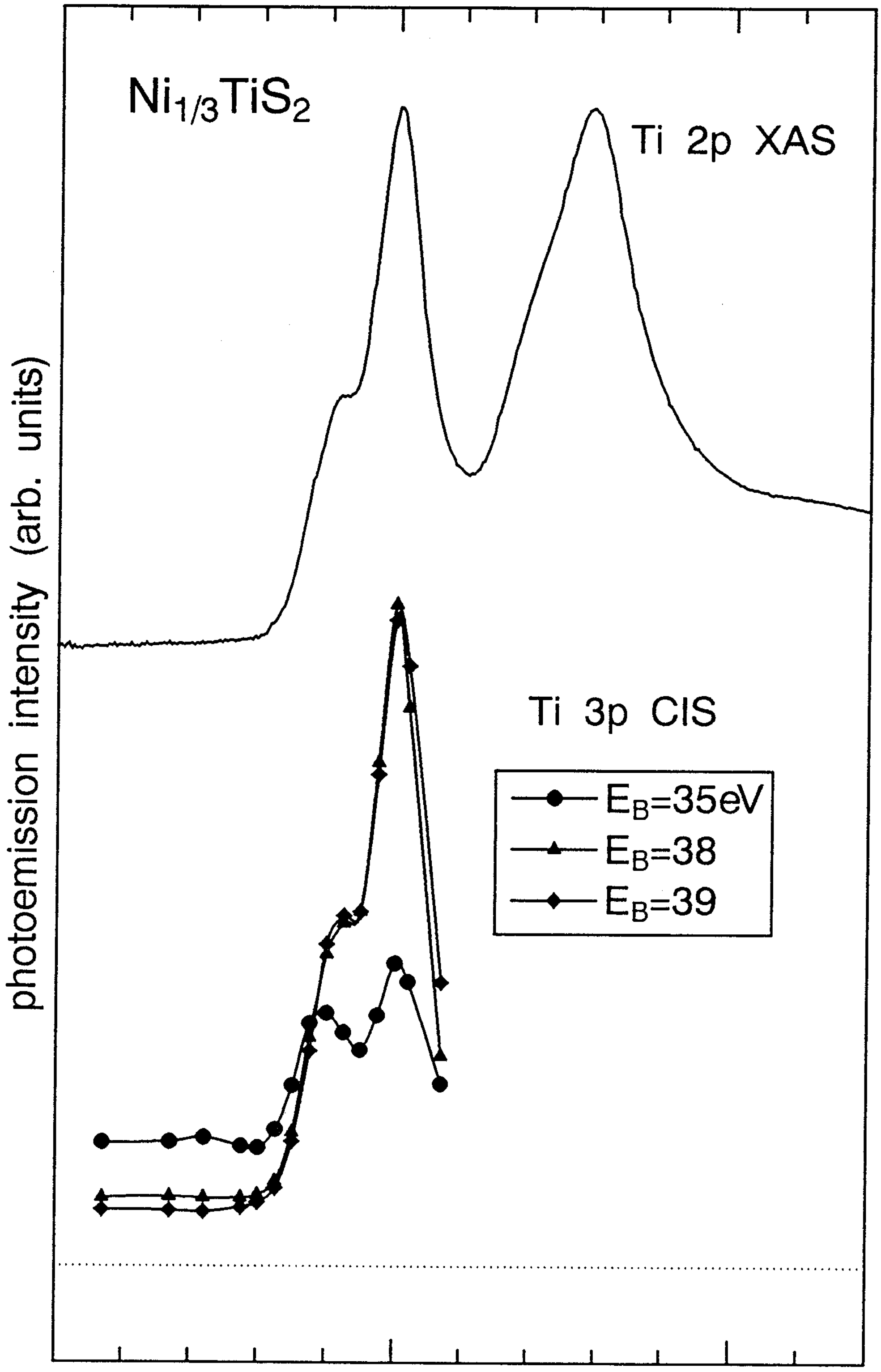
$Ni_{1/3}TiS_2$
Ti 2p XAS
Ti 3p CIS
E_B=35eV
E_B=38
E_B=39
photoemission intensity (arb. units)
−10
0
10
relative photon energy (eV)

(e)

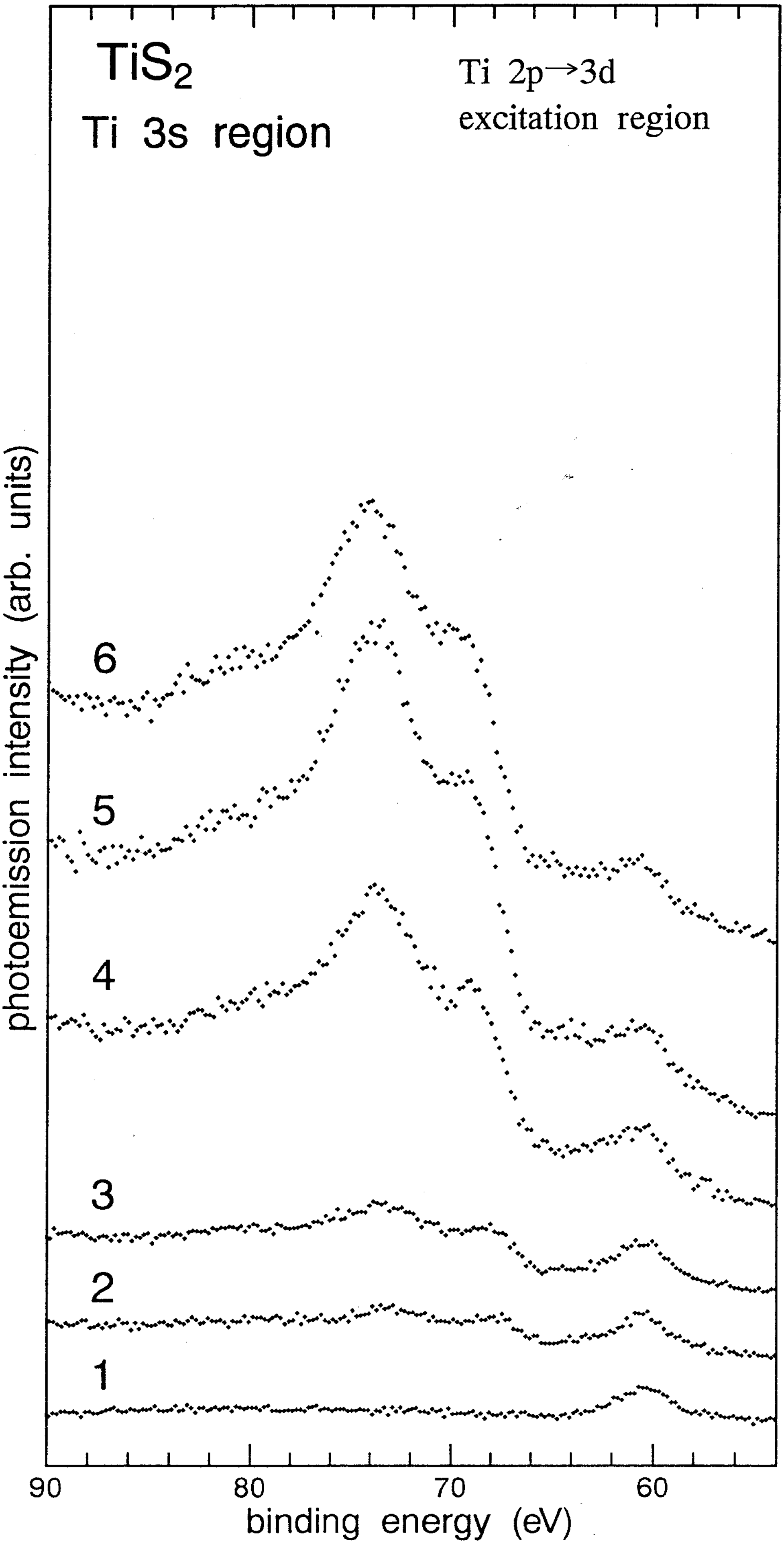
TiS$_2$
Ti 3s region
Ti 2p→3d
excitation region
photoemission intensity (arb. units)
6
5
4
3
2
1
90
80
70
60
binding energy (eV)

Fig. 2.17.

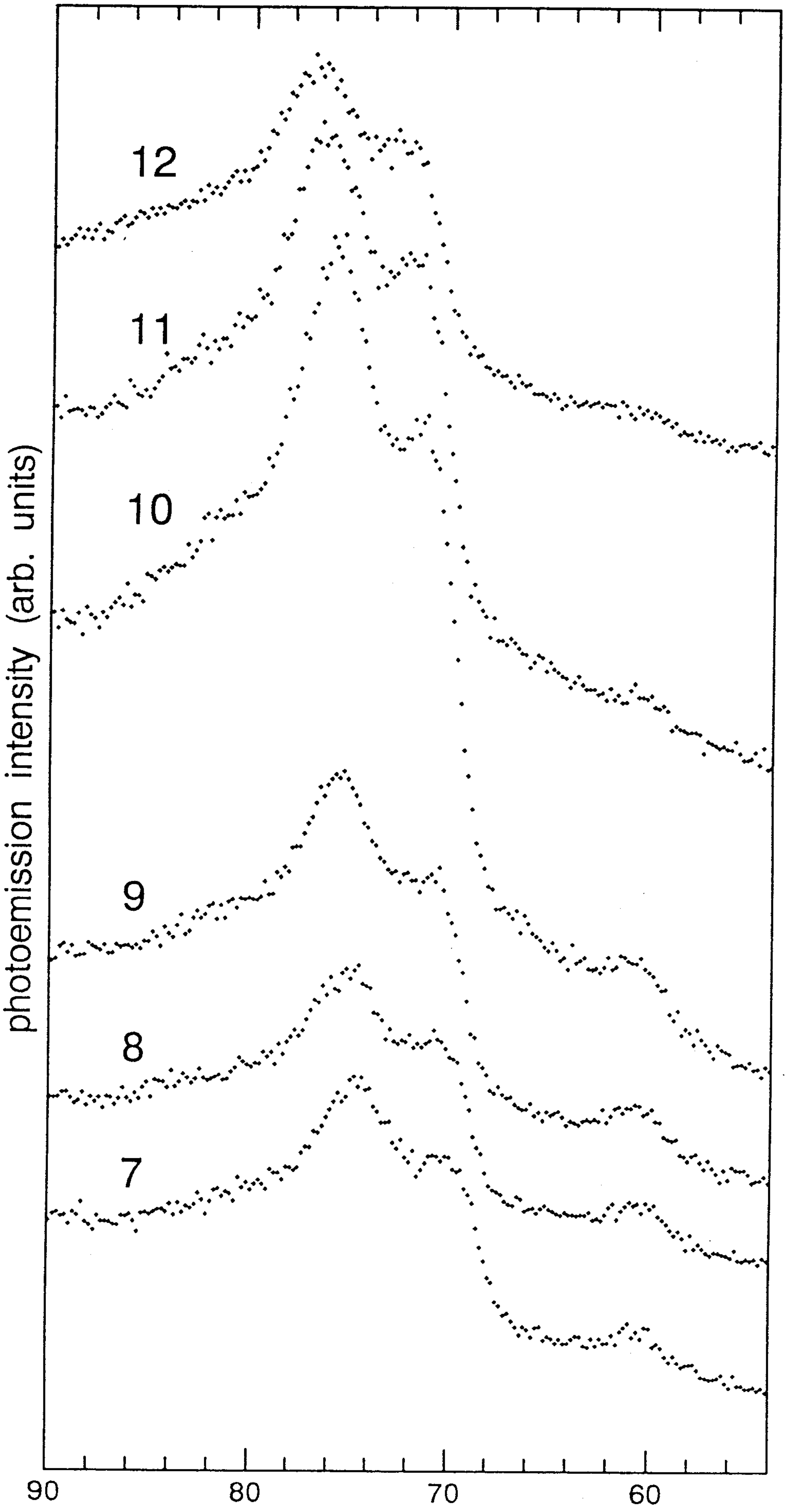
12
11
10
9
8
7
photoemission intensity (arb. units)
90
80
70
60
binding energy (eV)

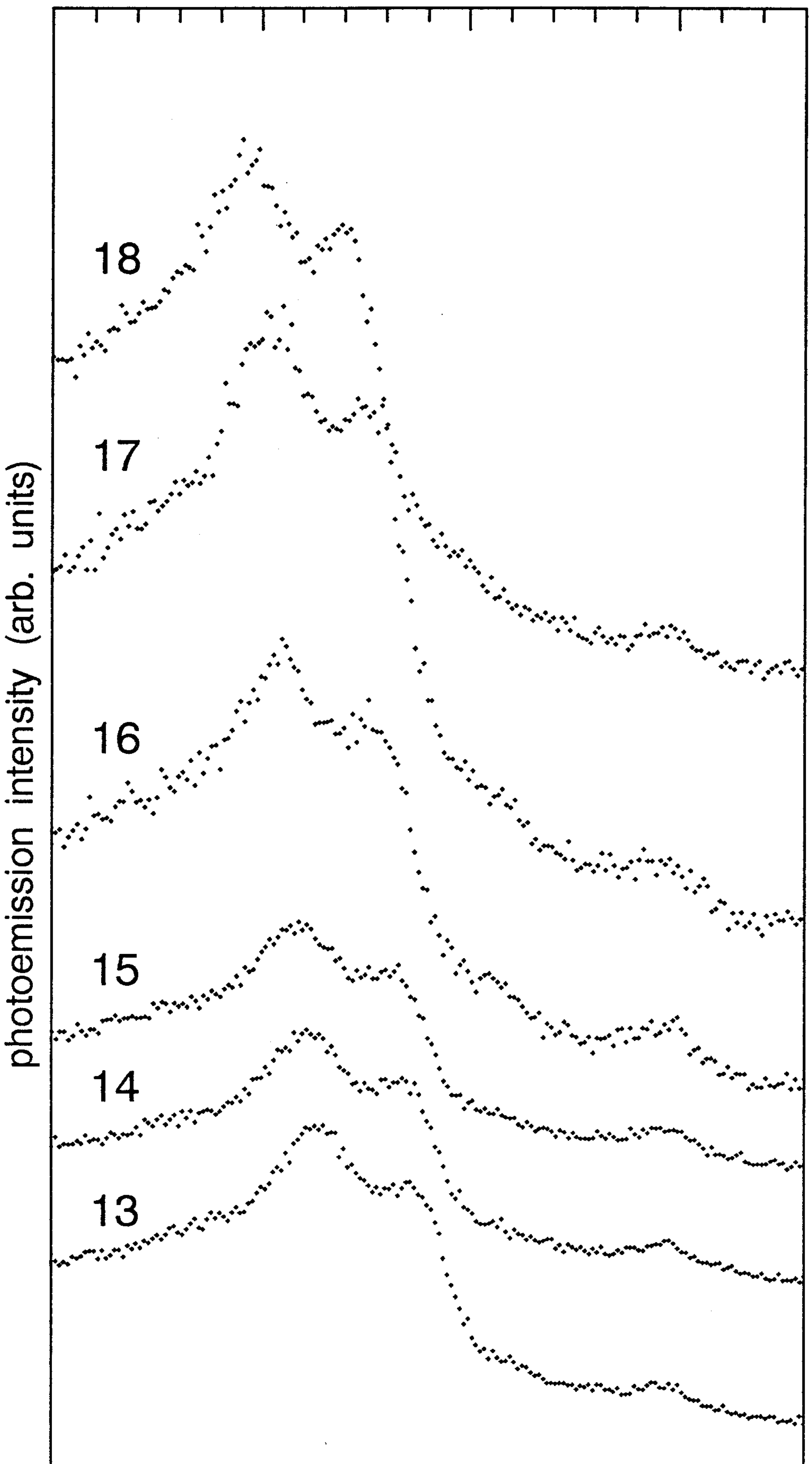
18
17
16
15
14
13
photoemission intensity (arb. units)
90
80
70
60
binding energy (eV)

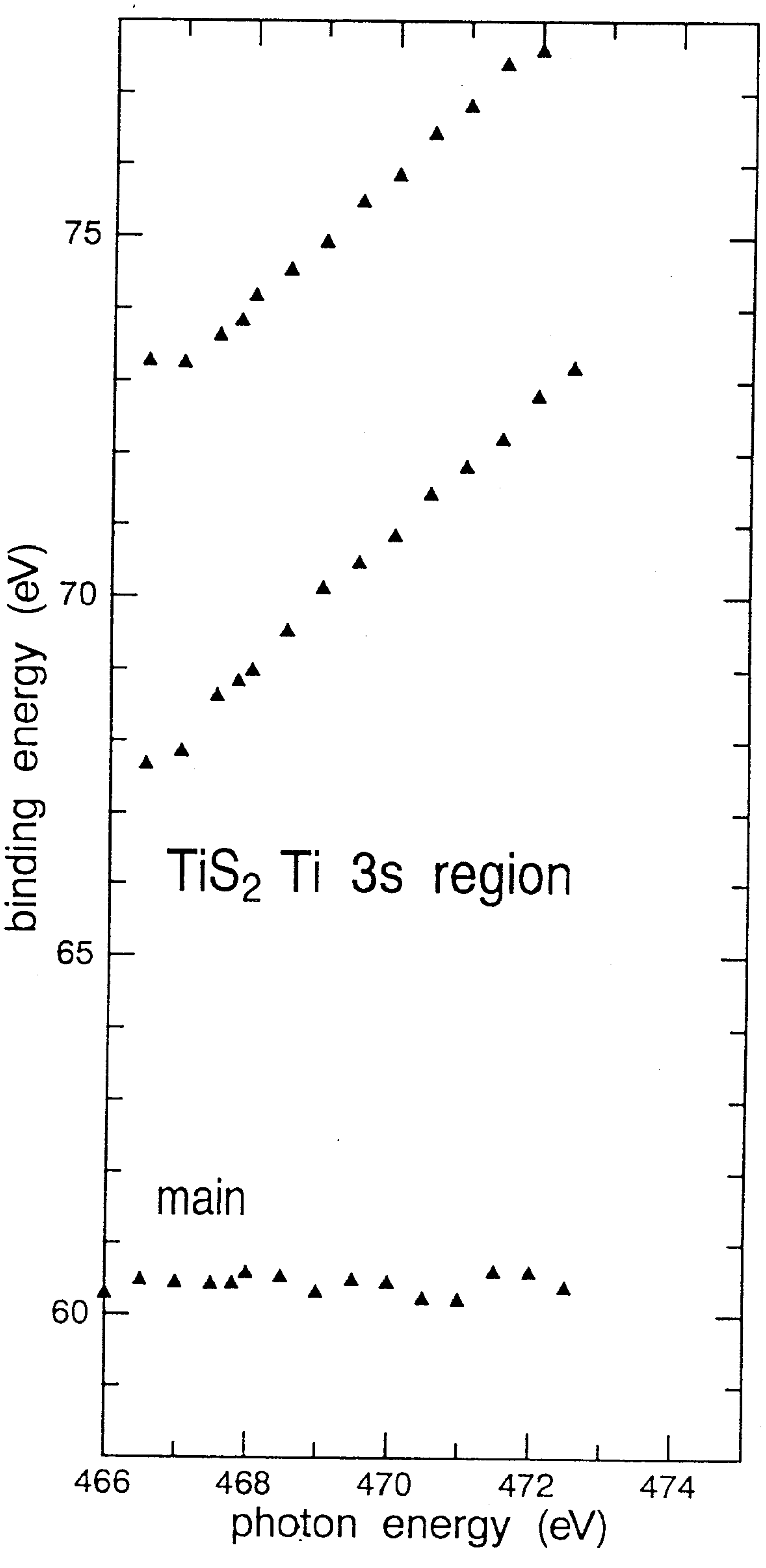
binding energy (eV)
75
70
65
60
TiS$_2$ Ti 3s region
main
466
468
470
472
474
photon energy (eV)

Fig. 2.18.

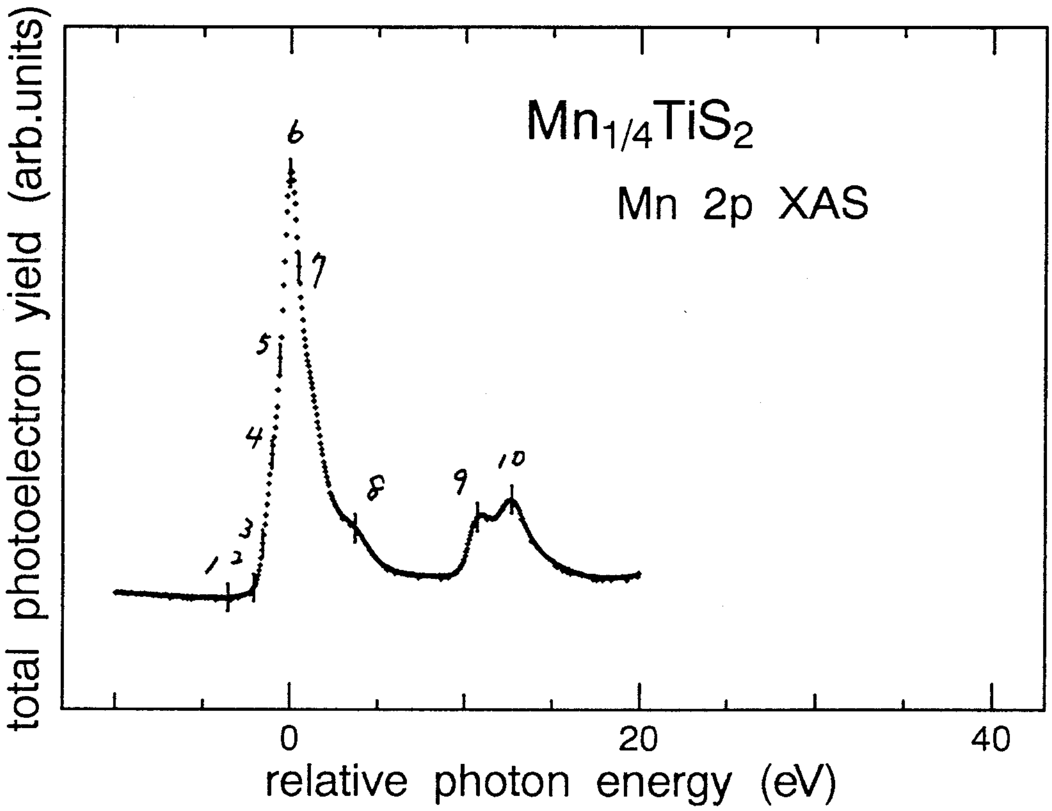
Mn$_{1/4}$TiS$_2$
Mn 2p XAS
total photoelectron yield (arb.units)
relative photon energy (eV)
0
20
40
1
2
3
4
5
6
7
8
9
10

Fig. 2.19. (a)

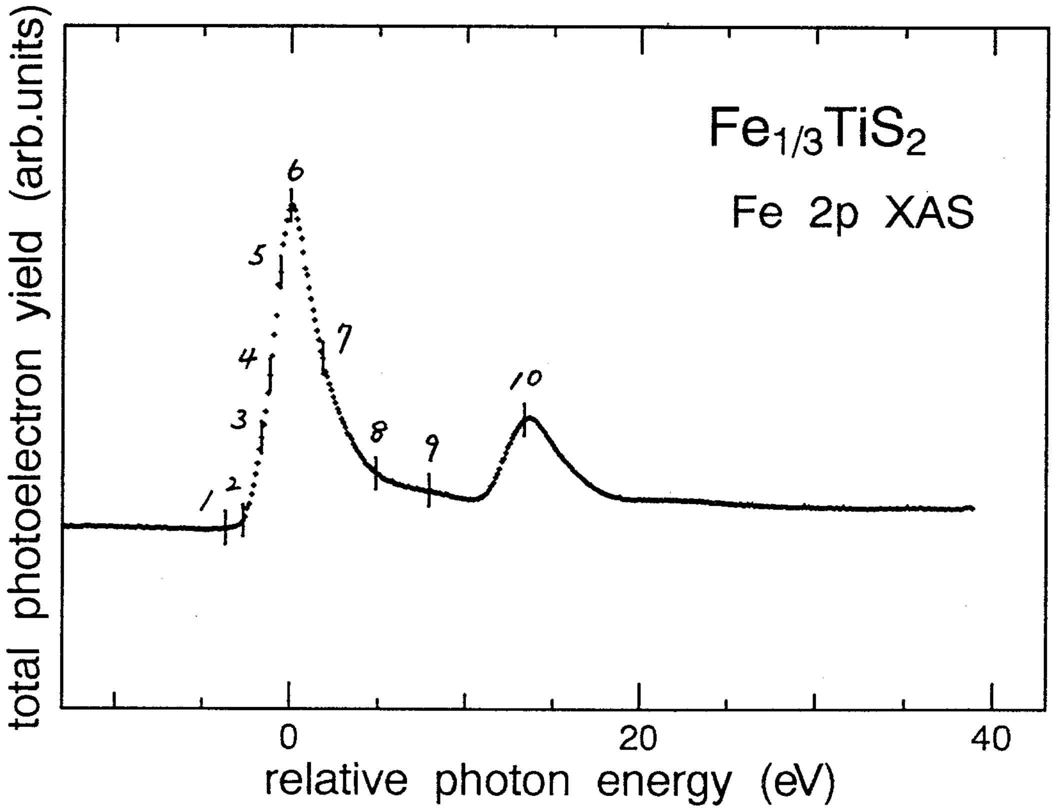
$Fe_{1/3}TiS_2$
Fe 2p XAS
total photoelectron yield (arb.units)
relative photon energy (eV)
0
20
40
1
2
3
4
5
6
7
8
9
10

(b)

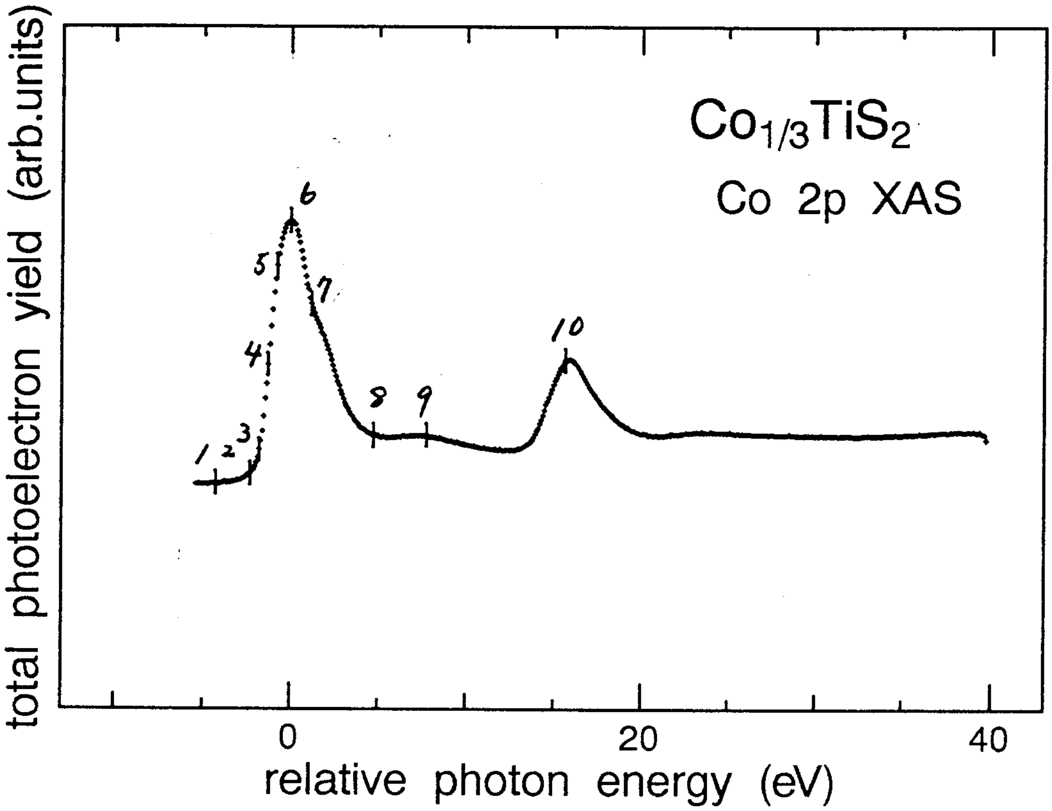
$Co_{1/3}TiS_2$
Co 2p XAS
total photoelectron yield (arb.units)
relative photon energy (eV)
0
20
40
1
2
3
4
5
6
7
8
9
10

(c)

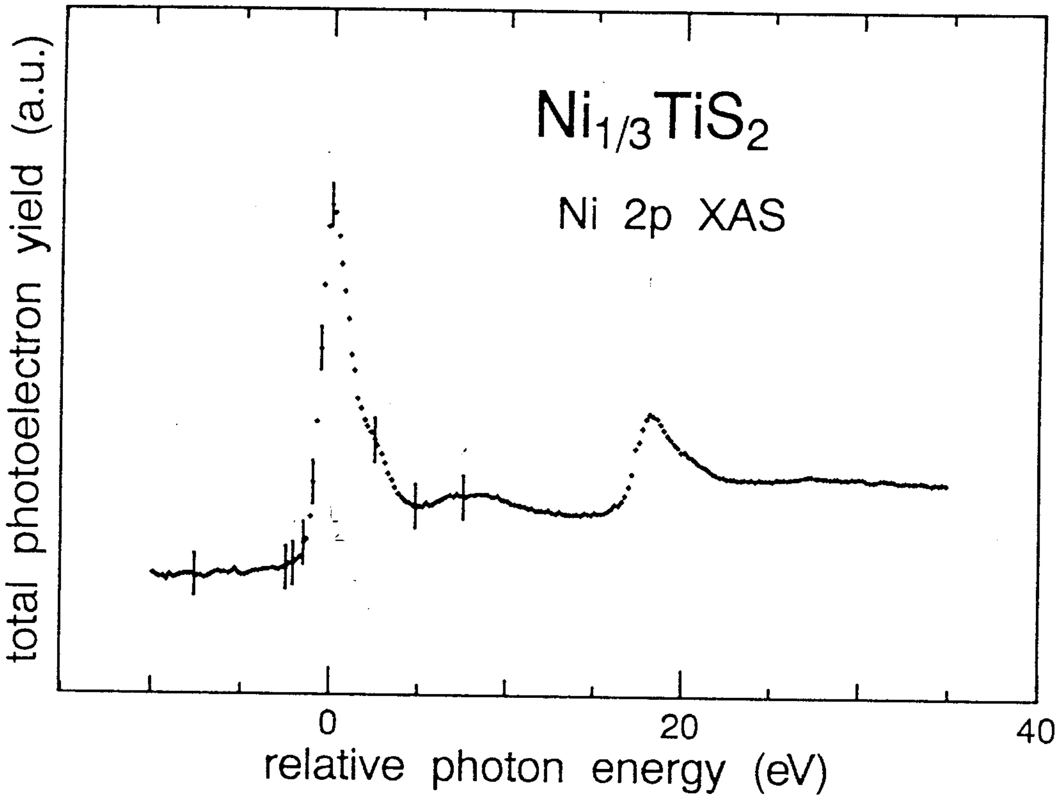
Ni$_{1/3}$TiS$_2$
Ni 2p XAS
total photoelectron yield (a.u.)
relative photon energy (eV)
0
20
40

(d)

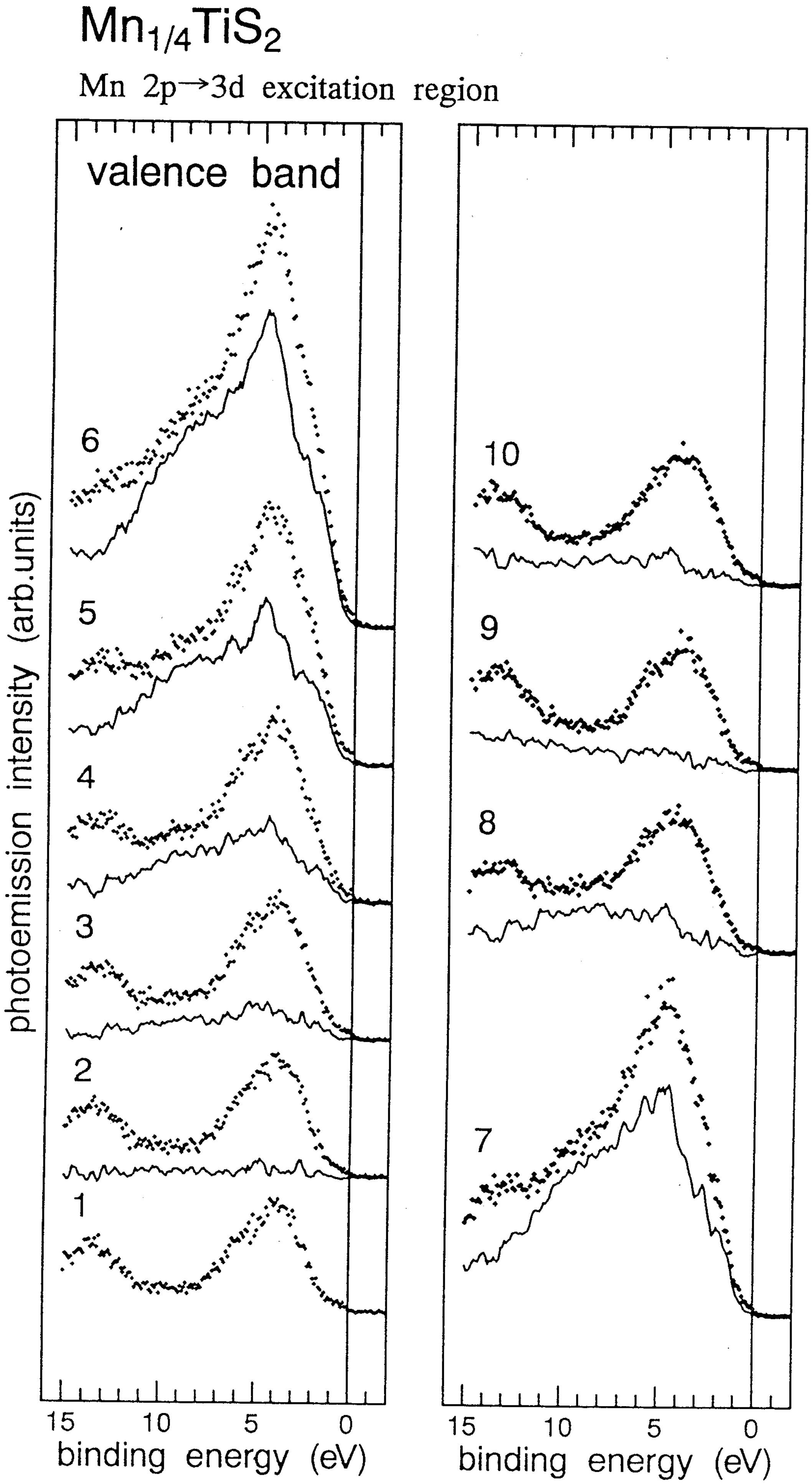
$Mn_{1/4}TiS_2$
Mn 2p→3d excitation region
valence band
photoemission intensity (arb.units)
6
5
4
3
2
1
10
9
8
7
15
10
5
0
binding energy (eV)
15
10
5
0
binding energy (eV)

(a)

Fig. 2.20.

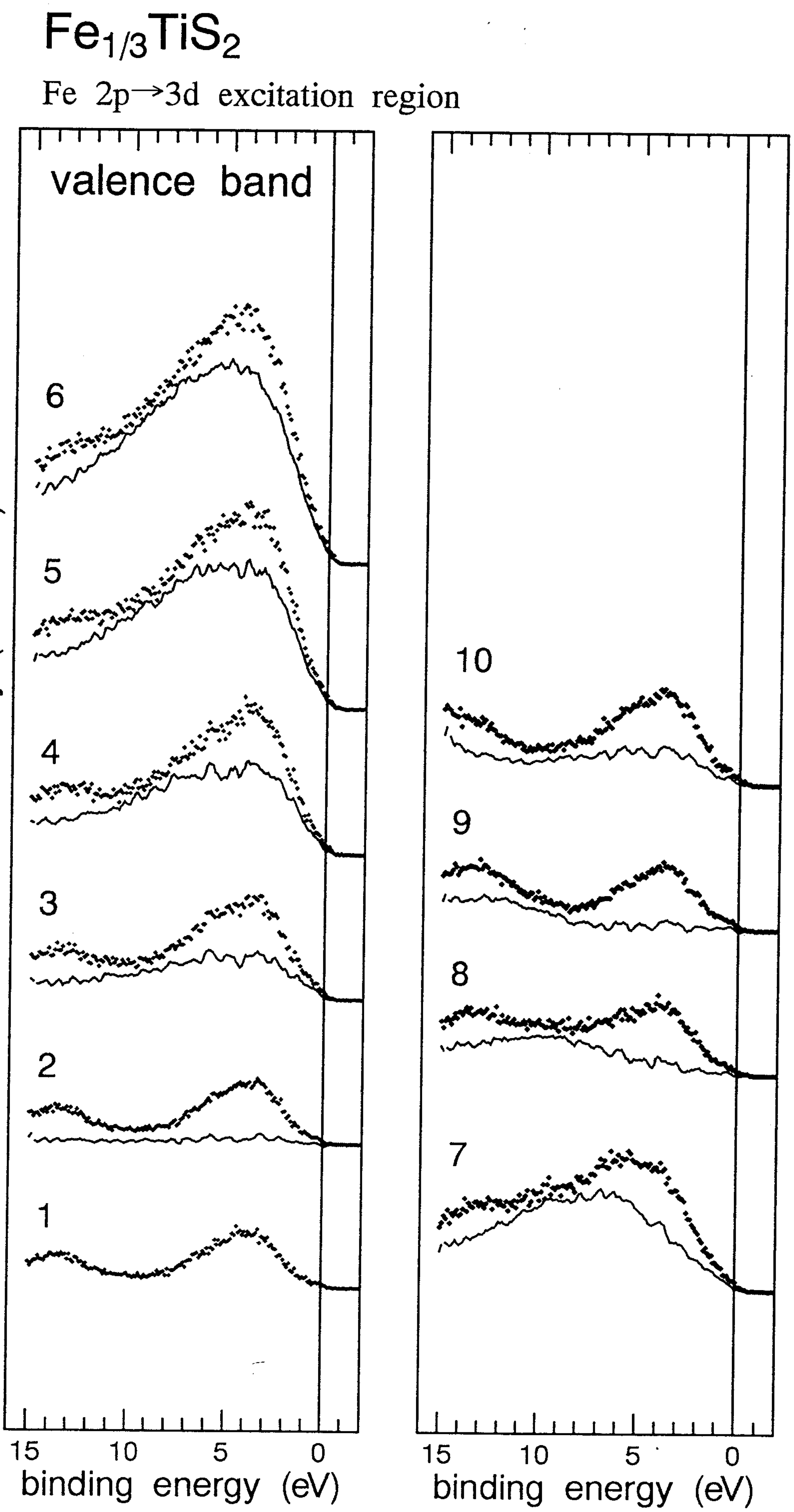
$Fe_{1/3}TiS_2$
Fe 2p→3d excitation region
valence band
photoemission intensity (arb.units)
6
5
4
3
2
1
10
9
8
7
15
10
5
0
binding energy (eV)
15
10
5
0
binding energy (eV)

(b)

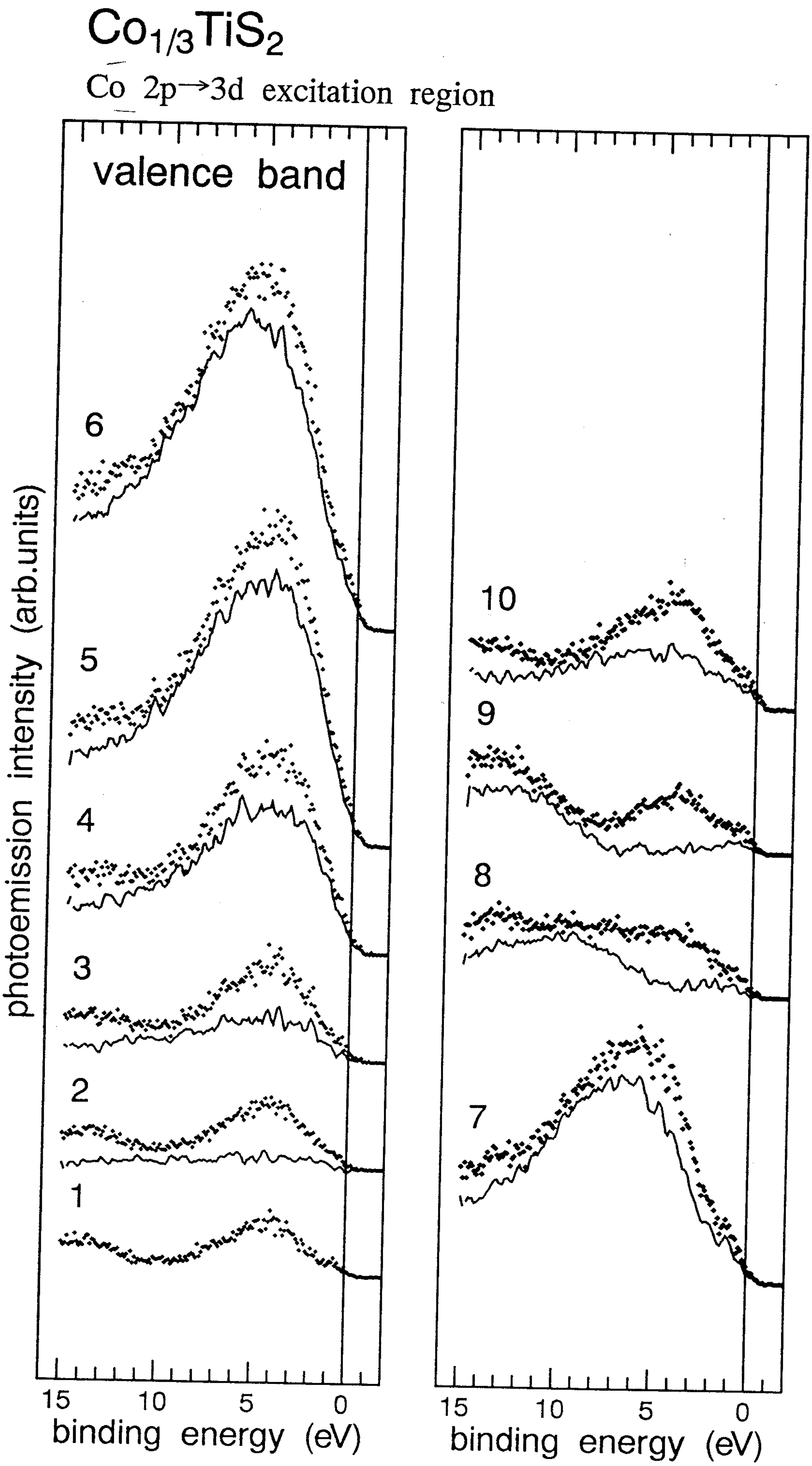
$Co_{1/3}TiS_2$
Co 2p→3d excitation region
valence band
photoemission intensity (arb.units)
1
2
3
4
5
6
7
8
9
10
15
10
5
0
binding energy (eV)
15
10
5
0
binding energy (eV)

(c)

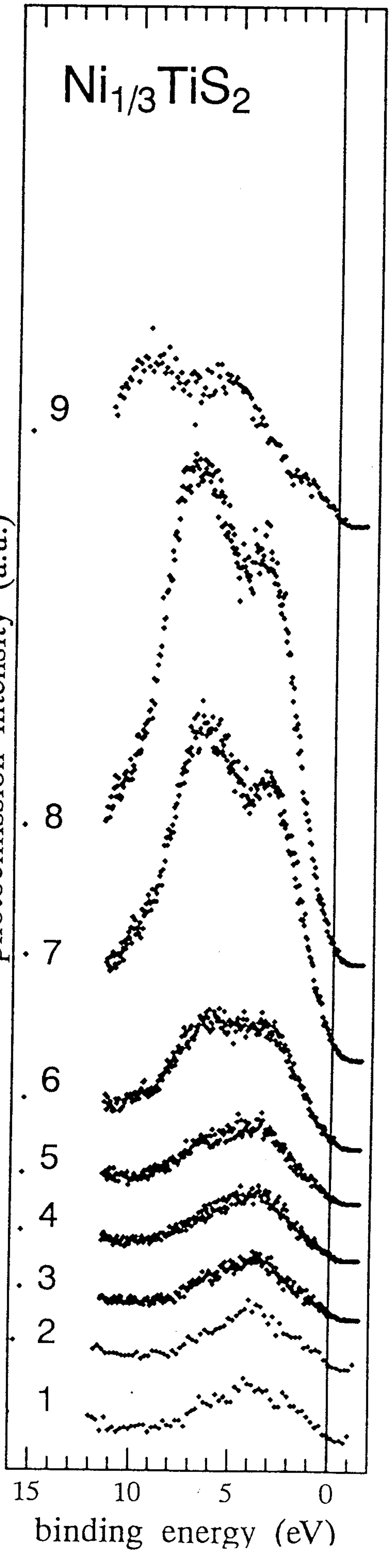
Ni$_{1/3}$TiS$_2$
9
8
7
6
5
4
3
2
1
photoemission intensity (a.u.)
15
10
5
0
binding energy (eV)

(d)

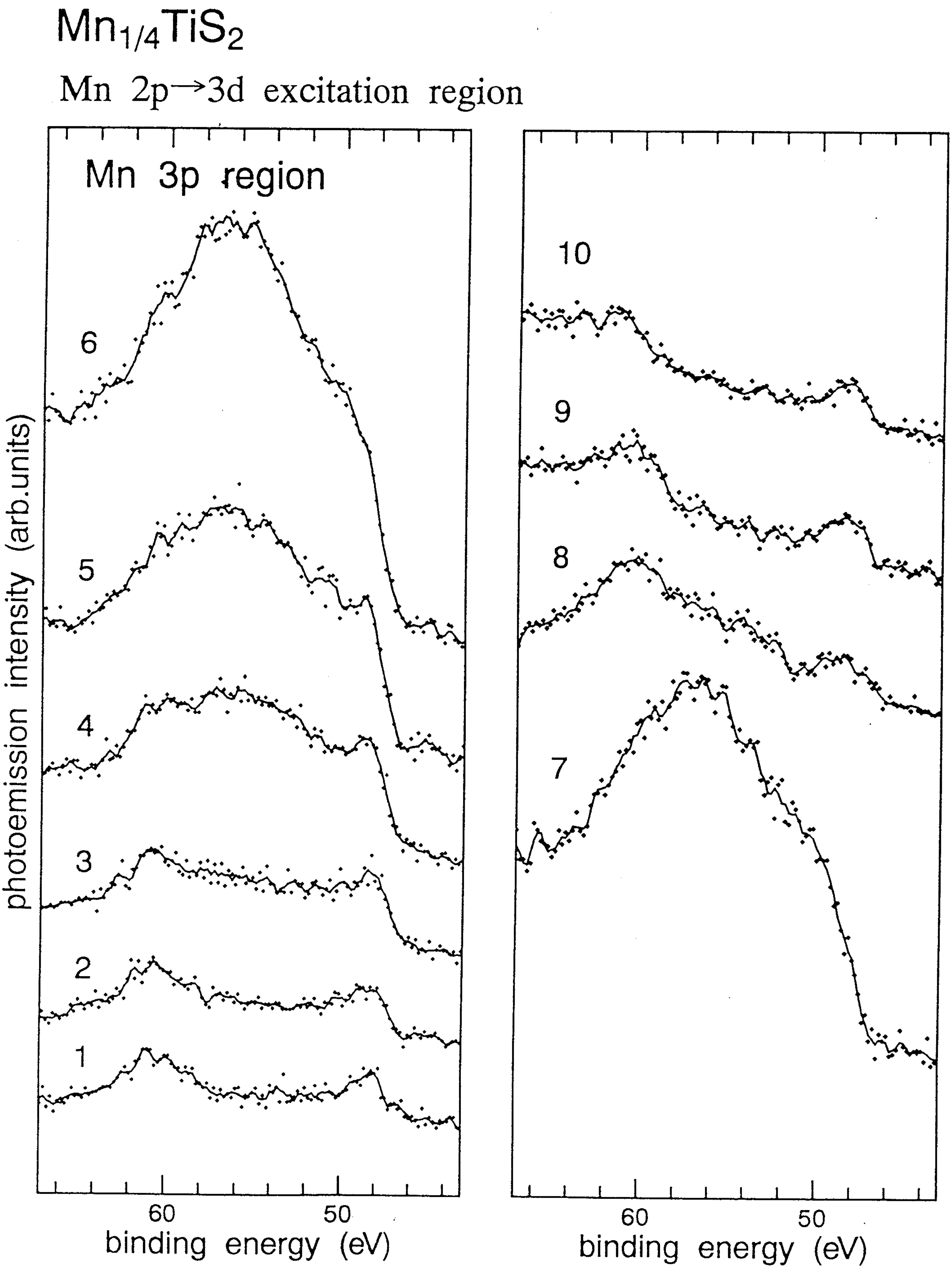
$Mn_{1/4}TiS_2$
Mn 2p→3d excitation region
Mn 3p region
photoemission intensity (arb.units)
1
2
3
4
5
6
7
8
9
10
60
50
60
50
binding energy (eV)
binding energy (eV)

Fig. 2.21.

(a)

$Fe_{1/3}TiS_2$

Fe 2p→3d excitation region

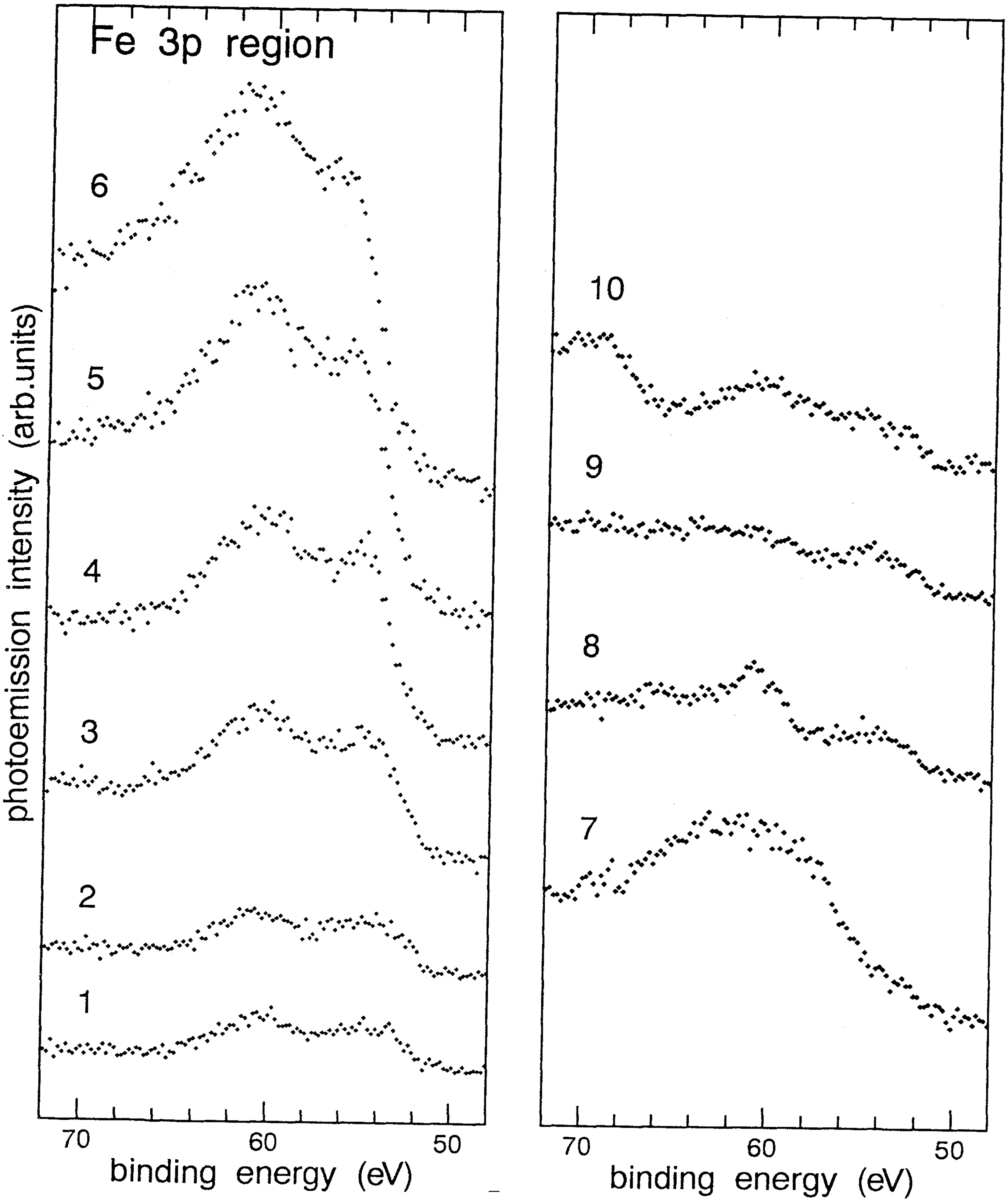

(b)

$Co_{1/3}TiS_2$

Co 2p→3d excitation region

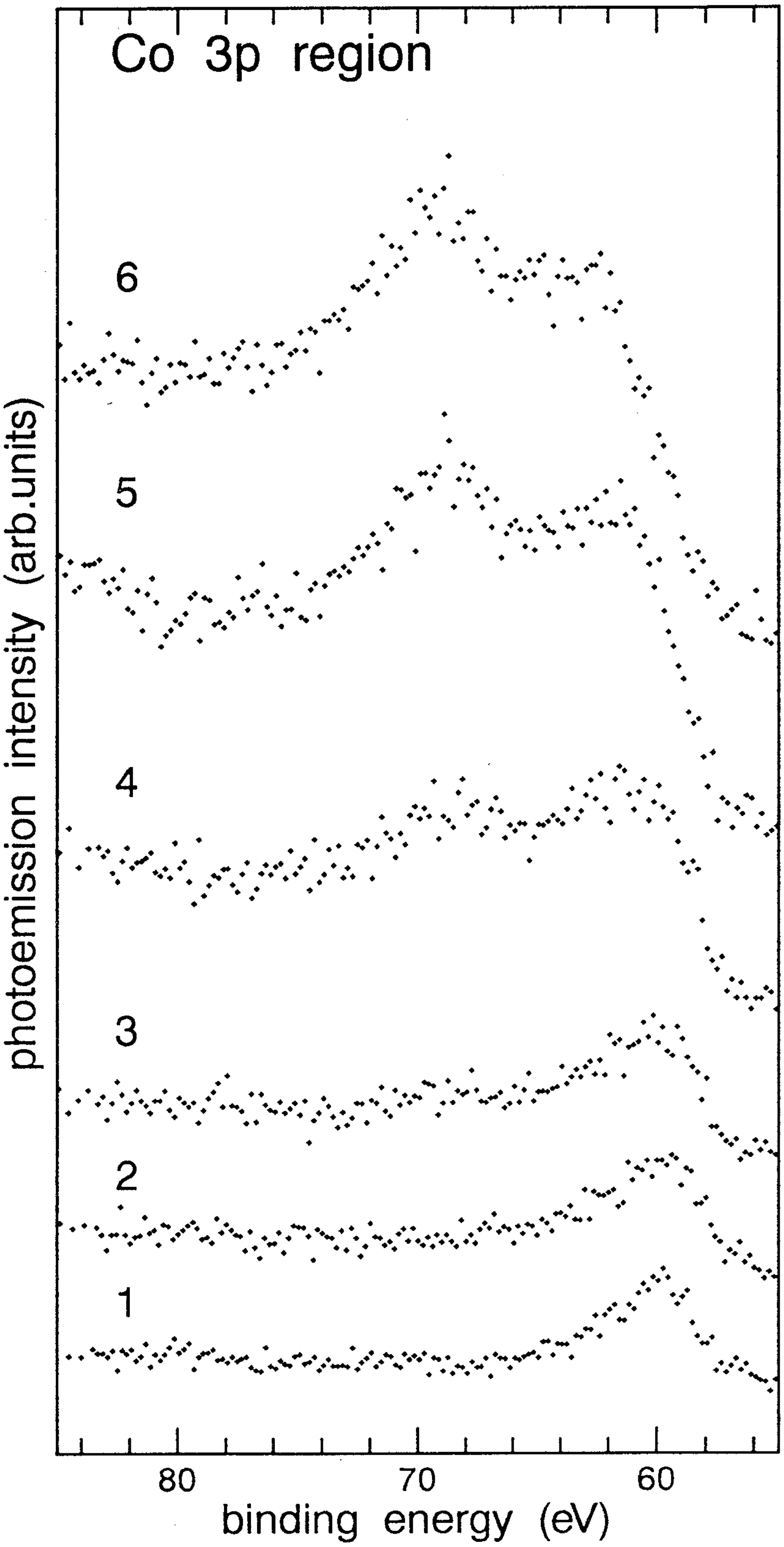

(c)

$Co_{1/3}TiS_2$

Co 2p→3d excitation region

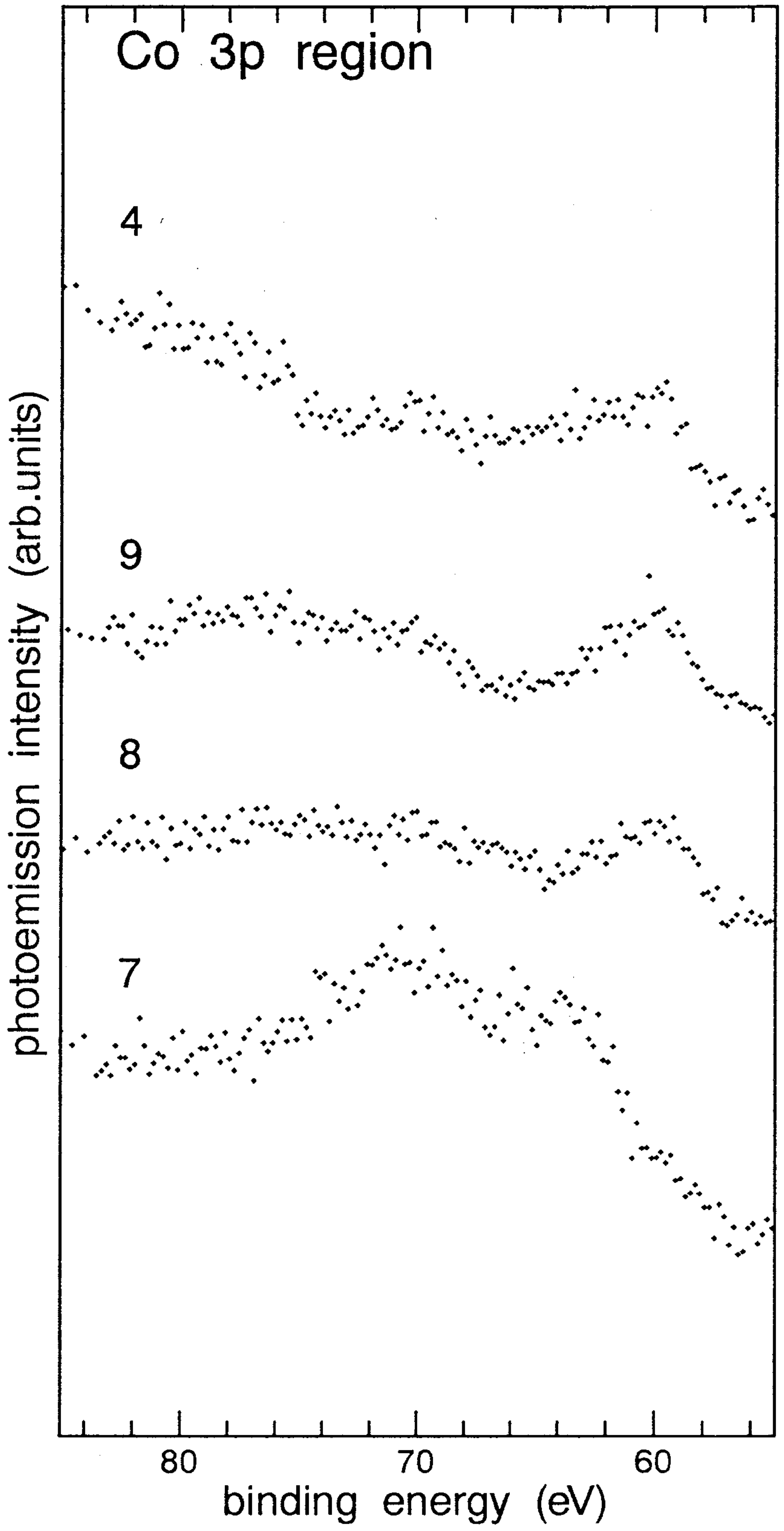

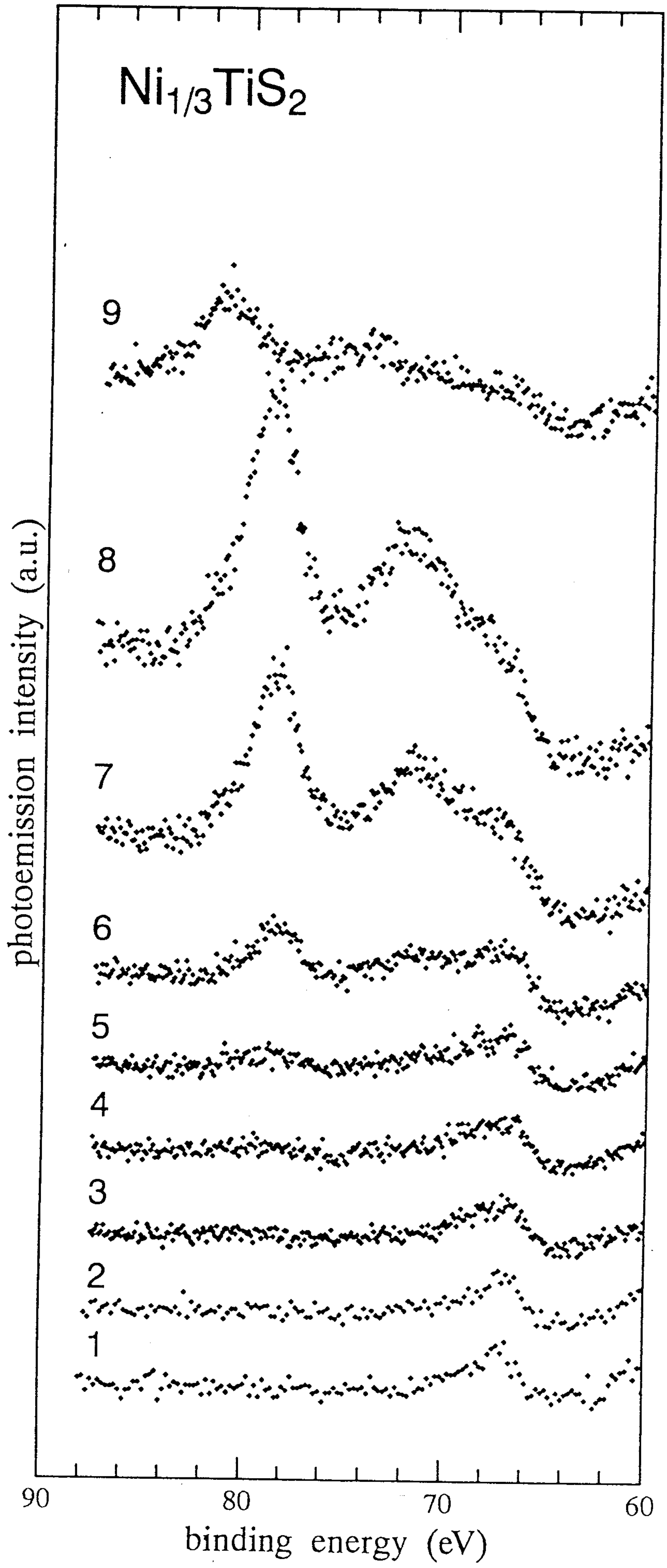

Ni$_{1/3}$TiS$_2$
9
8
7
6
5
4
3
2
1
photoemission intensity (a.u.)
90
80
70
60
binding energy (eV)

(d)

d^0 system in octahedral coordination

valence band photoemission

ground state wave function

$3d^0 \quad + \quad 3d^1(e_g)\underline{L}$

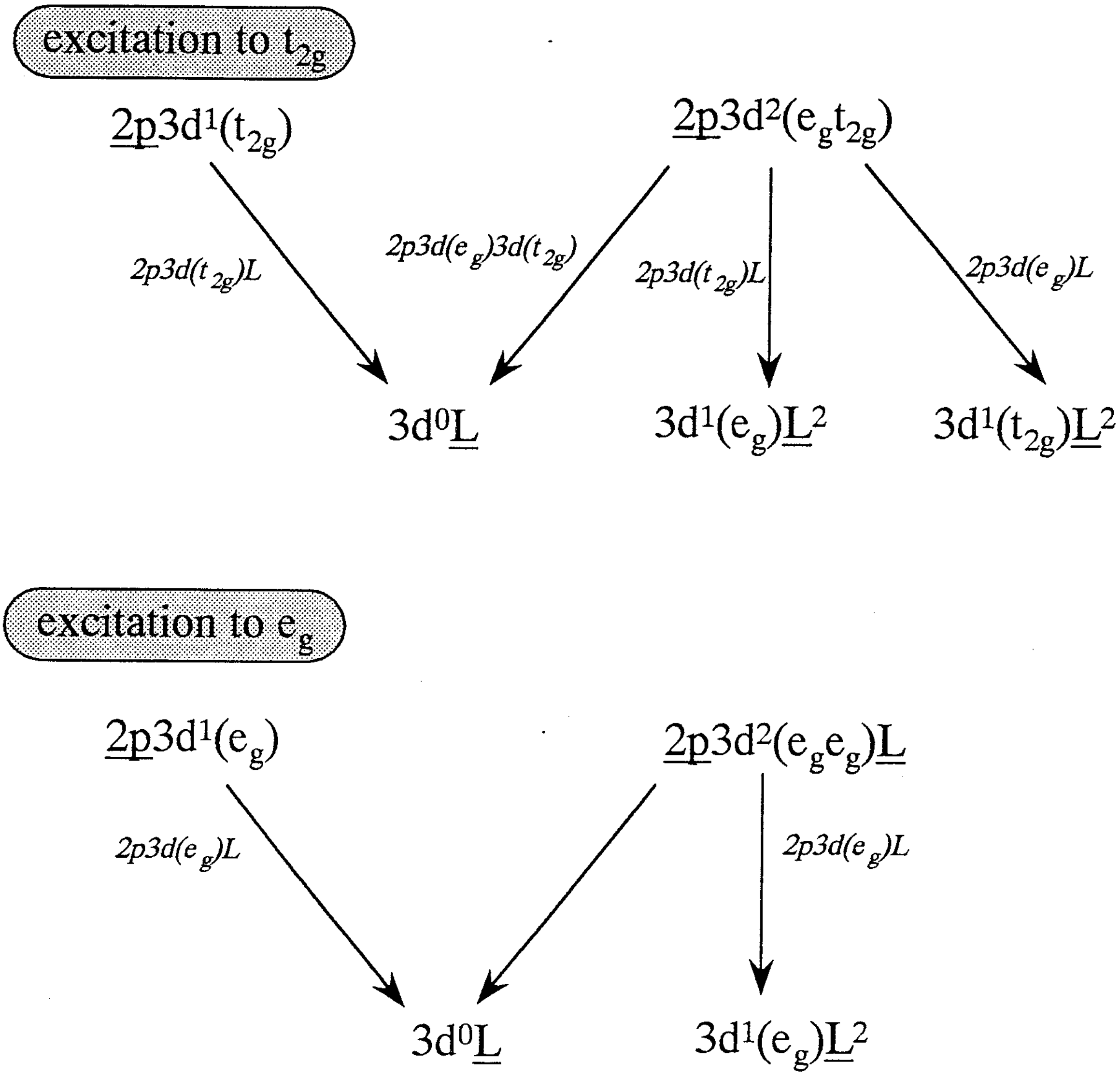

Fig. 2.22.

d^1 system in octahedral coordination

valence band photoemission

ground state wave function

$$3d^1(t_{2g}) + 3d^2(t_{2g}e_g)\underline{L}$$

excitation to t_{2g}

$$\begin{tikzcd}
\underline{2p}3d^2(t_{2g}t_{2g}) \arrow[d, "2p3d(t_{2g})3d(t_{2g})"'] & & & \underline{2p}3d^3(t_{2g}t_{2g}e_g)\underline{L} \arrow[dl, "2p3d(t_{2g})3d(t_{2g})"'] \arrow[dr, "2p3d(t_{2g})3d(e_g)"] & \\
3d^0 & & 3d^1(e_g)\underline{L} & & 3d^1(t_{2g})\underline{L}
\end{tikzcd}$$

excitation to e_g

$$\begin{tikzcd}
\underline{2p}3d^2(t_{2g}e_g) \arrow[d, "2p3d(t_{2g})3d(e_g)"'] & & & \underline{2p}3d^3(t_{2g}e_ge_g)\underline{L} \arrow[dl, "2p3d(t_{2g})3d(e_g)"'] \arrow[dr, "2p3d(e_g)3d(e_g)"] & \\
3d^0 & & 3d^1(e_g)\underline{L} & & 3d^1(t_{2g})\underline{L}
\end{tikzcd}$$

Fig. 2.23.

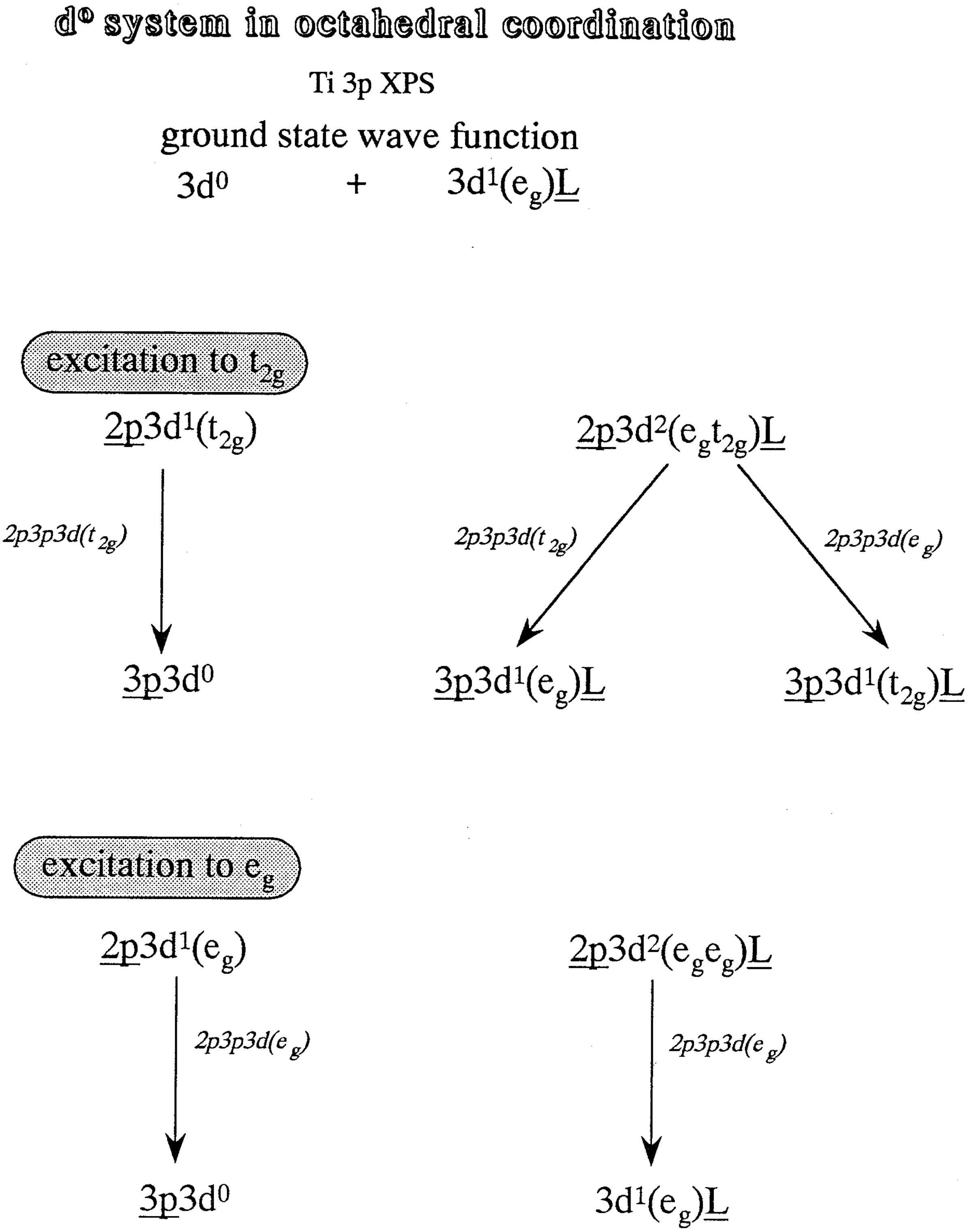
d^0 system in octahedral coordination
Ti 3p XPS
ground state wave function
$3d^0$ + $3d^1(e_g)\underline{L}$
excitation to t_{2g}
$\underline{2p}3d^1(t_{2g})$
$2p3p3d(t_{2g})$
$\underline{3p}3d^0$
$\underline{2p}3d^2(e_g t_{2g})\underline{L}$
$2p3p3d(t_{2g})$
$2p3p3d(e_g)$
$\underline{3p}3d^1(e_g)\underline{L}$
$\underline{3p}3d^1(t_{2g})\underline{L}$
excitation to e_g
$\underline{2p}3d^1(e_g)$
$2p3p3d(e_g)$
$\underline{3p}3d^0$
$\underline{2p}3d^2(e_g e_g)\underline{L}$
$2p3p3d(e_g)$
$3d^1(e_g)\underline{L}$

Fig. 2.24.

d^1 system in octahedral coordination

Ti 3p XPS

ground state wave function

$3d^1(t_{2g}) + 3d^2(t_{2g}e_g)\underline{L}$

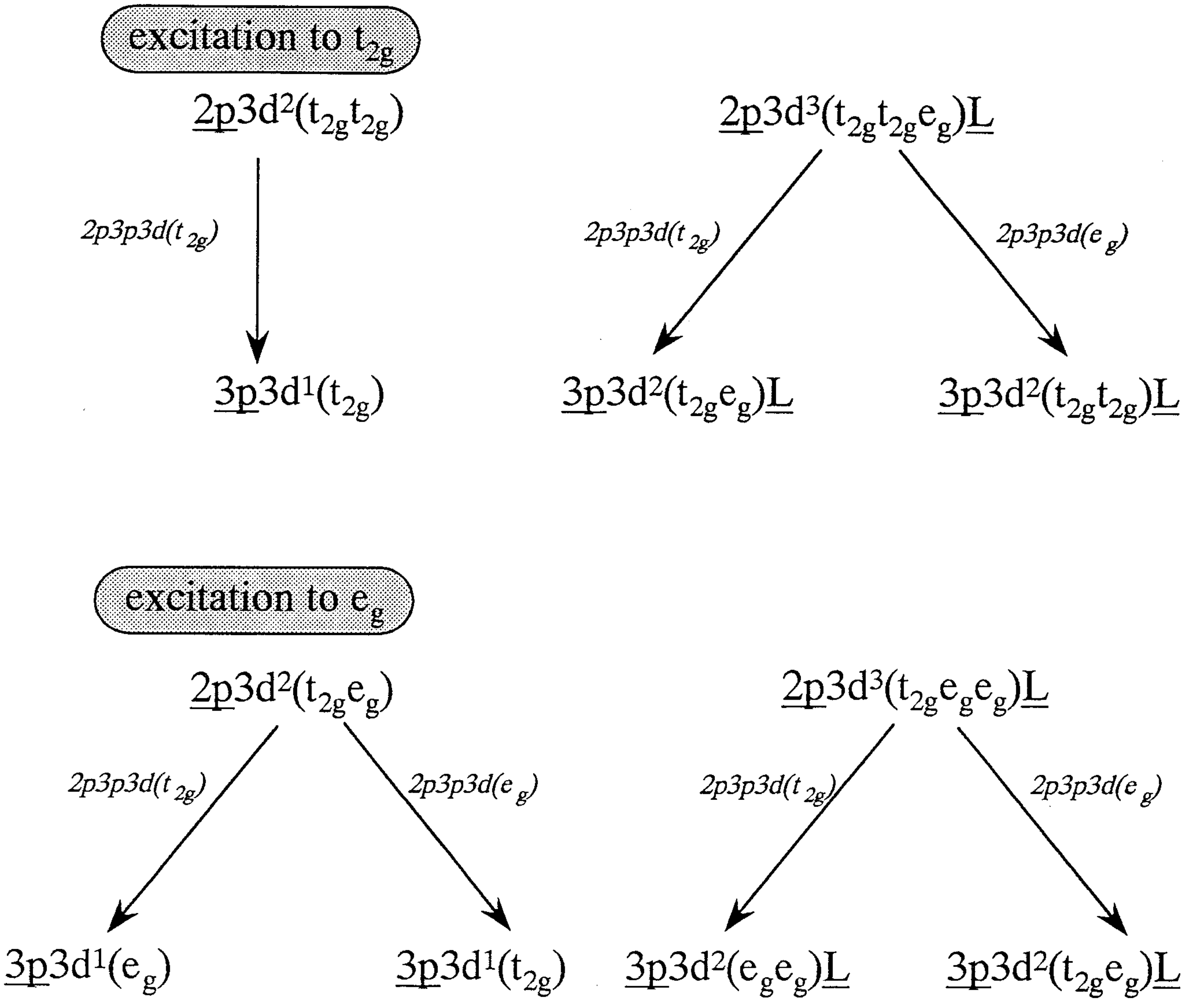

Fig. 2.25.